



HAL
open science

3D Ultrasound Localization Microscopy

Baptiste Heiles

► **To cite this version:**

Baptiste Heiles. 3D Ultrasound Localization Microscopy. Acoustics [physics.class-ph]. PSL Research University, 2019. English. NNT: . tel-02478291

HAL Id: tel-02478291

<https://theses.hal.science/tel-02478291>

Submitted on 13 Feb 2020

HAL is a multi-disciplinary open access archive for the deposit and dissemination of scientific research documents, whether they are published or not. The documents may come from teaching and research institutions in France or abroad, or from public or private research centers.

L'archive ouverte pluridisciplinaire **HAL**, est destinée au dépôt et à la diffusion de documents scientifiques de niveau recherche, publiés ou non, émanant des établissements d'enseignement et de recherche français ou étrangers, des laboratoires publics ou privés.



THÈSE DE DOCTORAT
DE L'UNIVERSITÉ PSL

Préparée à l'Ecole Supérieure de Physique et de Chimie Industrielles de
la Ville de Paris

3D Ultrasound Localization Microscopy

Soutenue par :

Baptiste HEILES

Le 20/12/2019

Ecole doctorale n° 564 :
Ecole Doctorale
Physique en Ile de France

Spécialité :
Acoustique



Composition du jury :

Hervé LIEBGOTT Professeur des Universités, IUT LYON/CREATIS	<i>Rapporteur</i>
Rik, VOS Associate Professor, ERASMUS MC	<i>Rapporteur</i>
Sylvie, LORTHOIS Directeur de Recherche, IMFT – CNRS	<i>Examinatrice</i>
Benoît, LARRAT Chargé de Recherche, CEA	<i>Examineur</i>
Mickaël, TANTER Directeur de Recherche, PhysMedParis – INSERM	<i>Invité,</i> <i>Président du Jury</i>
Olivier, COUTURE Directeur de Recherche, LIB – CNRS	<i>Directeur de Thèse</i>

Abstract

Ultrasound Localization Microscopy has demonstrated the ability to overcome the penetration/resolution conundrum in ultrasound imaging thanks to high frame rate imaging and contrast agents. However, this approach will fall short in its clinical translation if its main disadvantages aren't addressed: 1- long acquisition time 2- limited two dimensional field of view 3- motion artifacts 4-data overdose and 5- data processing times. Developing 3D ULM will allow to explore entire volumes within a few minutes of acquisition, giving access to all blood vessels down to micrometer size and imaging moving organs (i.e. a patient in a clinical setting).

The objective of this thesis was to perform, for the first time, volumetric ultrasound localization microscopy and unveil its potential in-vitro and in-vivo. For this purpose, I first developed new post-processing techniques, reducing 2D data processing times by a factor of 300, allowing implementation of ULM on 3D data and increasing image quality. Then, I designed new ultrasound sequences and proved that sub-wavelength features could be resolved in a tailor made wall-less phantom. I then demonstrated that 3D imaging of the rat brain microvasculature with blood flow velocimetry was achievable with micrometric resolution, and implemented 3D motion correction and image registration to provide whole brain imaging.

This new tool was used to investigate both the anatomy and the vascularization mechanisms in the brain. Making the transition from 2D ULM to 3D ULM paves the way towards better imaging of in vivo organs in the rat. Thanks to technological improvements 3D ULM will spread fast in ultrasound imaging research and reach all the way to clinical care.

Keywords : ultrasound localization microscopy, superresolution, superlocalization, ultrafast, brain imaging, 3D, 4D, volumetric imaging

Resumé

La microscopie par localisation ultrasonore a montré qu'il était possible de s'affranchir du compromis entre la pénétration et la résolution en échographie grâce aux ultrasons ultrarapides et à l'utilisation d'agents de contraste. Cependant, cette technique sera difficilement transposable dans un environnement clinique car elle implique : 1. de longs temps d'acquisitions, 2. un champ de vue limité à un plan, 3. l'impossibilité de corriger les mouvements hors plan, 4. des quantités de données importantes et 5. des temps de calculs extrêmement longs. En développant cette technique en 3 dimensions, il sera possible d'explorer des volumes anatomiques entiers en quelques minutes d'acquisition afin de voir la micro-vasculature mais aussi d'imager des organes soumis au mouvement (comme cela est le cas pour l'imagerie d'un patient).

L'objectif de cette thèse a été de démontrer qu'il était possible de faire de la microscopie par localisation ultrasonore en 3D sur des larges volumes, et de montrer son potentiel *in vitro* et *in vivo*. Le point de départ a été de développer des nouvelles techniques de localisation de particules, ce qui a permis de diviser par 300 le temps de calcul en 2D et de fournir une imagerie de meilleure qualité. Grâce à leur implémentation en 3 dimensions, elles ont rendu possible la microscopie par localisation ultrasonore en 3D dans des temps réduits. Ensuite, nous avons créé des séquences d'imagerie 4D spécifiques pour la microscopie en 3D et montré qu'il était possible d'imager avec une résolution sub-longueur d'onde un fantôme de canaux micro-fluidiques 3D. Ce fantôme a été développé spécifiquement pour démontrer la faisabilité de la technique en 3D. Après avoir éprouvé notre technique *in vitro*, nous l'avons appliquée *in vivo* sur le cerveau de rat et démontré qu'il était possible d'avoir accès à la vasculature ainsi qu'aux flux sanguins à une échelle de quelques microns. Une étape supplémentaire a été ajoutée dans le *framework* de l'algorithme afin de corriger le mouvement en 3 dimensions et de recalibrer des volumes superrésolus entre eux afin de produire le premier volume d'un cerveau de

rat entier *in vivo* avec une résolution de quelques microns (bulbe olfactif, cervelet et lobes principaux).

Le développement de la microscopie par localisation ultrasonore en 3D ouvre la voie vers une imagerie préclinique *in vivo* de meilleure qualité et plus rapide. Grâce aux innovations technologiques actuelles, l'utilisation de cette technique en recherche se fera de plus en plus fréquente jusqu'à être adoptée en clinique.

Mots clés : microscopie par localisation ultrasonore, superrésolution, superlocalisation, ultrafast, imagerie du cerveau, 3D, 4D, imagerie volumétrique

Table of contents

Abstract	3
Resumé	4
Table of contents	6
II. List of acronyms.....	14
I. Chapter 1 : General Introduction.....	18
I.1 Ultrasound Medical Imaging.....	18
I.2 Conventional echography.....	21
I.3 Plane-wave imaging	25
I.4 Ultrafast ultrasound applications : shear wave elastography, motion correction, and functional ultrasound.....	33
I.4.1 Shear wave elastography.....	33
I.4.2 Ultrafast motion correction.....	34
I.4.3 Ultrafast Doppler and functional Ultrasound	34
I.5 Ultrasound Localization Microscopy : a brief introduction	36
I.6 3D ultrasound imaging	43
I.7 Thesis objectives.....	47
I.7.1 Chapter 2 : Developing new techniques to achieve faster, better Ultrasound Localization Microscopy	48
I.7.2 Chapter 3 : Achieving <i>in vitro</i> volumetric ultrafast Ultrasound Localization Microscopy.....	48
I.7.3 Chapter 4 : Using <i>in vivo</i> volumetric ultrafast ULM as a blood flow sensor	48
I.7.4 Chapter 5 : Towards whole-brain imaging	49
II. Chapter 2: Developing new techniques to achieve faster, better Ultrasound Localization Microscopy	56
II.1 Introduction	56
II.2 State of the art	57
II.2.1 Detection of contrast agents.....	58
II.2.2 Isolating contrast agents.....	63
II.2.3 Localization of contrast agents.....	66
II.2.4 Tracking schemes	67
II.3 Achieving faster and higher quality localization.....	70
II.3.1 Localization schemes	71

II.3.2	Tracking scheme.....	80
II.3.3	Developing a universal framework for ULM.....	81
II.4	Developing methods to measure the algorithms' performance	83
II.4.1	In silico methods.....	84
II.4.2	<i>In vivo</i> methods.....	88
II.5	Results	90
II.5.1	In silico	90
II.5.2	In vivo 2D.....	95
II.6	Discussion	100
II.6.1	Universal Framework.....	100
II.6.2	In silico	102
II.6.3	In vivo 2D.....	104
II.7	Towards better imaging : applications	105
III.	Chapter 3: Achieving in vitro volumetric ultrafast ULM	118
III.1	Introduction to <i>in vitro</i> ULM.....	118
III.2	Manufacturing <i>in vitro</i> micrometric flow phantoms	121
III.3	4D ultrafast ultrasound sequence	123
III.4	ULM process applied to the detection of small microvessels	128
III.5	Results.....	130
III.6	Discussion.....	140
III.7	Conclusion	146
IV.	Chapter 4: Using <i>in vivo</i> volumetric ultrafast ULM as a blood flow sensor	152
IV.1	Introduction.....	152
IV.2	Materials and Methods.....	158
IV.2.1	Animals	158
IV.2.2	Physiological constants	160
IV.2.3	Isoflurane and Ketamin-Medetomidin acquisitions.....	161
IV.2.4	Ultrasound sequence.....	161
IV.2.5	ULM processing.....	163
IV.2.6	Additional processing for velocimetry analysis	163
IV.3	Results.....	165
IV.3.1	Density-based renderings for anatomical viewings.....	165
IV.3.2	Velocimetry renderings for qualitative analysis and vasculature labeling	171
IV.3.3	Velocimetry renderings for quantitative analysis of the vasculature	

	175
IV.3.4	Additional processing for velocimetry analysis in specific vessels.178
IV.4	Discussion 181
IV.4.1	Animal..... 181
IV.4.2	Ultrasound sequence..... 183
IV.4.3	ULM processing..... 184
IV.4.4	Anatomical variations 185
IV.4.5	Velocimetry results..... 186
IV.4.6	Additional processing for velocimetry analysis 186
IV.5	Conclusion 187
V.	Chapter 5: Towards whole-brain imaging 196
V.1	Anatomical whole-brain imaging: a state of the art 196
V.1.1	Material and methods..... 204
V.1.2	Results 214
V.1.3	Discussion 223
V.1.4	Conclusion 228
VI.	Chapter 6: Conclusion and perspectives 234
VI.1	Objectives 234
VI.2	Developing 3D ULM..... 237
VI.3	Perspectives..... 237
VI.3.1	Non-microbubble based ULM 238
VI.3.2	Non-localization based ULM 238
VI.3.3	Towards multi-modality imaging 239
VI.3.4	Clinical applications 239
	List of publications 243
	Publications in peer-reviewed journal: 243
	Under-review, in preparation publications:..... 243
	Appendix I..... 246
 250

Table of figures

Figure 1. Different displays in 3D ultrasound for obstetrics (Pashaj and Merz, 2013)	20
Figure 2. Formation of an image in conventional ultrasound (inspired by Emilie Macé’s Thesis)	22
Figure 3. Color doppler of 8 day-old premature girl, Power doppler of a 2 day-old boy with seizures (Lowe and Bailey, 2011)	24
Figure 4. Pulsed Doppler Overlaid with Color Doppler imaging of an 8-day old premature girl (Lowe and Bailey, 2011)	25
Figure 5. Formation of an image with plane wave ultrasound (inspired by Emilie Macé’s Thesis)	26
Figure 6. Notations for tilted plane wave (inspired by (Montaldo et al., 2009))	27
Figure 7 Coherent spatial compounding for plane wave imaging.....	31
Figure 8. Comparison of focused, plane wave and compounded plane wave imaging at 4.5Mhz (scale bar = 10mm).....	32
Figure 9. Implementation of functional Ultrasound on a rat undergoing 5 visual stimuli (Gesnik et al., 2017)	35
Figure 10. The basic principle behind near field scanning optical microscopy....	37
Figure 11 The concept of Superresolution with STED microscopy (“Introduction to super-resolution microscopy,” 2019).....	38
Figure 12. Penetration - resolution tradeoff in ultrasound.....	40
Figure 13. First Proof of concept of super-resolution imaging in ultrasound (Couture et al., 2011)	41
Figure 14. First demonstration of Super-Resolution <i>in vivo</i> using a Contrast-Pulse Sequencing mode on a clinically approved scanner on a mouse ear (Christensen-Jeffries et al., 2015).....	42
Figure 15. First demonstration of ULM in the rat brain with ultrafast (Errico et al., 2015).....	43
Figure 16. First demonstration of 3D ultrasound imaging with 2D scanning	44
Figure 17. Ultrafast Doppler Tomography on a Rat Brain (Demené et al., 2016)	45
Figure 18. Different types of arrays and their characteristics (Fernandez et al., 2003)	46
Figure 19. Steps in ultrasound super-resolution processing.....	60
Figure 20. Schematics describing tissue harmonic imaging (Cikes et al., 2019)..	63

Figure 21. Overlap between the transmit and receive passbands results in unwanted signal in harmonic mode	63
Figure 22. Framework for the iterative search of nearest-neighbor.....	69
Figure 23. Cross-correlation based tracking	70
Figure 24. The distance matrix for all particles in two subsequent frames and thresholding to prepare pairing (Song et al., 2018c)	71
Figure 25. Non interpolated and interpolated image of a microbubble obtained by simulation of a point-like scatterer using Verasonics Research Ultrasound Simulator ..	76
Figure 26. Gradient of the intensity of the interpolated point-like scatterer in basis (u,v)	77
Figure 27 Equipotential lines overlaid with gradient vector values for interpolated point-like scatterer.....	78
Figure 28. 1951 USAF resolution test chart (United States Air Force, 1951)	86
Figure 29. Norm of Velocity in target media with 6 different geometries.....	86
Figure 30. Typical beamformed image of scatterers in simulated media with added noise.....	87
Figure 31. Schematics explaining the concept of the statistical classification of particles in the case of a localization algorithm	88
Figure 32. Illustration of the Jaccard index measurement on two squares overlapping, Green is ground truth and Red is predicted	89
Figure 33. Power spectral density of the frequency analysis in Z-axis of the image	91
Figure 34. Histogram bins of the errors in two directions and RMSE for the different algorithms	92
Figure 35. Statistical classification results.....	93
Figure 36. Statistical indices results for 2D localization algorithms.....	94
Figure 37. Efficiency index results for localization algorithms	94
Figure 38. ULM renderings of in silico simulation	95
Figure 39. Rat brain microvasculature rendered with ULM with different localization algorithms.....	96
Figure 40. Zoomed in viewings of ULM renderings with the different localization schemes.....	97
Figure 41. ULM performed on a rat kidney with weighted average (Left Column) and radial symmetry (Right Column) based localization.....	98
Figure 42. Fourier Ring Correlation plotted with respect to resolution.....	99
Figure 43. Spatial Frequency Peak to Baseline analysis results.....	99

Figure 44. Running time of complete ULM processing for the different localization schemes.....	100
Figure 45. Radar chart combining the metrics score of the different algorithms.....	100
Figure 46. ULM imaging of the brain in mice.....	107
Figure 47. Ultrafast Doppler and ULM performed in a Rat's Pancreas	108
Figure 48. ULM imaging of tumor in mice.....	109
Figure 49. Spine imaging with Julien Claron, Sophie Pezet (performed by Vincent Hingot)	110
Figure 50. The Chicken Embryo Imaged with Conventional Microscope, Ultrafast Doppler and ULM	110
Figure 51. Young modulus as a function of agarose concentration(Ahearne et al., 2005).....	121
Figure 52. Modeling of the bifurcation.....	122
Figure 53. Schematic of custom made agar-based microvessel model (inspired by (Heiles et al., 2019))	123
Figure 54. Picture of the 4D echograph machine with the 2D matrix array and schematics of 2D plane wave transmissions (Image inspired from (Provost et al., 2014)).....	124
Figure 55. Schematized view of the 4D acquisition for 3D ULM <i>in vitro</i>	126
Figure 56. Typical slices of the 3D volume obtained after conventional beamforming. Additional filtering by the pre-processing technique. This technique is a very simple way to locate areas with high concentration of microbubbles	131
Figure 57. Isolated microbubbles in isolated microbubbles in different slices of the volumetric acquisition slices for 3 directions at two different times.....	133
Figure 58. Cumulated scatter plot of each center of microbubbles detected for different concentrations pre and post-beamforming	134
Figure 59. Trajectories and scatter plot of microbubbles detected	135
Figure 60. Slices of main and side canals	136
Figure 61. Velocity profiles in two orthogonal slices.....	139
Figure 62. Slices of main and side canals with cubic spline resampling and separability criterion.....	140
Figure 63. Compounded Plane Wave imaging and Multiplane wave compounded power Doppler imaging performed on a rat brain using a 2D fully addressed matrix array (image courtesy of Claire Rabut, (Rabut et al., 2019)).....	156
Figure 64. Multiplane wave compounded functional ultrasound performed on a rat	

brain using a 2D fully addressed matrix array (image courtesy of Claire Rabut, (Rabut et al., 2019))157

 Figure 65. Drawn schematic of the animal setup and real pictures of the experimental setup.....160

 Figure 66. Schematized view of the 4D acquisition for 3D ULM *in vivo*.....162

 Figure 67. Illustration of the four steps post-processing for vessel-specific velocimetry analysis.....164

 Figure 68. Anatomical 3D viewings of 3D ULM performed on a rat brain (color encoded based on microbubble density) next to contrast-enhanced power Doppler volumes obtained with the same sequence parameters.....166

 Figure 69. 500 μm thick slices of volumetric ULM performed on a rat brain (color encoded based on the density of microbubbles)168

 Figure 70. 50 μm slices of volumetric ULM performed on a rat brain (color encoded based on the density of microbubbles)170

 Figure 71. 500 μm slices of velocimetry performed on a rat brain anesthetized using Isoflurane (velocity is negative when going towards the top of the brain and positive when going towards the bottom).....172

 Figure 72. 500 μm slices of velocimetry performed on the same rat presented in the previous figure anesthetized using Ketamine Medetomidin (the convention for velocity is the same)174

 Figure 73. Normalized distribution of magnitude of velocities measured in the rat brain with two different anaesthesiae.....180

 Figure 74. Picture of the effect of ripped dura mater on a craniotomized rat and ultrasound power Doppler image of corresponding coronal plane183

 Figure 75. Anatomical structures in the brain (Girouard and Iadecola, 2006) .196

 Figure 76. 3D renderings of Sprague Dawley rat's skull198

 Figure 77. Slice of the rat brain at Bregma -1.08mm as featured in the Paxinos' Atlas with corresponding neuronal labeling199

 Figure 78. Whole-brain imaging of rat neuronal morphology with Golgi staining(Li et al., 2010) (VBN, 2015)200

 Figure 79. Brain-wide distribution of Thy-1 neurons imaged by LSM, STP, and fMost.....203

 Figure 80. Drilling procedure for whole-brain craniotomy of the rat206

 Figure 81. Schematized view of the 4D acquisition for 3D ULM *in vivo*.....208

 Figure 82. Translation estimation through 2D species (inspired by V. Hingot's thesis)209

Figure 83. Rotation and scaling estimation using 2D cross-correlation on the log-polar transform of the magnitude of the 2D Fourier transforms (inspired by V. Hingot’s thesis) 210

Figure 84. Motion Estimation and correction performed on 2D ULM of the rat brain (Hingot et al., 2017)..... 211

Figure 85. Schematics for Motion correction in 3D using two different approaches 212

Figure 86. SVD filtered imaging of tissue signal in the brain of a rat released from the stereotactic frame 214

Figure 87. Coronal and Sagittal planes projected volumetric ULM renderings obtained without, with BTB and with VTV and BTB motion correction 215

Figure 88. 3D density-based rendering of volumetric ULM on Sprague-Dawley rat brain overlaid on MRI model (Papp et al., 2014) and skull rat surface mesh generated from micro-CT scan (Kutikov) 216

Figure 89. Whole-brain imaging *in vivo* using 3D ULM with vasculature labeling 218

Figure 90. Enlarged volume view of the overlap between the two frontal hemispheres and the olfactory bulb..... 219

Figure 91. 500µm coronal cuts taken at various planes rendered based on density 220

Figure 92. 500 µm sagittal cuts taken at various planes rendered based on density 222

Figure 93. 500 µm transverse cuts taken at various planes rendered based on density 223

Figure 94. Illustration of the effect of motion on ULM renderings with and without motion correction algorithms..... 226

Figure 95. Predicting the outcome and evaluating response to treatment with transcranial ULM (Hingot, et al 2019, under review) 235

Figure 96. Transcranial Doppler imaging of the human brain: only large structures are visible (Holscher et al., 2007) 236

List of acronyms

ACA: Anterior Cerebral Artery
ASDIC : Anti-Submarine Detection Investigation Committee
ASIC : Application Specific Integrated Circuits
BTB : Block To Block
CBF : Cerebral Blood Flow
CBV : Cerebral Blood Volume
CLAHE : Contrast Limited Adaptive Histogram Equalization
CFI : Color Flow Imaging
CPS : Contrast-Pulse Sequencing
CPU : Central Processing Unit
CT-scan : Computerized Tomography scan
DAPI : 4',6-diamidino-2-phenylindole
DAS : Delay-And-Sum
DNA : Deoxyribonucleic acid
DTU : Danmarks Tekniske Universitet
EDV: End-Diastolic Velocity
fMRI: functional Magnetic Resonance Imaging
FRC : Fourier Ring Correlation
fUS: functional UltraSound
FWHM : Full Width at Half Maximum
GFP : Green Fluorescent Protein
GPU : Graphics Processing Unit
GSD : Ground state depletion
ICA : Internal Carotid Arteries
IQ : In-Quadrature
LGN : Left Geniculate Nucleus
LV : Left Ventricular
LVEF : Left Ventricular Ejection Fraction
MCA : Middle Cerebral Artery
MPWI : Multi Plane Wave Imaging
MRI : Magnetic Resonance Imaging
PALM : Photoactivated localization microscopy
PET : Positron Emission Tomography
PRF : Pulse Repetition Frequency
PSF : Point Spread Function
PSV: Peak Systole Velocity

PWI : Plane Wave Imaging

RAM : Random Access Memory

RESOLFT : REversible Saturable Optical Fluorescence Transitions

RFP : Red Fluorescent Protein

RI : Resistive Index

RMSE : Root Mean Square Error

ROI : Region OF Imaging

SARUS : Synthetic Aperture Real-time Ultrasound System

SC : Superior Colliculus

SNR : Signal to Noise Ratio

SOFI : Super-resolution optical fluctuation imaging

SONAR : SOund Navigation And Ranging

SPDM : Spectral Precision Distance Microscopy

STED : Stimulated emission depletion

STORM : Stochastic optical reconstruction microscopy

SVD : Singular Value Decomposition

THI : Tissue Harmonic Imaging

UFD-T: UltraFast Doppler Tomography

ULM : Ultrasound Localization Microscopy

VTV : Volume To Volume

I

General Introduction

I. Chapter 1 : General Introduction

Ultrasound is one of the most widely used imaging method (in France in 2013, 41 million radiographies, 26 million echographies, 4 million scanners, 3 million MRIs were billed to the Sécurité Sociale according to the Caisse Nationale d'Assurance Maladie).

This popularity can be explained by the good spatial and temporal resolution that it provides (Cobbold, 2005). It is able to image the vascular bed, bone, and soft tissues in a few microseconds in both 2D and 3D. Another reason for the popularity of this medical imaging tool is its price : on average, a patient will spend 30 euros for a radiography, 47 euros for an ultrasound scan, 119 euros for a CT-scan, 189 euros for an MRI (<http://www.livreblancimagerie.fr/>). Considering the insights it can provide about vascular function, tumour stage, osteoporosis or inflammation of the tendons, this is quite amazing. In this chapter, I will present a brief history of ultrasound medical imaging, the fundamentals of image formation in conventional and plane-wave imaging and its applications, along with a brief review of ultrasound localization microscopy and of 3D ultrasound imaging. Finally, we will present the objectives of this thesis and the outline of the manuscript.

I.1 Ultrasound Medical Imaging

Ultrasound has first seen the light as an imaging tool in 1918 when Paul Langevin and Constantin Chilowski demonstrated that ultrasound wave reflection could be used to map the surface of distant objects by measuring the time of flight. The obvious military interest of such a technique led to the development of the ASDIC (Anti-Submarine Detection Investigation Committee) (Moulin) and later, SONAR (SOund Navigation And Ranging) (an extended historical review of SONAR used in anti-submarine warfare is available in (Williams and Hackmann, 1984)).

In the second quarter of the XXth century, pushing further the measurement of time of flight, ultrasound demonstrated its ability to map the echogenicity of a medium. Using this method on tissues, ultrasound soon became a medical imaging tool with the first published work on transmission of ultrasound in the brain published in 1942 by Dr. Dussik in Austria. It is now one of the most widely used imaging techniques in the world because its ability to accurately measure geometric properties of tissues and map blood flow and vasculature in a few seconds. In obstetrics, it is the go-to tool to diagnose cardiac malfunction in a foetus, detect malformations, predict trisomy or simply finding out the genre of the baby. Its real-time ability is much appreciated by doctors and its

portability makes it the ideal tool to perform pre-diagnosis at bedside, in operating rooms or even in small private practices. It is a highly versatile tool that can image most soft tissues, blood flow, surfaces, and volumes, perform remote histotripsy surgery in the brain or the heart but also image and treat bone-related diseases such as osteoporosis (Pashaj and Merz, 2013). To image blood flow, several techniques can be used such as continuous wave Doppler, Pulsed wave Doppler or Color Flow Imaging (CFI).

Continuous-wave Doppler uses the Doppler shift in frequency between the transmitted and receive signals caused by moving red blood cells to estimate blood velocity. Early systems implementing continuous wave Doppler had separate transmit and receive transducers and were not directional, thus leading to misinterpretation of the direction of the flow (Szabo, 2004). (Kato and Izumi, 1966) and (McLeod, 1967) subsequently showed ways to discriminate direction using respectively the heterodyne technique and phase-quadrature demodulation.

Contrary to continuous-wave Doppler which measures velocity along its beam, Pulsed Wave Doppler can measure velocity at a precise location thanks to the adjustment of pulse length. Instead of comparing the Doppler shift in between transmit and receive signal, each received echo is compared to the echoes resulting from previous transmissions. The relative delay between echoes is dependent on the length traveled by the scatterer away from the transducer. (Bonnetfous and Pesque, 1986). It has a larger variable aperture than Continuous wave Doppler and can be steered in any direction. Color Flow Imaging processes phase, amplitude and frequency information affected by the Doppler shift to render grayscale image of tissue overlaid with colored images depicting velocity amplitude and direction of the flows (Merritt, 1987). Additionally, the amplitude of Doppler can be calculated by summing the norm of the IQ signals over a period of time bringing higher sensitivity to small vessels and slow velocities in a mode called Power Doppler (Szabo, 2004). Doppler imaging is now a modality on its own used frequently in a clinical setting by cardiologists, hepato-gastroenterologists, or even general practitioners.

Ultrasound suffers several disadvantages, including poor contrast and user-dependency. But the modality is also limited by its dependence on the frequency of the emitted wave since it is inversely related to the wavelength, which defines resolution. Because of frequency-dependent attenuation, the depth of imaging is limited by a trade-off between resolution and penetration. To attain several centimeters in-depth, the frequency has to be reduced (wavelength increased) and the resolution can be worsened to about **1 mm**. Bone is also particularly attenuating to ultrasound waves because of the structure of the spongy structure encased in two compact layers. This makes imaging of

the human brain challenging when other techniques such as PET or MRI are not impacted and can provide wonderful insights not only on how the brain looks but on how it performs (Poldrack, 2018).

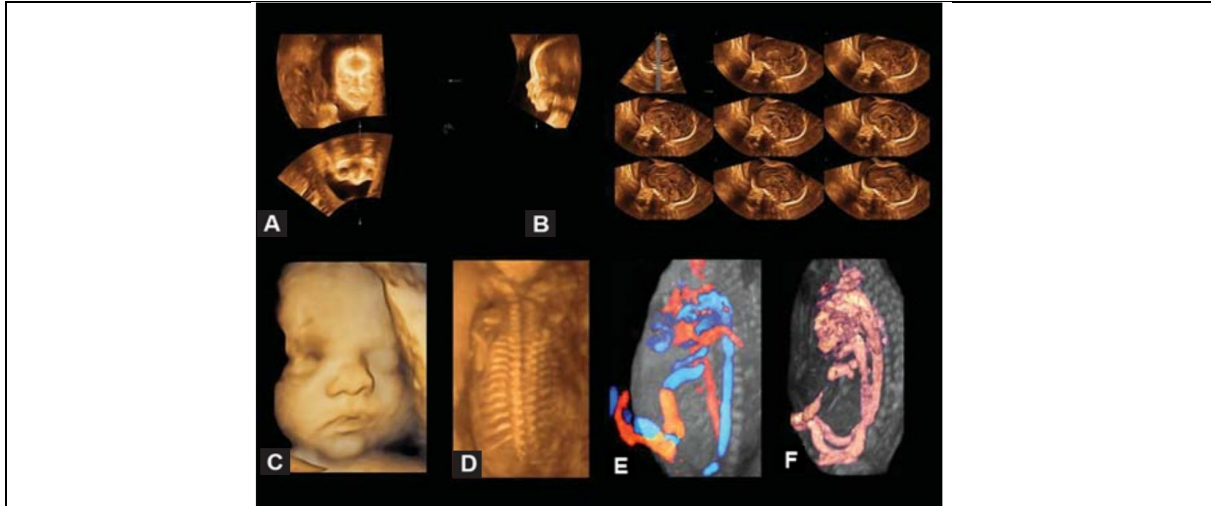


Figure 1. Different displays in 3D ultrasound for obstetrics (Pashaj and Merz, 2013)

- a) Multiplanar view (fetal face)
- b) Tomographic view (fetal brain with sagittal planes)
- c) Surface view (face)
- d) Transparent view (spine)
- e) Glass body view with Color Doppler imaging of blood flow
- f) Glass body view with Power Doppler imaging of blood flow

Thanks to plane-wave imaging, the frame rate of ultrasound imaging has dramatically increased. This opened up new perspectives to both the clinical and fundamental research field which we will detail briefly in this paragraph before explaining how it works in I.3. High frame rate allows to measure the elasticity of tissues and perform accurate motion correction for shear wave elastography (Bercoff and Minin, 2011). This new technique was applied successfully to detect breast tumors or perform better echocardiography (Tanter and Fink, 2014). Additionally to high frame rate B-mode imaging and elastography, ultrafast Doppler was developed allowing fast imaging of vascular changes. In neuroscience, this mode was used to measure vascular changes in the brain under different stimuli, making it the first tool to be able to reflect neuronal activity deep in the brain with micrometric resolution in a millisecond timeframe (Macé et al., 2011).

Further along, the technological advances for transducer technology and parallel

processing allowed ultrasound to enter the third dimension by using 2D matrix array probes. Its use is mostly limited in the medical field to obstetrics or echocardiography but in research, various pre-clinical or clinical applications have been found : more precise echocardiography with motion correction, volumetric mapping of neuronal activity in the rat brain, large arteries imaging to measure vascular changes.

Finally, one of the most recent advancements in ultrasound tackled the penetration-resolution paradigm : axial resolution and penetration are proportional to the ultrasound frequency meaning high-resolution imaging is possible only in superficial layers of the body. Ultrasound Localization Microscopy was demonstrated in 2D and proved to achieve both higher axial and lateral resolution *in vitro* and *in vivo* for pre-clinical and clinical studies (Couture et al., 2018).

A long way has been walked from SONAR to make echography one of the most versatile imaging methods in medical studies. After presenting in detail the physics involved with these different innovations, we will present our ideas to go further with ultrasound and transform it as an operator-independent tool for deep angiography.

I.2 Conventional echography

Echography takes place in three steps : firstly, emission of an ultrasound wave in the region of imaging, secondly, recording the echoes from either backscattering or reflection from the medium and finally, separating these echoes to produce an image of the echogenicity of the medium, depending of the density, compressibility modulus and tissue microstructure (Szabo, 2004). This final step is called beamforming.

To produce an ultrasound wave, the piezoelectric effect is used. An electrical current is applied to a transducer made of piezoelectric material, which will deform and produce an acoustic wave (Cobbold, 2005).

For conventional B-mode imaging, a series of transducers are arranged in a linear fashion and can be driven independently by electrical current. By specifying at which time the electrical current is applied to each transducer, the wavefront of the ultrasound wave produced can be modified. Let's say the wavefront emitted by a group of transducers is spherical, it will focus at a specific depth depending on the curvature of the wavefront. It is also able to focus in the lateral direction by applying an angle to the curvature : the symmetry axis of the time delays is at an angle with the axis of the probe. This is called emission focusing. Now when the echoes are recorded on all transducers, it is possible to find out the precise sources of these echoes along the insonified line: other

lines will contain both information from the spherical echo of the source centered in that line but also weaker echoes originating from sources further away in the lateral direction. This is called reception focusing. The process of formation of an image is depicted in Figure 2.

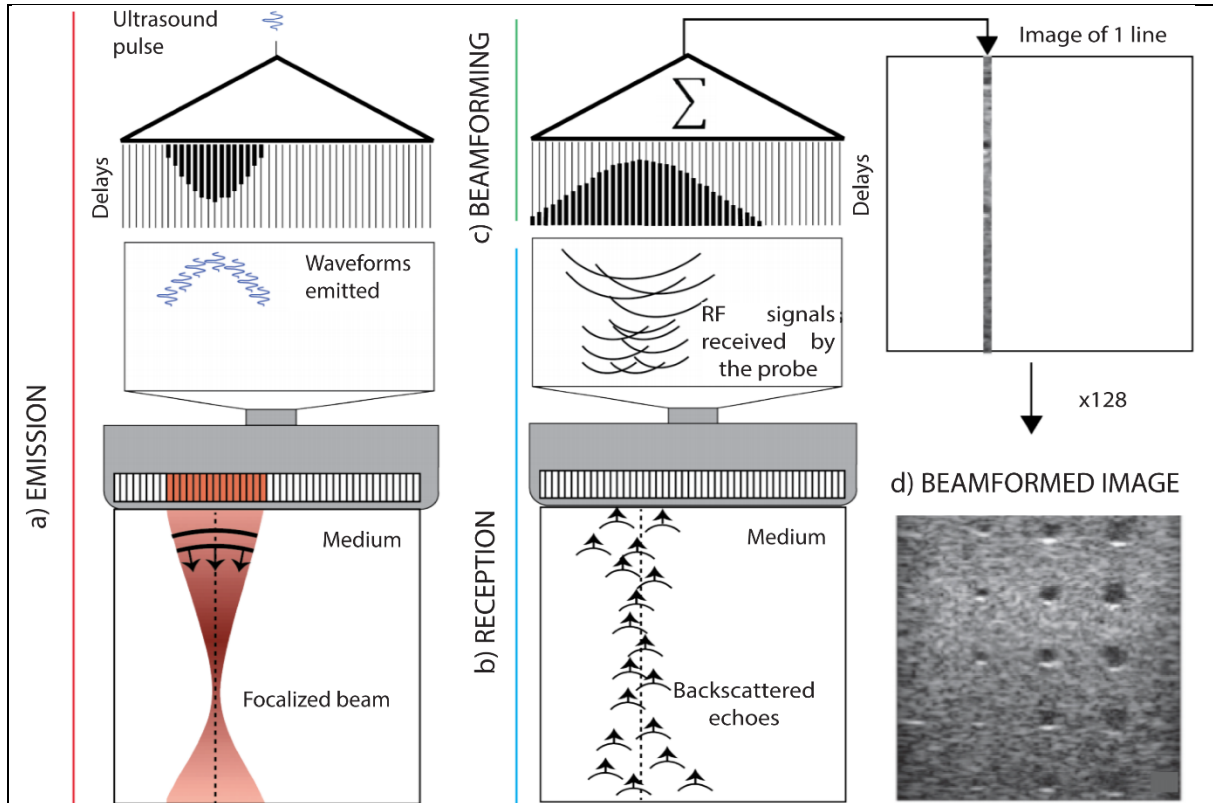


Figure 2. Formation of an image in conventional ultrasound (inspired by Emilie Macé's Thesis)

- a) Emission of an ultrasound pulse with calculated delays by a group of transducers to focus on a specific line
- b) Reception of multiple echoes from scatterers by the transducers
- c) Reception focusing by summation of the received echoes with corresponding delays
- d) Formation of the final image

Additionally, because a lot of sub-wavelength scatterers are usually present in the region of imaging, there is Rayleigh scattering taking place which produces a speckle effect in the final image.

Because of the emission focusing for conventional B-mode imaging, a scanning method has to be employed to render an entire image. The focal spot is translated along the lateral axis and as many emissions as there are transducers are realized. For each

emission, reception focusing is put in place to reconstruct each line. Considering that the process of pulse-echo lasts a few tens of a microsecond and that hundreds of emissions are required for each image, conventional ultrasound imaging can be performed at a few tens of Hertz. Improvement of image quality is possible by using several focal spots in the axial direction or by steering the wavefront with the transducer array to decrease speckle-noise : such a method is called compounding.

Conventional Doppler imaging can perform velocimetry based on M-mode imaging. Instead of emitting only once per line of focus, several emissions will take place at a frequency $f_{acq} = 1/T$. Let's consider two successive pulses with the same waveform $e(t)$ at frequency f_{acq} for emission (t) :

$$E(t) = e(t) + e(t - T)$$

The recorded signal on the transducer array is written :

$$S(t) = e(a \times (t - t_0)) + e(a \times (t - t_0) - T),$$

or

$$S(t) = e(a \times (t - t_0)) + e(a \times \left(t - t_0 - \frac{T}{a}\right))$$

where $a = 1 - 2 \times \frac{v}{c} \cos(\theta)$, (v, θ) being respectively the speed magnitude at which a scatterer moves, and its angle to the probe, and c the speed of sound. a is a measure of the contraction of time which originates from the Doppler effect. The perceived echo will be out of phase by a shift proportional to $\left(\frac{T}{a} - T\right)$, the latter term because of our initial phase shift, the first because of the motion of the source point. The phase shift is :

$$\varphi = 2\pi f_{US} \left(\frac{T}{a} - T\right) = 2\pi f_{US} 2T \times \frac{v}{c} \cos(\theta)$$

with f_{US} the central frequency of the emitted ultrasound wave.

The received signal will thus vary with a frequency

$$f_D = \frac{1}{2\pi} \frac{d\varphi}{dt} = \frac{2f_{US}v}{c} \cos(\theta)$$

This phase shift is observable by measuring the frequency at which the received signal varies for multiple impulsions. While the modelization is a bit more complex for multiple echoes, the underlying concept is the same and Doppler imaging has proven to

be able to image flows with maximum speeds of : $v_{max} = \frac{f_{acq} \times c}{4f_{US} \cos(\theta)}$.

It is possible to repeat the emission/reception sequence several times on each line and then steer the beam electronically to sample the field entirely. By evaluating the phase shift in between each pulse it is possible to measure speed in every point of the image (Kasai et al., 1985). This mode is called Color-Doppler imaging (illustrated in Figure 3). Rather than calculating the speed, it is also possible to calculate the energy of the signal, this is called Power-Doppler imaging. It is much more sensitive to smaller vessels but fails to provide the direction of the flow (Rubin et al., 1997, 1994).

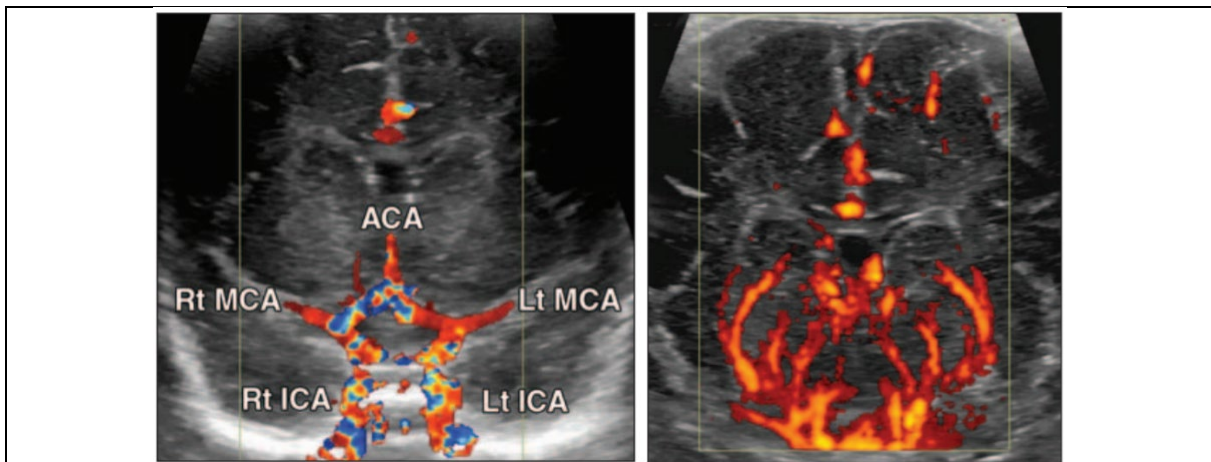


Figure 3. Color doppler of 8 day-old premature girl, Power doppler of a 2 day-old boy with seizures (Lowe and Bailey, 2011)

- a) Color Doppler obtained through the circle of Willis illustrates right (Rt) and left (Lt) internal carotid arteries (ICA), right and left middle cerebral arteries (MCA), and anterior cerebral (ACA) arteries.
- b) Power Doppler image using linear-array transducer reveals hyperemic flow in lenticulostriate and thalamoperforate arteries of basal ganglia and thalami

Another method to measure speed with conventional ultrasound is to work on the spectral content of the received signal by applying a Fourier transform. This method dubbed Spectral Doppler or Pulsed Doppler requires a lot more samples than Color-Doppler and thus is limited to a specific point in the image (see Figure 4).

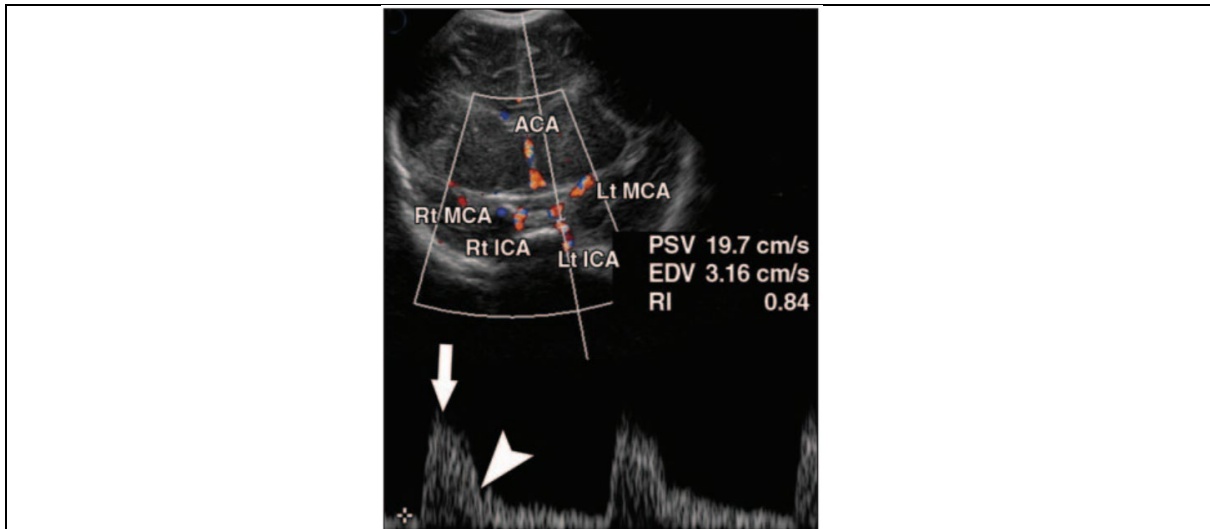


Figure 4. Pulsed Doppler Overlaid with Color Doppler imaging of an 8-day old premature girl (Lowe and Bailey, 2011)

The user chooses a specific area (defined by the vertical line) to analyze, producing a spectrogram shown below the image. This allows precise blood flow analysis, here one can see the rapid systolic upstroke (white arrow), and a gradual decline in flow during diastole (white arrowhead). Further analysis provided by the machine shows normal Peak Systole Velocity (PSV), End-Diastolic Velocity (EDV), and Resistive Index (RI).

I.3 Plane-wave imaging

Instead of using a few transducers and performing emission focusing, let's assume all transducers are driven at the same time. The wave emitted is no longer spherical but is plane. The first description of this technique dates back to 1977 when (C Bruneel et al., 1977) used the interaction between acoustic waves and a light beam to process the backscattered ultrasonic signals and reach an imaging rate of 1000 Hz. In the same year, (C. Bruneel et al., 1977) proposed a system achieving similar imaging rates without using optics but a second array of transducers in charge of performing phase inversion by mixing received signals with a reference signal. In 1983, (Shattuck et al., 1983) published a paper describing a parallel processing technique for data acquisition to reach high-speed imaging. They also suggested averaging frame rates to reduce noise : instead of focusing reception along the same direction as the emission, it uses multiple directions and thus increases the number of images formed by a single transmit. Thanks to tremendous technological progress, (Sandrin et al., 1999) showed that the echoes could be recorded back by all the transducers digitally rather than in an analog manner. In that way, the

imaging rate is only limited by the travel time of the ultrasound. A synthetic focusing in reception is possible *a posteriori* by applying a specific delay law to each of the transducers and summing all of their contributions. The issue is that the signal to noise ratio is quite low compared to conventional B-mode as the echoes from multiple sources are all mixed owing to lack of emission focusing. When delay and sum beamforming is applied, the echoes from the reception focused line are affected by echoes from other lines as well. However, the advantage of such a process lies in high frame rate, only one emission is needed to produce an image instead of 128 or 256 depending on the number of transducers, and it can detect fast happening phenomena in the region of imaging which is very useful for motion estimation (Tanter et al., 2002) or shear wave elastography (Sandrin et al., 1999).

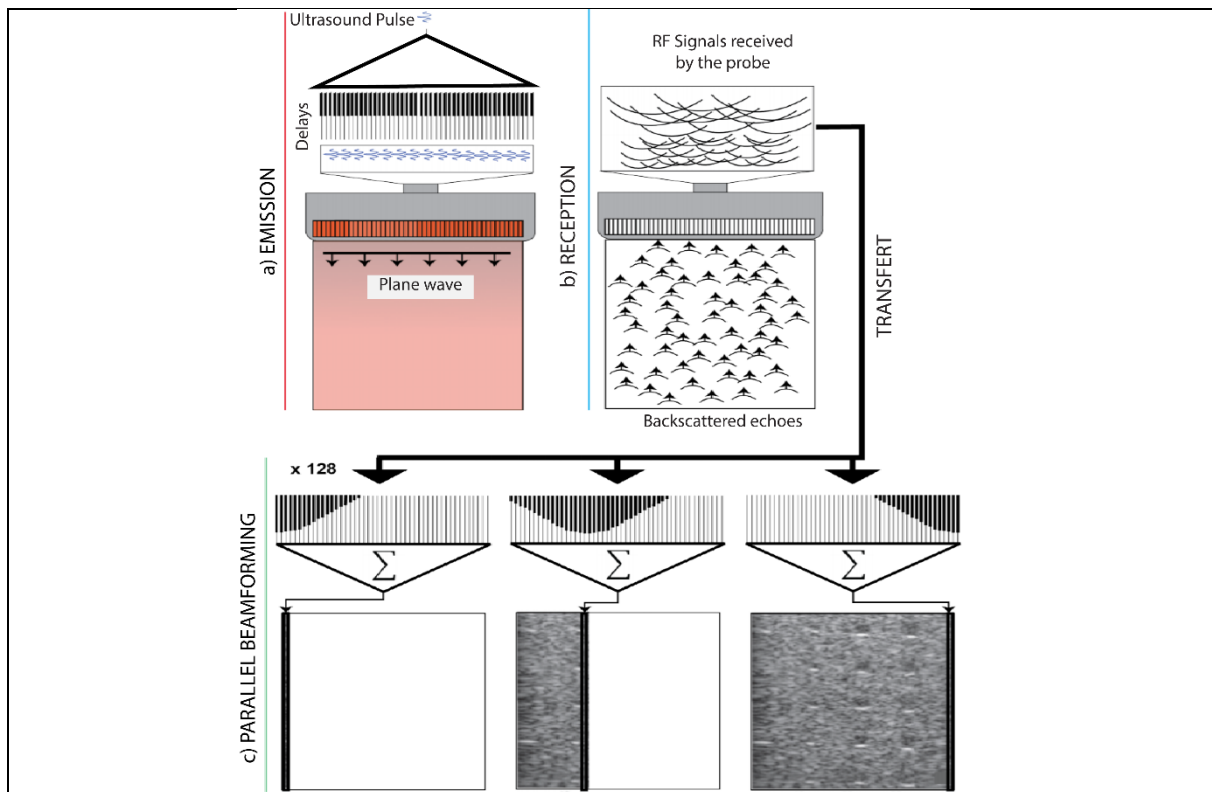


Figure 5. Formation of an image with plane wave ultrasound (inspired by Emilie Macé's Thesis)

- a) Emission of an unfocused plane wave with all of the transducers with the same time delays
- b) Reception of multiple echoes from scatterers with all of the transducers
- c) Reception focusing for each line using delay and sum beamforming

In 2009, (Montaldo et al., 2009) proved that it was possible to use plane wave imaging and produce a high-quality image. Instead of using only one plane wave to

reconstruct an image, several angled plane waves are emitted.

The beamforming technique for plane wave imaging is exposed below and illustrated in Figure 6.

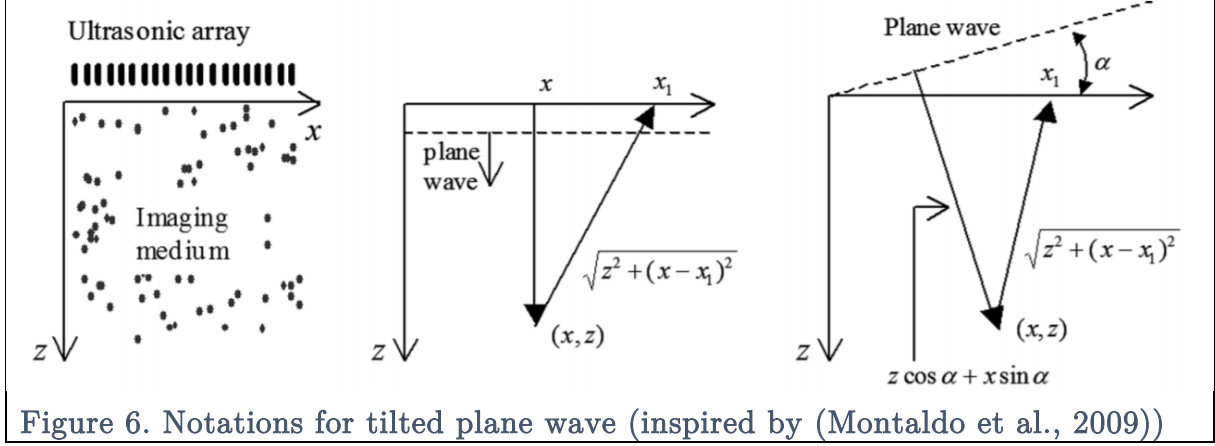


Figure 6. Notations for tilted plane wave (inspired by (Montaldo et al., 2009))

Let's assume that a tilted plane wave at the frequency f_0 is sent into the medium.

Each point of the image is obtained by adding coherently the contribution of each scatterer over an aperture $2a$, meaning we will build the signal of each pixel by summing the delayed radiofrequency signals (Delay And Sum beamforming) with delay τ :

$$s(x, z) = \int_{x-a}^{x+a} RF(x_1, \tau(x_1, \alpha, x, z)) dx_1$$

Because we are dealing with digital signals, the sampling is not continuous in time but done at $f = 4f_0 = 4 \frac{\omega}{2\pi}$. We can write the RF signal at the transducer x_1 at all times t_{FT} as

$$RF(x_1, t_{FT}) = A(x_1, t_{FT}) * \cos(\omega t_{FT} + \phi(x_1, t_{FT}))$$

Equation 1

To simplify the notation, we will now write $RF_{x_1}(t_{FT}) = RF(x_1, t_{FT})$, $A_{x_1}(t_{FT}) = A(x_1, t_{FT})$, $\phi_{x_1}(t_{FT}) = \phi(x_1, t_{FT})$.

The signal IQ for “in-phase” and “in quadrature” for a signal $u(t)$ at the frequency f_0 is defined as :

$$IQ(t) = u(t) + j * u\left(t + \frac{1}{4f_0}\right)$$

For our RF signal, we can thus write :

$$IQ_{x_1}(t_{FT}) = RF_{x_1}(t_{FT}) + j * RF_{x_1}\left(t_{FT} + \frac{1}{4f_0}\right)$$

And :

$$IQ_{x_1}(t_{FT}) = A_{x_1}(t_{FT}) \cos(\omega t_{FT} + \phi_{x_1}(t_{FT})) \\ + jA_{x_1}\left(t_{FT} + \frac{1}{4f_0}\right) \cos\left(\omega\left(t_{FT} + \frac{1}{4f_0}\right) + \phi_{x_1}\left(t_{FT} + \frac{1}{4f_0}\right)\right)$$

Separating real and complex parts:

$$\Re\left(IQ_{x_1}(t_{FT})\right) = A_{x_1}(t_{FT}) \cos(\omega t_{FT} + \phi_{x_1}(t_{FT}))$$

$$\Re\left(IQ_{x_1}(t_{FT})\right) = A_{x_1}(t_{FT}) \cos(\omega t_{FT}) \cos(\phi_{x_1}(t_{FT})) - A_{x_1}(t_{FT}) \sin(\omega t_{FT}) \sin(\phi_{x_1}(t_{FT}))$$

Equation 2

And because $\frac{\omega}{4f_0} = \frac{\pi}{2}$

$$\Im\left(IQ_{x_1}(t_{FT})\right) = A_{x_1}\left(t_{FT} + \frac{1}{4f_0}\right) \cos\left(\omega\left(t_{FT} + \frac{1}{4f_0}\right) + \phi_{x_1}\left(t_{FT} + \frac{1}{4f_0}\right)\right) \\ = A_{x_1}\left(t_{FT} + \frac{1}{4f_0}\right) \cos\left(\omega t_{FT} + \frac{\omega}{4f_0} + \phi_{x_1}\left(t_{FT} + \frac{1}{4f_0}\right)\right) \\ = -A_{x_1}\left(t_{FT} + \frac{1}{4f_0}\right) \sin\left(\omega t_{FT} + \phi_{x_1}\left(t_{FT} + \frac{1}{4f_0}\right)\right)$$

thus leading to

$$\Im\left(IQ_{x_1}(t_{FT})\right) = -A_{x_1}\left(t_{FT} + \frac{1}{4f_0}\right) \sin(\omega t_{FT}) \cos\left(\phi_{x_1}\left(t_{FT} + \frac{1}{4f_0}\right)\right) \\ - A_{x_1}\left(t_{FT} + \frac{1}{4f_0}\right) \cos(\omega t_{FT}) \sin\left(\phi_{x_1}\left(t_{FT} + \frac{1}{4f_0}\right)\right)$$

Equation 3

We measure $RF_{x_1}(T)$ and $RF_{x_1}\left(T + \frac{1}{4f_0}\right)$, and $T = n\frac{1}{f_0} = n\frac{2\pi}{\omega}$ because we sample the signals at f_0 , thanks to Equation 1 and Equation 2 we write:

$$\Re\left(IQ_{x_1}(T)\right) = RF_{x_1}(T) \\ = A_{x_1}(T) \cos(\omega T) \cos(\phi_{x_1}(T)) - A_{x_1}(T) \sin(\omega T) \sin(\phi_{x_1}(T)) \\ = A_{x_1}(T) \cos\left(\omega \frac{n * 2 \pi}{\omega}\right) \cos(\phi_{x_1}(T)) - A_{x_1}(T) \sin\left(\omega \frac{n * 2 \pi}{\omega}\right) \sin(\phi_{x_1}(T))$$

thus

$$\Re\left(IQ_{x_1}(T)\right) = RF_{x_1}(T) = A_{x_1}(T) \cos\left(\phi_{x_1}(T)\right)$$

Equation 4

Similarly thanks to Equation 1 and because $T + \frac{1}{4f_0} = n \frac{2\pi}{\omega} + \frac{\pi}{2\omega}$

$$\begin{aligned} \Im\left(IQ_{x_1}(T)\right) &= RF_{x_1}\left(T + \frac{1}{4f_0}\right) \\ \Im\left(IQ_{x_1}(T)\right) &= -A_{x_1}\left(T + \frac{1}{4f_0}\right) \sin(\omega T) \cos\left(\phi_{x_1}\left(T + \frac{1}{4f_0}\right)\right) \\ &\quad - A_{x_1}\left(T + \frac{1}{4f_0}\right) \cos(\omega T) \sin\left(\phi_{x_1}\left(T + \frac{1}{4f_0}\right)\right) \\ &= -A_{x_1}\left(T + \frac{1}{4f_0}\right) \sin\left(\omega\left(n \frac{2\pi}{\omega}\right)\right) \cos\left(\phi_{x_1}\left(T + \frac{1}{4f_0}\right)\right) \\ &\quad - A_{x_1}\left(T + \frac{1}{4f_0}\right) \cos\left(\omega\left(n \frac{2\pi}{\omega}\right)\right) \sin\left(\phi_{x_1}\left(T + \frac{1}{4f_0}\right)\right) \\ &= -A_{x_1}\left(T + \frac{1}{4f_0}\right) \sin(n * 2\pi) \cos\left(\phi_{x_1}\left(T + \frac{1}{4f_0}\right)\right) \\ &\quad - A_{x_1}\left(T + \frac{1}{4f_0}\right) \cos(n * 2\pi) \sin\left(\phi_{x_1}\left(T + \frac{1}{4f_0}\right)\right) \end{aligned}$$

thus

$$\Im\left(IQ_{x_1}(T)\right) = RF_{x_1}\left(T + \frac{1}{4f_0}\right) = -A_{x_1}\left(T + \frac{1}{4f_0}\right) \sin\left(\phi_{x_1}\left(T + \frac{1}{4f_0}\right)\right)$$

Equation 5

We need to calculate $RF\left(x_1, \tau(x_1, \alpha, x, z)\right)$ to perform DAS beamforming. The issue is that because of sampling, we do not know RF at all times t_{FT} but at specific times $T, T + \frac{1}{4f_0}$. A simple way to remedy this is to approximate $RF(\tau)$ by writing

$$A_{x_1}(\tau) \approx A_{x_1}(T), \quad A_{x_1}\left(\tau + \frac{1}{4f_0}\right) \approx A_{x_1}\left(T + \frac{1}{4f_0}\right), \quad \text{and} \quad \cos\left(\phi_{x_1}(\tau)\right) \approx \cos\left(\phi_{x_1}(T)\right),$$

$$\cos\left(\phi_{x_1}\left(\tau + \frac{1}{4f_0}\right)\right) \approx \cos\left(\phi_{x_1}\left(T + \frac{1}{4f_0}\right)\right) \text{ with } T \text{ the closest sample available to}$$

τ .

We make the assumption that, $A(T) = A\left(T + \frac{1}{4f_0}\right)$, $\phi\left(T + \frac{1}{4f_0}\right) = \phi(T)$ which is correct if we assume a narrowband excitation, meaning the modulating signal $A_{x_1}(t)e^{j\phi_{x_1}(t)}$ varies slowly with time (Ranganathan et al., 2004). This assumption is useful to be able to calculate $\cos(\phi(t))$ and $\sin(\phi(t))$ based on $RF_{x_1}(T)$, and $RF_{x_1}\left(T + \frac{1}{4f_0}\right)$:

$$\begin{aligned}\Re\left(IQ_{x_1}(T)\right) &= A_{x_1}(T) \cos\left(\phi_{x_1}(T)\right) = A_{x_1}\left(T + \frac{1}{4f_0}\right) \cos\left(\phi_{x_1}\left(T + \frac{1}{4f_0}\right)\right) \\ \Im\left(IQ_{x_1}(T)\right) &= -A_{x_1}\left(T + \frac{1}{4f_0}\right) \sin\left(\phi_{x_1}\left(T + \frac{1}{4f_0}\right)\right) = -A_{x_1}(T) \sin\left(\phi_{x_1}(T)\right)\end{aligned}$$

Under this approximation and assumption, we can calculate RF at all time delays τ by writing in IQ:

$$IQ_{x_1}(\tau) = \Re\left(IQ_{x_1}(\tau)\right) + j \Im\left(IQ_{x_1}(\tau)\right) = RF_{x_1}(\tau) + j RF_{x_1}\left(\tau + \frac{1}{4f_0}\right)$$

And drawing from **Equation 2**

$$\begin{aligned}\Re\left(IQ_{x_1}(\tau)\right) &= RF_{x_1}(\tau) \approx A_{x_1}(T) \cos(\omega\tau) \cos\left(\phi_{x_1}(T)\right) - A_{x_1}(T) \sin(\omega\tau) \sin\left(\phi_{x_1}(T)\right) \\ &= RF_{x_1}(T) \cos(\omega\tau) + RF_{x_1}\left(T + \frac{1}{4f_0}\right) \sin(\omega\tau)\end{aligned}$$

and drawing from **Equation 3**

$$\begin{aligned}\Im\left(IQ_{x_1}(\tau)\right) &= RF_{x_1}\left(\tau + \frac{1}{4f_0}\right) \\ &\approx -A_{x_1}\left(T + \frac{1}{4f_0}\right) \sin(\omega\tau) \cos\left(\phi_{x_1}\left(T + \frac{1}{4f_0}\right)\right) \\ &\quad - A_{x_1}\left(T + \frac{1}{4f_0}\right) \cos(\omega\tau) \sin\left(\phi_{x_1}\left(T + \frac{1}{4f_0}\right)\right) \\ &\approx -RF_{x_1}(T) \sin(\omega\tau) + RF_{x_1}\left(T + \frac{1}{4f_0}\right) \cos(\omega\tau)\end{aligned}$$

It is possible to avoid making the first approximation by estimating the value of RF at time delay τ using ponderations with $RF(T)$, $RF\left(T + \frac{1}{4f_0}\right)$, or other interpolation schemes.

The traveling time from the original source of the plane wave to the receiving transducer can be approximated as :

$$\tau(x_1, \alpha, x, z) = \tau_{ec} + \tau_{rec}$$

$$\tau(x_1, \alpha, x, z) = \frac{(z * \cos(\alpha) + x * \sin(\alpha))}{c} + \frac{(z + \sqrt{(x - x_1)^2})}{c}$$

with c the speed of sound in the medium.

For each pixel at an instant t_{ST} (slow time), with $i \in [-a; a]$ corresponding to the transducer number and $2a$ the aperture, the beamformed signal is thus :

$$s(x, z, t_{ST}) = \sum_{i \in [x-a; x+a]} I(i, \tau(i, \alpha, x, z)) + j * Q(i, \tau(i, \alpha, x, z))$$

here $I(i, \tau(i, \alpha, x, z))$ is the closest sample acquired in the machine to the time delay τ . This signal is complex and can be rewritten :

$$s(x, z, t_{ST}) = I(x, z, t_{ST}) + j * Q(x, z, t_{ST})$$

In the end, one obtains a complex matrix of size (Nz, Nx, Nt) . The maximum number of (Nz, Nx) is limited by respectively the axial and lateral resolution.

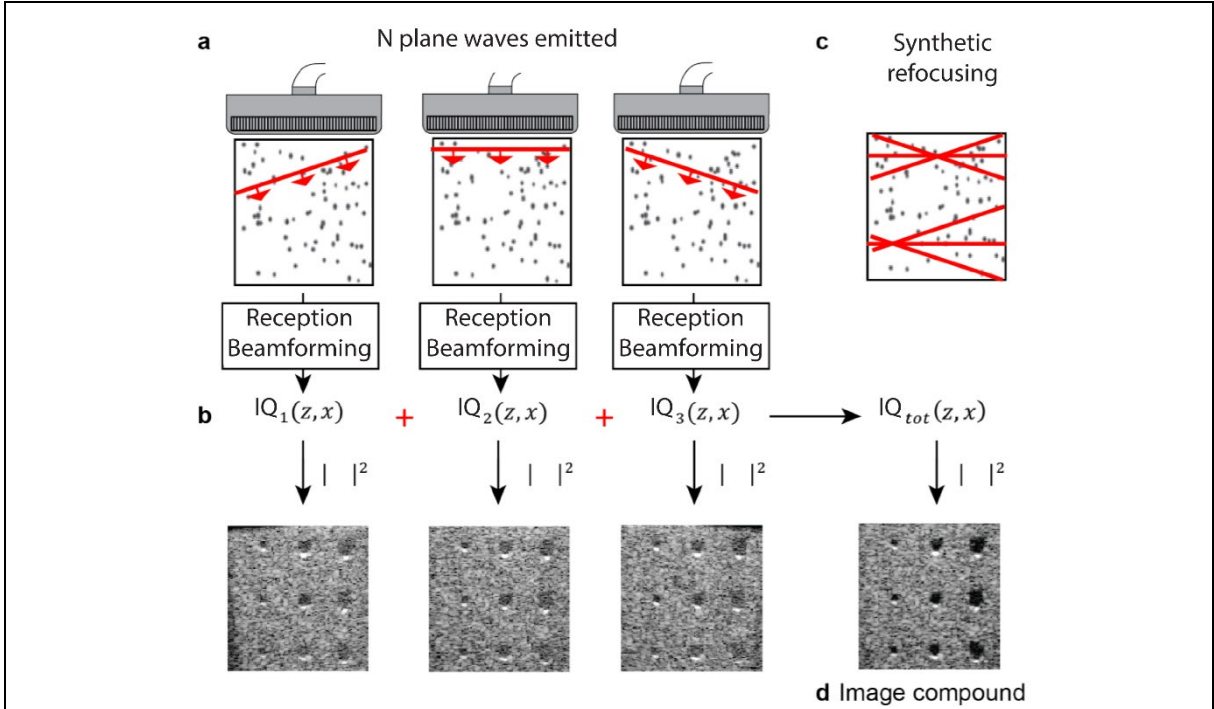
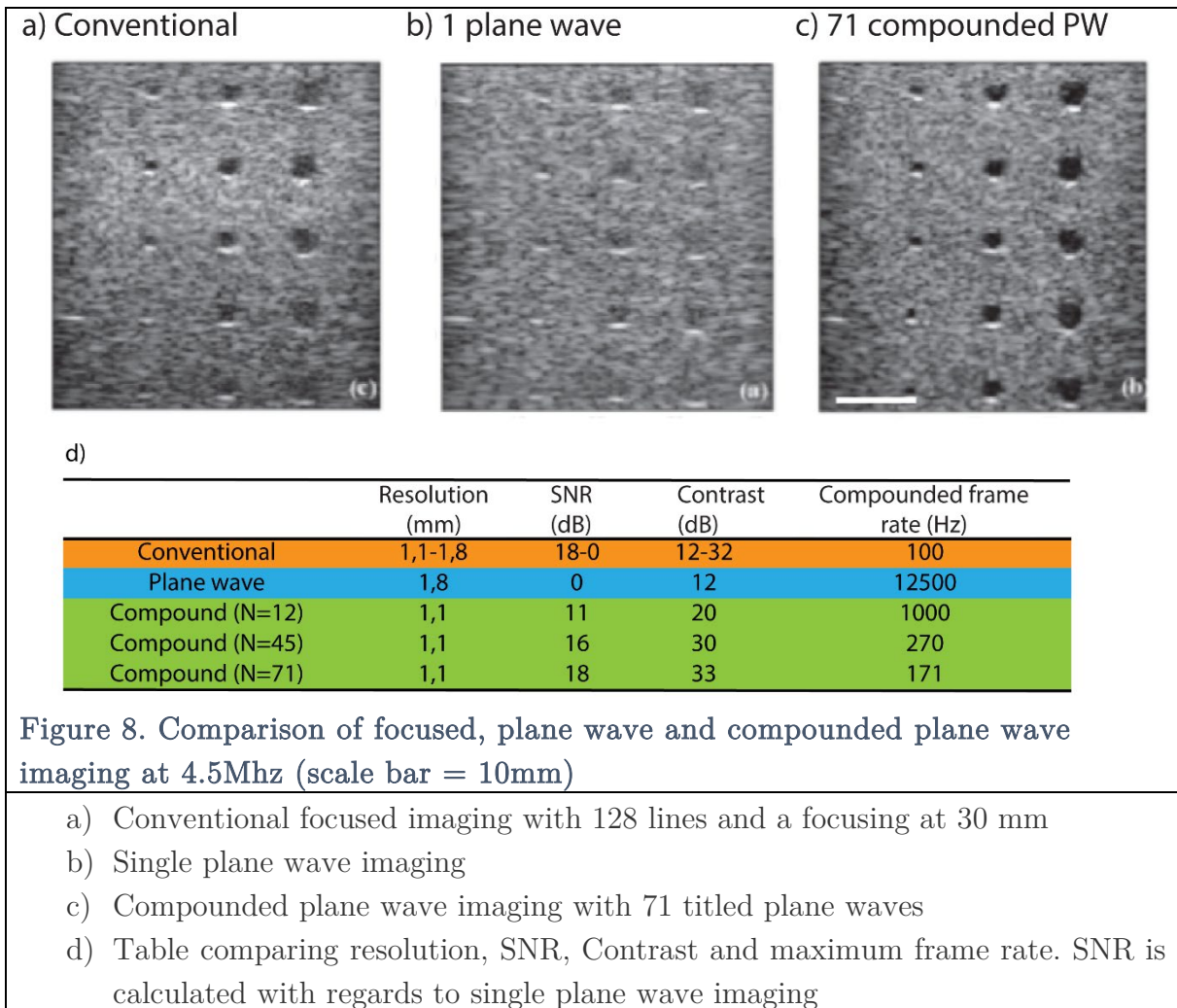


Figure 7 Coherent spatial compounding for plane wave imaging

For each angled plane wave, the associated IQ is calculated and then summed to render a final image IQ_{tot}

- N plane waves with different angles are emitted using the ultrasound system.
- The IQ signals are beamformed.
- Synthetic focusing is performed using appropriate delays on the plane waves
- The IQ signals beamformed are added coherently to render the final compounded image.

(Montaldo et al., 2009) has demonstrated that to obtain similar lateral resolution with compounded plane wave imaging to conventional imaging, the number of angles needs to be at least : $n = \frac{L}{\lambda F}$, with F the f-number and L the total length of the array. As far as the axial resolution is concerned, it only depends on the length of the pulse and the center frequency. To further develop image formation in compounded plane wave, we build the image in the same way as mentioned above for each plane wave. The final compound image is the addition of each of these plane waves.



The advantage of such a technique over conventional B-mode imaging is that the number of angles to achieve similar signal to noise ratio is much lower than the number of transducers, thus increasing the imaging frame rate from a few tens of Hz to several thousands. Another advantage is that the energy is more homogeneously distributed in the image with plane wave rendering a more homogeneous image.

I.4 Ultrafast ultrasound applications : shear wave elastography, motion correction, and functional ultrasound

I.4.1 Shear wave elastography

(Bercoff et al., 2004) demonstrated that it was possible to measure tissue elasticity using only ultrasound. The technique dubbed Supersonic Shear-wave Imaging is based on the generation of shear waves deep in the tissue and measure induced motion with ultrasound. Although several publications exposed various methods to measure elasticity (Nightingale et al., 2002; Sandrin et al., 1999; Sarvazyan et al., 1998), this new technique creates a near cylindrical shear wave cone allowing real-time visualization of wave propagation.

If an ultrasound beam is focused during a long enough time ($>100\mu\text{s}$), the radiation pressure-induced will “push” the tissues in the opposite direction of the originating beam. Because of the elastic properties of tissues, this small deformation will propagate mimicking an almost spherical shear wave. Unfortunately, using a single push is not enough as the amplitude will decrease rapidly due to diffraction. Jeremy Bercoff demonstrated that it was possible to generate a Mach cone by producing these “push” at different depth at a rate corresponding to supersonic speed (thus needing the ultrafast capability of the ultrasound scanner). The constructive interference in between shear waves makes a cylindrical wave with increased amplitude compared to a single “push”. When imaging the region where that wave propagates in 2D at a high enough frame rate, one can see a plane wave propagating at a speed depending on the tissue elasticity which ranges from $[1 - 20] \text{ m/s}$.

To reconstruct an elasticity map of the ROI, an ultrafast acquisition is made to follow tissue deformation. The correlation between each pixel of successive images is calculated and the lag between the maximum correlation peak can be used to calculate the velocity of the shear wave. It is then possible to calculate the group velocity of the shear wave thanks to a time of flight algorithm. By assuming that the wave is plane, and tissue is homogeneous, isotropic and non-viscous, we can write :

$$|\widehat{G}^*(z, x)|_{\omega=\omega_0} = \rho c_g(z, x)^2,$$

And $\widehat{G}^*(z, x)$ is an estimator of the dynamic shear modulus, ρ the density of tissue, c_g the group velocity of the shear wave (Macé et al., 2009).

As the correlation between each pixel is needed, the temporal sampling of the ROI needs to be high and thus requires ultrafast ultrasound (the velocity of a shear wave in

tissue is typically a few meters per second (Bercoff et al., 2004)).

Thanks to shear-wave imaging, it is possible to detect tumors in soft tissues such as breast cancer clinically, and in research is used to measure elasticity in the brain to detect ischemia, image changes in tissues due to arterial pressure (Tanter and Fink, 2014).

I.4.2 Ultrafast motion correction

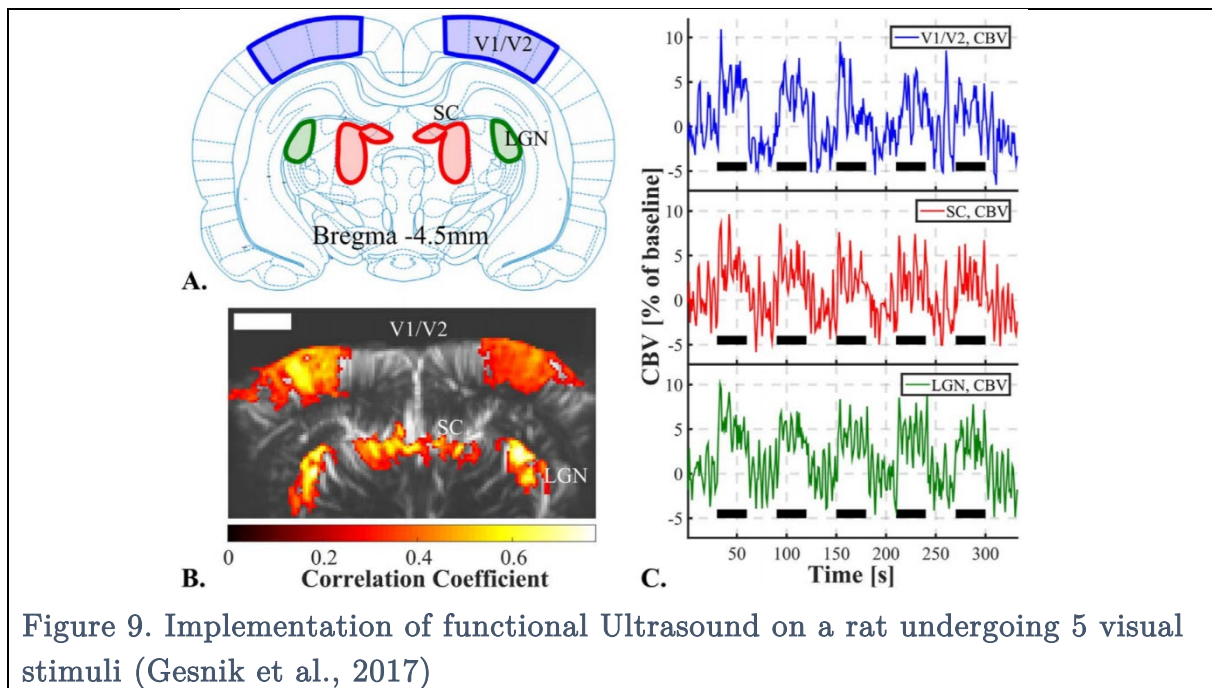
Another application of ultrafast is motion correction. By sending a plane wave in a medium and receiving on two subapertures with different steering angles, (Tanter et al., 2002) demonstrated that it was possible to deduce the time shift due to displacement occurring between two plane wave insonications. This is based on a 1D-cross correlation algorithm of speckle in between two successive images. For compound imaging, $2 \times N_{angles}$ are thus emitted, and the average over all emission angles of the displacement calculated is computed to render a displacement map. The idea behind (Pernot et al., 2004), is to calculate a large number of these time shifts at high frame rate and to solve for 3D displacements with a least-square method. The motion is thus estimated and can be compensated for in 3 dimensions in real-time thanks to ultrafast. This process was used in therapy with High-Intensity Focused Ultrasound to compensate for breathing induced motion in transcranial or transcostal applications(Tanter et al., 2007).

I.4.3 Ultrafast Doppler and functional Ultrasound

Ultrafast Doppler, or ultrasensitive Doppler is a versatile and non-contrast method to assess blood flow. It takes advantage of the very high frame rate brought by Plane Wave Imaging and of high sensitivity brought by compounded plane wave imaging. Longer ensembles to average to reconstitute the Doppler signal give better sensitivity to blood flow. Its high frame rate makes it suitable to follow small and fast hemodynamic changes. It was demonstrated that ultrafast ultrasound was able to map haemodynamic changes better than conventional focused Doppler imaging (Bercoff and Minin, 2011). In particular, during neuronal activation, blood flow increases due to neurovascular coupling. Monitoring blood flow can then reveal parts of the brain with an increased blood supply; i.e. activated regions.

On a craniotomized rat, this technique was able not only to observe these haemodynamic changes in specific areas of the brain but also proved that there was a link between these changes and neuronal activity (Macé et al., 2011). As such, stimulation of the rat's vibrissae induced an increase of blood flow in both the barrel

cortex and the lateral thalamus. The neuronal pathway of the vibrissae is known to go from their position on the rat's face or nostrils to the barrel cortex passing by the trigeminal nerve and the lateral thalamus. It was shown that individual vibrissae response could be precisely mapped in both of these areas. Later, (Gesnik et al., 2017; Osmanski et al., 2014), showed that olfactive and visual stimuli could also be observed using functional Ultrasound, and (Rahal et al., 2019) showed that alteration of the neuronal circuits caused by pain is also visible with fUS, opening a new direction for pain imaging. Finally, this technique was demonstrated on vigil and freely moving mice in (Tiran et al., 2017), remedying to the problem of anesthesia-induced neurological effects. It was also demonstrated in newborns (Demene et al., 2017) and in perioperative of tumor surgery on humans (Imbault et al., 2017).



- Coronal schematic view of the rat brain at Bregma -4.5 mm with the delimitations of Visual Cortex (V1/V2), Lateral Geniculate Nucleus (LGN) and Superior Colliculus (SC)
- fUS imaging of the vision-induced activity at Bregma -4.5 mm, with superimposition of the correlated pixels (hot scale) over the brain vasculature (greyscale). The precision of the map allows retrieving the shape of the 3 vision-related structures present in that coronal slice. Scale bar=2 mm.
- Mean CBV signal over responding pixels in the visual cortices (blue, up), SC (red, middle) and LGN (green, bottom) during that single imaging session composed of 5 flickering screen stimulation trials

These papers have proved that fUS could be used as an alternative to fMRI with

major advantages such as : portability, high spatial and temporal resolution, independence from O₂ variations due to breathing variations (to which BOLD was proved to be dependent on (Murphy et al., 2013)). Limitations remain such as the need for a craniotomy or skull thinning in the rat, limited field of view for other types of animals. In 2016, the first proof of concept of transcranial functional ultrasound using microbubbles was presented, opening the way towards no-surgery functional ultrasound (Errico et al., 2016). As far as other models are concerned, it was proven that fUS could be implemented on newborns by using a specific area in their skull where it has not fused yet (Demene et al., 2017) and also in humans undergoing tumor removal in the brain (and as such have had their brain exposed without the skull) (Imbault et al., 2017).

I.5 Ultrasound Localization Microscopy : a brief introduction

The quest towards enhanced resolution is an obsession among scientists, whether they be biologists, astronomers or doctors. One of the first acknowledged microscopists was not even a scientist : Antonie van Leeuwenhoek developed a magnification microscope with lenses made out of melted soda-lime glass to see the threads of the fabric he sold as a draper (Hamou, 1995). A curious man, he applied his lenses to various organic objects, becoming the first to see and measure microbes, bacteria, muscle fiber, etc... He had a considerable advantage over other microscopists such as Robert Hooke thanks to the simplicity of his process for creating lenses. Hooke even complained about the field of microscopy being monopolized by him: “ [microscopes] are now reduced almost to a single Votary, which is Mr. *Leeuwenhoek*; besides whom, I hear of none that make any other Use of that Instrument, but for Diversion and Pastime” [Hooke 1692, published in 1726 in *Philosophical Experiments and Observations*]. The want for improved resolution is such that the paternity of the microscope is a difficult question whose answer includes the likes of Cornelius Drebbel, Constantijn Huygens, Antonie Van Leeuwenhoek, Galileo Galilei, Zacharias Janssen.

Much later in time, Edward Hutchinson Synge suggested placing samples much closer to the source of light in a microscope, which by passing through an aperture of size much smaller than the wavelength would be concentrated in a beam the size of the aperture. This is now known as Near-Field Scanning Optical Microscopy and was the first technique to break the Abbe diffraction limit. In the near-field, the resolution is comparable to the distance to the aperture (Fink and Tanter, 2010).

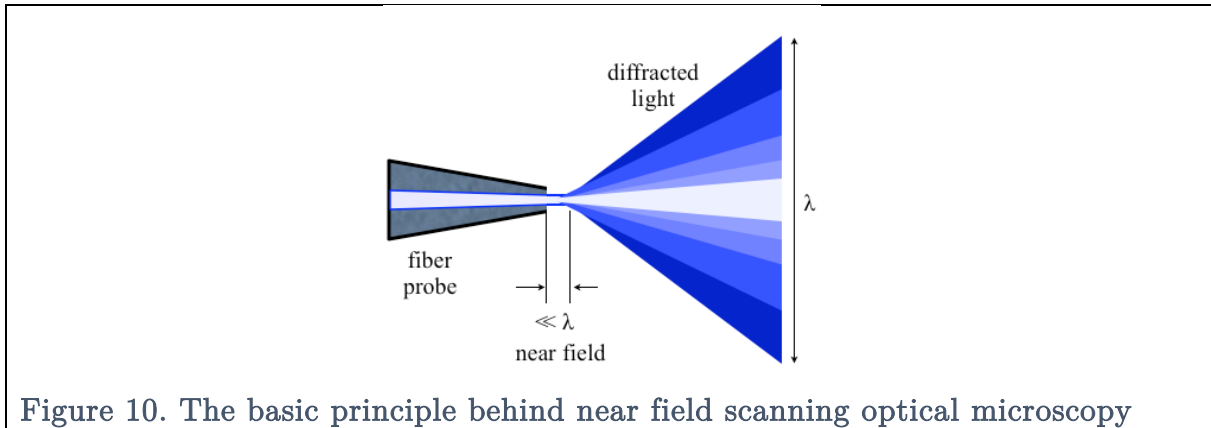


Figure 10. The basic principle behind near field scanning optical microscopy

Another way to improve resolution is to change the source of light. For example, using electrons instead of photons that have a wavelength up to 100,000 times smaller, allow achieving images with resolution down to 50 pm . Finally, one can use the properties of the imaged sample to extract more information than just visual appearance. For example, by illuminating the sample with light at a given wavelength, one can excite fluorescence induced in particular areas (such as Green Fluorescent Protein in cells' genes, or DAPI in DNA), and collect this emitted fluorescence to map these areas. This allows to classify different types of cells or map DNA in biological samples.

However, this technique is still limited in its resolution by Abbe's diffraction limit which states that a microscope with a numerical aperture NA , and illuminates the sample with a light at wavelength λ can produce an image with a maximum lateral resolution

$$d = \frac{\lambda}{2.NA}$$

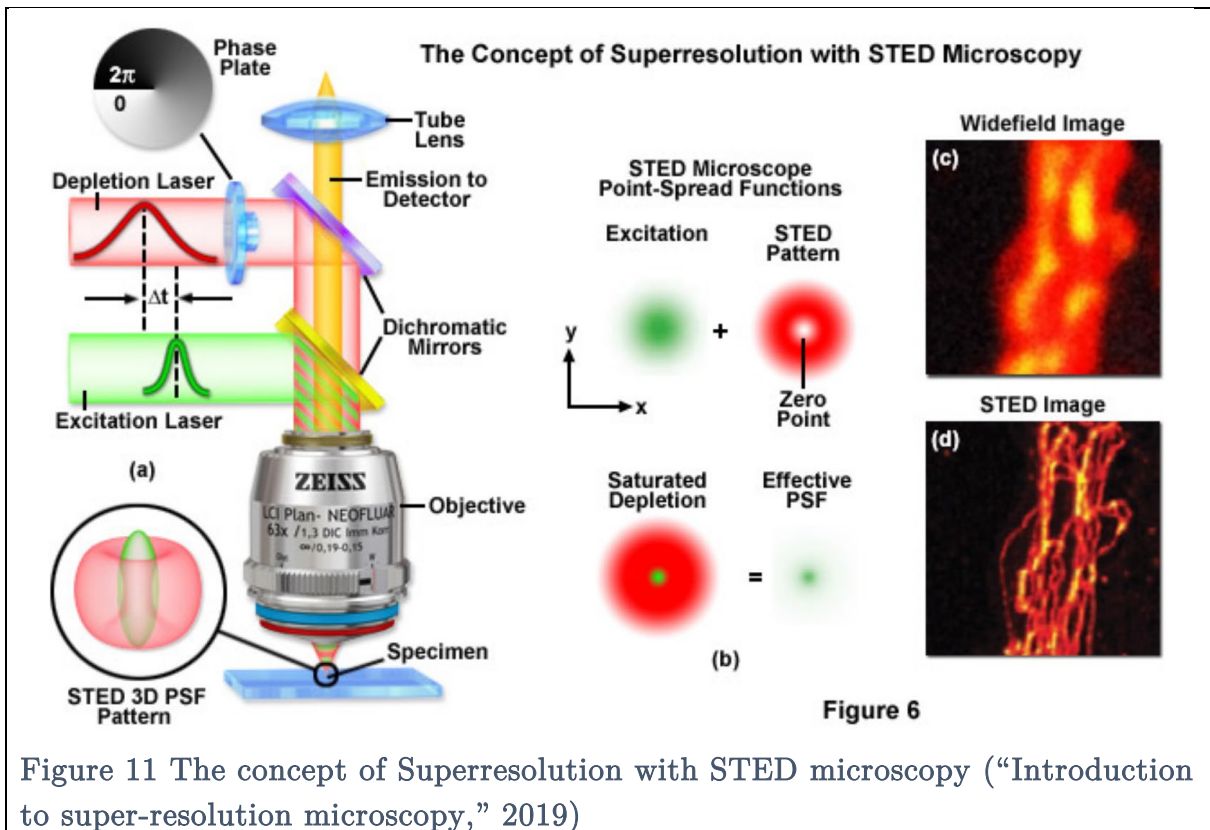
A new field has emerged in the last decade that surpassed Abbe's diffraction limit and Rayleigh's criterion of separation for two punctual sources :

$$d = 1,22 \frac{\lambda}{2.NA}$$

(where 1.22 updates the Abbe's diffraction limit in regard to the Airy pattern of the Point Spread Function (PSF) defined by a Bessel function). This field dubbed "super-resolution microscopy" relies on the modification of fluorophores used in fluorescence microscopy.

The idea behind achieving resolution below the diffraction limit was first introduced by Stefan Hell and his team when they had the idea of REversible Saturable Optical Fluorescence Transitions (RESOLFT) (Hell et al., 2003; Hell and Kroug, 1995; Hell and Wichmann, 1994). Deterministic super-resolution (STED, GSD, SSIM) achieve PSF modifications by relying on a time-sequential readout of fluorophore photoswitching.

They modify the energy released by the fluorophores instead of letting them emit light freely. In STED microscopy, the region of imaging is illuminated by two synchronized collinear sources : one is an excitation laser beam, the other one is a red-shifted depletion laser beam - usually called the STED beam. At the zero point of the STED beam (see Figure 11), the fluorophores will fluoresce freely but the fluorophores at the STED beam will go back to their non-fluorescent state. The effective PSF is thus reduced below the diffraction limit (Hell and Wichmann, 1994). By moving this specific position around the region of imaging, one can map individual positions of single fluorophores emitting light given that the specific position is contained in a small area. The dark state, on the other hand, is quite large and englobes an area around the bright state (“Super-Resolution Microscopy,” 2017). The transition from bright to dark state is what distinguishes STED, GSD, and SSIM in terms of technological process.



Another way to achieve sub-diffraction resolution is called stochastic super-resolution and does not modify spatial sampling of fluorescent emissions but relies on temporal modification: fluorophores will be made active at different times individually and allow separation by capturing high frame rate imaging of these different activations (Betzig et al., 2006; Hess et al., 2006; Rust et al., 2006). The exact position of the particle is then computed to allow mapping of the fluorophores with much higher resolution than

what is stated by the Rayleigh's criterion as even though they are spatially close, their temporal decorrelation allows spatial decorrelation. The different techniques (SOFI, SPDM, PALM, STORM etc..) vary either by how they localize the particles or by what kind of particle parameters they use (i.e. concentration, GFP, RFP, Alexa488, etc..).

In the ultrasound field, the progress towards increased resolution followed a similar path to optics. The axial resolution in an ultrasound image is limited by the length of the pulse emitted by the probe $d_{axial} = \frac{SPL}{2} = \frac{n\lambda}{2}$, with SPL corresponding to Spatial Pulse Length (Cikes et al., 2019). The length of the pulse is linked to the wavelength because the bandwidth of ultrasound transducers typically ranges between 50-100%. It corresponds to the Rayleigh criterion which defines the smallest distance needed between reflectors to be able to separate them. The lateral resolution depends on the width of the ultrasound beam emitted. For focused ultrasound, the pressure field of a focused beam at a depth z can be written :

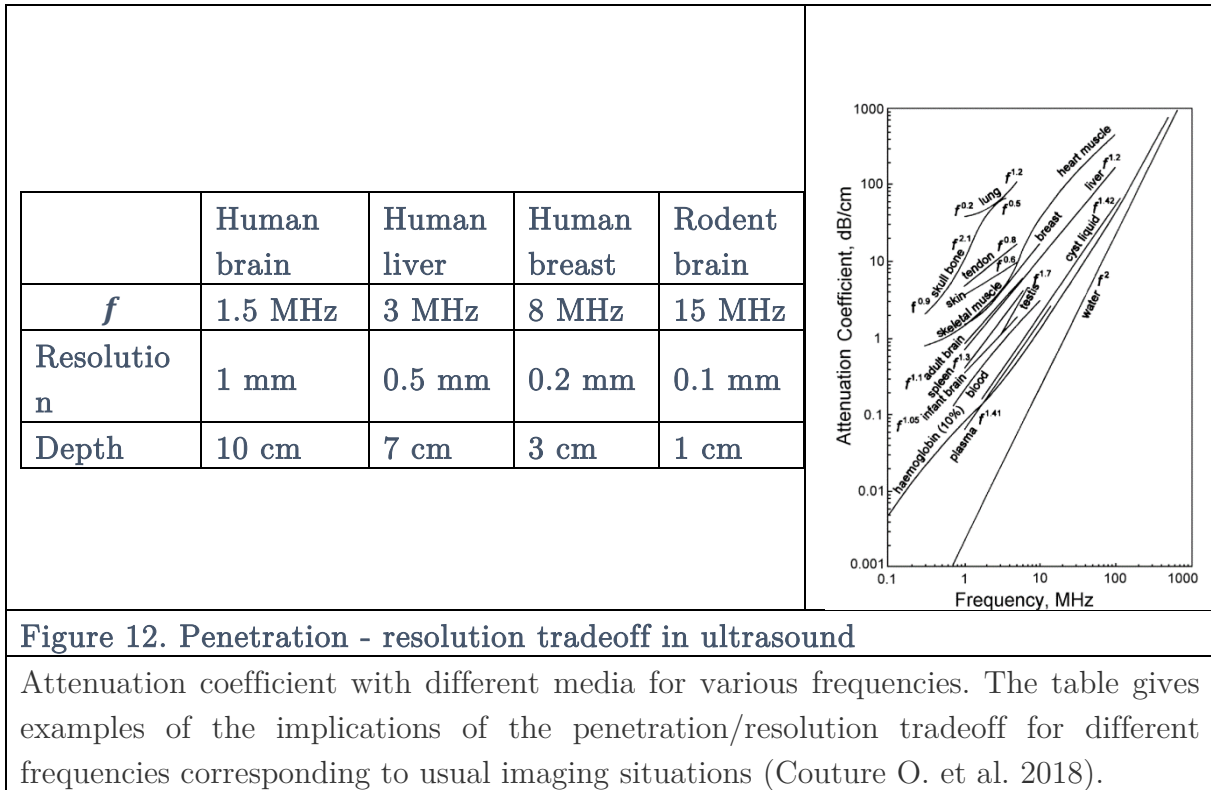
$$p(x, z) = sinc\left(\frac{\pi x D}{\lambda z}\right)$$

That means that the lateral resolution at a depth z is $d_{lateral} = \lambda \frac{z}{D} = \lambda f_{number}$, with D the aperture used to form the beam.

As mentioned above, plane wave imaging not only improves frame rate but also spatial resolution (Montaldo et al., 2009). The coherent plane-wave compounding resolution depends on which type of reconstruction is used to form the image. (Garcia et al., 2013) and (Jiqi Cheng and Jian-yu Lu, 2006) proposed two schemes to improve lateral resolution.

Another way to improve resolution is to implement multi-focus imaging. Because the resolution is maximum at the focal spot, transmitting successive waves with different focal depths allows having improved axial resolution in as many depths as needed.

All of these techniques bring on resolution improvement but are still ruled by the penetration-resolution conundrum and are limited by the wavelength. We saw earlier that resolution depended on the emission's frequency, the higher the frequency is, the better the resolution. However, higher frequency means lower penetration.



In 2010, (Olivier Couture et al., 2011) thought to use contrast agents as single particles moving in the blood to mimic Single Molecule Localization Microscopy. Contrast agents have been used for decades in ultrasound imaging to improve Signal to Noise Ratio in vascular imaging of small vessels thanks to the increased intensity brought by high concentration of contrast agents in the blood. By lowering the concentration of contrast agents to have separable sources in a beaker, letting the bubbles move freely, and recording at a high frame rate this motion, the team demonstrated that it was possible to achieve higher resolution than conventional ultrasound in both directions.

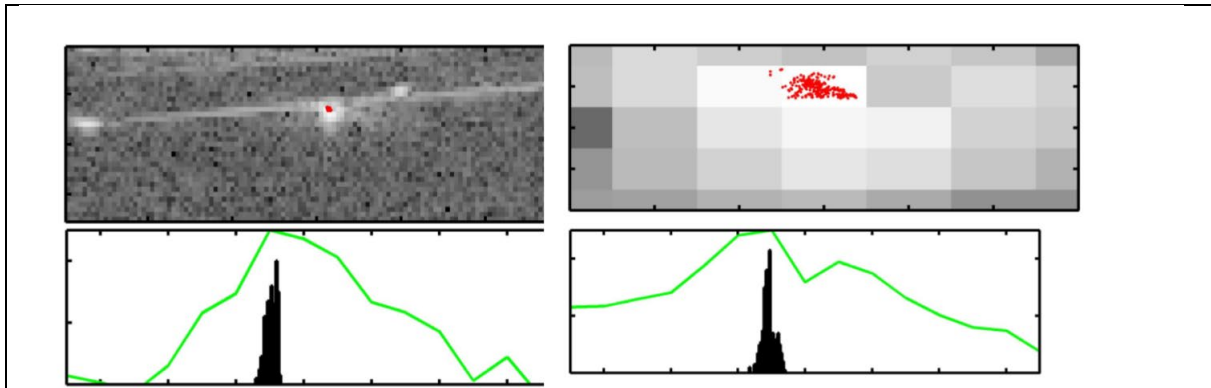


Figure 13. First Proof of concept of super-resolution imaging in ultrasound (Couture et al., 2011)

- a) Left column : Ultrafast imaging of a 100 μm channel in its axial and lateral directions with a 5MHz transducer with overlapped positions of single microbubbles localized (in red)
- b) Right column : Intensity curves in the axial and lateral directions of the channel (in green) with histogram bin of the number of single microbubbles localized (in black).

The width and height of the channel are measured with much higher resolution with the super-resolution technique (Couture et al., 2011).

This proof of concept was matured into an entirely new field of ultrasound imaging with several seminal papers demonstrating the capability of that technique *in vitro*, *in vivo*, in 3D with a limited field of view, and most recently in humans and *in ovo*.

The role of microbubbles acting as stochastic sources is fundamental to the principle of ULM and works hand in hand with ultrafast imaging. In the beginning, several teams have demonstrated that a higher resolution can also be attained when using lower frame rates (Ackermann and Schmitz, 2016; Christensen-Jeffries et al., 2015; O' Reilly and Hynynen, 2013; Opacic et al., 2018; Viessmann et al., 2013) which allows to use conventional scanners in a clinical setting as only a few echographs are capable of obtaining high frame rate and being entirely programmable.

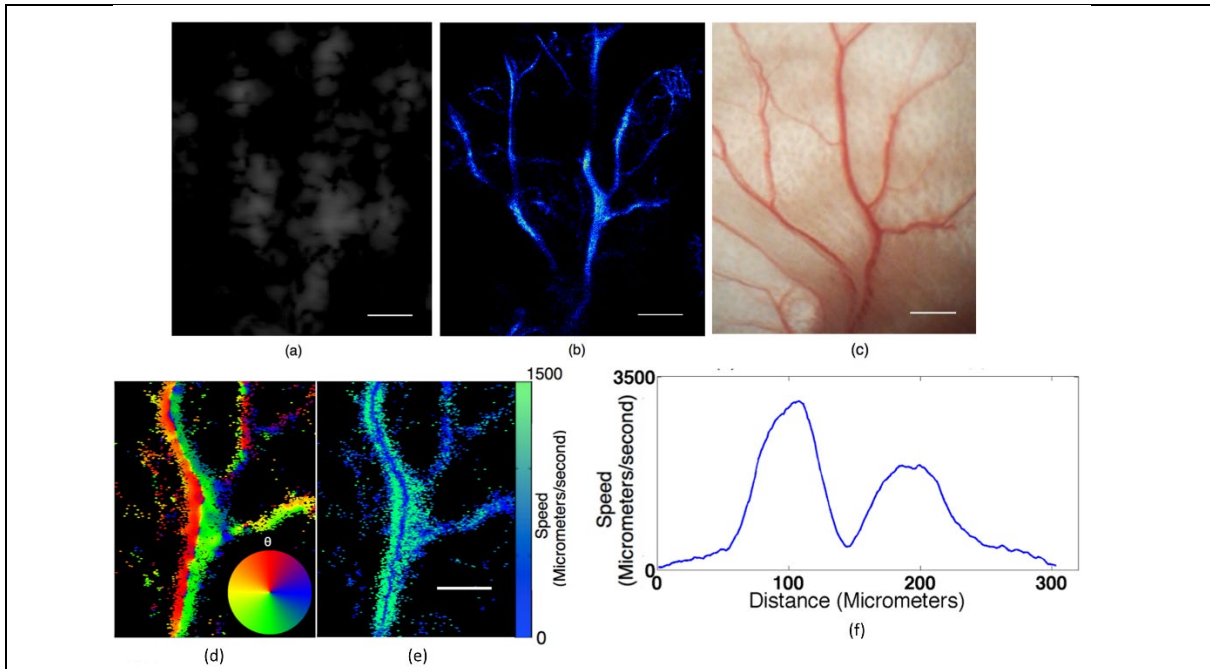


Figure 14. First demonstration of Super-Resolution *in vivo* using a Contrast-Pulse Sequencing mode on a clinically approved scanner on a mouse ear (Christensen-Jeffries et al., 2015)

- a) A single high microbubble concentration image frame acquired using conventional Cadence™ CPS imaging mode.
- b) Super-resolution image created as a probability density map where brightness represents the number of bubbles localized in a given location.
- c) Corresponding optical image of the vasculature within the same mouse-ear acquired in vivo. Scale bars, 1 mm.
- d) Magnified image section from Fig. 14.b) where what appeared initially to be one vessel can be differentiated into an adjacent artery and vein with opposing flows.
- e) shows the corresponding speed of flow through the vessels, where speeds above 1500 $\mu\text{m/s}$ are set to the maximum on the color bar.
- f) Corresponding average flow profile over 400 μm (white box). In both, two vessel profiles can be clearly identified by a distinct slow flow separation, where faster flow is apparent in the centers of the vessels. Scale bar, 500 μm .

Fortunately, our team at Institut Langevin had access to clinically approved and programmable ultrafast echographs (Aixplorers®) thanks to their longtime partnership with Supersonic Imagine, France. The first demonstrations in our institute were thus made with ultrafast and allowed to produce the first super-resolution images of a rat brain (Errico et al., 2015).

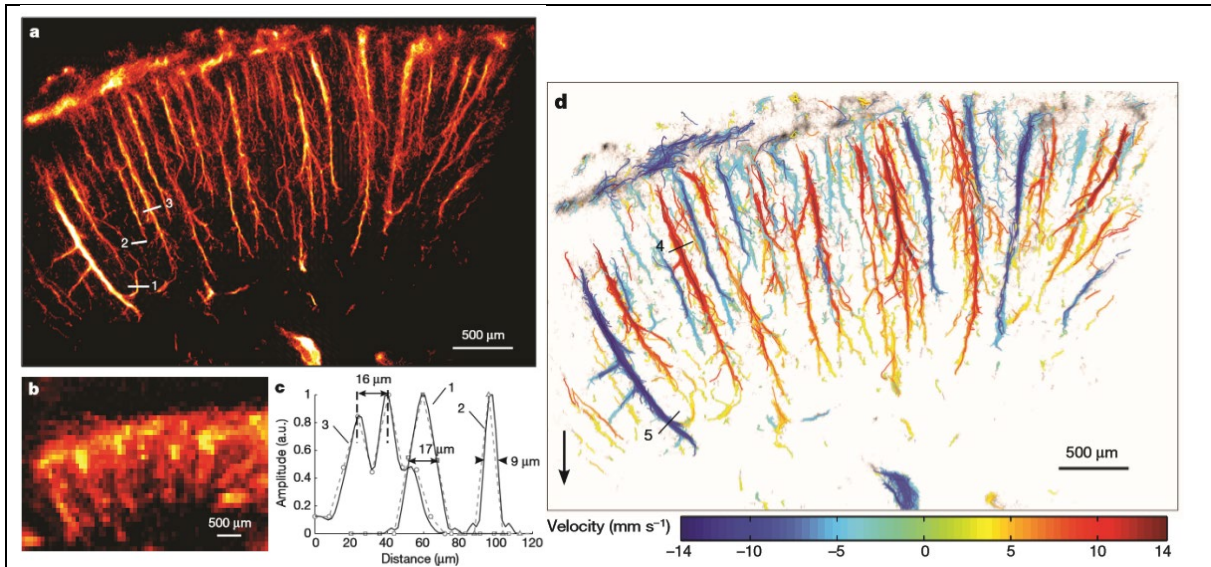


Figure 15. First demonstration of ULM in the rat brain with ultrafast (Errico et al., 2015)

- a) Super-resolved rendering of the cortex of a rat brain obtained with 75000 images acquired at 15MHz with a 500Hz compounded frame rate
- b) Ultrafast power Doppler of the same region of imaging with 3 angled emissions at 15MHz
- c) Interpolated profiles along the lines marked in a display 9 μm vessels (2) and resolve two vessels closer than 16 μm (3). a.u., arbitrary units
- d) Velocimetry of microbubbles with sign corresponding to the vertical direction of the flow and colored according to magnitude.

I.6 3D ultrasound imaging

The first attempt at 3D imaging dates back to 1956 when Howry et al published a design to move a transducer in a 2D scanning motion in water to image a 3D wire mesh. The image produced was projected on a cathode ray tube (Howry et al., 1956).

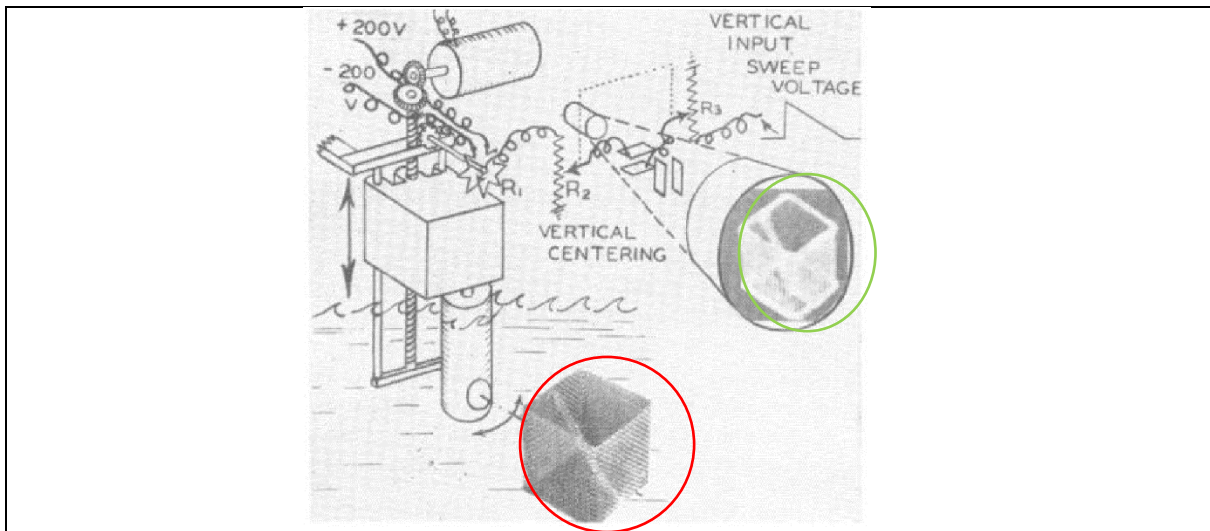


Figure 16. First demonstration of 3D ultrasound imaging with 2D scanning

Design for 3D ultrasound imaging using a mechanical scanner and a single transducer immersed in water. The wire mesh is circled in red while its projection after ultrasound scanning is circled in green.

The first developments of 3D imaging followed a similar idea, using one transducer or a 1D array to retrieve ultrasound images but coupling them with a mechanical scanner to acquire another dimension. These systems were of course quite slow in terms of frame rate but proved that the 3rd dimension could be retrieved with minimal adjustments to the principle of ultrasound. They also paved the way towards a stereoscopic or tomographic reconstruction of ultrasound images. In 1972, (Robinson, 1972) exposed a method to produce 3D renderings of 2D digitized ultrasound scans. By interpolating the line data orthogonal to a transverse scan, the method proved able to visualize data in all dimensions. The process was slow and expensive because of limited computing power. In the next decade, teams around the world improved on translated 2D reconstruction (Brinkley et al., 1978, n.d.; Greenleaf, 1982).

The next step in 3D reconstruction with mechanical scanning was opened up by the shift from translation based on rotation based motion (Ghosh et al., 1982). More recently, the use of ultrafast ultrasound was implemented with rotation based scanning. Thanks to high frame rate and high sensitivity, this technique called Ultrafast Doppler Tomography allowed to image a rat brain in 3 dimensions with information of blood flow with a millisecond temporal resolution in each plane (Demené et al., 2016).

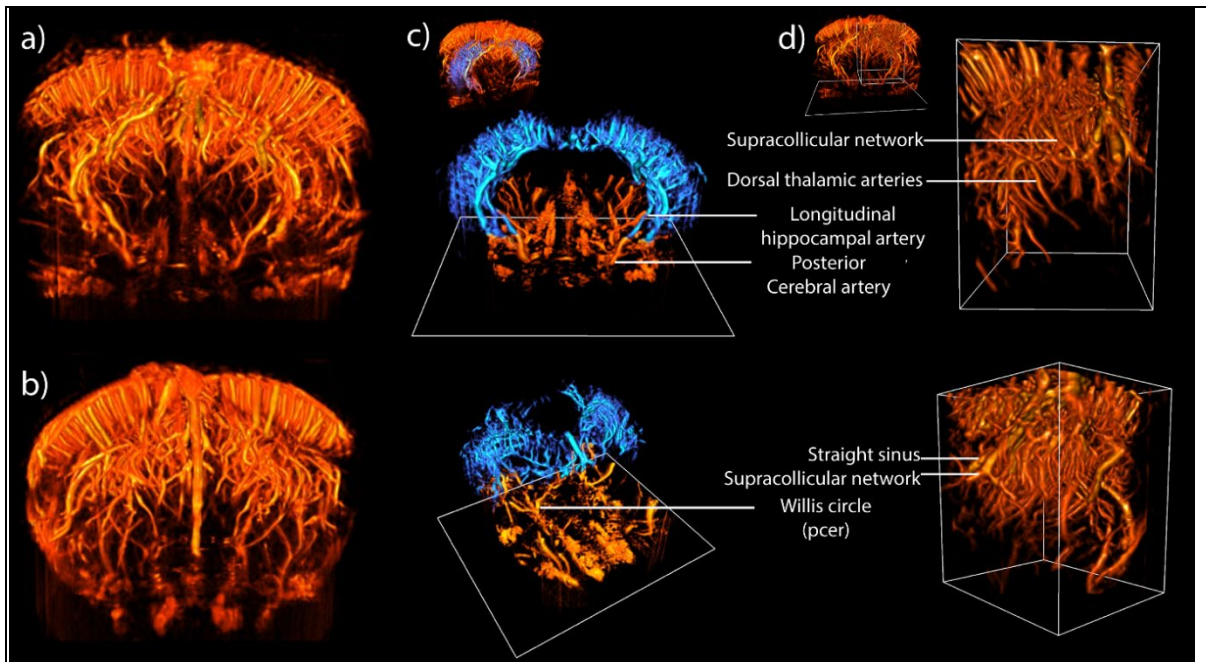


Figure 17. Ultrafast Doppler Tomography on a Rat Brain (Demené et al., 2016)

a),b) Front and rear view of a complete volume acquired on a rat brain in UFD-T.
 c) Manually segmented view of the hippocampus (in blue) connected to deep vascular structures.
 d) Zoomed-in view of the colliculus and the cortical vessels in the caudal region.

Thanks to technological advances in probe manufacturing, new designs emerged with 1.25D, 1.5D, and 1.75D arrays (see Figure 18).

The improvement brought by 1.75D and 2D arrays can be reduced to the capability of steering in two planes rather than only one plane. 1.25D and 1.5D offer a significant gain in elevation performance compared to conventional 1D arrays as they are able to modify respectively their aperture and their apodization, focusing and aperture.

The first implementation of high-speed ultrasound in 3D was demonstrated in 1991 by (Olaf T. von Ramm et al., 1991) using electronic steering on a 2D matrix array and a new method for parallel processing to achieve a high frame rate of about 60Hz – mentioned above as Explososcan. Since then, the field of 3D ultrasound imaging has been shown to provide intracardiac images with a 2D catheter array transducer (Light et al., 2001) with conventional echographs but limited frame rates. New technologies for 2D matrix arrays such as Row and Column Addressed Probes (Christiansen et al., 2015; Rasmussen et al., 2015; Rasmussen and Jensen, 2013) recently allowed to reach high spatial and temporal sampling using limited channels echographs.

Array types	1D linear	1.5D	1.75D	2D
Focusing capability	in azimuth	in azimuth	in elevation and azimuth	in elevation and azimuth
Array geometry	full	full	full	sparse
Independent rows	N/A	no*	yes	yes
No. of rows \times No. of lateral elements	$1 \times N$	$(2 - 4) \times N$	$(2 - 8+) \times N$	$N \times N$
Electrical focusing in elevation	no	yes (symmetric)	yes	yes
Electrical steering in elevation	no	no	limited	yes
Mechanical focusing	yes	yes	yes	no

*1.5D arrays have independent symmetrically paired rows.

Figure 18. Different types of arrays and their characteristics (Fernandez et al., 2003)

a) 1D are the most widely used probes
 1.5D and 1.75D are matrix arrays but with a limited 3rd dimension
 2D matrix arrays are square matrix arrays that provide isotropic or close to isotropic capabilities

b) Schematics of elevation wiring in multi-D transducers

The last technique is called 4D ultrasound imaging and has been developed concurrently at Institut Langevin and at Danmarks Tekniske Universitet (DTU). The main difference between these two approaches is technological.

(Provost et al., 2014) described a 4D ultrasound scanner which was made of 4 programmable echographs from Supersonic Imagine® (Aixplorer v6). These 4 echographs were rearranged in a horizontal fashion to be separated in 4 stages on top of each other. This design allowed to plug in the arrays with limited length of cable. On top of the scanners, a master computer with 128GB of RAM, a GTX 1080Ti with 8Gb of RAM (Nvidia Corporation®) and a 2.5 GHz CPU was connected to each stage with an optic fiber interface. This allowed to send and receive instructions or data at a high transfer rate. Two schemes are possible : either the master computer is only used to pass initial instructions to the echographs and then the data is stored on the echographs' computers and processed until transferred, or the master computer is used to drive the echographs independently and retrieves data in real-time for on-board processing. The main advantage of the first technique is a 4 fold increase in computational power but as the echographs' computers are non-upgradable, this increase can be significantly lower when the master computer is upgraded. The disadvantage of the latter scheme is the need to wait for the data to be transferred which can take a long time even with fiber optics as ultrafast volumetric data size tends to increase dramatically. This system is highly

versatile and relatively simple to drive and served to produce many proofs of concepts for 3D imaging such as : 3D shear-wave and flow imaging *in vivo* (Provost et al., 2016), 4D ultrafast flow imaging (Correia et al., 2016), 3D elastic tensor imaging (Correia et al., 2018), simultaneous tissue and blood flow Doppler imaging (Papadacci et al., 2019).

At Danmarks Tekniske Universitet, the Synthetic Aperture Real-time Ultrasound System was developed. The goal of this custom-made system is to be able to acquire and process synthetic aperture data. SARUS hosts 64 boards each capable of transmitting and receiving 16 channels making it a 1024 channel scanner. Each board can store up to 2GB of data for processing using Field-Programmable Gate Arrays (FPGAs). The stored data can later be transferred to a processing server using 64 1GBps Ethernet interfaces. The main advantage of this system is that it was tailor-made for 3D flow imaging purposes and as such has penetration depth and time accuracy similar to conventional 2D commercial scanners. Thanks to FPGAs, its beamformer is 100 to 200 times faster than traditional scanners. It served to present and prove the feasibility of : 3D continuous vector flow imaging (Holbek et al., 2015), its implementation *in vivo* for common carotid artery characterization (Holbek et al., 2017), synthetic aperture vector flow imaging for transthoracic echocardiography (Villagómez-Hoyos et al., 2016).

Other teams around the world are moving on towards 4D imaging, whether it be based on regrouping 4 machines together (Petrusca et al., 2018), or exploring the field of multiplexed probes, sparse arrays or RCAs (Austeng and Holm, 2002; Brunke and Lockwood, 1997; Karaman et al., 2009; Lockwood et al., 1998; Martínez-Graullera et al., 2010; Ramalli et al., 2015; Turnbull and Foster, 1991), or using numerical based approach to tackle compressed-sensing approaches on 4D imaging (Besson et al., 2019). For an extensive review of sparse arrays and their evolution please consult chapter 4 and complementarily, Emmanuel Roux’s very comprehensive state of the art in his thesis published recently (Roux, 2019).

I.7 Thesis objectives

As we have seen, the ultrasound field has seen major breakthroughs in the last two decades with a programmable and ultrafast scanner, shear-wave elastography, ultrasensitive Doppler and functional imaging, the leap forward in the 3rd dimension and the undoing of the penetration/resolution tradeoff. The first two of these breakthroughs were allowed by significant progress in hardware technology such as parallel programming and the increase in GPU power.

The main objective of this thesis is to engineer 4D ULM using a 2D matrix array image a large volume in as little time as possible while reaching 10 times higher resolution and dispense with operator-dependency. To achieve this goal, we first describe methods to accelerate the signal processing to achieve microbubble localization. Secondly, we implement ULM with a matrix transducer array and show it *in vitro*. Thirdly, we demonstrate its potential in an *in vivo* model. Finally, we show that it is possible to image whole organs using this technique, giving unprecedented imaging of the whole rat brain *in vivo*. We have divided these achievements in 4 different chapters.

I.7.1 Chapter 2 : Developing new techniques to achieve faster, better Ultrasound Localization Microscopy

We outlined the diversity of ULM schemes in this introduction. We believe that the need for a universal framework with fast and high-quality images is crucial to the development of the technique. To achieve this, we first looked for a faster and less computationally expensive method for microbubble localization. Then, we improved the tracking of microbubbles by switching our view on the problem to an assignment approach seeking to minimize both distance between microbubbles and overall distance traveled. We then searched for parallelization based optimization of the algorithm both in two and three dimensions. Finally, we designed metrics and used *in silico* and *in vivo* datasets to provide a way to perform quality assessment of our algorithms. This led to several applications both *in vitro* and *in vivo* that proved our framework to be robust and easily portable.

I.7.2 Chapter 3 : Achieving *in vitro* volumetric ultrafast Ultrasound Localization Microscopy

In parallel to the development of the framework mentioned in the previous section, we tested the new algorithms and techniques with an *in vitro* phantom. The goal of this chapter is to provide a simple method for manufacturing *in vitro* microvascular phantom with three-dimensional characteristics and prove that 3D ULM is feasible. The phantoms allowed testing both our ultrasound sequences and our algorithms at a minimal cost and with basic equipment. The *in vitro* study opened up the way towards *in vivo* implementation of the technique.

I.7.3 Chapter 4 : Using *in vivo* volumetric ultrafast ULM as a blood flow sensor

After demonstrating the capabilities of 3D ULM *in vitro*, we decided to port our technique on an animal model. We chose to image the rat brain. This choice was

motivated by the well-established vascular structures in the brain and by the experience that was acquired at our lab with such a model. Following the initial developments, we decided to investigate the possibility of using volumetric ULM as a blood flow sensor to outline the vascular effects brought by two different anesthesia. Additionally to our demonstration of the abilities of ULM, this chapter helped us to develop significant skills in craniotomy surgery and move further in brain imaging.

I.7.4 Chapter 5 : Towards whole-brain imaging

We developed a large craniotomy model to have access to the whole rat brain without the skull barrier. The combination of ULM and of that technique allowed us to perform whole-brain super-resolution imaging for the first time. We believe that the vascular mapping and the velocimetry information contained in our data will be useful to neuroscientists, biologists and ultrasound physicists alike.

Concluding remarks and perspectives will follow in the final chapter of this document.

- Ackermann, D., Schmitz, G., 2016. Detection and Tracking of Multiple Microbubbles in Ultrasound B-Mode Images. *IEEE Trans. Ultrason. Ferroelectr. Freq. Control* 63, 72–82. <https://doi.org/10.1109/TUFFC.2015.2500266>
- Austeng, A., Holm, S., 2002. Sparse 2-D arrays for 3-D phased array imaging - design methods. *IEEE Trans. Ultrason. Ferroelectr. Freq. Control* 49, 1073–1086. <https://doi.org/10.1109/TUFFC.2002.1026019>
- Bercoff, J., Minin, 2011. Ultrafast Ultrasound Imaging, in: *Ultrafast Ultrasound Imaging, Ultrasound Imaging - Medical Applications*. p. 23.
- Bercoff, J., Tanter, M., Fink, M., 2004. Supersonic shear imaging: a new technique for soft tissue elasticity mapping. *IEEE Trans. Ultrason. Ferroelectr. Freq. Control* 51, 396–409. <https://doi.org/10.1109/TUFFC.2004.1295425>
- Besson, A., Perdios, D., Wiaux, Y., Thiran, J.-P., 2019. Joint Sparsity With Partially Known Support and Application to Ultrasound Imaging. *IEEE Signal Process. Lett.* 26, 84–88. <https://doi.org/10.1109/LSP.2018.2880571>
- Betzig, E., Patterson, G.H., Sougrat, R., Lindwasser, O.W., Olenych, S., Bonifacino, J.S., Davidson, M.W., Lippincott-Schwartz, J., Hess, H.F., 2006. Imaging Intracellular Fluorescent Proteins at Nanometer Resolution. *Science* 313, 1642–1645. <https://doi.org/10.1126/science.1127344>
- Bonnefous, O., Pesque, P., 1986. Time Domain Formulation of Pulse-Doppler Ultrasound and Blood Velocity Estimation by Cross Correlation 13.
- Brinkley, J.F., Moritz, W.E., Baker, D.W., 1978. Ultrasonic three-dimensional imaging and volume from a series of arbitrary sector scans. *Ultrasound Med. Biol.* 4, 317–321. [https://doi.org/10.1016/0301-5629\(78\)90020-0](https://doi.org/10.1016/0301-5629(78)90020-0)
- Brinkley, J.F., Muramatsu, S.K., McCallum, D., Popp, R.L., n.d. IN VITRO EVALUATION OF AN ULTRASONIC THREE-DIMENSIONAL IMAGING AND VOLUME SYSTEM 14.
- Bruneel, C., Nongaillard, B., Torguet, R., Bridoux, E., Rouvaen, J.M., 1977. Reconstruction of an acoustical image using an ‘acousto-electronic’ lens device. *Ultrasonics* 15, 263–264. [https://doi.org/10.1016/0041-624X\(77\)90037-3](https://doi.org/10.1016/0041-624X(77)90037-3)
- Bruneel, C, Torguet, R., Rouvaen, K.M., Bridoux, E., Nongaillard, B., 1977. Ultrafast echotomographic system using optical processing of ultrasonic signals. *Appl Phys Lett* 30, 4.
- Brunke, S.S., Lockwood, G.R., 1997. Broad-bandwidth radiation patterns of sparse two-dimensional vernier arrays. *IEEE Trans. Ultrason. Ferroelectr. Freq. Control* 44, 1101–1109. <https://doi.org/10.1109/58.655635>
- Christensen-Jeffries, K., Browning, R.J., Tang, M.-X., Dunsby, C., Eckersley, R.J., 2015. In Vivo Acoustic Super-Resolution and Super-Resolved Velocity Mapping Using Microbubbles. *IEEE Trans. Med. Imaging* 34, 433–440. <https://doi.org/10.1109/TMI.2014.2359650>
- Christiansen, T.L., Rasmussen, M.F., Bagge, J.P., Moesner, L.N., Jensen, J.A., Thomsen, E.V., 2015. 3-D imaging using row-column-addressed arrays with integrated

- apodization— part ii: transducer fabrication and experimental results. *IEEE Trans. Ultrason. Ferroelectr. Freq. Control* 62, 959–971. <https://doi.org/10.1109/TUFFC.2014.006819>
- Cikes, M., D’hooge, J., Solomon, S.D., 2019. Physical Principles of Ultrasound and Generation of Images, in: *Essential Echocardiography*. Elsevier, pp. 1-15.e1. <https://doi.org/10.1016/B978-0-323-39226-6.00001-1>
- Cobbold, R.S.C., 2005. *Foundations of Biomedical Ultrasound* 14.
- Correia, M., Deffieux, T., Chatelin, S., Provost, J., Tanter, M., Pernot, M., 2018. 3D elastic tensor imaging in weakly transversely isotropic soft tissues. *Phys. Med. Biol.* 63, 155005. <https://doi.org/10.1088/1361-6560/aacfaf>
- Correia, M., Provost, J., Tanter, M., Pernot, M., 2016. 4D ultrafast ultrasound flow imaging: *in vivo* quantification of arterial volumetric flow rate in a single heartbeat. *Phys. Med. Biol.* 61, L48–L61. <https://doi.org/10.1088/0031-9155/61/23/L48>
- Couture, O., Besson, B., Montaldo, G., Fink, M., Tanter, M., 2011. Microbubble ultrasound super-localization imaging (MUSLI). *IEEE*, pp. 1285–1287. <https://doi.org/10.1109/ULTSYM.2011.6293576>
- Couture, O., Hingot, V., Heiles, B., Muleki-Seya, P., Tanter, M., 2018. Ultrasound localization microscopy and super-resolution: a state-of-the-art. *IEEE Trans. Ultrason. Ferroelectr. Freq. Control* 1–1. <https://doi.org/10.1109/TUFFC.2018.2850811>
- Demene, C., Baranger, J., Bernal, M., Delanoe, C., Auvin, S., Biran, V., Alison, M., Mairesse, J., Harribaud, E., Pernot, M., Tanter, M., Baud, O., 2017. Functional ultrasound imaging of brain activity in human newborns. *Sci. Transl. Med.* 9, eaah6756. <https://doi.org/10.1126/scitranslmed.aah6756>
- Demené, C., Tiran, E., Sieu, L.-A., Bergel, A., Gennisson, J.L., Pernot, M., Deffieux, T., Cohen, I., Tanter, M., 2016. 4D microvascular imaging based on ultrafast Doppler tomography. *NeuroImage* 127, 472–483. <https://doi.org/10.1016/j.neuroimage.2015.11.014>
- Errico, C., Osmani, B.-F., Pezet, S., Couture, O., Lenkei, Z., Tanter, M., 2016. Transcranial functional ultrasound imaging of the brain using microbubble-enhanced ultrasensitive Doppler. *NeuroImage* 124, 752–761. <https://doi.org/10.1016/j.neuroimage.2015.09.037>
- Errico, C., Pierre, J., Pezet, S., Desailly, Y., Lenkei, Z., Couture, O., Tanter, M., 2015. Ultrafast ultrasound localization microscopy for deep super-resolution vascular imaging. *Nature* 527, 499–502. <https://doi.org/10.1038/nature16066>
- Fernandez, A.T., Gammelmark, K.L., Dahl, J.J., Keen, C.G., Gauss, R.C., Trahey, G.E., 2003. Synthetic Elevation Beamforming and Image Acquisition Capabilities Using an 8×128 1.75D Array 50, 18.
- Fink, M., Tanter, M., 2010. Multiwave imaging and super resolution. *Phys. Today* 63, 28–33. <https://doi.org/10.1063/1.3326986>

- Garcia, D., Tarnec, L.L., Muth, S., Montagnon, E., Poree, J., Cloutier, G., 2013. Stolt's f-k migration for plane wave ultrasound imaging. *IEEE Trans. Ultrason. Ferroelectr. Freq. Control* 60, 1853–1867. <https://doi.org/10.1109/TUFFC.2013.2771>
- Gesnik, M., Blaize, K., Deffieux, T., Gennisson, J.-L., Sahel, J.-A., Fink, M., Picaud, S., Tanter, M., 2017. 3D functional ultrasound imaging of the cerebral visual system in rodents. *NeuroImage* 149, 267–274. <https://doi.org/10.1016/j.neuroimage.2017.01.071>
- Ghosh, A., Nanda, N.C., Maurer, G., 1982. Three-dimensional reconstruction of echocardiographic images using the rotation method. *Ultrasound Med. Biol.* 8, 655–661. [https://doi.org/10.1016/0301-5629\(82\)90122-3](https://doi.org/10.1016/0301-5629(82)90122-3)
- Greenleaf, J.F., 1982. Three-dimensional imaging in ultrasound. *J. Med. Syst.* 6, 579–589. <https://doi.org/10.1007/BF00995508>
- Hamou, P., 1995. Microscopie et témoignage oculaire: l'exemple d'Antony Van Leeuwenhoek (1673-1723). *Rev. Nord* 77, 775–798.
- Hell, S.W., Jakobs, S., Kastrop, L., 2003. Imaging and writing at the nanoscale with focused visible light through saturable optical transitions. *Appl. Phys. Mater. Sci. Process.* 77, 859–860. <https://doi.org/10.1007/s00339-003-2292-4>
- Hell, S.W., Kroug, M., 1995. Ground-state-depletion fluorescence microscopy: A concept for breaking the diffraction resolution limit. *Appl. Phys. B Lasers Opt.* 60, 495–497. <https://doi.org/10.1007/BF01081333>
- Hell, S.W., Wichmann, J., 1994. Breaking the diffraction resolution limit by stimulated emission: stimulated-emission-depletion fluorescence microscopy. *Opt. Lett.* 19, 780. <https://doi.org/10.1364/OL.19.000780>
- Hess, S.T., Girirajan, T.P.K., Mason, M.D., 2006. Ultra-High Resolution Imaging by Fluorescence Photoactivation Localization Microscopy. *Biophys. J.* 91, 4258–4272. <https://doi.org/10.1529/biophysj.106.091116>
- Holbek, S., Hansen, K.L., Bouzari, H., Ewertsen, C., Stuart, M.B., Thomsen, C., Nielsen, M.B., Jensen, J.A., 2017. Common Carotid Artery Flow Measured by 3-D Ultrasonic Vector Flow Imaging and Validated with Magnetic Resonance Imaging. *Ultrasound Med. Biol.* 43, 2213–2220. <https://doi.org/10.1016/j.ultrasmedbio.2017.06.007>
- Holbek, S., Pihl, M.J., Ewertsen, C., Nielsen, M.B., Jensen, J.A., 2015. In vivo 3-D vector velocity estimation with continuous data, in: 2015 IEEE International Ultrasonics Symposium (IUS). Presented at the 2015 IEEE International Ultrasonics Symposium (IUS), IEEE, Taipei, Taiwan, pp. 1–4. <https://doi.org/10.1109/ULTSYM.2015.0235>
- Howry, D.H., Posakony, G., Cushman, C.R., Holmes, J.H., 1956. *Three-Dimensional and Stereoscopic Observation of Body Structures by Ultrasound*. *J. Appl. Physiol.* 9, 304–306. <https://doi.org/10.1152/jappl.1956.9.2.304>
- Imbault, M., Chauvet, D., Gennisson, J.-L., Capelle, L., Tanter, M., 2017. Intraoperative

- Functional Ultrasound Imaging of Human Brain Activity. *Sci. Rep.* 7, 7304.
<https://doi.org/10.1038/s41598-017-06474-8>
- Introduction to super-resolution microscopy, 2019.
- Jiqi Cheng, Jian-yu Lu, 2006. Extended high-frame rate imaging method with limited-diffraction beams. *IEEE Trans. Ultrason. Ferroelectr. Freq. Control* 53, 880–899.
<https://doi.org/10.1109/TUFFC.2006.1632680>
- Karaman, M., Wygant, I.O., Oralkan, O., Khuri-Yakub, B.T., 2009. Minimally Redundant 2-D Array Designs for 3-D Medical Ultrasound Imaging. *IEEE Trans. Med. Imaging* 28, 1051–1061. <https://doi.org/10.1109/TMI.2008.2010936>
- Kasai, C., Namekawa, K., Koyano, A., Omoto, R., 1985. Real-Time Two-Dimensional Blood Flow Imaging Using an Autocorrelation Technique 7.
- Kato, K., Izumi, T., 1966. On a method of indication of reverse flow in the ultrasonic Doppler flowmeter, in: *Proceedings of the Ioth Meeting of the Japan Society of Ultrasonics in Medicine*.
- Light, E.D., Idriss, S.F., Wolf, P.D., Smith, S.W., 2001. Real-time three-dimensional intracardiac echocardiography. *Ultrasound Med. Biol.* 27, 1177–1183.
[https://doi.org/10.1016/S0301-5629\(01\)00421-5](https://doi.org/10.1016/S0301-5629(01)00421-5)
- Lockwood, G.R., Talman, J.R., Brunke, S.S., 1998. Real-time 3-D ultrasound imaging using sparse synthetic aperture beamforming. *IEEE Trans. Ultrason. Ferroelectr. Freq. Control* 45, 980–988. <https://doi.org/10.1109/58.710573>
- Lowe, L.H., Bailey, Z., 2011. State-of-the-Art Cranial Sonography: Part 1, Modern Techniques and Image Interpretation. *Am. J. Roentgenol.* 196, 1028–1033.
<https://doi.org/10.2214/AJR.10.6160>
- Macé, E., Cohen, I., Gennisson, J., Miles, R., Tanter, M., Fink, M., 2009. Ultrasound transient elastography of the brain : an in vivo feasibility study in small animals. Presented at the International Conference on the ultrasonic measurement and imaging of Tissue Elasticity.
- Macé, E., Montaldo, G., Cohen, I., Baulac, M., Fink, M., Tanter, M., 2011. Functional ultrasound imaging of the brain. *Nat. Methods* 8, 662–664.
<https://doi.org/10.1038/nmeth.1641>
- Martínez-Graullera, O., Martín, C.J., Godoy, G., Ullate, L.G., 2010. 2D array design based on Fermat spiral for ultrasound imaging. *Ultrasonics* 50, 280–289.
<https://doi.org/10.1016/j.ultras.2009.09.010>
- McLeod, F.D.J., 1967. A Directional Doppler Flow Meter, in: *Digest 7th Int. Conf. Med. Biol. Eng.*
- Merritt, C.R.B., 1987. Doppler color flow imaging. *J. Clin. Ultrasound* 15, 591–597.
<https://doi.org/10.1002/jcu.1870150904>
- Montaldo, G., Tanter, M., Bercoff, J., Benech, N., Fink, M., 2009. Coherent plane-wave compounding for very high frame rate ultrasonography and transient elastography. *IEEE Trans. Ultrason. Ferroelectr. Freq. Control* 56, 489–506.
<https://doi.org/10.1109/TUFFC.2009.1067>

- Moulin, J., 2005. Asdic & Sonar. Mar. Forces Nav. Hors-sér. 12H.
- Murphy, K., Birn, R.M., Bandettini, P.A., 2013. Resting-state fMRI confounds and cleanup. *NeuroImage* 80, 349–359. <https://doi.org/10.1016/j.neuroimage.2013.04.001>
- Nightingale, K., Soo, M.S., Nightingale, R., Trahey, G., 2002. Acoustic radiation force impulse imaging: in vivo demonstration of clinical feasibility. *Ultrasound Med. Biol.* 28, 227–235. [https://doi.org/10.1016/S0301-5629\(01\)00499-9](https://doi.org/10.1016/S0301-5629(01)00499-9)
- O'Reilly, M.A., Hynynen, K., 2013. A super-resolution ultrasound method for brain vascular mapping: Super-resolution ultrasound method for brain vascular mapping. *Med. Phys.* 40, 110701. <https://doi.org/10.1118/1.4823762>
- Olaf T. von Ramm, Stephen W. Smith, Henry G. Pavy Jr., 1991. High-speed Ultrasound Volumetric Imaging System- Part II: Parallel Processing and Image Display.
- Olivier Couture, Mickael Tanter, Mathias Fink, n.d. Patent 889 Cooperation Treaty (PCT)/FR2011/052810.
- Opacic, T., Dencks, S., Theek, B., Piepenbrock, M., Ackermann, D., Rix, A., Lammers, T., Stickeler, E., Delorme, S., Schmitz, G., Kiessling, F., 2018. Motion model ultrasound localization microscopy for preclinical and clinical multiparametric tumor characterization. *Nat. Commun.* 9. <https://doi.org/10.1038/s41467-018-03973-8>
- Osmanski, B.-F., Pezet, S., Ricobaraza, A., Lenkei, Z., Tanter, M., 2014. Functional ultrasound imaging of intrinsic connectivity in the living rat brain with high spatiotemporal resolution. *Nat. Commun.* 5, 5023. <https://doi.org/10.1038/ncomms6023>
- Papadacci, C., Finel, V., Villemain, O., Goudot, G., Provost, J., Messas, E., Tanter, M., Pernot, M., 2019. 4D simultaneous tissue and blood flow Doppler imaging: revisiting cardiac Doppler index with single heart beat 4D ultrafast echocardiography. *Phys. Med. Biol.* 64, 085013. <https://doi.org/10.1088/1361-6560/ab1107>
- Pashaj, S., Merz, E., 2013. Current Role of 3D/4D Sonography in Obstetrics and Gynecology. *Donald Sch. J. Ultrasound Obstet. Gynecol.* 7, 400–408. <https://doi.org/10.5005/jp-journals-10009-1310>
- Pernot, M., Tanter, M., Fink, M., 2004. 3-D real-time motion correction in high-intensity focused ultrasound therapy. *Ultrasound Med. Biol.* 30, 1239–1249. <https://doi.org/10.1016/j.ultrasmedbio.2004.07.021>
- Petrusca, L., Varray, F., Souchon, R., Bernard, A., Chapelon, J.-Y., Liebgott, H., N'Djin, W., Viallon, M., 2018. Fast Volumetric Ultrasound B-Mode and Doppler Imaging with a New High-Channels Density Platform for Advanced 4D Cardiac Imaging/Therapy. *Appl. Sci.* 8, 200. <https://doi.org/10.3390/app8020200>
- Poldrack, R., 2018. *The New Mind Readers: What Neuroimaging Can and Cannot Reveal about Our Thoughts.* Princet. Univ. Press.
- Provost, J., Papadacci, C., Arango, J.E., Imbault, M., Fink, M., Gennisson, J.-L., Tanter,

- M., Pernot, M., 2014. 3D ultrafast ultrasound imaging *in vivo*. *Phys. Med. Biol.* 59, L1–L13. <https://doi.org/10.1088/0031-9155/59/19/L1>
- Provost, J., Papadacci, C., Demene, C., Gennisson, J.-L., Tanter, M., Pernot, M., 2016. 3-D Ultrafast Doppler Imaging Applied to the Noninvasive and Quantitative Imaging of Blood Vessels in Vivo 12.
- Rahal, L., Thibaut, M., Rivals, I., Lenkei, Z., Sitt, J.D., Tanter, M., Pezet, S., 2019. Functional ultrafast ultrasound imaging reveals brain networks alterations linked with chronic inflammatory pain in rats. *Rev.*
- Ramalli, A., Boni, E., Savoia, A.S., Tortoli, P., 2015. Density-tapered spiral arrays for ultrasound 3-D imaging. *IEEE Trans. Ultrason. Ferroelectr. Freq. Control* 62, 1580–1588. <https://doi.org/10.1109/TUFFC.2015.007035>
- Ranganathan, K., Santy, M.K., Blalock, T.N., Hossack, J.A., Walker, W.F., 2004. Direct sampled I/Q beamforming for compact and very low-cost ultrasound imaging. *IEEE Trans. Ultrason. Ferroelectr. Freq. Control* 51, 1082–1094. <https://doi.org/10.1109/TUFFC.2004.1334841>
- Rasmussen, M.F., Christiansen, T.L., Thomsen, E.V., Jensen, J.A., 2015. 3-D imaging using row-column-addressed arrays with integrated apodization - part i: apodization design and line element beamforming. *IEEE Trans. Ultrason. Ferroelectr. Freq. Control* 62, 947–958. <https://doi.org/10.1109/TUFFC.2014.006531>
- Rasmussen, M.F., Jensen, J.A., 2013. 3D ultrasound imaging performance of a row-column addressed 2D array transducer: a simulation study, in: Bosch, J.G., Doyley, M.M. (Eds.), . p. 86750C. <https://doi.org/10.1117/12.2007083>
- Robinson, D.E., 1972. Display of Three-Dimensional Ultrasonic Data for Medical Diagnosis. *J. Acoust. Soc. Am.* 52, 673–687. <https://doi.org/10.1121/1.1913157>
- Roux, E., 2019. 2D sparse array optimization and operating strategy for real-time 3D ultrasound imaging.
- Rubin, J.M., Bude, R.O., Carson, P.L., Bree, R.L., Adler, R.S., 1994. Power Doppler US: A Potentially Useful Alternative to Mean Frequency-based Color Doppler US. *Radiology*.
- Rubin, J.M., Bude, R.O., Fowlkes, J.B., Spratt, R.S., Carson, P.L., Adler, R.S., 1997. Normalizing Fractional Moving Blood Volume Estimates with Power Doppler US: Defining a Stable Intravascular Point with the Cumulative Power Distribution Function. *Radiology*.
- Rust, M.J., Bates, M., Zhuang, X., 2006. Sub-diffraction-limit imaging by stochastic optical reconstruction microscopy (STORM). *Nat. Methods* 3, 793–796. <https://doi.org/10.1038/nmeth929>
- Sandrin, L., Catheline, S., Tanter, M., Hennequin, X., Fink, M., 1999. Time-Resolved Pulsed Elastography with Ultrafast Ultrasonic Imaging. *Ultrason. Imaging* 21, 259–272. <https://doi.org/10.1177/016173469902100402>
- Sarvazyan, A.P., Rudenko, O.V., Swanson, S.D., Fowlkes, J.B., Emelianov, S.Y., 1998.

- Shear wave elasticity imaging: a new ultrasonic technology of medical diagnostics. *Ultrasound Med. Biol.* 24, 1419–1435. [https://doi.org/10.1016/S0301-5629\(98\)00110-0](https://doi.org/10.1016/S0301-5629(98)00110-0)
- Shattuck, D.P., Weinschenker, M.D., Smith, S.W., 1983. Explososcan: A parallel processing technique for high speed ultrasound imaging with linear phased arrays 75, 10.
- Super-Resolution Microscopy, 2017. , in: *Super-Resolution Microscopy : A Practical Guide*. Wiley-VCH Verlag GmbH & Co. KGaA, Weinheim, Germany, pp. I–XVII. <https://doi.org/10.1002/9783527802074.fmatter>
- Szabo, T.L., 2004. *Diagnostic ultrasound imaging: inside out*, Academic Press series in biomedical engineering. Elsevier Academic Press, Amsterdam ; Boston.
- Tanter, M., Bercoff, J., Sandrin, L., Fink, M., 2002. Ultrafast compound imaging for 2-D motion vector estimation: application to transient elastography. *IEEE Trans. Ultrason. Ferroelectr. Freq. Control* 49, 1363–1374. <https://doi.org/10.1109/TUFFC.2002.1041078>
- Tanter, M., Fink, M., 2014. Ultrafast imaging in biomedical ultrasound. *IEEE Trans. Ultrason. Ferroelectr. Freq. Control* 61, 102–119. <https://doi.org/10.1109/TUFFC.2014.2882>
- Tanter, M., Pernot, M., Aubry, J.-F., Montaldo, G., Marquet, F., Fink, M., 2007. Compensating for bone interfaces and respiratory motion in high-intensity focused ultrasound. *Int. J. Hyperthermia* 23, 141–151. <https://doi.org/10.1080/02656730701209996>
- Tiran, E., Ferrier, J., Deffieux, T., Gennisson, J.-L., Pezet, S., Lenkei, Z., Tanter, M., 2017. Transcranial Functional Ultrasound Imaging in Freely Moving Awake Mice and Anesthetized Young Rats without Contrast Agent. *Ultrasound Med. Biol.* 43, 1679–1689. <https://doi.org/10.1016/j.ultrasmedbio.2017.03.011>
- Turnbull, D.H., Foster, F.S., 1991. Beam steering with pulsed two-dimensional transducer arrays. *IEEE Trans. Ultrason. Ferroelectr. Freq. Control* 38, 320–333. <https://doi.org/10.1109/58.84270>
- Viessmann, O.M., Eckersley, R.J., Christensen-Jeffries, K., Tang, M.X., Dunsby, C., 2013. Acoustic super-resolution with ultrasound and microbubbles. *Phys. Med. Biol.* 58, 6447–6458. <https://doi.org/10.1088/0031-9155/58/18/6447>
- Villagómez-Hoyos, C.A., Stuart, M.B., Bechsgaard, T., Nielsen, M.B., Jensen, J.A., 2016. High frame rate synthetic aperture vector flow imaging for transthoracic echocardiography, in: Duric, N., Heyde, B. (Eds.), . Presented at the SPIE Medical Imaging, San Diego, California, United States, p. 979004. <https://doi.org/10.1117/12.2216707>
- Williams, M., Hackmann, W., 1984. *Seek and Strike: Sonar, Anti-Submarine Warfare and the Royal Navy, 1914–1954*. Her Majesty's Stationery Office.

II

Developing new techniques to achieve faster, better
Ultrasound Localization Microscopy

II. Chapter 2: Developing new techniques to achieve faster, better Ultrasound Localization Microscopy

II.1 Introduction

Rupture of the half-wavelength limit in ultrasonic imaging using Ultrasound Localization Microscopy involves capturing several thousands of frames for conventional techniques (i.e. excluding schemes involving machine learning or deep learning algorithms (Bar-Zion et al., 2017) (Solomon et al., 2018)). Similarly to the localization microscopy field in optics, the time needed to acquire a large number of events has been identified as the bottleneck in broad usage of this tool (Hingot et al., 2019). In optics, achieving faster imaging rate has shifted the focus towards increasing the labeling density while retaining epi-illumination to a minimum (Lu et al., 2019) or reducing the post-processing times while retaining high localization precision (Henriques et al., 2010). A broad assessment of available post-processing techniques has been conducted twice by Daniel Sage's team at Ecole Polytechnique Federale de Lausanne (EPFL) through a worldwide challenge at IEEE International Symposium on Biomedical Imaging and led to two seminal papers (Sage et al., 2015) and (Sage et al., 2018).

In the field of ultrasound, the context is different as the first demonstration of the technique was done using an ultrafast capability ultrasound scanner meaning high frame rate was already attainable (Couture et al., 2011). The reason for this is that the authors of this paper were aiming to demonstrate that microbubbles could be used as distinct sources creating fast happening events in the region of imaging and would be a mean to mimick photoactivatable fluorescent sources. In the same conference, another team led by Fabian Kiessling used microbubbles as a probing agent to map perfusion in a tumor (Siepmann et al., 2011). Using appropriate filtering, they managed to reduce the imprint of the microbubble to a single illuminated pixel corresponding to the centroid. Contrary to ULM, the resolution of the image is not improved *per se* because the pixel size remains the same and so they do not need to accumulate a very large number of images. These two papers showed two very different approaches to improve resolution for ultrasonic imaging :

- using contrast agents as separable sources to increase the resolution of the image through accumulation of a large number of frames
- using contrast agents as tracers to reduce the width of blood vessels through

morphological operations

One can see that the race towards the reduction of acquisition time had already begun in the early days of ULM. It also has to be noted that both of these two proofs used localization algorithms and for the latter, suggested using tracking algorithms to perform velocimetry, building the starting arch for the second race to be held : achieving faster, better localization. In this chapter, I will present a state of the art of each of the steps required to perform ULM, then I will describe the method and framework I designed to achieve faster and higher quality ULM using new localization, tracking algorithms. I developed two new localization methods based on optical-based super-resolution. The challenge resides not only in adapting the theory for ultrasound, developing an efficient algorithm within our framework but also dealing with lower SNR in ultrasound and solving for another dimension. In another section, I will introduce new metrics to measure the performance of these newly introduce methods in an effort to compare the state of the art to our method. Finally, after a discussion section, I will present the application of our method to several cases in our lab.

II.2 State of the art

In this section, we will present a state of the art of each of the steps required to perform ULM. As mentioned in chapter 1, ULM is a multi-step ultrasound imaging method. The general layout is presented in Figure 19. Firstly, one needs to acquire a large number of frames in the region of imaging. Then, a detection process takes place to enhance the signal of microbubbles. Close microbubbles are isolated. Localization of the position of the microbubbles beyond the diffracted-limited resolution is performed. Additionally, for high frame rate imaging, tracking of microbubbles is implemented. Finally, density or velocity-based renderings are used to represent vascular mapping.

II.2.1 Detection of contrast agents

Achieving better localization starts with having suitable images to work with. That means that the algorithm needs to detect and isolate microbubbles before localizing their centers. A number of schemes have been developed to distinguish microbubbles from surrounding signal whether it be tissue or noise.

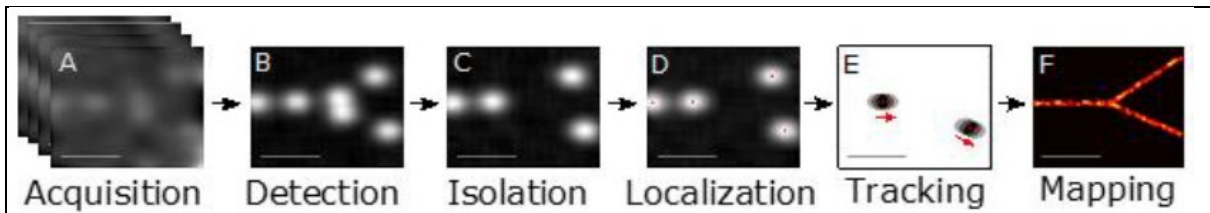


Figure 19. Steps in ultrasound super-resolution processing.

- a) Acquisition of ultrasound data over time from the contrast-enhanced vascular region.
- b) Detection of signals from microbubble contrast agents.
- c) Isolation of individual microbubble signals, overlapping or interfering signals are rejected.
- d) Localization of the microbubble to a precision beyond the diffraction-limited resolution.
- e) Tracking of the microbubbles through consecutive frames to establish velocity profiles.
- f) Mapping of the accumulated localizations gathered over the series of frames produces an image of the vascular structure far beyond the diffraction limit.

The first detection of microbubbles was fortuitously observed in echocardiography in (Gramiak, Raymond and Shah, M Pravin, 1968). They measured clouds of echoes in M-mode after injection of physiological saline in the left atrium. They validated the use of saline as an ultrasonic contrast medium in the anatomic identification of the mitral valve and postulated that the clouds of echoes were caused by mini bubbles either already present in the solution or caused by the injection rate. It feels natural then that the first attempts at microbubble detection used fundamental imaging : (Ophir and Parker, 1988) compiles the properties of microbubbles that could be used to our advantage:

1. Increasing backscatter contrast

- if the characteristic dimension of the scatterer is of an order of magnitude smaller than the imaging wavelength and has density and speed of sound mismatch, then it will create a spherical wave at distance R of the scatterer with the scattered intensity $I_s = \frac{I_i \sigma}{4\pi R^2}$ where I_i is the intensity distributed at the point where the scatterer is by the emission, σ the scattering cross-section (defined by Morse and Ingard in Theoretical Acoustics). For a cloud of m microbubbles, the scattering cross-section of the cloud is m times the cross-section of an individual microbubble (Newhouse et al., 1980). The backscatter power received

by the transducer will be increased compared to a medium without microbubble.

The problem with the fundamental imaging approach is that it is only sensible to large clouds of bubbles and not to a few bubbles. In echocardiography, large clouds of bubbles serve to delimitate valves, chambers, aortas but as soon as the ratio of tissue to blood increases, bubbles are no longer visible.

- Additionally to the scattering of the emitted wave, bubbles will oscillate and emit a wave of their own modelizable by a harmonic oscillator. The resonance frequency depends on the radius of the bubble a , the ambient fluid's pressure p_0 , and density ρ_0 and the adiabatic constant γ : $f_0 = \frac{1}{2\pi a} \sqrt{\frac{3\gamma p_0}{\rho_0}}$. Medically approved contrast agents typically have a size less than 5 μm which gives a resonant frequency in between 1 and 10 MHz (European Medical Agency and Committee for Medicinal Products for Human Use, 2017). (Mackay and Rubissow, 1978) first used this formula to evaluate the number of microbubbles in a medium by comparing the echo intensity measured to a calibrated value on a single microbubble with varying diameter. They deduced the maximum size of the bubble capable of producing the measured echo and then varied the ambient pressure in the medium to discriminate between larger or smaller than resonant microbubbles thus producing a range of density of microbubbles in the medium.

2. Attenuating contrast

While enhancing contrast has been favored in the history of contrast agents, it has to be pointed out that in the beginning it was thought that resonant bubbles would absorb a sufficient amount of energy to provide attenuation in specific organs (Ophir and Parker, 1988). This property has received scarce attention in the biomedical imaging community.

3. Speed of sound variations

Combining the two approaches of the characterization the oscillation of the microbubble and of attenuation, measuring the changes in the speed of

sound of specific zones in the region of imaging can be used to calculate the amount of contrast agents in the tissue and compare it with values before injection. This was thought to be useful for tissue perfusion studies. However, because these need large amounts of microbubbles and because the speed of sound calculation depends largely on the medium in between the probe and the imaging region, this is less practical than the identification of the vascular system via B-mode image formation or manipulation.

The use of contrast agents for speed of sound variation and attenuating contrast has not seen the applications (Ophir and Parker, 1988) mentioned however it has seen tremendous success in increasing contrast for conventional and harmonic imaging, flipping the ratio of blood to tissue ratio at about -20dB to a situation with blood and bubble to tissue ratio at about +20dB (Wilson and Burns, 2010).

As explained above, a bubble changes morphologically to the pressure of an ultrasonic wave. During the compression phase, the bubble will shrink on itself and then expand again during the rarefaction phase. However, these vibrations are related linearly to the amplitude of the acoustic pressure only for low pressures. For higher amplitudes, radial excursion can increase indefinitely until destruction and the morphological changes become non-linear : switching from the mass-spring model mentioned above to a more sophisticated model combining the Rayleigh-Plesset equation and the polytropic gas law with the boundary condition for free gas bubble and to the Marmottant model for coated bubbles (de Jong et al., 2009). The backscattered signal from the bubble thus contains harmonics of the transmitted fundamental frequency. Tissue does not show such a strong behavior (but still behaves non-linearly) and can thus be discriminated against. That is what harmonic imaging exploits : by transmitting signals at a frequency f and receiving signals at $2f$, it is picking up signals from the second harmonics of the backscattered signals and enhancing bubble separation from tissue (Figure 20). To minimize spectral overlap between fundamental and the second harmonic parts of the received signal band narrowing is imposed on the transducer bringing forward a trade-off between detection and axial resolution. To perform well, that technique also needs high transmit intensities, which can cause bubble disruption in the case of slow-moving bubbles. This technique has shown considerable image quality improvement even without microbubbles and is now a technique on its own called Tissue Harmonic Imaging (THI). However, it has shown good potential in microbubble detection and isolation to achieve super-resolution in (Viessmann et al., 2013).

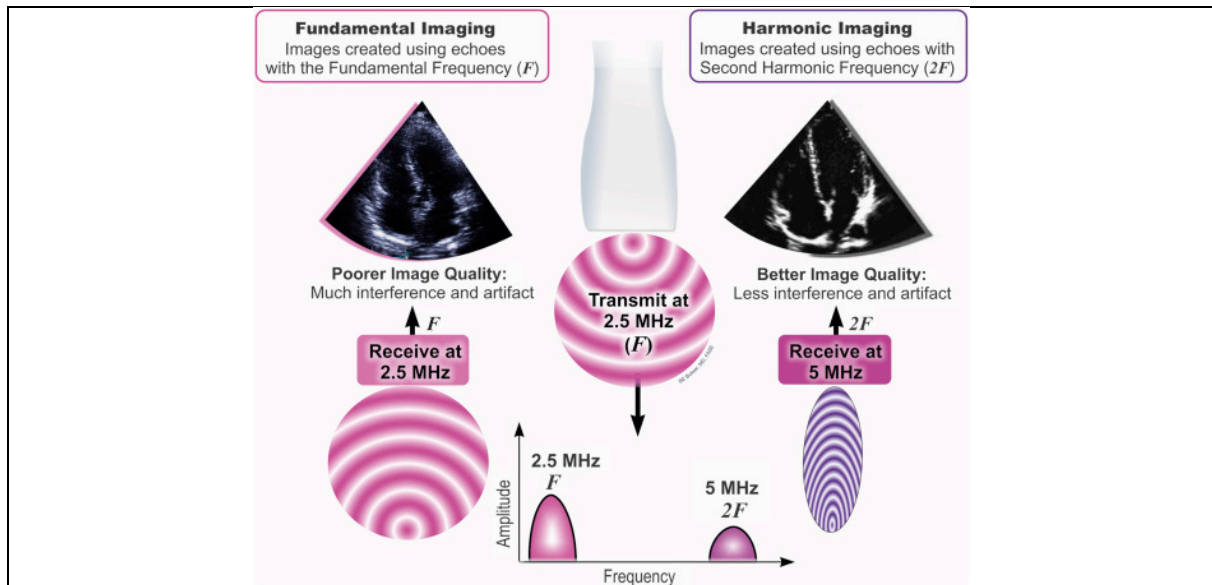


Figure 20. Schematics describing tissue harmonic imaging (Cikes et al., 2019)

Tissue harmonic imaging allows for improved image quality by using second-order harmonics in which specific frequencies of ultrasound induce tissue vibrations at twice the frequency. Listening for such higher frequencies of returning ultrasound allows for dramatic improvement of the signal-to-noise ratio. Second-harmonic imaging provides images with clearly ameliorated tissue definition and less affected by acoustic noise and artifacts (right)

As it has been shown that Contrast to Tissue Ratio increases as a function of the order of the harmonic frequency, (Bouakaz et al., 2002) developed super-harmonic imaging which is based on the same principle as conventional harmonic imaging but uses higher than 2 orders harmonics. The increase in bubble detection was successfully demonstrated *in vivo* however, the need to image with a specific probe is a deterrent to a wider usage (Lin et al., 2017).

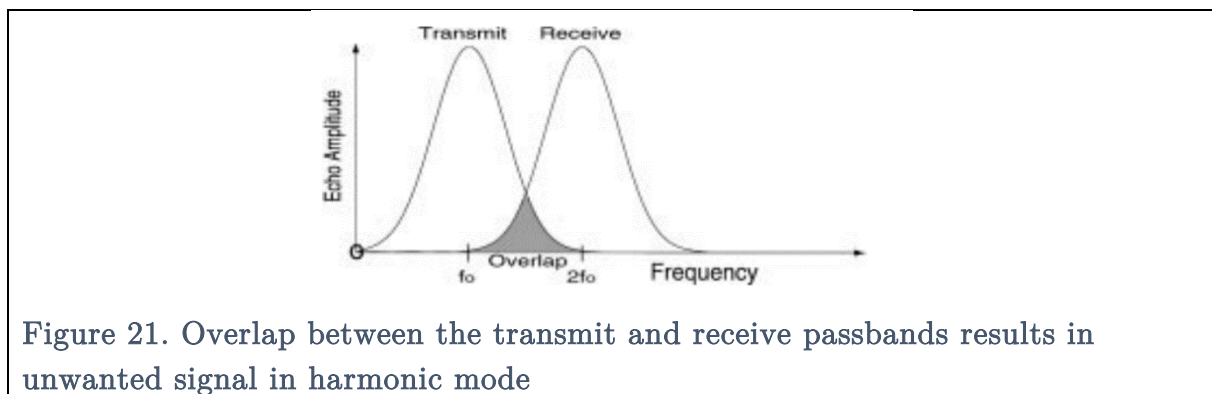


Figure 21. Overlap between the transmit and receive passbands results in unwanted signal in harmonic mode

Exploiting further the non-linear behavior of bubbles, another kind of imaging called pulse inversion has seen the light that alleviates this compromise by using a single frequency transmit but repeating it twice. The first pulse is transmitted similarly to conventional mode ultrasound, but the second pulse, transmitted after a delay T , is the inverse of the first pulse. For linear scattering, the sum of the received signals will be zero (given the region of imaging does not move between the two pulses), for all other scattering, the sum will be different than zero (Simpson et al., 1999). Another advantage of this technique compared to harmonic imaging is that it performs well at low Mechanical Indexes and thus reduces the destruction of bubbles prolonging their circulation time (Simpson and Burns, 1998). The problem with this technique is the need to transmit several pulses thus decreasing the imaging rate which can be a problem for applications where high frame rate is needed to correct for motion. Similarly to pulse inversion, it was shown that modulating pulse amplitudes rather than phase, achieves similar results (Eckersley et al., 2005).

Multi-pulse ultrasound contrast imaging has been developed to detect the presence of contrast agents based on destruction. One pulse is emitted at high frequency, low amplitude, single cycle for imaging followed by another one at low frequency, high amplitude, and multiple cycles that destructs all contrast agents. Finally, the first pulse is re-emitted with the same characteristics. Local decorrelation analysis is then performed on a sliding window in the frequency domain to detect areas where contrast agents are (Frinking et al., 1998). This technique presents two major disadvantages for single particle detection which is the need for two frequencies (i.e. transducers with large broadband or two different transducers), and destruction of bubbles alleviates time-dependent measurement. However, it performs very well for all contrast agents (de Jong et al., 2009) and is used routinely for disruption-reperfusion.

Similarly to the principle of harmonic imaging, sub-harmonic imaging uses waves generated by gas bubbles at half the transmitted frequency (Shankar et al., 1998). As the onset of subharmonics appears at low acoustic pressures at twice the resonance frequency of the bubble, and because the tissue is less visible at these pressures, it has a better Contrast to Tissue Ratio than conventional harmonic imaging. However, the resonance frequency of conventionally used bubbles is quite low thus providing low resolution for subharmonic imaging.

Finally, plane wave imaging, a method that uses parallel transmits and angled waves to achieve imaging at very high frame rates has been demonstrated to be able to detect microbubbles in media with minimal tissue signal (Couture et al., 2009), and later to isolate single microbubbles (Couture et al., 2011), in vitro canals with tissue-mimicking

media (Christensen-Jeffries et al., 2017; Desailly et al., 2013; Heiles et al., 2019), and *in vivo* if associated with an appropriate filter (Desailly et al., 2015; Errico et al., 2015a; Song et al., 2018b). In 2017, an in-depth study of SVD filtering demonstrated that it outperformed the gold standard non-linear sequence power modulated pulse inversion (Desailly et al., 2017). (Leavens et al., 2007) had used coded nonlinear excitations, but the technique of multi-plane wave imaging recently emerged. MPWI is similar to PWI but sends tilted plane waves quasi simultaneously with different polarities. Radiofrequency data is then decoded to recover angles according to the Hadamard matrix chosen for the transmits and then beamformed accordingly. This technique has been shown to improve SNR in conventional B-mode and Doppler imaging (Tiran et al., 2015). Subsequently to this, multiplane wave imaging was also implemented for contrast agents in combination with amplitude modulation to improve CTR (Gong et al., 2018).

II.2.2 Isolating contrast agents

After the detection of contrast agents is implemented, ULM needs to be able to isolate single particles, given that the concentration of bubbles is *on par* with the Rayleigh criterion for close signal separation. In several types of imaging, the Rayleigh criterion is not met as they involve a high concentration of UCA. Another factor that can prevent ULM is microbubble destruction, slow imaging rate compared to vascular flow or low SNR. In descending order of popularity, the techniques used to perform ULM are:

- Compounded plane wave imaging/multi-plane wave imaging
- Conventional B mode imaging
- “Contrast imaging” in conventional scanners (pulse inversion, amplitude modulation)
- Multi-focus imaging

For contrast imaging, isolated bubbles are usually already visible without the need for additional filtering except if the UCA is off-resonance or weakly responding. In that case, the UCA needs to be changed or the sequence needs to be adapted but very little can be done in post-processing.

For PWI or conventional B-mode or Multi-focus, isolating contrast agents is done in post-processing. The simplest and original method is to rely on a frame to frame substraction. As shown in early work by (Couture et al., 2011; Siepmann et al., 2011), that technique removes static signal and enhances the detection of microbubble motion. If tissue or the medium around microbubble has slow motion compared to the flow of microbubble, this technique isolates UCA signal from everything else and enables

localization (Desailly et al., 2013). Recently (Heiles et al., 2019) have shown the limits of differential imaging for fast and highly concentrated microbubbles where the imaging rate was too low and singular value decomposition had to be used instead. This can also be done with multiple added frames : (Christensen-Jeffries et al., 2015; Viessmann et al., 2013) use a rolling background and subtract it to each image containing potential bubble signal. The rolling background pools images with low total intensity to measure background signal and slow-moving microbubbles.

The singular value decomposition theorem states that any rectangular matrix belonging to either the real or the complex domain can be rewritten in a basis represented by a diagonal matrix with non-negative real numbers of the diagonal. In ultrasound, this theorem has been used to create a filter based on spatiotemporal decorrelation of the signal (Demene et al., 2015; Forsberg et al., 1991; Ledoux et al., 1997). Given a succession of frames of size N_z, N_x during time N_t , the SVD of its Casorati matrix of size $(N_z * N_x, N_t)$, produces a basis of N_t vectors. The SVD decomposition can be written:

$$S = U\Sigma V^*$$

Where V and U are unitary matrices and $*$ is the conjugate transpose operation. The matrix Σ is diagonal and its values $\sigma_{1 < i < N_t}$ are called the singular values of the matrix A . Conventionally, highest values are the first and low values are last. These vectors express different levels of spatiotemporal coherence of the signals. The matrix Σ can be written:

$$\Sigma = \sum_{i=1}^{N_t} \sigma_i A_i$$

By selecting a subset of $[1: N_t]$ and reconstruct S with a partial representation of Σ , it is possible to filter certain spatio-temporal fluctuations in the image. Blood, bubbles, noise have low spatiotemporal coherence whereas tissue, bone have high spatiotemporal coherence because of low deformation, cohesion, staticity... For microbubbles, rejecting 10% of the highest energy vectors or even less is sufficient to increase CTR and enable single-particle localization (Errico et al., 2015a).

In some cases, it has been shown that differential imaging with an additional filter can perform well for the isolation of UCA. (Song et al., 2018b) have compared adding 2D Gaussian filtering or Non-Local Means filtering after differential imaging. 2D Gaussian filtering is based on the convolution of the image with a Gaussian kernel the size and the standard deviation adapted to the Point Spread Function of the imaging system. It blurs the signal of a microbubble making it more distinguishable compared to

noise signal but does not perform well on low intensities. Non Local Means filtering is a pixel oriented filtering. For each pixel of the image, it will compute the average intensity of a neighbor area \wp . It will do the same for all pixels in an interrogation zone chosen by the user, and will replace the value of the original pixel with a weighted average value of all the averaged intensities in the interrogation zone. The value at a given pixel i with intensity I_i will become:

$$I_i^{filt} = \sum_{j \in \wp} w(i, j) * I_j,$$

with \wp the subset of the image corresponding to the interrogation path, I_j the intensity at pixel j

$$and w(i, j) = \frac{1}{N_\wp} e^{-\frac{\|I_i - I_j\|_2^2}{h^2}},$$

with N_\wp the normalization factor ensuring the sum of w is 1 and h a parameter controlling the amount of filtering.

These two techniques have shown good results with filtering moving microbubbles from tissue but have poor results when it comes to non-moving microbubbles as can be the case for targeted contrast agents or very slow flow.

A simpler technique based on a simple high-pass filter over time was also demonstrated to show good results when the image quality is high enough (Hingot et al., 2019). When in place, this approach is favorable to SVD or NLM filtering as its relation to temporal variation of the signal is direct whether, in SVD, the threshold values are chosen based on habit or visual appreciation of the user, and NLM filtering does not take time into account at all.

Additional steps are sometimes put in place after these filters to sort microbubble signal from speckle signal side lobes or noise. For example, (O' Reilly and Hynynen, 2013) will reject a frame in its super-resolution process if it can not identify one clear source: if a local maximum with intensity greater or equal than 50% of the maximum of the image, the frame is taken out of the process. This improves the detection by selecting only one bubble per frame but drastically reduces the number of images available to work with and thus increases acquisition time. In (Christensen-Jeffries et al., 2015), the binarized signal of identified microbubble is compared to the pre-measured PSF of the ultrasound system to reject multiple bubbles and noise.

II.2.3 Localization of contrast agents

ULM leans on the hypothesis that the bubble is really small compared to its diffraction-limited image. The localization of the center of the PSF corresponds

approximately to the position of the microbubble. Using fast and efficient algorithms is crucial to the quality of ULM imaging. Several schemes have been developed with different qualities.

The first demonstration of the technique in (Couture et al., 2011) was performed on the channel radio-frequency data where a single-source yield a parabolic shape on the channel-time matrix. To determine the position of the microbubble, it isolated the parabola generated by the reflection of a transmitted plane wave from a microbubble for each transducer channel and calculated the summit. It was used again in (Desailly et al., 2013) to demonstrate ULM in three dimensions with a 1.5D array. The issue with this technique is that all single point scatterers in an image appear as parabolas in radiofrequency data and the question arises of how to distinguish a bubble from other scatterers without having an image in the spatial domain. When the bubbles are sparse and float in canals with little or no reflection, the task of localizing them in the RF data is easy. When you have tissue, bone, strong reflections from the media, the bubbles signatures become mixed with other signals and are very hard to filter. The trick usually employed is to resort to beamforming, filtering in the spatial domain, pinpointing local maxima and going back to the RF data using these *a priori* positions as microbubble signals. (Desailly et al., 2015) showed that this technique yielded localization with precision close to a Monte-Carlo analytical model based on random time-delays added by the scanning system : median standard deviation calculated from the experimental model and the positions simulated had a correlation coefficient $\rho = 0.88$ and a p -value= 0.02. However, the density of microbubbles localized per image seemed to be quite low compared to *in vivo* concentrations.

At around the same time, (Siepmann et al., 2011) also performed localization of centroid of the microbubbles in an already very fine grid as they used a 40 MHz probe. They are not improving resolution by doing accumulation but they opened the way towards localization by interpolation. Drawing from that technique, (Errico et al., 2015a) interpolated beamformed images of filtered microbubbles in the rat brain on a grid 10 times finer than original resolution with a Lanczos kernel. (Ackermann and Schmitz, 2016) used a similar method by convolving the bubble with a Gaussian kernel and then relied on local maxima on interpolated grids. That method is very precise in detecting individual microbubbles as was shown in the optics field (Sage et al., 2015) but is quite slow and requires heavy computation. Methods using full deconvolution of the PSF fail because of low SNR in ultrasound and have not been implemented so far. Methods involving the intensity weighted center of mass on interpolated images have also been

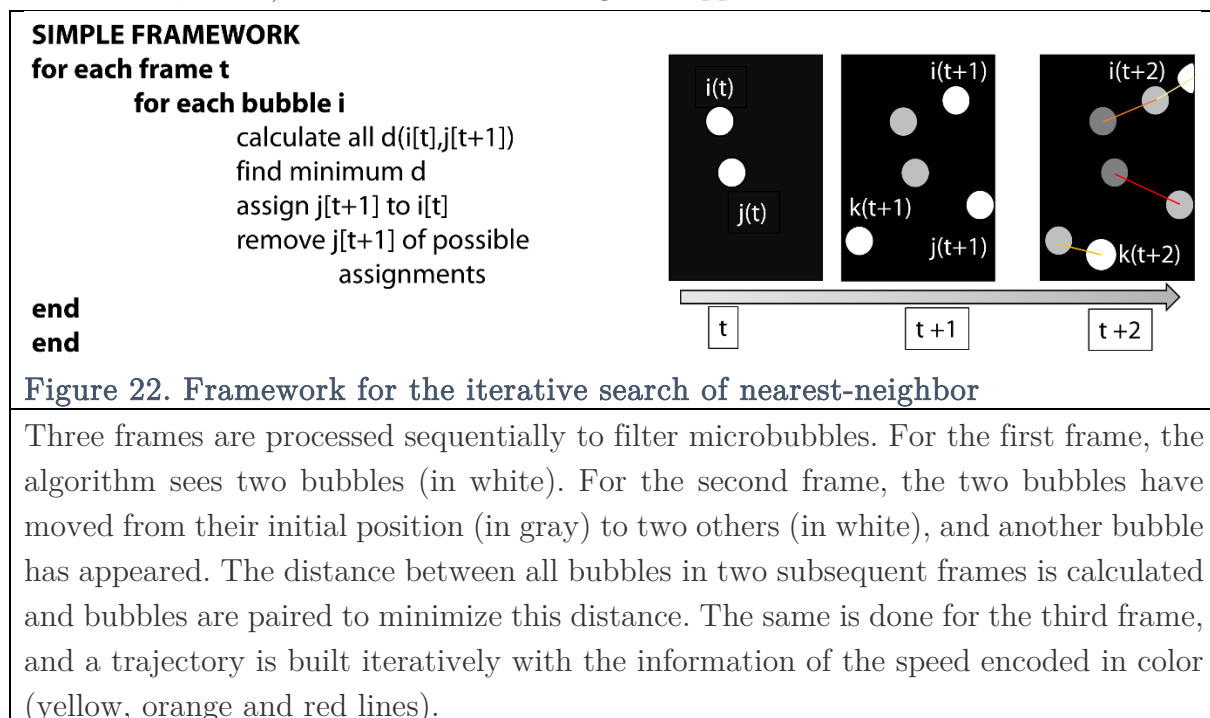
used in (Christensen-Jeffries et al., 2015; Viessmann et al., 2013). (O'Reilly and Hynynen, 2013) have demonstrated that Gaussian fitting performs well in 3 dimensions given that the standard deviation of the Gaussian model is calculated with the PSF of the system.

Unfortunately, all of these methods require interpolation of the beamformed data, implying long calculation times and intensive use of random-access memory.

II.2.4 Tracking schemes

(Siepmann et al., 2011) concluded their study in this way : “To make functional analysis complete, the velocity of the blood needs to be detected as well. The usage of tracking algorithms may provide additional information on the microbubble velocity. Further research will thus include the correlation of the individual bubbles in subsequent frames to track their motion.” Subsequent demonstrations of ULM included tracking algorithms.

Using search windows around each microbubble, (Christensen-Jeffries et al., 2015; Errico et al., 2015a) relied on a nearest-neighbor approach.



In Particle Tracking Velocimetry, the simplest way to perform tracking of individual particles is done through cross-correlation in an interrogation window. However, it has been shown that while these perform well with datasets of high spatial and temporal sampling, it fails when the number of particles to track (i.e. seeding) is

high. This is the paradigm between PIV – high seeding high information density - and PTV –low density low information density but better velocimetry (Bondur et al., 2019; Grant, 1997). The advantage of such a technique though is that it works with non-super-resolved data. One could imagine calculating a map of velocity for all vessels using cross-correlation between microbubbles and then using that information to perform filtering in another tracking algorithm post-localization.

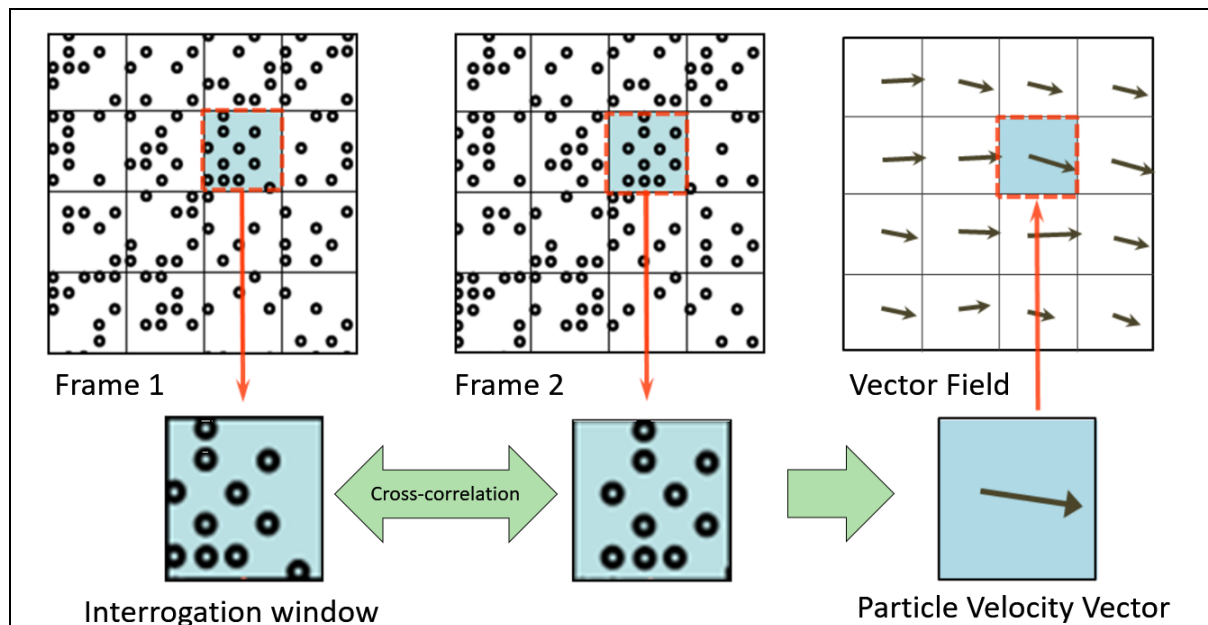


Figure 23. Cross-correlation based tracking

For each frame, the cross-correlation is computed over an interrogation window. The maxima of cross-correlation are computed and are converted into a particle velocity vector. The size of the pixel of the vector field depends on the interrogation window. This can be reduced by using a sliding window at higher computation costs.

(Ackermann and Schmitz, 2016; Opacic et al., 2018) have developed an approach based on multi-target tracking which uses a Markov chain Monte Carlo scheme. This approach was developed as an alternative to multiple hypothesis trackers and specifically for cases where a large number of targets are present in a dense and noisy environment. In cases where microbubbles are hard to detect and temporal sampling is low, this scheme has yielded good results albeit very long calculation times.

(Solomon et al., 2018) used a Kalman filter to iteratively construct tracks with mixed results in terms of image quality.

(Song et al., 2018c) has developed a partial assignment algorithm based on bipartite graph pairing. After building a matrix of distances of all microbubbles, it will iteratively pair a microbubble i in a frame N with its closest neighbor j in frame $N + 1$,

adding the condition that there are no closer microbubbles in frame N to neighbor j . If there are it will assign this microbubble to neighbor j rather than the other, loop back to find a new candidate for microbubble i , except if it can not find one and in that case, microbubble i will get discarded. As this process is done for each microbubble and can not be parallelized, it is quite slow but yields good results in terms of imaging quality and velocimetry albeit no significant improvement was demonstrated compared to the algorithm used in our implementation.

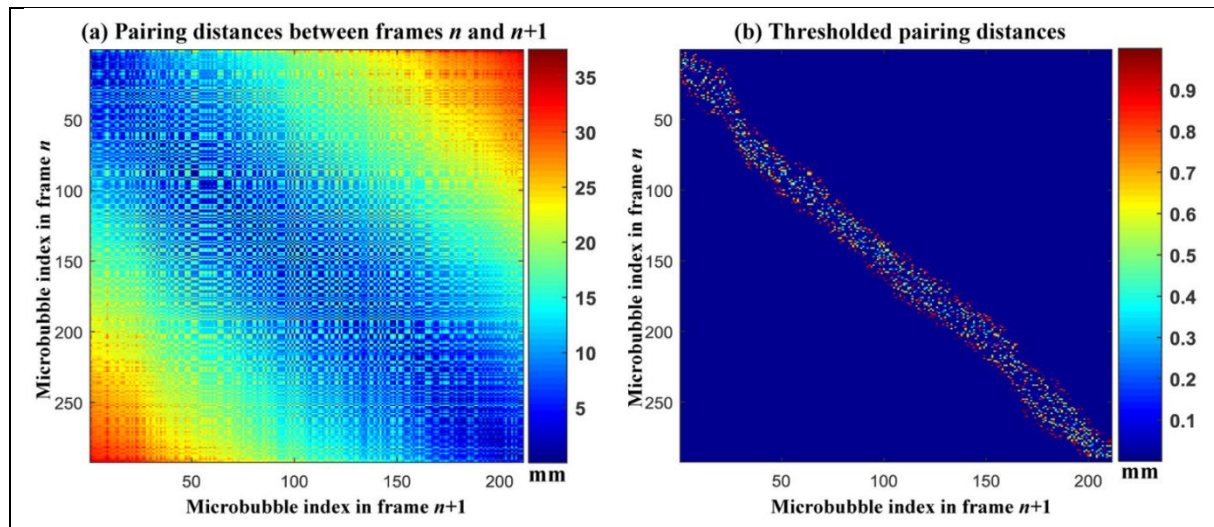


Figure 24. The distance matrix for all particles in two subsequent frames and thresholding to prepare pairing (Song et al., 2018c)

For each subsequent frame, the distance matrix is computed and filtered to prevent pairing in between bubbles too far from each other. This matrix is symmetric. A complex iterative algorithm is then put in place to pair microbubbles and compare all previous pairings to each other.

Finally, new approaches to bypass the localization process through a dynamical method based on sparse recovery have been implemented on *in silico* models with success in (Alberti et al., 2018).

II.3 Achieving faster and higher quality localization

In 2 dimensions or in 3 dimensions with limited field of views, slow and heavy interpolation-based localizing schemes are not a major problem, however, in our case, we planned to use a 32x32 matrix array probe yielding data from 1024 transducers to

perform volumetric imaging. The size of each image is thus 8 fold compared to conventional 2D imaging. Moreover, Matlab is the go-to software to process ULM data at many laboratories and is notoriously slow in 3D implementations - a couple of web searches with the keywords “3D”, “slow” and “Matlab” will confirm this.

Another aspect where speed is crucial and where we often forget the advantage of fast-running algorithms is when we need to test out many parameters. As explained above, ULM is a process involving many steps, sometimes as much as 15 and every step can be controlled with one to four parameters. Changing each of these to test out different approaches involves hundreds of runs. As time is money (and time is a scarce resource in a Ph.D. thesis), I have tried to design faster and cheaper ULM. On the quest to design this, I also kept in mind that the image quality had to be as good as or better than the existing schemes.

The most time-consuming steps in ULM are localization and tracking. Localization is usually computationally expensive because it has to interpolate the images and then manipulate these images to perform localization which can be complex (ex in (Christensen-Jeffries et al., 2015; O' Reilly and Hynynen, 2013; Viessmann et al., 2013)). Tracking is slow either because it is usually a process comparing each bubble to its neighbor and to subsequent frames (and even preceding frames in the framework developed in (Song et al., 2018b)). The complexity of the nearest-neighbor algorithm is $O(n^2)$ in the brute force method. If you select a window around each microbubble, assuming there are m bubbles around each candidate, the complexity becomes $O(mn)$. If the algorithm involves going back once to preceding frame on each bubble, the complexity increases to $O(m^2n^2)$. Our first quest is to bypass interpolation and find a fast and precise localization algorithm. Our second quest is to simplify tracking to reduce complexity. Our third quest is to try and parallelize programming to reduce the impact of doing the same process on thousands of frames.

II.3.1 Localization schemes

II.3.1.1 Interpolation based

The easiest way to localize the microbubbles based on their beamformed signal with the enhanced resolution is to use interpolation in 2 dimensions with the appropriate kernel. We have chosen to test out bilinear, bicubic, Lanczos and spline interpolation. Bilinear is equivalent to defining the center of the microbubble as the pixel centered in the image grid (no shift can be calculated and it will be like writing that the center in super-resolved coordinates is simply the center in the low resolved coordinates divided by the interpolation factor). This was chosen to show that localization affects the quality

of the image and that tracking plays a fundamental role in improving the quality of the image after localization. The upscaling resolution factor or interpolation factor is linked to the desired pixel size in the final image and thus to the maximum resolution attainable.

II.3.1.2 Weighted average

Similarly to our field, researchers in the optics field of localization microscopy have been trying to reduce computation times. Most notably, (Henriques et al., 2010) proposed to calculate centroids of single-particle by weighting their neighboring intensities. The previous implementation of the weighted average in ultrasound involved interpolating data. Let's assume you have an image of a bubble composed of a grid of $[N_z, N_x]$ pixels. To recover the position of the centroid, the interpolation schemes will upsample that image on a grid of $[N_z * res, N_x * res]$ pixel, with *res* the upscaling resolution factor and then either find the maximum intensity or the centroid of the intensity distribution. The intensity I_{sr} coming out of the interpolation will be expressed as a linear combination of original intensities :

$$I_{sr}(i, j) = \sum_{(k_i, k_j) \in Z_q} I_k \phi_{int}(i - k_i, j - k_j)$$

where (i, j) belongs to the interpolated space Z_{sr} and (k_i, k_j) belongs to the original space Z_q .

The function ϕ_{int} is called the synthesis function and can take many forms as long as it satisfies the interpolation property : it must vanish for all already known samples of the intensity except for the origin where it must take the value 1 - more simply put, if the intensity is known at the pixel in the departure grid, interpolation can not change its value in the arrival grid. This is the classical approach to interpolation. There is a more general approach where the synthesis function does not satisfy the interpolation property, not necessarily finite support and where the coefficients are calculated based on the original intensity values but are not necessarily equal to them. The operation defined above is a discrete convolution equation.

Our assumption under the weighted average localization scheme is that one does not need to calculate all of the intensities on the refined grid to perform localization, but we can calculate the position of the maximum intensity based on centroids. Mathematically speaking, our problem becomes :

$$z_c = \left\{ z \in Z_{sr} / I_{sr}(z) = \max_{z \in Z_{sr}} I \right\}$$

$$x_c = \left\{ x \in X_{sr} / I_{sr}(x) = \max_{x \in X_{sr}} I \right\}$$

with (z_c, x_c) the coordinates of the centroid, (Z_{sr}, X_{sr}) the subset of coordinates

in the superresolved basis, and I the intensity of the image.

Thankfully, we can guess where the maximum will be based on prior knowledge of our function I_k . We assume that we have centered our subset space Z_k on the maximum known value of I_k at z_{ck} . If we assume a Gaussian distribution of the intensity in our subset, the sub-pixel location of the peak can be estimated by calculating the centroid of the intensities (Welch, 1993). In an image with intensities $I(i, j)$, we can define the image moments as :

$$M_{pq} = \sum_i \sum_j i^p j^q I(i, j),$$

and the centroid is defined by

$$(z_c, x_c) = \left\{ \frac{M_{10}}{M_{00}}, \frac{M_{01}}{M_{00}} \right\}$$

This centroid is equal to the location of the peak only if the intensity is Gaussian and in our discrete case, it can be written as :

$$z_c = \frac{\sum_{i=-\lfloor \frac{fwhm_z}{2} \rfloor}^{\lfloor \frac{fwhm_z}{2} \rfloor} \sum_{j=-\lfloor \frac{fwhm_x}{2} \rfloor}^{\lfloor \frac{fwhm_x}{2} \rfloor} I(i, j) w_z(i, j)}{\sum_{i=-\lfloor \frac{fwhm_z}{2} \rfloor}^{\lfloor \frac{fwhm_z}{2} \rfloor} \sum_{j=-\lfloor \frac{fwhm_x}{2} \rfloor}^{\lfloor \frac{fwhm_x}{2} \rfloor} I(i, j)}$$

$$x_c = \frac{\sum_{i=-\lfloor \frac{fwhm_z}{2} \rfloor}^{\lfloor \frac{fwhm_z}{2} \rfloor} \sum_{j=-\lfloor \frac{fwhm_x}{2} \rfloor}^{\lfloor \frac{fwhm_x}{2} \rfloor} I(i, j) w_x(i, j)}{\sum_{i=-\lfloor \frac{fwhm_z}{2} \rfloor}^{\lfloor \frac{fwhm_z}{2} \rfloor} \sum_{j=-\lfloor \frac{fwhm_x}{2} \rfloor}^{\lfloor \frac{fwhm_x}{2} \rfloor} I(i, j)}$$

with the weights defined as :

$$w_z(i, j) = z_{ck} - \left\lfloor \frac{fwhm_z}{2} \right\rfloor$$

$$w_x(i, j) = x_{ck} - \left\lfloor \frac{fwhm_x}{2} \right\rfloor$$

In terms of algorithm, it is useful to calculate these coordinates using matrices to take advantage of parallel computing. For every bubble localized, if the full width at half maximum is estimated to be 3, we will thus express the weights as the matrix

$$W_z = \begin{bmatrix} -2 & -2 & -2 & -2 & -2 \\ -1 & -1 & -1 & -1 & -1 \\ 0 & 0 & 0 & 0 & 0 \\ 1 & 1 & 1 & 1 & 1 \\ 2 & 2 & 2 & 2 & 2 \end{bmatrix}$$

$$W_x = \begin{bmatrix} -2 & -1 & 0 & 1 & 2 \\ -2 & -1 & 0 & 1 & 2 \\ -2 & -1 & 0 & 1 & 2 \\ -2 & -1 & 0 & 1 & 2 \\ -2 & -1 & 0 & 1 & 2 \end{bmatrix}$$

and we will multiply them to the submatrix containing the bubble.

Compared to other schemes, the number of operations is limited to the number of dimensions of your bubble (either 2 or 3) and because the operation is just a matrix operation, it can be parallelized. The steps taking time are matrix construction and rearrangement and additional filtering to ensure z_c and x_c .

A way to speed up this is to rearrange your dataset of images from a 3D matrix $[N_z, N_x, N_t]$ to a 2D matrix $[N_z * N_t, N_x]$. After getting the local maxima, all values outside of a scanning window the size of the bubble are set to zero, the density index of the matrix decreases from 1 to $\frac{N_{particles} * (2 * fwhm_z - 1) * (2 * fwhm_x - 1)}{N_z N_x N_t}$, which for common rat brain 2D ULM is equal to around 0,00004. The weighted average calculation is operated on the whole matrix. Values corresponding to the local maxima are isolated with a matrix operation and aggregated in a cell which is later kept for tracking with its corresponding intensity value (non-interpolated) and the index of its frame. The same principle is kept for the radial symmetry based framework.

II.3.1.3 Radial symmetry

The weighted average is very fast but is sensitive to noise. Compared to iterative Gaussian fitting, for example, it has been shown to perform poorly if the size of the interrogation window is too narrow (Fisher and Naidu, 1996). For determination of the axial position, it will use the same coefficients regardless of lateral displacement and respectively for the lateral position.

We could use other properties of the beamformed response of a bubble. For example, the intensity gradient in every point of a symmetric intensity profile centered on its maximum is always directed towards that maximum. We can then locate that center by minimizing its distance to equipotential lines (i.e. orthogonals to the gradient).

We will demonstrate a method first used in (Parthasarathy, 2012) that relies on radial symmetry, and we will then extend it to three dimensions.

Let I be a 5x5 matrix containing a bubble :

$$I = \begin{bmatrix} I_{11} & I_{12} & I_{13} & I_{14} & I_{15} \\ I_{21} & I_{22} & I_{23} & I_{24} & I_{25} \\ I_{31} & I_{32} & I_{33} & I_{34} & I_{35} \\ I_{41} & I_{42} & I_{43} & I_{44} & I_{45} \\ I_{51} & I_{52} & I_{53} & I_{54} & I_{55} \end{bmatrix}$$

The image of an interpolated bubble will be used to illustrate our process but the reader should keep in mind that we work on non-interpolated data.

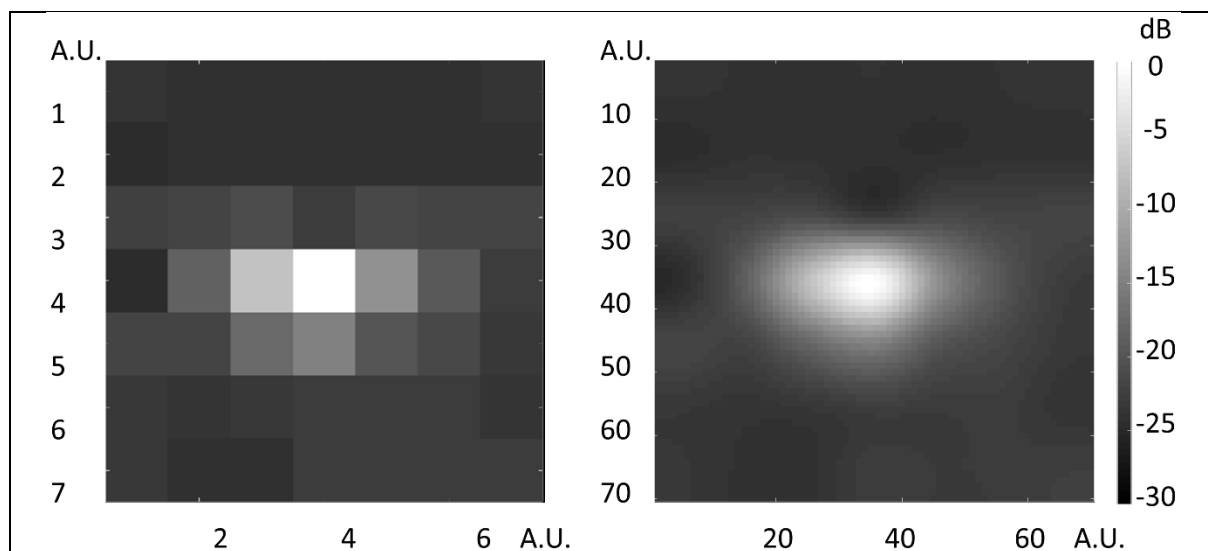
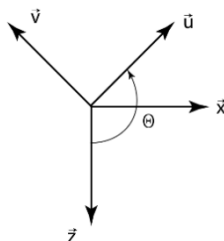


Figure 25. Non interpolated and interpolated image of a microbubble obtained by simulation of a point-like scatterer using Verasonics Research Ultrasound Simulator

The scatterer is slightly shifted from the center of the image (coordinates (30,30)). The interpolation is based on a Lanczos kernel at a factor 10.

We define (\vec{u}, \vec{v}) the basis as the rotation of the original basis (\vec{z}, \vec{x}) , rotated by $\theta = +\frac{3\pi}{4}$:



and the rotation matrix:

$$R_{(\vec{x}, \vec{z}) \rightarrow (\vec{u}, \vec{v})} = \begin{bmatrix} \cos(\theta) & -\sin(\theta) \\ \sin(\theta) & \cos(\theta) \end{bmatrix} = -\frac{\sqrt{2}}{2} \begin{bmatrix} 1 & 1 \\ -1 & 1 \end{bmatrix}$$

and $R^{-1} = R_{(\vec{u}, \vec{v}) \rightarrow (\vec{x}, \vec{z})} = \begin{bmatrix} \cos(\theta) & \sin(\theta) \\ -\sin(\theta) & \cos(\theta) \end{bmatrix} = -\frac{\sqrt{2}}{2} \begin{bmatrix} 1 & -1 \\ 1 & 1 \end{bmatrix}$

We set $dIdv = I(1:N_z - 1, 1:N_x - 1) - I(2:N_z, 2:N_x)$, and $dIdu = I(1:N_z - 1, 2:N_x) - I(2:N_z, 1:N_x - 1)$.

The line given by the equation $dIdu \cdot \vec{u} + dIdv \cdot \vec{v}$ is the line that defines the gradient of intensity according to the basis (\vec{u}, \vec{v}) .

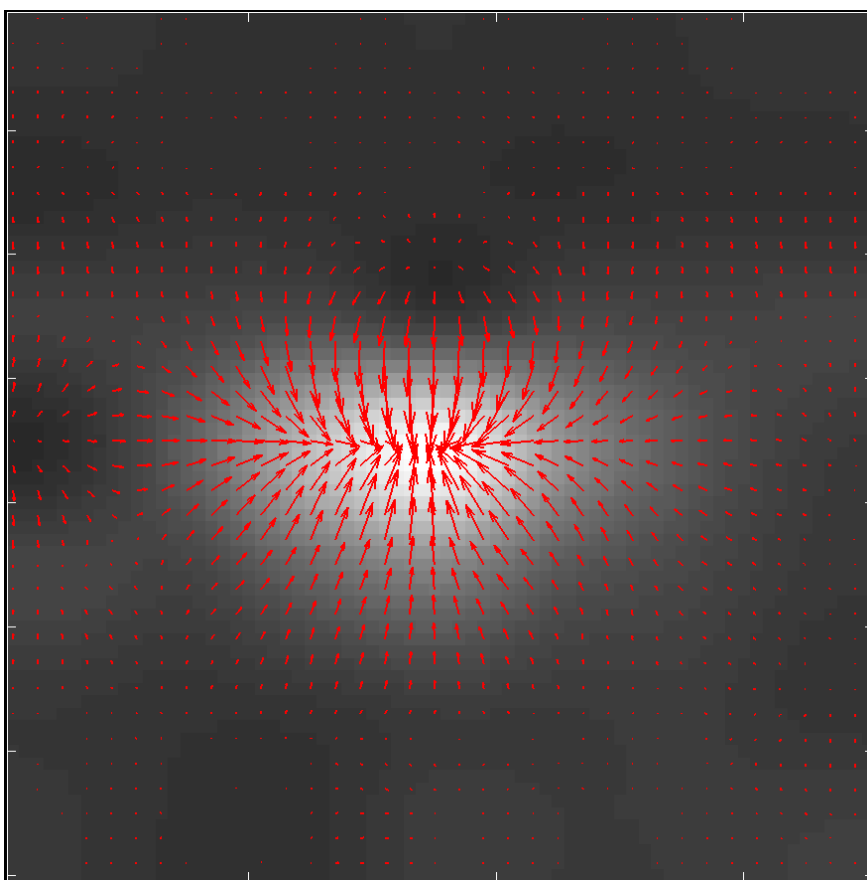


Figure 26. Gradient of the intensity of the interpolated point-like scatterer in basis (\mathbf{u}, \mathbf{v})

The red arrows have a direction based on the 2D gradient of the intensity at each pixel. We only overlaid a $10 \times$ undersampled dataset of the gradient for visualization purposes.

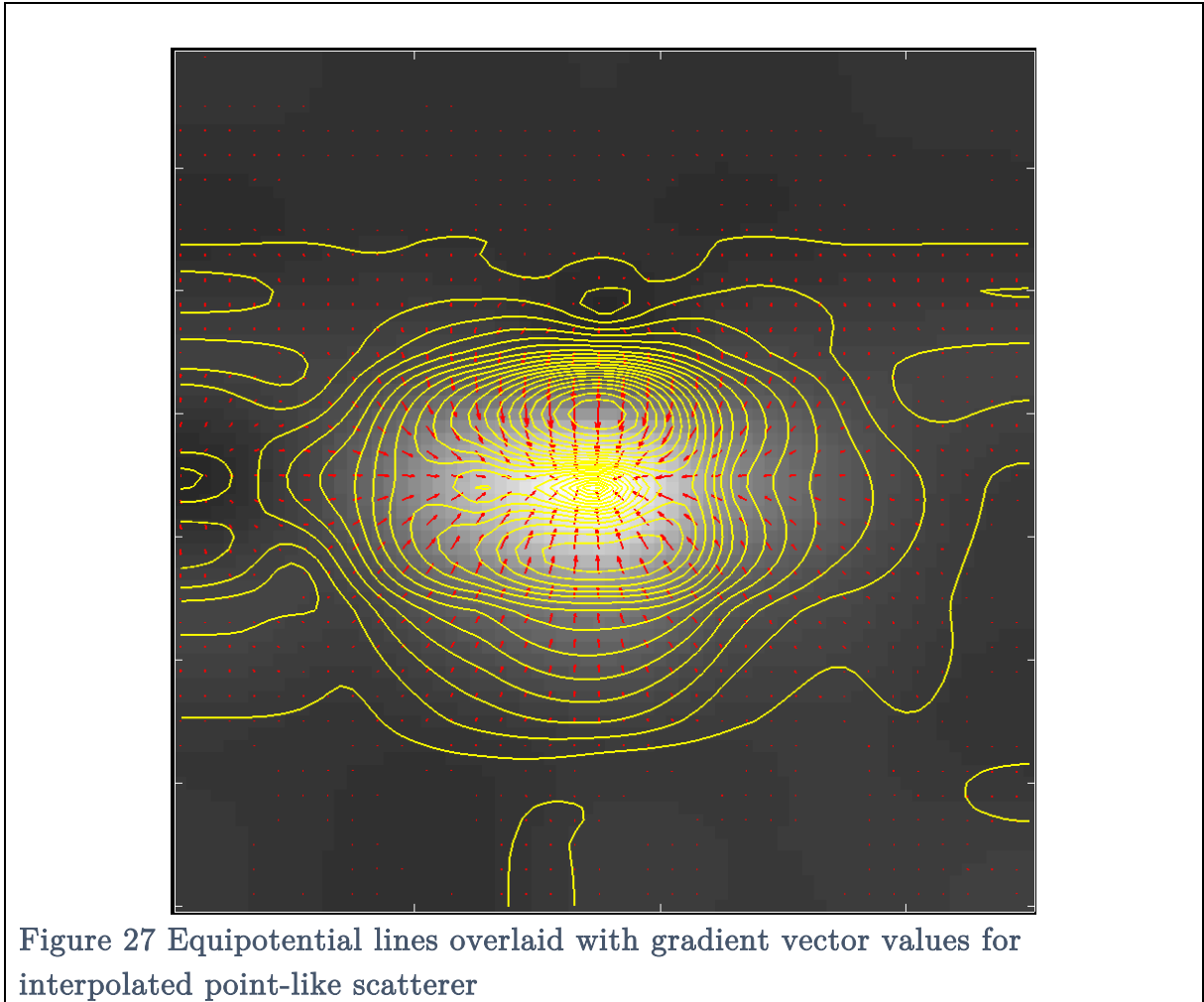
The line given by the equation $(\mathbf{u} \cdot \vec{u} + \mathbf{v} \cdot \vec{v})(dIdu \cdot \vec{u} + dIdv \cdot \vec{v}) = \vec{0}$ will define the subset (\mathbf{u}, \mathbf{v}) of coordinates defining an orthogonal to the intensity gradient and we can write it as:

$$\begin{aligned}
 \begin{bmatrix} u \\ v \end{bmatrix}^T \begin{bmatrix} dIdu \\ dIdv \end{bmatrix} = 0 &\Leftrightarrow \begin{bmatrix} u \\ v \end{bmatrix}^T \cdot R_{(\bar{u}, \bar{v}) \rightarrow (\bar{z}, \bar{x})} \begin{bmatrix} dIdu \\ dIdv \end{bmatrix} = 0 \\
 &\Leftrightarrow \begin{bmatrix} u \\ v \end{bmatrix}^T \cdot -\frac{\sqrt{2}}{2} \begin{bmatrix} 1 & -1 \\ 1 & 1 \end{bmatrix} \begin{bmatrix} dIdu \\ dIdv \end{bmatrix} = 0 \\
 &\Leftrightarrow [u \ v] \cdot \begin{bmatrix} dIdu - dIdv \\ dIdu + dIdv \end{bmatrix} = 0 \\
 &\Leftrightarrow u \cdot (dIdu - dIdv) + v \cdot (dIdu + dIdv) = 0
 \end{aligned}$$

Let $(u_k, v_k) = (z_k, x_k)$ be the coordinates belonging to the orthogonal to the gradient, we need to find the center (z_c, x_c) minimizing the distance to the orthogonal of the gradient. If we want our basis to be centered around (z_c, x_c) , the equation above becomes:

$$(z_k - z_c) - m(x_k - x_c) = 0$$

with $m = \frac{dIdu + dIdv}{dIdv - dIdu}$.



The distance from the point $C(z_c, x_c)$ to the point $K(z_k, x_k)$ belonging to the line

directed by the vector \vec{u}_d orthogonal to the gradient in K is

$$d(c, K \in \vec{u}_d) = \frac{\|\vec{KC} \wedge \vec{u}_d\|}{\|\vec{u}_d\|}$$

thus

$$d(c, K \in \vec{u}_d) = d_k = \frac{|(z_k - z_c) - m(x_k - x_c)|}{1 + m^2}$$

Let $\chi^2 = \sum_k d_k^2 w_k$ with w_k a weight given to each pixel. The goal of this is to compensate for low SNR in areas where the gradient is low, and :

$$w_k = \frac{dImag^2}{\sqrt{(z_k - z_c)^2 + (x_k - x_c)^2}}$$

$$\text{and } dImag^2 = dIdu^2 + dIdv^2$$

As w_k , is defined with respect to (z_c, x_c) , we will use the classical weighted average method as an initial guess of (z_c, x_c) to calculate each w_k . To find the maximum intensity point, one must minimize all of the distance d_k , for example, minimize the sum of all distances d_k . We will thus differentiate χ^2 with respect to (z_c, x_c) and solve for (z_c, x_c) .

$$\begin{aligned} \frac{\partial \chi^2}{\partial x_c} &= \frac{\partial \sum_k d_k^2 w_k}{\partial x_c}, \\ &= \sum_k \frac{\partial \left(\frac{((z_k - z_c) - m_k(x_k - x_c))^2 w_k}{m_k^2 + 1} \right)}{\partial x_c} \\ &= \sum_k \frac{2((z_k - z_c) - m_k(x_k - x_c))m_k w_k}{m_k^2 + 1} \end{aligned}$$

solving for $\frac{\partial \chi^2}{\partial x_c} = 0$ leads to

$$\begin{aligned} \sum_k \frac{m_k w_k}{m_k^2 + 1} ((z_k - z_c) - m_k(x_k - x_c)) &= 0 \\ \sum_k \frac{m_k w_k}{m_k^2 + 1} * z_c - \sum_k \frac{m_k^2 w_k}{m_k^2 + 1} * x_c &= \sum_k \frac{m_k w_k}{m_k^2 + 1} * (z_k - m_k x_k) \end{aligned}$$

and for $\frac{\partial \chi^2}{\partial z_c} = 0$

$$\sum_k \frac{w_k}{m_k^2 + 1} * z_c - \sum_k \frac{m_k w_k}{m_k^2 + 1} * x_c = \sum_k \frac{w_k}{m_k^2 + 1} * (z_k - m_k x_k)$$

If we write this with matrices, it becomes :

$$\begin{bmatrix} \sum_k \frac{m_k w_k}{m_k^2 + 1} & \sum_k \frac{m_k^2 w_k}{m_k^2 + 1} \\ \sum_k \frac{w_k}{m_k^2 + 1} & \sum_k \frac{m_k w_k}{m_k^2 + 1} \end{bmatrix} = \begin{bmatrix} \sum_k \frac{m_k w_k}{m_k^2 + 1} * (z_k - m_k - x_k) \\ \sum_k \frac{w_k}{m_k^2 + 1} * (z_k - m_k x_k) \end{bmatrix}$$

Calculating the values of (z_c, x_c) , is straightforward from the expression above:

$$\text{Let } \Omega = \begin{bmatrix} \sum_k \frac{m_k w_k}{m_k^2 + 1} & \sum_k \frac{m_k^2 w_k}{m_k^2 + 1} \\ \sum_k \frac{w_k}{m_k^2 + 1} & \sum_k \frac{m_k w_k}{m_k^2 + 1} \end{bmatrix}$$

$$\begin{bmatrix} z_c \\ x_c \end{bmatrix} = \Omega^{-1} \begin{bmatrix} \sum_k \frac{m_k w_k}{m_k^2 + 1} * (z_k - m_k x_k) \\ \sum_k \frac{w_k}{m_k^2 + 1} * (z_k - m_k x_k) \end{bmatrix}$$

Translating this into Matlab is rendered easy by ready-made functions to calculate cross product, L1-norm, matrix inversion... For Matlab implementation, the result is :

```
dIdu = I(1:Nz-1,2:Nx)-I(2:Nz,1:Nx-1);
dIdv = I(1:Nz-1,1:Nx-1)-I(2:Nz,2:Nx);
m = -(dIdv + dIdu) ./ (dIdu-dIdv);
dImag2=dIdu^2+dIdv^2 ;
w = dImag2./sqrt((zk-zc).^2+(xk-xc).^2);
Omega21 = sum(sum(w./(m^2+1)));
Omega12 = sum(sum(m^2*(w./(m^2+1))));
Omega11 = sum(sum(m.*w./(m^2+1)));
ZK1 = sum(sum(Omega11*(zk-m*xk)));
ZK2 = sum(sum(Omega12*(zk-m*xk)));
det = Omega11*Omega11 - Omega12*Omega21;
xc = (ZK1*Omega21 - Omega11*ZK2)/det;
zc = (ZK1*Omega11 - Omega12*ZK2)/det;
```

The 3D version of that demonstration follows the same principle. What adds complexity to the problem is that the norm of $\vec{KC} \wedge \vec{u}_d$ has 3 terms instead of 1 making the partial derivatives of χ^2 much longer to compute. The inverse of matrix Ω is also much harder to compute. The demonstration is done in Appendix B.

Additionally to the calculation of the center using radial symmetry, several other operations have been implemented.

Because radial symmetry is solely based on diagonals, if the bubble signal is centered in one direction but not the other, the algorithm will project the shift in one

direction to the other. This leads to minimization of the shift in one direction and introduces an error in both directions. Fortunately, as we have already calculated the centroid coordinates for our initial guess, we have information on the shifts prior to radial symmetry calculation. We have thus implemented a safe-guard to prevent diagonal projection based on the value of that initial guess. If the centroid shift is less than $1 \mu m$ in one direction, then we estimate that the radial symmetry based algorithm will lead to erroneous calculation and decide to use the initial guess as our final value.

Sometimes, the number of local maxima present in the image is quite high meaning that there could be several bubbles close to each other. This leads to strong variations in the intensity gradient and in turn, the lines orthogonal to the gradient do not cross in the center of the image. One could remove these lines by observing their directions (i.e. values of m) and only keep lines that converge to a similar point. However, this means adding a control loop during the building of the m matrix which slows down the algorithm considerably. Moreover, to make sure that we are actually keeping lines converging to a similar point and that this point is indeed the center of the main bubble, we would need to add a second control loop after the center coordinates are calculated meaning iterating twice or more. We simply chose to use the centroid shift without going further in our calculation. The advantage of not removing this bubble is two-fold, it will keep the same number of bubble in each frame making the parallelization of the algorithm possible (the infamous problem of ensuring transparency in parallel programming in Matlab), and we believe that if two bubbles are too close in one frame, they will grow distant in the subsequent frames and thus will get linked in the Hungarian based tracking algorithm.

The last filter is based on the size of the bubble. The second moment of the image of a bubble is twice the Gaussian width of the intensity distribution. We can thus estimate the width of the bubble. If that width is larger than a fixed threshold of 2.5 pixels, we keep the centroid shift to evaluate the center.

II.3.2 Tracking scheme

II.3.2.1 *Tracking based on the Kuhn-Munkres algorithm for pairing*

After microbubbles positions are measured and stored, a tracking algorithm was implemented based on the Hungarian method or Kuhn-Munkres algorithm for assignment (Kuhn, 1955). For each particle, the squared distance to all of the particles in the subsequent frame is computed. We obtain a vector containing $N_{particles}(t + dt)$, the number of particles in the frame ($t + dt$). In total, for each frame, we will obtain a matrix of size $N_{particles}(t) * N_{particles}(t + dt)$. By applying the Kuhn-Munkres algorithm, we

are able to find the optimal pairing for the subsequent frames by minimizing the total squared distance. The Kuhn-Munkres algorithm allows considerable gain of time as its time complexity has been proven to be $O(n^3)$ (EDMONDS, 1972). This algorithm is then looped on every frame. One advantage of this method is that it supports partial assignment (i.e. it will not pair a microbubble if there is no good candidate).

We also studied the possibility of crossing trajectories: when two microbubbles cross paths, they reach a certain position where they are next to each other. In a crossing vessel scenario, we have 4 points $A(t), A(t + dt), B(t), B(t + dt)$. If the Euclidian distance between two points is minimized for A regardless of the minimization for B, there are cases where $d(A(t), B(t + dt)) < d(A(t), A(t + dt))$ and $d(B(t), B(t + dt)) < d(B(t), A(t + dt))$. However for our algorithm this is not authorized as the pairing should be unique. Using the direction information from the trajectories, it is also possible to exclude crossing trajectories. A rejection filter is then applied to the microbubble position registered to eliminate microbubbles which do not follow long enough tracks : tracks smaller than 15 frames – 30 ms – are considered invalid. This threshold is justified by the fact that in a 3D volume, we should be able to reconstruct the tracks of the microbubble as long as they stay in the field of view which is considerably larger than the micro canal transverse axis. If a track is less than 30 ms, it could come from either noisy signals, or from incomplete tracking of a microbubble because of a pairing failure. In any case, a track of 30 ms contains a small enough amount of information to be dispensed with.

The tracks are then used to compute velocity measurement based on the compounded volume rate in three dimensions using a differentiate method without interpolation. Each particle has its velocity computed through its trajectory and according to its temporal sampling. This follows the traditional Lagrangian approach to calculate velocity fields as demonstrated experimentally in (Bondur et al., 2019). The accuracy of these velocities is thus influenced by the accuracy of both particle assignment and the tracking algorithm.

II.3.3 Developing a universal framework for ULM

Additionally to the computation time challenge, one must organize all the bricks described in section State of the art of that chapter so that it is easy to read and to execute. The goal behind this is to widen the use of ULM in ultrasound imaging. The framework is described below :

II.3.3.1 Data acquisition

Depending on the scanner's capability, one can either choose to work with RF data or with IQ data. For all 2D cases, the beamformed data is acquired to take advantage of the $N_{transmits} * SPPW$ compression, $SPPW$ being SamPles Per Wavelength.

Another limiting factor is the rate at which data can be transferred from the acquisition cards to the computer memory. Except for 500Hz/1000Hz 2D imaging of the rat brain with beamforming on the fly, the transfer rate can be so low that one needs to suspend transmits after a certain amount of images are acquired to prevent buffer deletion/replacement on the acquisition card. For 2D imaging with more than 3 angles, the pause represents 10% of the total time of acquisition (i.e. 2s of continuous imaging takes 2.2s).

Sometimes, it can be an advantage to modify the way one acquires data specifically for ULM. Let's say one needs to pause to save data to the main computer's disk but also happens to have a very large amount of RAM on that computer. Instead of waiting for the data to be transferred from the acquisition cards to the RAM and then wait for the CPU to transfer data from the RAM to the hard drive, one could acquire continuously for half a minute or a bit more (acquiring 30 000 images at 1000Hz for example) and then wait for a long time that data has been migrated from RAM to hard drive (usually more than 10 minutes depending on which hard drive technology is used). This is particularly helpful in *in vivo* experiment where *boli* are preferred instead of continuous perfusion. For a bolus of 0.2 mL of Sonovue injected in a rat, the microbubbles concentration starts decreasing after 10s and becomes negligible after one minute. As fewer microbubbles mean less information, there is a tradeoff between recording more images with fewer microbubbles and stopping, discarding the end of the bolus and allow for images to be saved. The advantage of such a framework is to have more continuous frames and thus improving the performance of both spatio-temporal filtering and of tracking and velocimetry algorithms.

II.3.3.2 Loading and beamforming

I.1.1.1.1 LOADING

Loading of the RF or IQ data is performed sequentially : a number of blocks fixed by the user is loaded in the RAM of the computer. This number is constrained by the size of the RAM available and the RAM needed for the next processes, and by the time step B. takes compared to step C.to E. which will be run in parallel to the current step. A diagram was produced at the end of this section for reference.

I.1.1.1.2 OPTIONAL STEP FOR RADIOFREQUENCY DATA :

In the case where radiofrequency is transferred from the acquisition card to the computer's hard drive, beamforming needs to be implemented *a posteriori*. We transfer the data on hard drive disks, throughout the whole acquisition and then beamform the data on our own computer thus bypassing the possibly slower computer present in the scanner. After beamforming the data, we use the normal framework described below.

II.3.3.3 Filtering

After beamforming, or in case one is working with beamformed data, spatio-temporal filtering is implemented. Either a one-step SVD filtering or a two-step highpass+SVD filtering is chosen. In our case, we eliminate the fewest possible vectors from singular value decomposition. For volumetric acquisitions of 185 images of a rat brain, only 5 of the highest energy vectors are removed from the original dataset. For plane imaging of a rat brain, it can be as few as 4 removed vectors out of 1000. These values will differ depending on motion, coupling medium, probe or scanner used, microbubble velocities. In the two-step highpass filtering+SVD case, the highpass 2nd order Butterworth filtering is applied before SVD, filtering low frequencies corresponding to tissue with a cut frequency of 50Hz. This allows lowering the number of singular vectors removed in SVD.

Note : For 2D acquisitions, this step is done straight after loading to optimize calculation time.

II.3.3.4 Optional step for motion correction frame by frame

In the case of a block by block acquisition of moving organs, we implement a motion correction algorithm. The algorithm used is based on image registration. Using an iterative image registration based algorithm, motion correction is performed frame by frame. For each block, a reference image is set and displacement is calculated for each frame. This displacement is then applied to the images and SVD filtering is performed another time to compensate for motion. These images will be used in subsequent steps.

II.3.3.5 Localization, tracking, and velocimetry

The localization scheme chosen is then applied to the dataset (a block at a time). It is applied to each block independently and in parallel. In the case of tracking, the running time will increase dramatically, sometimes making it impossible to fit this step in the time it takes to perform step B.

II.3.3.6 Motion correction block by block

For each block, the 1st image of tissue is compared to the reference image chosen for the acquisition (usually the 1st image of the 1st block). SVD filtering is used to keep tissue signal in the images by selecting only the highest energy vectors complementary to the SVD percentage used to decorrelate bubbles from tissue (i.e. if 5 values are removed to filter out the tissue, these 5 values are kept to retain tissue signal). The displacement is applied *a posteriori* to the tracks. The detailed motion correction algorithm used is explained in chapter 4.

II.4 Developing methods to measure the algorithms' performance

The field of ULM needs metrics to quantitatively assess the quality of the localization schemes. (Christensen-Jeffries et al., 2017; Song et al., 2018c, 2018a) have published results on improved localization schemes and have attempted to combine metrics to measure this improvement. However, the absence of a common training data set and of clearly define metrics for quality assessment makes it difficult to compare these papers to each other Inspired by (Sage et al., 2018, 2015), Arthur Chavignon and I have developed a routine to measure the performance of the various algorithms for localization. The first step is to create a simulated dataset of microbubbles flowing in various geometries and create metrics to measure localization performance. The second step is to test out these algorithms on 2D data of rat brain and kidney and measure their performance. The third step which remains to be done is to pool our data and our metrics together and give access to the community of ULM.

II.4.1 In silico methods

The media simulated comprised of 8 tubes with various geometries with various complexity (see Figure 29):

- A pseudo double helix (300 and 200 μm)
- A curved tube with constant diameter and a horseshoe pattern (100 μm)
- 3 curved tubes with 3 different diameters (50, 10, and 5 μm)
- 2 spreading tubes with a constant diameter (10 μm)

The goal of having this kind of simulation is to have a universal target that can be used by researchers to train their algorithms similar to the United States Air Force resolution test chart used in optics (United States Air Force, 1951) (see Figure 28).

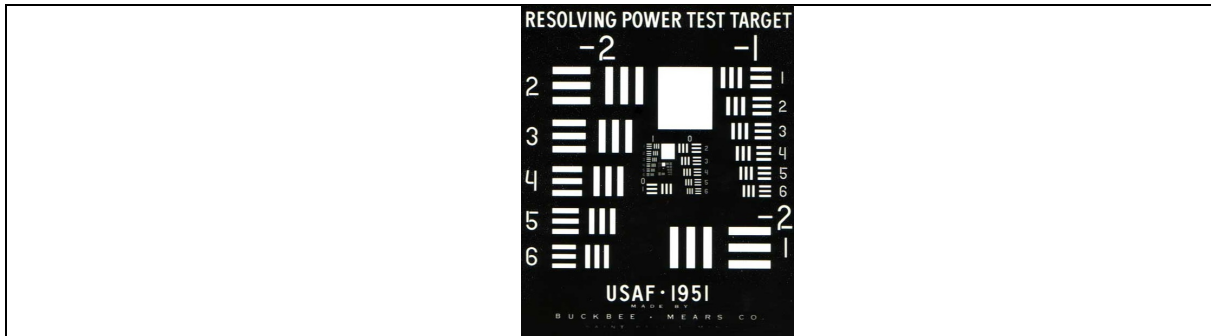


Figure 28. 1951 USAF resolution test chart (United States Air Force, 1951)

The 1951 USAF resolution test chart is a microscopic optical resolution test device. Originally designed by the US Air Force to provide an easy way to measure the resolution of satellites, it is now widely used in optical engineering laboratories for the same purpose.

To simulate moving microbubbles, we chose initial positions at random in the media and recorded it as a point like scatterer. For each of these positions, a trajectory calculated by Poiseuille's law was assigned. We considered that microbubbles could not jump from one trajectory to another and so had to follow the same trajectory for as long as it is simulated. While we are aware that a scatterer is not an exact representation of a microbubble, we believe that it is a good candidate to study the imprecisions of the different algorithms developed and rate them against each other.

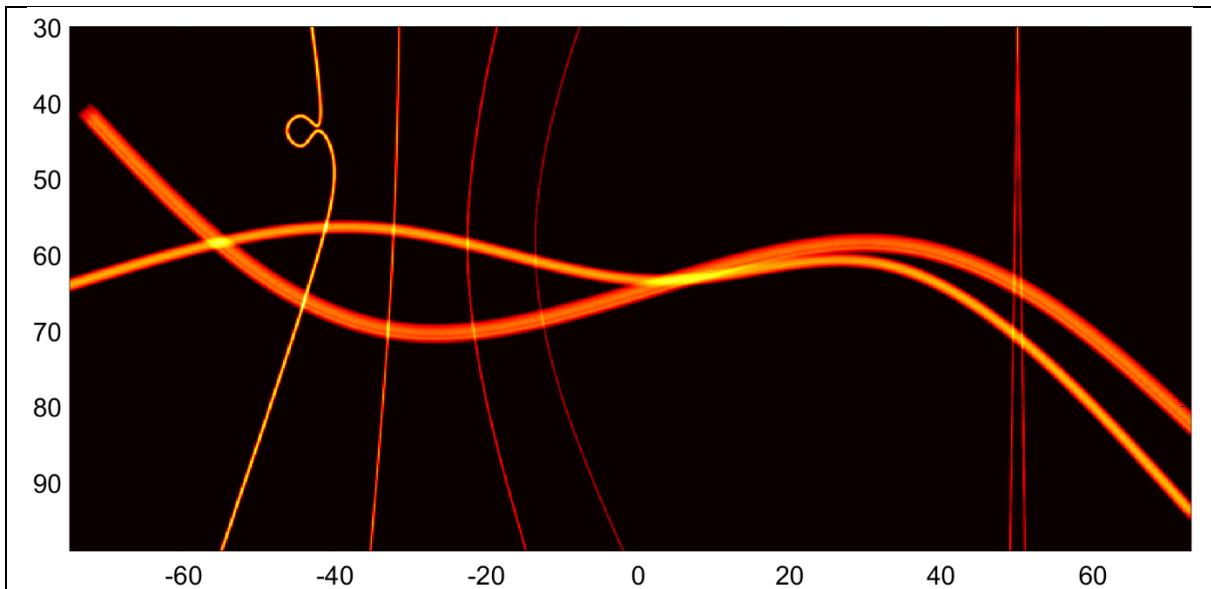


Figure 29. Norm of Velocity in target media with 6 different geometries

The velocity was calculated according to Poiseuille's law in a circular tube. For each pixel, the intensity represents the sum of the velocity norms at this pixel, thus the crossings in between vessels appear more intense.

Using the Verasonics Research Ultrasound Simulator, we simulated

radiofrequency and beamformed images of a moving scatterer in a $7 \times 14,9$ mm² area insonified with 3 tilted plane waves with a 15MHz probe. For each image in the simulation, we added clutter noise modeled by a Gaussian filtered white Gaussian noise. This noise was added after delay and sum beamforming was implemented. The parameters for the white Gaussian Noise were matched with a typical -30dB noise present in our *in vivo* images : we used wgn function in Matlab to generate a 1D vector of $N = N_x N_z$ white Gaussian noise samples at -30dBW power with 0.2 Ohm impedance. Normalized by the maximum intensity value of the beamformed image, it was then filtered using a Gaussian kernel of size 1.5. Reshaped to match the size of the beamformed image, it was added to the intensity of the beamformed image. We found that this modelization produced visually similar data as what we observe *in vivo* (see Figure 30).

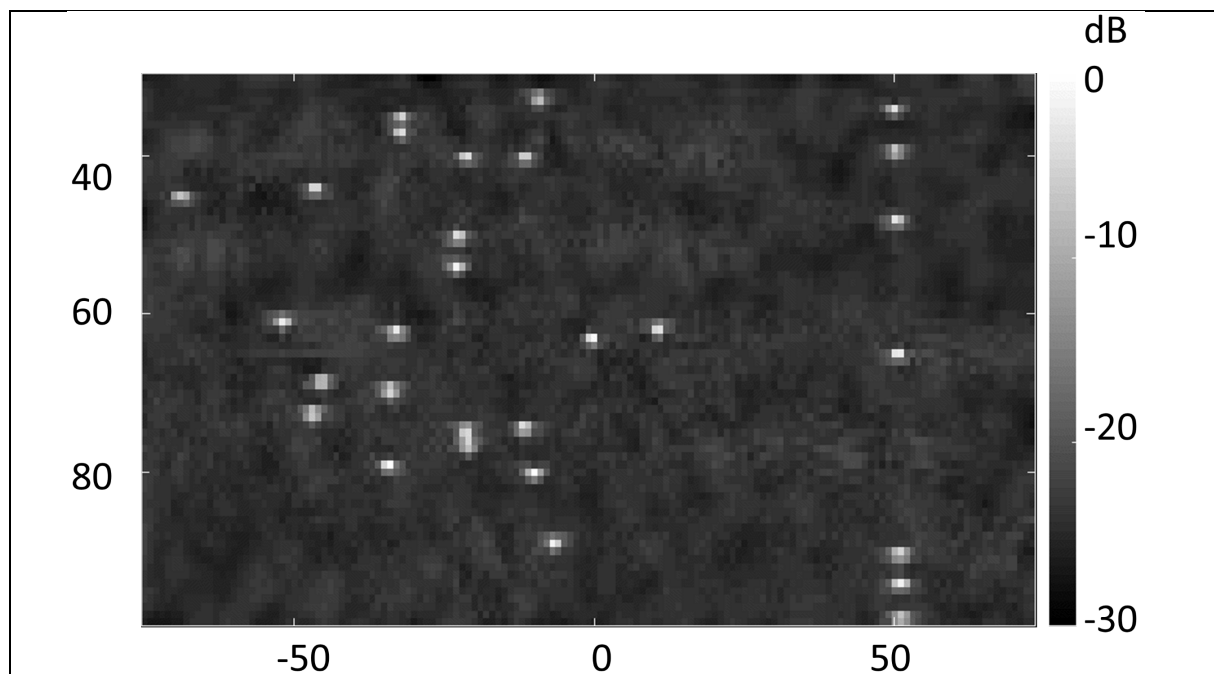


Figure 30. Typical beamformed image of scatterers in simulated media with added noise

The density of scatterers per image can be modified thanks to a seeding parameter in the simulation. One can see that the channel walls are not simulated. The need for filtering is thus minimal.

The main advantage of having simulated microbubbles in a media is that we have access to the ground truth. We can thus compute not only localization errors from our algorithm but we can define several logical cases for each localization. To judge whether the localization corresponds to the scatterer simulated we simply compute the distance in between the localized and the simulated scatterer, and it has to be strictly below $\frac{\lambda}{4}$:

- True-positives (TP) : a scatterer was simulated and a scatterer was localized in the neighborhood by the algorithm.
- False-positive (FP): a scatterer was localized but no scatterer was simulated in the neighborhood
- False-negative (FN): no scatterer was localized within a distance $\frac{\lambda}{4}$ of the simulated scatterer.

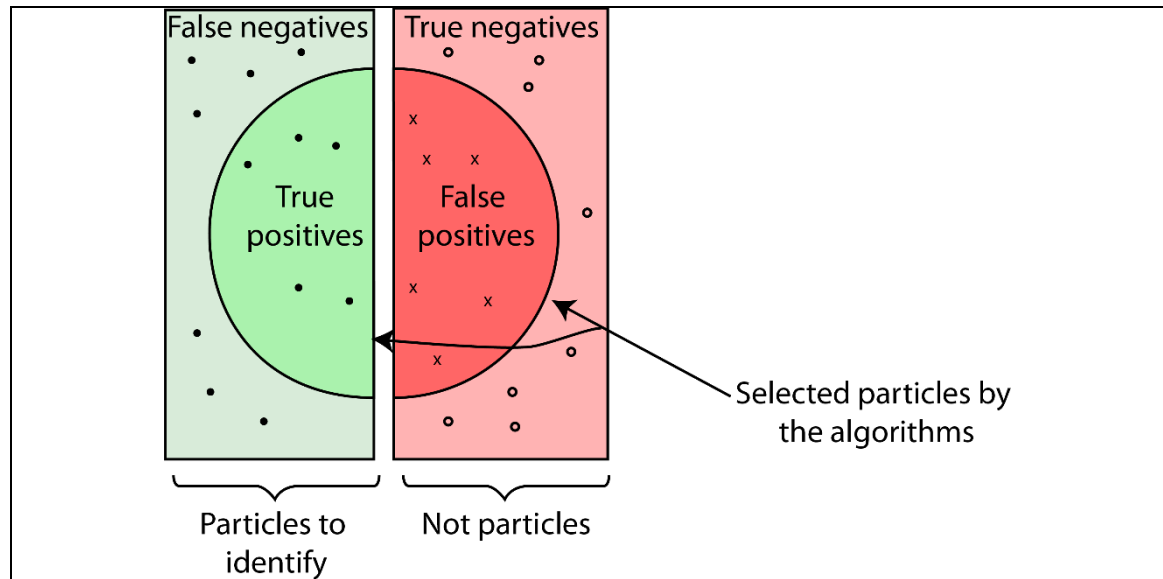


Figure 31. Schematics explaining the concept of the statistical classification of particles in the case of a localization algorithm

The points in black correspond to actual scatterers present in the region of imaging. The crosses correspond to what was identify as scatterers but are something else. In the case of a localization algorithm, the True Negative is an empty ensemble as we don't aim to classify scatterers with the algorithm but only detect. We don't classify each pixel of the media as belonging to a particle or not but we identify certain patterns in intensity as particles.

Thanks to statistical classification we can calculate statistical metrics. We define the Jaccard index as :

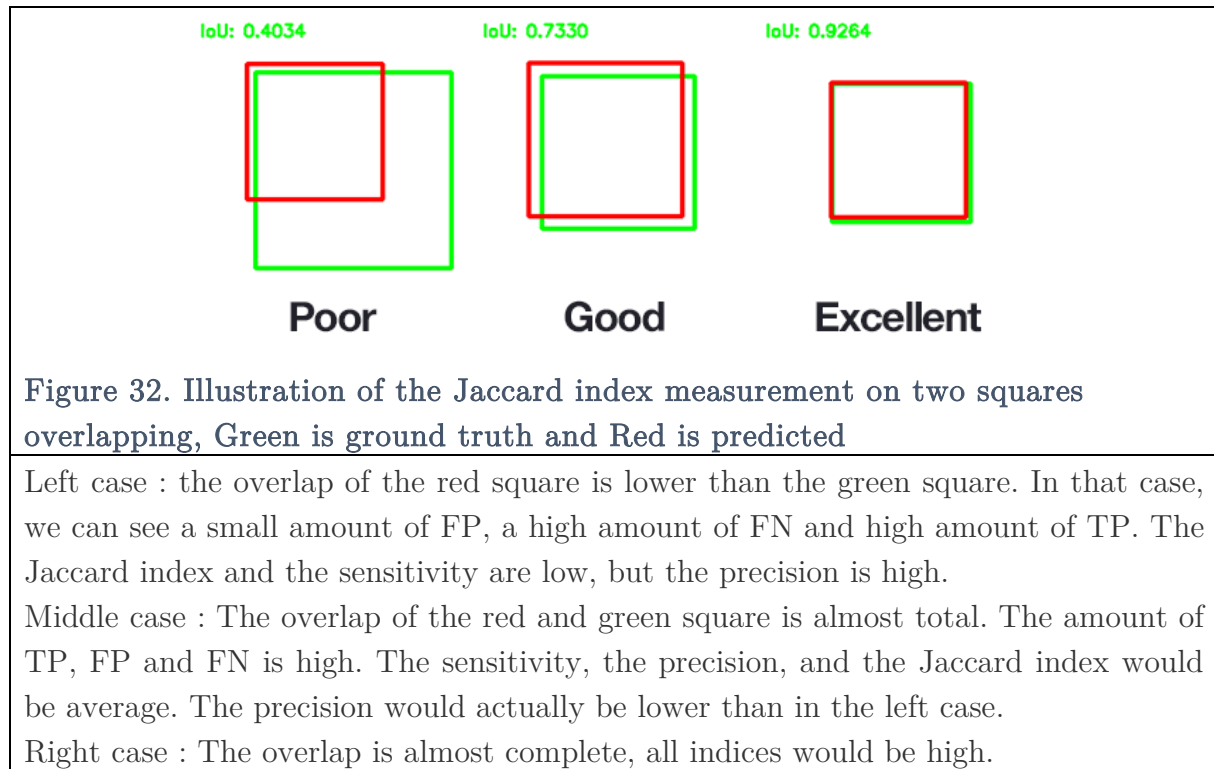
$$JAC = \frac{TP}{FN + TP + FP}$$

We can also define positive predictive value (precision) p and recall (sensitivity):

$$p = \frac{TP}{FP + TP}, r = \frac{TP}{FN + TP}$$

This index is a measure of the similarity of two different sets of data, how many

of the true bubbles we found over how many we could find. *In silico* it serves to compare the algorithms to the ground truth. The precision index is a measure of how many of the bubbles that we localized are actually bubbles. It answers the question : of all particles selected, how many are microbubbles? The recall index is a measure of how many of the bubbles that we were supposed to localize have we found. It answers the question : of all bubbles to identify, how many were selected?



As we have *a priori* knowledge of where the scatterers are supposed to be, we can measure the error in all two directions Z, X and calculate the average Root Mean Square Error. The scatterers bubbles are paired with the similar neighborhood as for statistical classification : $\frac{\lambda}{4}$

$$\begin{aligned} \delta_z(i) &= z_i^0 - z_i \\ \delta_x(i) &= x_i^0 - x_i \\ RMSE &= \frac{1}{N} \sum_i^N \sqrt{(x_i - x_i^0)^2 + (z_i - z_i^0)^2} \end{aligned}$$

Combining the two measures above, we can define an efficiency index:

$$E = 100 - \sqrt{(100 - JAC)^2 + \alpha^2 RMSE^2}$$

We use that efficiency index to compare the algorithms in between each other *in silico*. The advantage of that index is to combine our two measures, rank the algorithms

in between each other and determine which is actually better at localizing the correct bubbles with fewer errors.

II.4.2 *In vivo* methods

To provide further insight into how localization algorithms affect ULM renderings, we decided to train them on *in vivo* datasets. Our algorithms were first tested out on 2D rat brain imaging. The protocol followed to acquire those images is identical to the protocol described in chapter 4. As mentioned above, the framework adopted included Hungarian assignment based tracking as the other methods for tracking were either dubbed too computationally expensive (cross-correlation, iterative pairing with nearest-neighbor approach) or offered limited improvement in image quality based on our experience (bipartite graph pairing). Several post-processing techniques are implemented on the trajectories detected and are detailed in the next chapter.

As we do not have access to the ground truth *in vivo*, we require other indices to benchmark the results or adapt the existing indices.

Introduced in (Saxton and Baumeister, 1982), Fourier ring correlation has been demonstrated to be an appropriate descriptor of cross-resolution between two images (Van Heel, 1987). It is defined as :

$$FRC = \frac{\sum F_1 F_2^*}{\sqrt{\sum |F_1|^2 \sum |F_2|^2}}$$

where F_1, F_2 are the Fourier transform of the two images (spatial frequencies are represented), and F_2^* is the complex conjugate of F_2 .

In our case, we generated two images for each localization schemes based on half the trajectories generated. As our dataset consists of a very large number of frames (192,000 and 228,000 frames for respectively the 2D brain and kidney experiments), we can make the assumption that for most of the vessels we have at least two trajectories available. Thanks to (Hingot et al., 2019), we can infer that most of the small vessels (below 30 μm) are already visible.

Aliasing or grid-effects have been largely reported or seen in the literature (Christensen-Jeffries et al., 2017, 2015; Errico et al., 2015b; Heiles et al., 2019; Song et al., 2018c). We decided to quantify that grid effect by looking at the spatial frequency content of the ULM images.

Let $I(\mathbf{z}, \mathbf{x})$ be our ULM rendering. The frequency content F_z, F_x are calculated as:

$$F_z = FFT\left(\sum_x I(z, x)\right)$$

$$F_x = FFT\left(\sum_z I(z, x)\right)$$

The fundamental frequency for each spectral analysis is localized and the two first peaks are localized on the power spectral density. The peak to baseline value is computed for each peak, the sum gives us an index expressed in a logarithmic scale that quantifies aliasing.

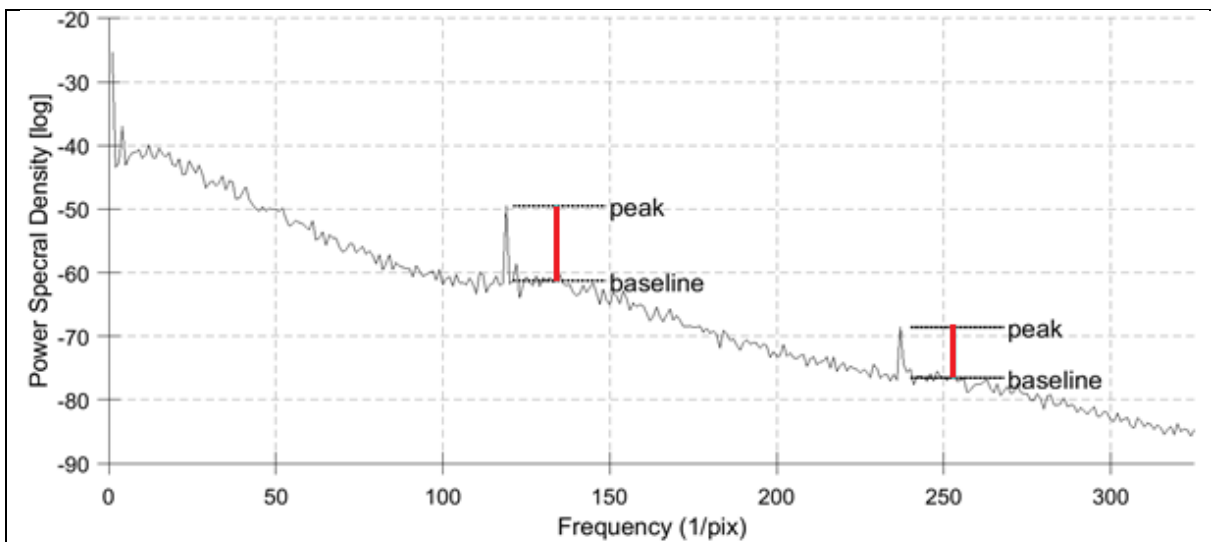


Figure 33. Power spectral density of the frequency analysis in Z-axis of the image

The peak to baseline values are measured automatically using custom made implementation of the `findpeaks` function in Matlab®

II.5 Results

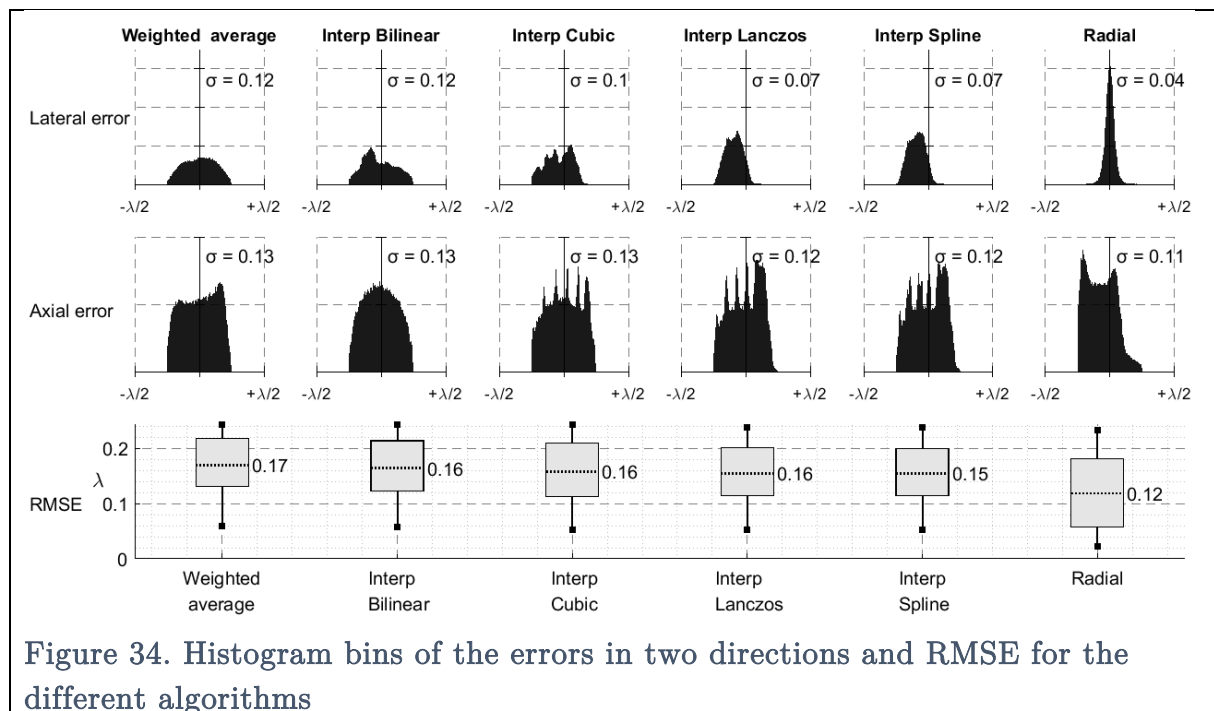
II.5.1 In silico

The algorithms tested on these data are: 3 different types of interpolation and center localization by maximal intensity, weighted average and our radial symmetry based localization. For each particle belonging to the ensemble $\{TP + FP\}$, the lateral and axial error is computed. The histograms of the distribution of the error are plotted below. As we do not pair particles and point-like scatterers which are further away than

$\frac{\lambda}{4}$ in all directions, the histogram bins are null after $\frac{\lambda}{4}$.

The standard deviation of the error is overlaid on the graph. The standard deviation of the weighted average error in the lateral direction is the highest with the bilinear interpolation scheme at $\sigma = 0.12$. The lowest standard deviation of the error is achieved with the radial symmetry scheme. The profiles of the histograms are almost identical for most localization schemes except for the radial symmetry based algorithm. That bin count follows a Laplace like distribution while interpolation schemes follow a larger band distribution.

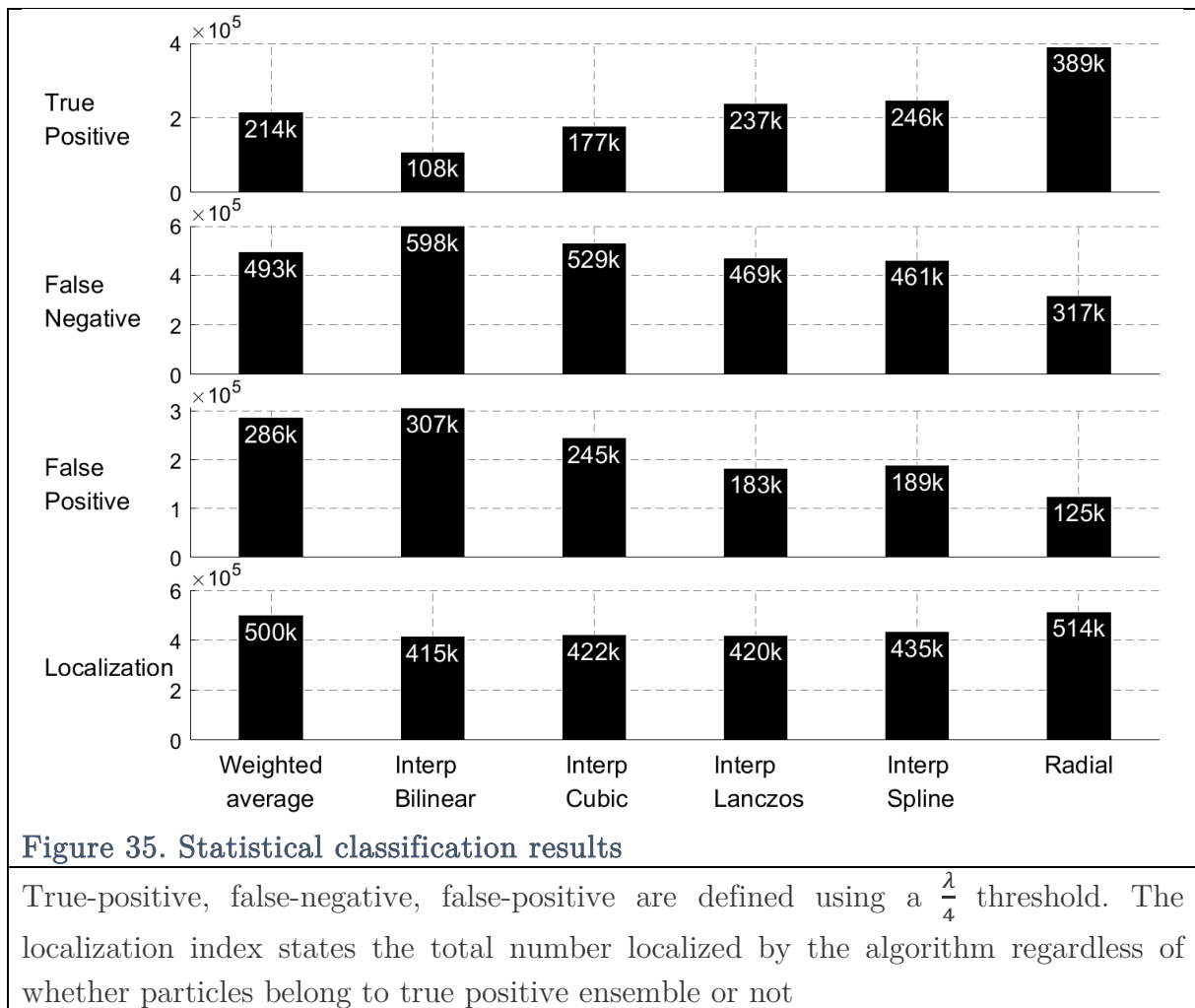
The standard deviations of the axial errors are close in value and there is no clear advantage in between schemes. The standard deviation of the axial error made by the radial symmetry based is still the lowest. The distributions are not centered around a peak value except for the bilinear interpolation scheme.



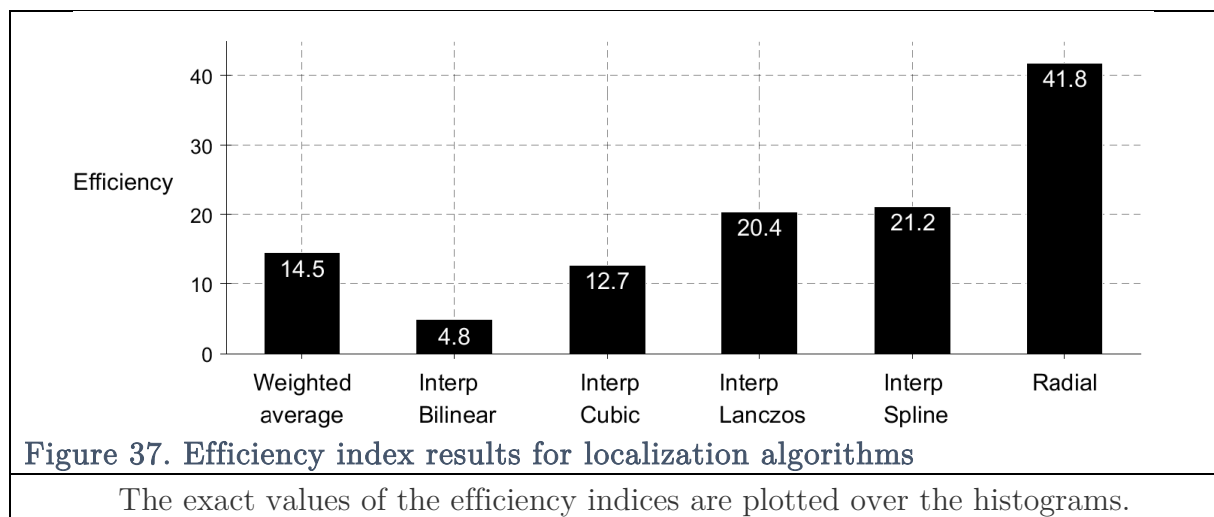
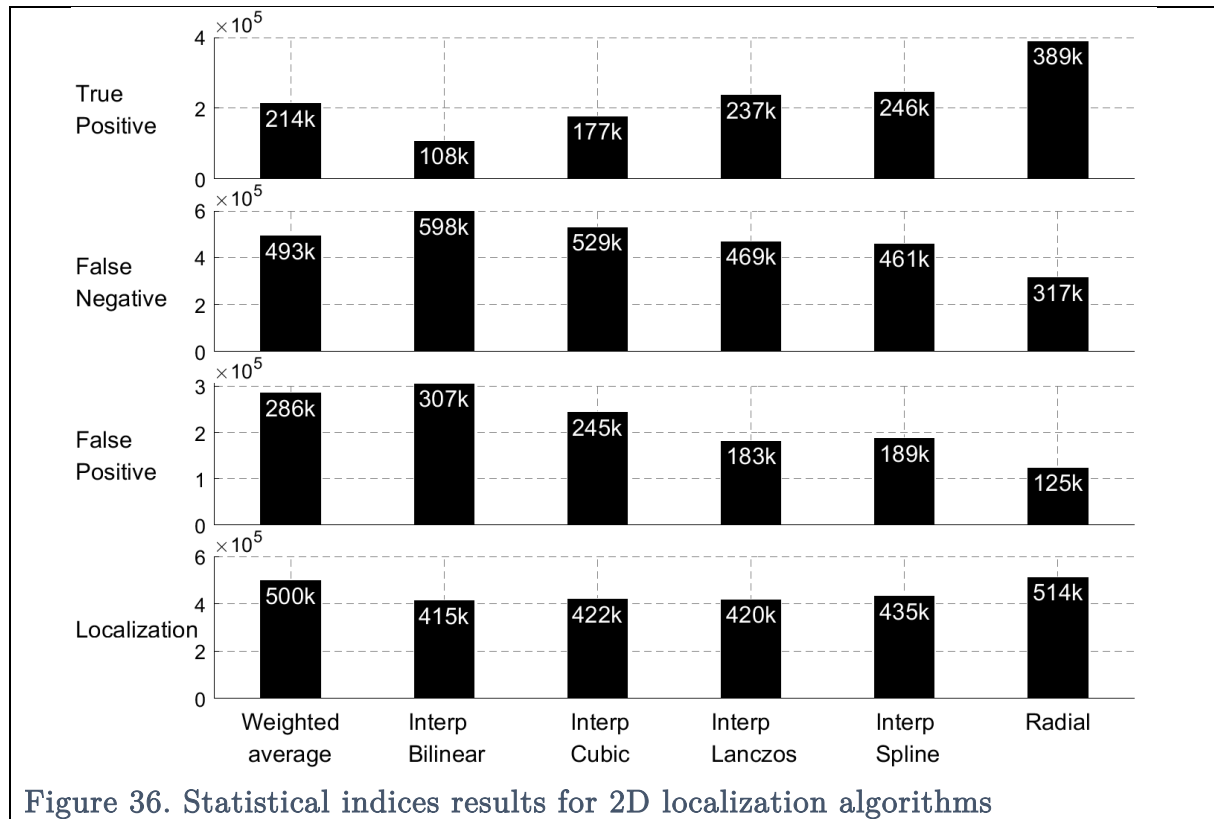
The RMSE is plotted as a bar plot. The lowest average RMSE is the radial symmetry based localization algorithm with a value of $RMSE = 0,118\lambda$. The standard deviation of the radial symmetry based RMSE is however quite high due to a uniform distribution of the axial error.

The cardinality of the TP, FP and FN ensembles were measured for each algorithm and are plotted below. The number of TP is particularly low for the bilinear interpolation scheme, and the radial symmetry based algorithm is 3.6 times better. On the other hand, the amelioration of False Positive is 2.5 fold, and for False Negative is

1.9 fold in the advantage of the radial symmetry based algorithm. Considering all values, the localization index (which is the sum of TP and FP) is also improved in this algorithm with a 1.2 fold increase from bilinear interpolation to radial. The localization index is roughly identical for all interpolation schemes but is higher for weighted average thanks to a sharp increase in the FP cardinality. The statistical indices defined previously are plotted in Figure 36. The bilinear interpolation has the lowest precision and sensitivity. The spline and Lanczos interpolation have similar precision, slightly above almost identical weighted average and cubic interpolation values. The sensitivity of the weighted average and cubic interpolation is however different from each other, reflecting the difference between FP and FN in the two schemes. The weighted average is at almost the same sensitivity as the Lanczos and spline interpolation with $r = 30.2, r = 33.6, r = 34.8$ respectively. The radial symmetry based algorithm is largely ahead compared to the other algorithms with a gain in precision and sensitivity of 74% and 63% respectively for the second-best algorithm.



The Jaccard index reflects a similar ranking as the precision index, with the radial symmetry based ranked 1st with $JAC = 46.8\%$, the Lanczos and spline interpolation *ex aequo*, then the weighted average and finally the cubic and bilinear interpolation.



The efficiency index calculation is summed up in Figure 37. As for the Jaccard index and similarly to the RMSE ranking, the radial symmetry based localization algorithm is 1st followed with the Lanczos and spline interpolation with only slightly

different values. The worst scheme is the bilinear interpolation scheme which has an efficiency index 10 times lower than the radial symmetry based. The weighted average is a little bit better than the cubic interpolation schemes but still quite far from the Lanczos and spline interpolation.

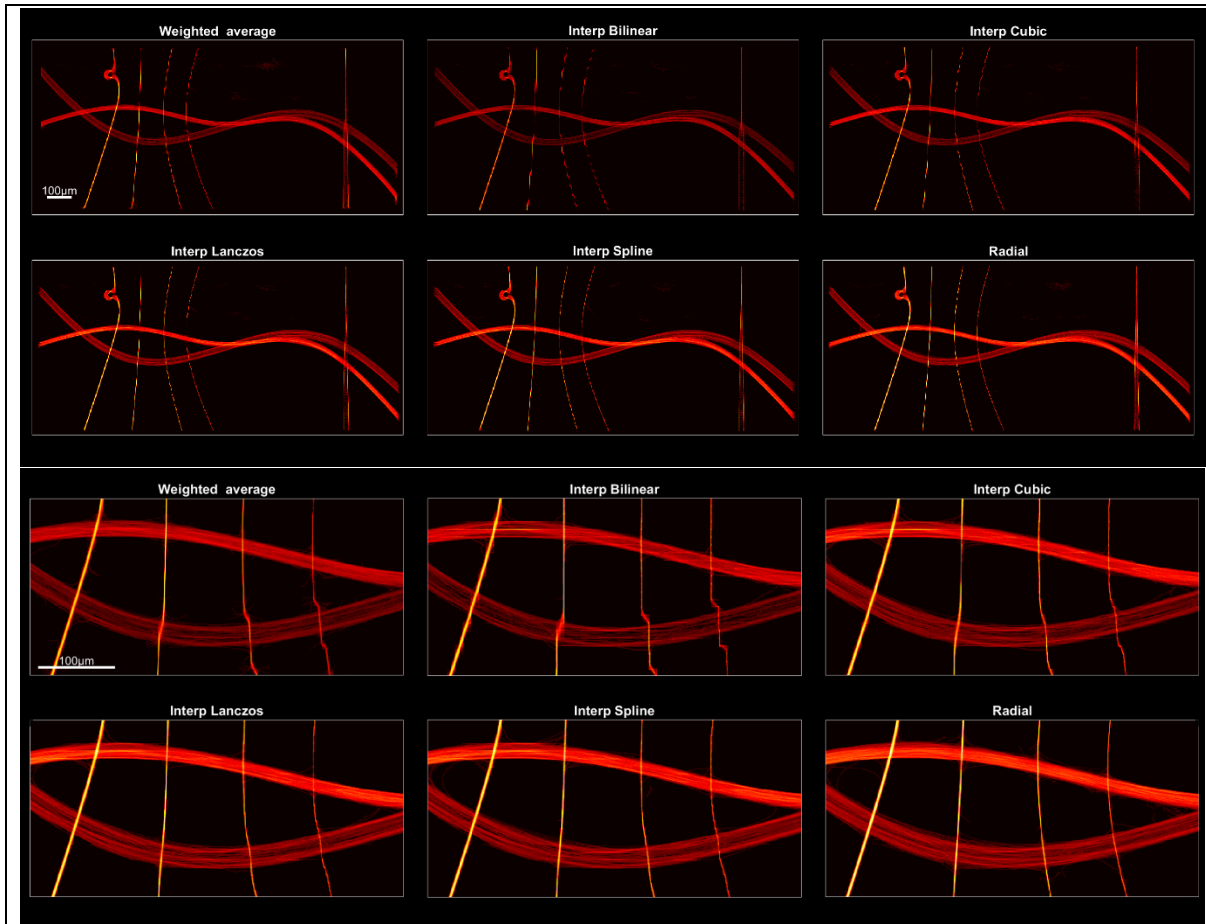


Figure 38. ULM renderings of in silico simulation

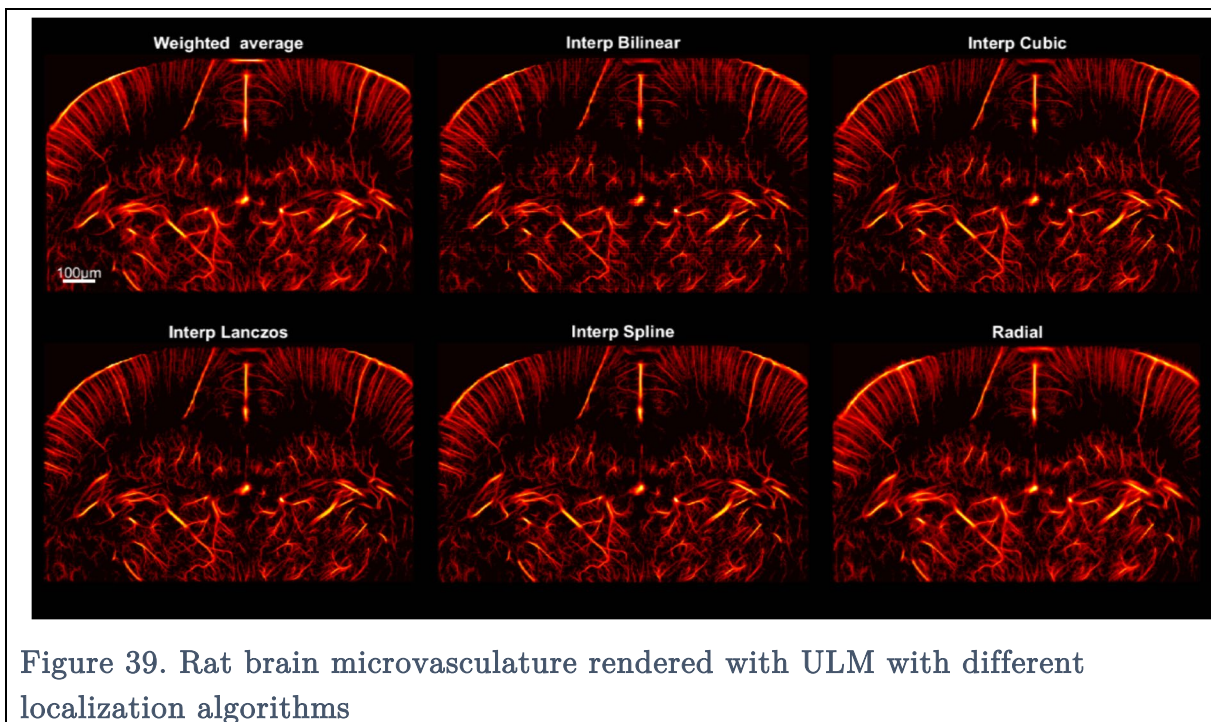
- a) Large view of the ULM rendering showing all of the structures simulated
- b) Enlarged view to illustrate the more precise impact of localization algorithms

The whole view of the ULM rendering shows all the structures simulated. There is notable difference however of how accurate these renderings are. For the bilinear interpolation localization algorithm, the grid effect is the worse, appearing in all of the structures except for the pseudo-double helix. Whole areas have very low density which makes them almost invisible except when zooming (see **FIGURE 38b**). The weighted average and the cubic interpolation scheme seem to suffer similar grid effects on the same tubes. The spline and Lanczos interpolation only suffer gridding on the two smaller curved tubes. The radial, on the other hand, adapts completely and does not suffer from any gridding on any curved tubes. The horseshoe is the worst rendered structure in every

scheme but the radial, spline, and Lanczos interpolation seem to yield the rendering closest to what was simulated, especially in terms of the curvature before and after the horseshoe. The two spreading tubes are not at all well resolved in the three worst localization algorithms. They converge together as soon as they get closer than 50 μm and appear almost parallel due to high grid effect. For the less grid affected localization algorithms, they converge later at a value of 3 μm . The radial produces a peculiar shape where the tubes seem to diverge again after converging.

II.5.2 In vivo 2D

The first aspect we looked at was the image quality of the ULM renderings. The brain vasculature is rendered in Figure 39.



The bilinear interpolation based ULM performs very poorly *in vivo* as the simulation predicted. The vessels in the cortex suffer from considerable gridding making their structure disorganized. The vessels in the subcortical region seem to be also affected by aliasing even though it is less perceivable in this figure. The cubic interpolation also suffers from gridding as predicted, however, the weighted average localization-based ULM is in appearance non gridded. To further investigate the effects of localization, we zoomed in a specific region where the grid effect is maximum, and where there is a large variety of vessel size. The results are presented in Figure 40. Our conclusion based on the previous figure holds partially. The bilinear and cubic interpolation are still massively

subjected to gridding and we can see some grids appear in specific regions in the weighted average scheme (indicated by white triangles in Figure 40). For the three best-ranked algorithms, almost no gridding is present in the images *in vivo*. One considerable difference can be noted though between the radial symmetry based ULM and the interpolation schemes: the vessels seem more detailed and sharp in the interpolation schemes. In the radial, there seems to be a lot of small crossing trajectories in between the brightest and larger vessels. This observation is confirmed by looking at the number of localizations made for each algorithm (see Table 1). There is complex microvasculature made of capillaries in between the arteriole/venule system, and we think that to some extent, the radial symmetry might be detecting more microbubbles passing through that system.

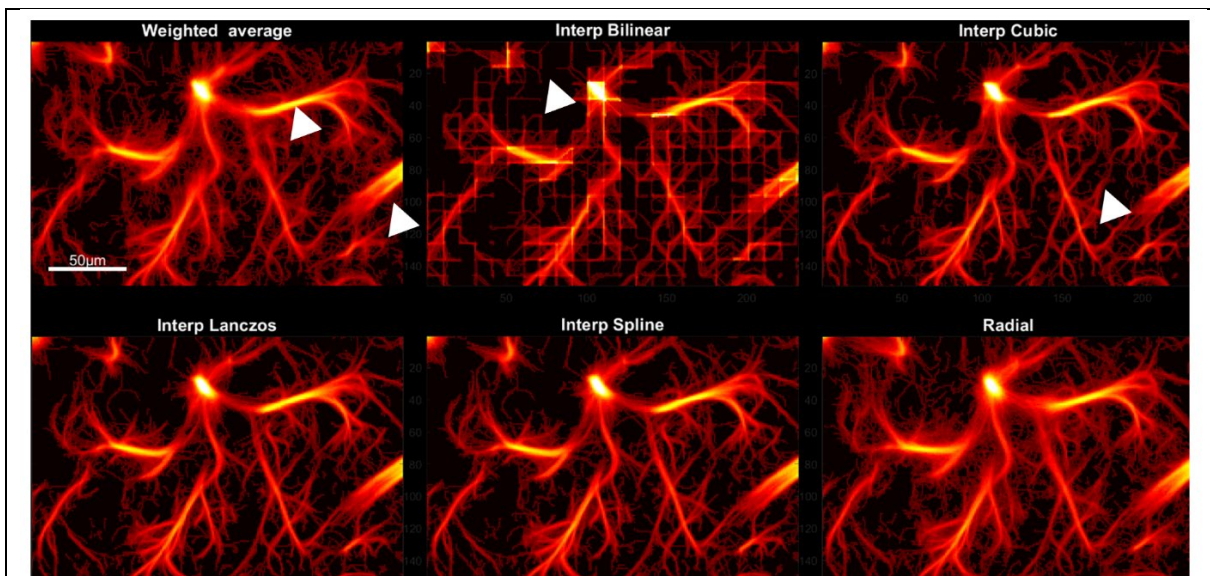


Figure 40. Zoomed in viewings of ULM renderings with the different localization schemes

White triangles indicate zones where aliasing happens

Algorithm	Weighted average	Bilinear interpolation	Cubic interpolation	Lanczos interpolation	Spline interpolation	Radial symmetry-based
Number of localizations (in millions)	4.6	1.3	3.6	3.8	3.9	4.8

Table 1. Total number of localizations for each algorithm

This improvement in image quality brought by radial symmetry compared to weighted average scheme was also seen in other organs:

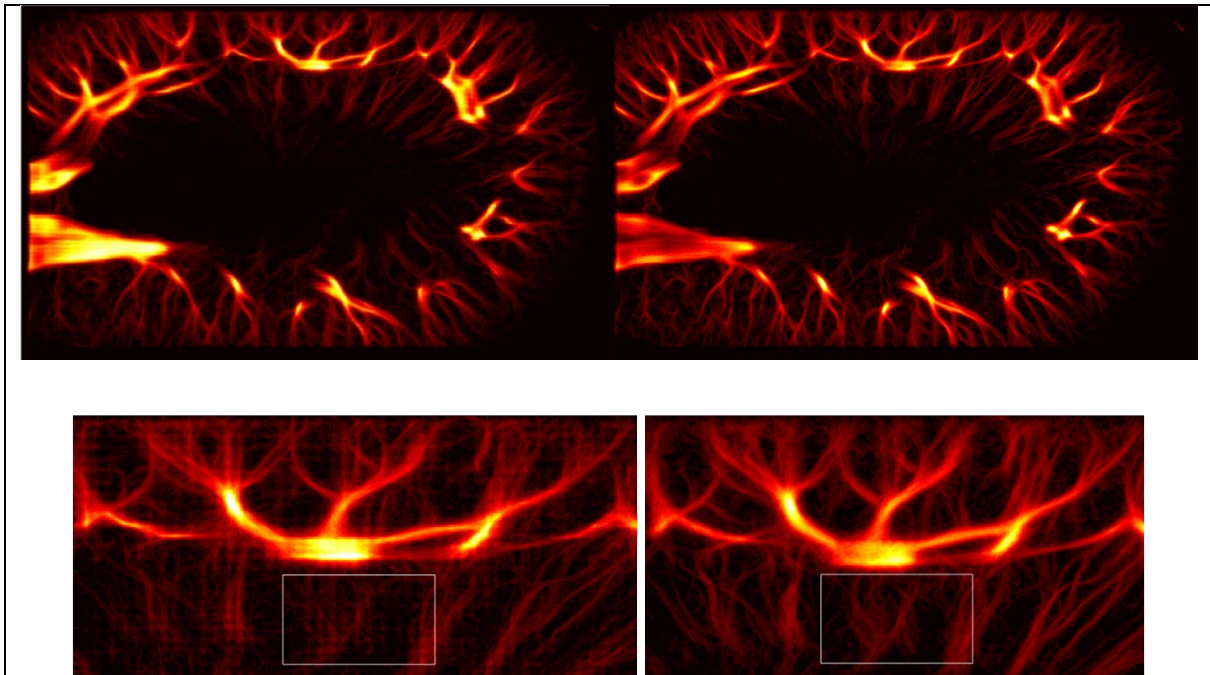
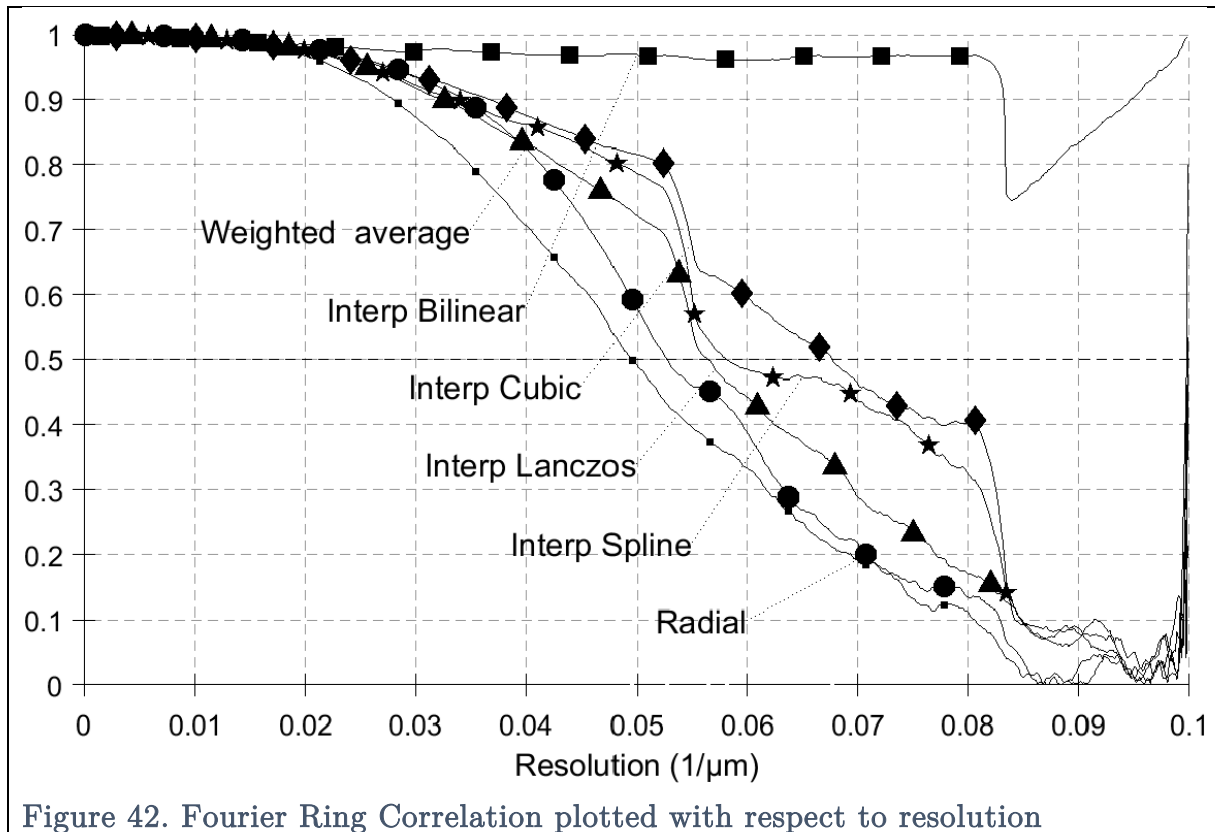


Figure 41. ULM performed on a rat kidney with weighted average (Left Column) and radial symmetry (Right Column) based localization

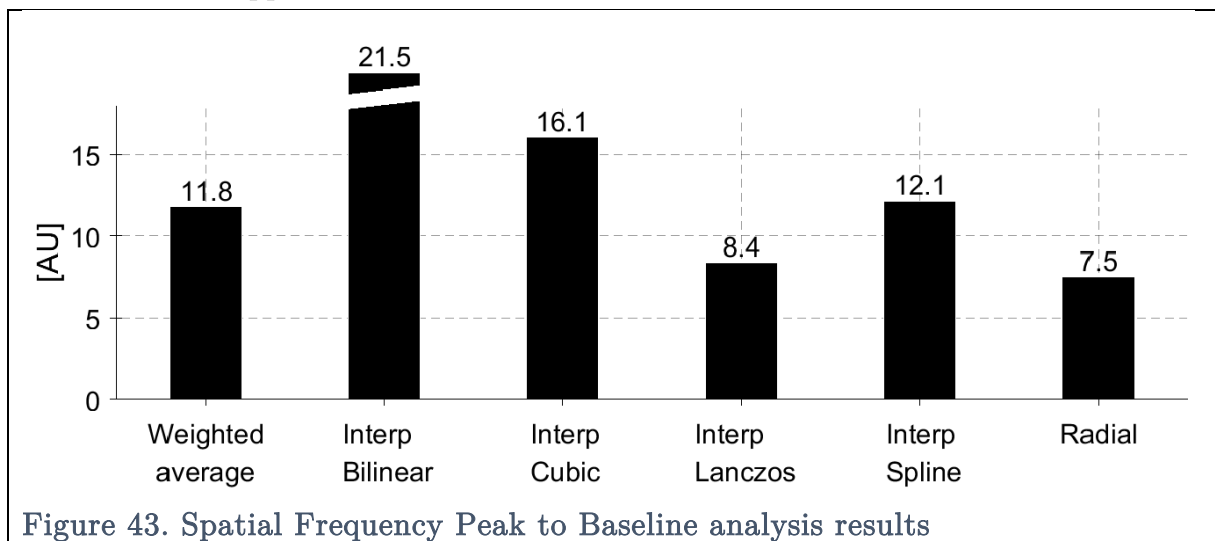
The white square focus on a region where thin vessels are present, its dimensions are $110 \times 80 \mu m$. In that particular area, we can see the sharper detail brought by radial symmetry because of the attenuation of the grid effect

For example in the rat kidney, we can see a considerable improvement in the definition of the small vessels. Less grids are present in the image and sharp delineation of vessels helps us identify the underlying structure of the vasculature. Looking closely, we can see that the ends of the branches wrap around areas with no visible vasculature. We hypothesize that these could be areas where glomerules are present but lack resolution to confirm this.

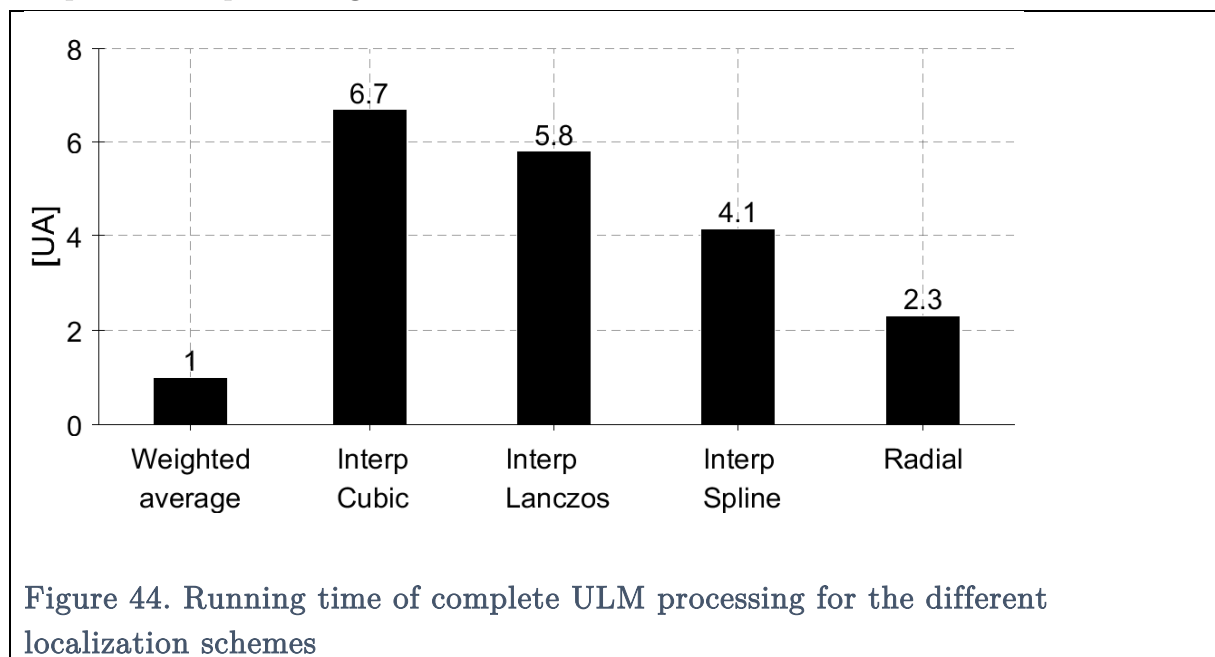
The Fourier Ring correlation results are presented in (Figure 42). This metric points out the weighted average and bilinear interpolation localization as the method with the highest spatial frequencies, with the bilinear interpolation having a FRC of one almost regardless of the resolution. Considering the preceding figures, it is clear that the FRC does not represent appropriately the spatial resolution in the presence of gridding.



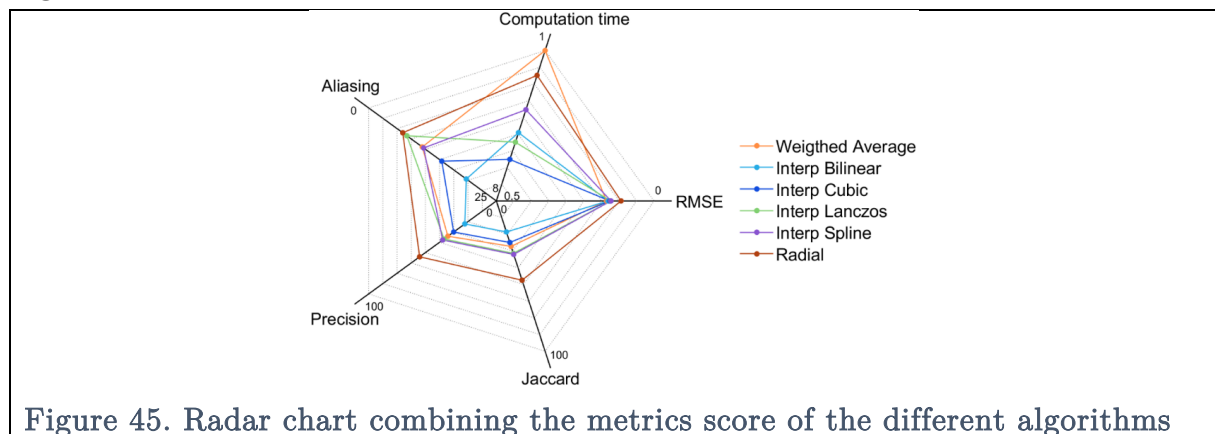
The spatial frequency peak to baseline analysis detailed in the methods section is presented in Figure 43. As what has already been seen in the visual analysis of ULM renderings, the bilinear interpolation scheme fares worse when it comes to gridding. The cubic interpolation also has a large score that is in line with what was observed. The spline and weighted average seem to have the same level of gridding. The radial and Lanczos interpolation scheme come out on top with values almost 3 times less than the worst scheme. The previously made observation that radial symmetry has less sharp vessels does not appear in our measure.



Finally, we have compared the running time of the different algorithms. As we have mentioned in the introduction, the original idea behind the work exposed here was to prepare the field for 3D ULM. As volumes weigh a lot more than images and running time increases with data size, the goal was to have a fast running algorithm yielding good quality results. The fastest algorithm was the weighted average, running in under 3 minutes for 190,000 images including filtering and tracking. The radial symmetry based is the second-fastest. The slowest running algorithm is as predicted the cubic interpolation which takes 20 minutes to run. We compared the running times with respect to the weighted average and compiled the result in Figure 44. Running time of complete ULM processing for the different localization schemes.



Finally, to help the field compare and choose an algorithm for localization, we have produced a radar chart combining all the previous metrics. The chart is drawn in Figure 45



II.6 Discussion

II.6.1 Universal Framework

The universal framework developed has allowed rendering ULM images much quicker than the conventional sequential algorithm used in other publications. The main advantage of this beyond faster ULM results is that it allowed us to test many parameters in a small amount of time. For 3D imaging especially, it was crucial to reduce the computation times. If we were to use the sequential process with the fast weighted average method, localization and tracking alone can take up to 14 hours. As the whole process has in between 6 to 12 parameters, running a combination of those is time expensive. The idea is to shorten the time to run the process as much as possible. In the end, a combination of fast calculation and reducing the size of the dataset was applied. We've seen that a dataset of 40 000 images is enough to give an idea of the impact of parameter modification for both localization and tracking.

In the case where the computers on the echographs are lacking computational power, we advise transferring radiofrequency data directly to the hard drive. Doing this allows bypassing the beamforming process which can take too much time to allow parallel execution with transfer. This parallel execution is usually put in place for 2D data as such: RF data is transferred on the DAQ cards, then on the RAM. As soon as it reaches the RAM, it is transferred to the GPU RAM and beamformed. It is then retransferred to the RAM and saved to the hard drive. While this is done, RF data continues to be transferred from the DAQ cards to the RAM continuously. For 4D imaging, this is impossible as the computers are aging and beamforming of 185 volumes takes about 4 minutes. If newer GPUs could be used (such as the NVidia GeForce RTX 2080 Ti), the beamforming time could be decreased to as low as 16 seconds. The alternate scheme where RF data is transferred and saved without prior beamforming is thus chosen.

For filtering, we've seen that several schemes can be applied. Either SVD alone is used or it is used after a high-pass 2nd order Butterworth filter. SVD filtering has been demonstrated to efficiently filter out tissue from microbubble signal (Errico et al., 2015a), but because it relies on principal component analysis, it is hard to predict how slow-moving microbubbles or high density of microbubbles will be affected by filtering (Heiles et al., 2019; Hingot et al., 2019). Using a highpass filter before operating the SVD allows minimizing the number of vectors removed and thus decrease the impact of such an unknown parameter.

In (Errico et al., 2015a), a method to localize the center of the microbubble with an interpolation of the desired super-resolution factor was proposed. While this allows to work directly on beamformed images, the interpolation method is costly both in time and processing power for 2D analysis. For 3D, it becomes unmanageable as the data interpolated by a factor of 10 sees its size increases by a factor of 1000. Interpolating one volume of 11.9 MBytes (0.2 second of acquisition at 500 Hz imaging rate) would yield 11.9 GBytes of additional data. As we are required to do the ULM process on thousands of volumes, this technique becomes rapidly memory expensive. A novel localization technique was thus implemented. (Sage et al., 2018) recently published an extensive paper about the different techniques available to perform Single Molecule Localization Microscopy and rated the different algorithms. As we want to lower computational cost as much as possible and have an easy to package tool, it seemed according to this study that QuickPALM is a good candidate for translation to 3D ULM.

The original QuickPALM algorithm is coded in Java for the ImageJ platform (Schneider et al., 2012). It is readily usable for 2D images if one chooses to work with images in a graphical format. As we choose to work with beamformed data we could also work with images but we would lose the information of phase present in the IQs. We ported the QuickPALM algorithm from Java to Matlab in 2D at first and then extended it into three dimensions for *in vitro* experiments (Heiles et al., 2019). The drift correction filter based on fiduciary landmarks was abandoned in our implementation of this algorithm in the 3D *in vitro* study because the *in vitro* technique is not subject to motion and also because no fiduciary landmarks were present in the gel. We worked in Matlab to make this code as fast as possible using parallelization of the mathematical operations to take advantage of multiple cores CPUs. We decided to use the method based on the calculation of the center of mass of the low-resolved bubble through its intensity profile to carry out our first demonstration of the feasibility of 3D ULM using a matrix array.

This technique while being more manageable also proves to be considerably faster (we calculated in 2D that for 75000 frames, the interpolation approach takes 12 hours 30 minutes on a high performance 4 cores processor PC, Intel i7-6700 at 3.4 GHz and an NVIDIA GeForce GTX1080, while the weighted average method takes only 2 minutes 40s).

After developing the weighted average method and proving that 3D ULM was feasible in a reasonable amount of time and with “conventional” computers, we tried to improve our localization method. Rather than using the centroid approach, we chose to go back to the determination of maximum intensity. As we want to retain calculation time to a minimum, we wanted to have a method that worked on beamformed images of

bubbles without any need for interpolation. Our attention turned to intensity gradient approaches such as the radial symmetry based localization.

The advantage of the radial symmetry algorithm is that even though the mathematical calculation can seem intricate, the actual operations needed can be rewritten with a simple matrix approach. This makes it perfect for Matlab. As demonstrated above, less than 20 algebraic operations are needed to deduce the coordinates of the center in 2D including the initial guess. While it is a lot more than the 4 operations for the centroid method, it is still quite low. From the *in silico* results, it is clear that radial symmetry localizes the center of the scatterer more accurately in the X-axis. In the Z-axis, the gain is clear from the weighted average but absent compared to interpolation schemes. However, the speed gain is such that while one could use a hybrid approach for 2D imaging, computation time becomes so critical for 3D that interpolation is not something we recommend.

II.6.2 In silico

In Figure 34, we have compiled the errors made by the localization algorithms as histogram bins. The advantage of this visualization is that it allows seeing the distribution symmetry. For the radial symmetry based, we can see that the lateral error distribution is symmetrical and the peak is sharp, meaning that its overall error in this direction will have a low standard deviation $\sigma = 0.04$, and that its error will be low. This is probably due to diagonal calculation of the gradient. However, we can see that for the axial error, none of the distributions are actually symmetric and this is due to the PSF not being symmetrical in this direction. This error due to asymmetry can be compensated for because it is a static error and will be the same wherever the point like scatterer is simulated. The distribution though will never be symmetrical.

Another interesting aspect brought by this distribution point of view is the peaks localized in the cubic, Lanczos and spline interpolation schemes for the axial error. They are periodic with a frequency corresponding to a $\frac{\lambda}{10}$ grid. We hypothesize that this is due to the grid chosen for interpolation as $10 \times (N_z \times N_x)$. It can not be seen in the bilinear as its kernel is given by a simple linear regression and can not have a negative second-order derivative.

The statistical indices in Figure 36 confirm that the radial symmetry based localization scheme is more precise than other schemes. This is due to a low localization error, and as such a high cardinality of true positives. As the total number of TP+FN is finite, this also means that the sensitivity index is high. For the weighted average scheme,

we measure a high precision and high sensitivity although its localization error is the highest among the schemes (see Figure 34). Figure 35 gives us a glimpse into why this happens: the TP and FN values are almost identical to the best interpolation schemes. Comparing weighted average and cubic interpolation who have almost the same standard deviation, directional errors and RMSE, we can go further into our analysis. The distribution axial error of the cubic interpolation has $\frac{\lambda}{10}$ peaks but the distribution of the weighted average is smooth. That means that there will be jumps in the localizations. We hypothesize that this will cause a significant increase in the number of false negatives and decrease in the number of true positives.

The efficiency index Figure 37 aims at combining the numerical and statistical metrics. As we have seen in the previous paragraph, the metrics are not always easy to comprehend and do not give the same performance ranking. Summing up the Jaccard indices and the RMSE into one index is helpful to discriminate the algorithms. In the end, the radial symmetry localization algorithm comes out on top with an efficiency twice as high as the second bests. The weighted average fares better than the cubic interpolation because of a higher Jaccard index.

The grid effect is particularly true for interpolation-based localization. It is very similar to quantization in its form and we hypothesized that it is due to low SNR in certain regions. To verify our hypothesis, we decided to use the bilinear interpolation scheme for localization, a kernel that can not localize bubbles precisely. This scheme will always return the center pixel of the bubble as it is based on linear interpolation and will identify the maximum value as the center pixel. We can see that using this scheme, massive gridding is produced even though this effect is corrected by the tracking algorithm. This means that in other interpolation schemes, gridding comes from a reprojection of the localized center towards the center of the original pixel grid. It can be linked to low SNR in certain regions following this line of thought : if SNR is low, the FWHM of the intensity decreases so much that not enough information is present in the profiles to perform accurate interpolation or localization. The algorithms thus tend to calculate a very low value of the shift in the direction of low SNR and all the positions align along that. This is confirmed by looking at where aliasing happens in the Lanczos and spline interpolation scheme. In the large vessels, the number of events is sufficient to compensate that effect, but for smaller vessels, the density of microbubbles is too low and the grid effect pops up again. This is especially true in the spline scheme where the finest vessel ($5 \mu\text{m}$) with a $\frac{\lambda}{10}$ variation in the axial direction. One interesting approach to confirm that line of reasoning would be to simulate more particles in that vessels and

implement the spline interpolation scheme with different interpolation factors. *In vivo* the interpolation factor depends on the maximum theoretical resolution attainable, and as such, we advise that these values are matched.

This grid effect can either be corrected by applying a Gaussian kernel to the final image but will blur structures or by smoothing the trajectories of the bubbles to mimick an anti-alias filter. The latter method is preferred as it retains image sharpness.

Fortunately for us, it seems that this effect is considerably lowered in the radial symmetry based localization. By using information along the diagonals, it seems the centers are more uniformly distributed in the SR pixel than for other interpolation. The quality improvement brought by radial symmetry based localization in 2D imaging alleviates all temptation to use the other algorithms presented.

II.6.3 In vivo 2D

Figure 39 shows the ULM renderings of a rat brain *in vivo*. While it seems that most renderings are equivalent when looking at a global image, the zoomed-in version in Figure 40 shows many differences. The gridding confirms what was observed *in silico*. The spline and Lanczos interpolation seem to have very sharp delineation of the vessels whereas the radial symmetry based ULM has many small trajectories going in and out of the most intense vessel. The first impression when looking at that image is that radial symmetry localization has more noise than its interpolation-based counterpart. However, the *in silico* metrics tell us that the radial symmetry based localization is more sensitive and more precise, meaning that there are more correctly localized bubbles in the radial symmetry ULM rendering. It is confirmed by looking at the total number of particles localized (see Table 1), where the increase in number of bubbles localized in the radial symmetry based algorithm is 21%. We thus conclude that the small trajectories in between vessels are also small vessels that can represent the capillary bed.

The index devised to measure the grid effect seems to work well as it is confirmed visually : no gridding is present in the images with a low index.

The Fourier Ring Correlation measure of the resolution is a metrics used in the optics field (Banterle et al., 2013). In our case, it identifies the localization scheme producing the worst images as the one with highest resolution. We think that this is due to the grid effect. The spectral content of a highly gridded image is large as it contains many spatial harmonics. In opposition, the spectral content of an image with a smooth intensity distribution is lower. As such, the bilinear interpolation has an almost constant Fourier Ring Correlation value, giving it an absurd infinite resolution. The cubic interpolation scheme FRC has a slightly more realistic profile and has a theoretical

resolution of $16\ \mu\text{m}$. The spline-based interpolation, on the other hand, is $19\ \mu\text{m}$. Considering the quality of the images generated by these two different schemes that contradict these results, we deem the FRC unusable in our implementation.

The time factor which was measured with respect to the fastest algorithm is critical to fast testing of many different parameters. If the algorithm of localization runs for tens of hours before being able to deliver a full image, changing parameters and waiting for the result will take days. This becomes critical in 3D as the third dimension makes everything longer. In our team, we chose to give priority to speedy calculations. That meant that in 2D, it only takes us 3 minutes to perform full ULM on 192,000 images. This implementation appears much faster than other algorithms used across the world. It could improve the applicability of ULM, by allowing a simultaneous acquisition and reconstruction. In a clinical setting, that also means that the practitioner does not have to wait for its result and can either make another image in a matter of minutes or deliver his diagnosis.

II.7 Towards better imaging : applications

Thanks to the improvement brought by the novel algorithms for localization and tracking and to the universal framework implemented, successful applications for 2D and 3D ULM were found in the lab. Through collaborations, we have managed to image brain, kidneys, and tumors in mice, the spine in rats, kidney, heart, and pancreas in rats, chicken embryos, and even brought our expertise along to the first transcranial ULM imaging of the human brain.

Vincent Hingot worked on making 2D ULM a quantitative tool to assess ischemic stroke lesions and consequences in mice. The model of thromboembolic stroke was used, and rtPA was then injected to treat the stroke. As a result, ULM was used transcranially to look at damaged portions of the brain and identify biomarkers [Hingot et al, under review] (see Figure 46).

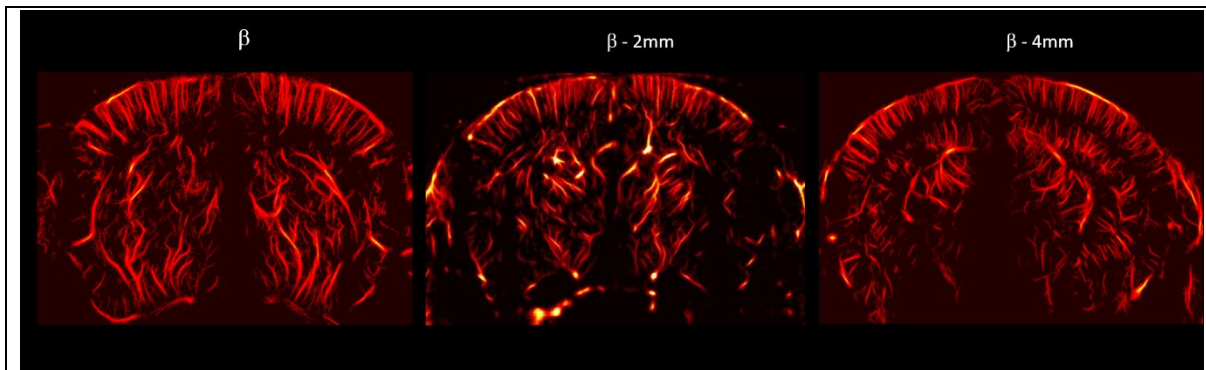


Figure 46. ULM imaging of the brain in mice

Three different Bregma planes were acquired in the mice with a probe centered 15MHz

In our quest to image vasculature and anatomical details, we tried together with Vincent Hingot and Pauline Lopez (a pediatric surgeon) imaging the Langerhans islets in a rat's pancreas. The pancreas was exposed out of the rat's belly and set on an acoustic absorbing material. ULM managed to image the large arteries and veins as well as small vasculature but failed to reveal smaller vessels and Langerhans islets. The resolution gain provided was not as big as expected as the motion was too high and the structures too small even with a motion compensation scheme.

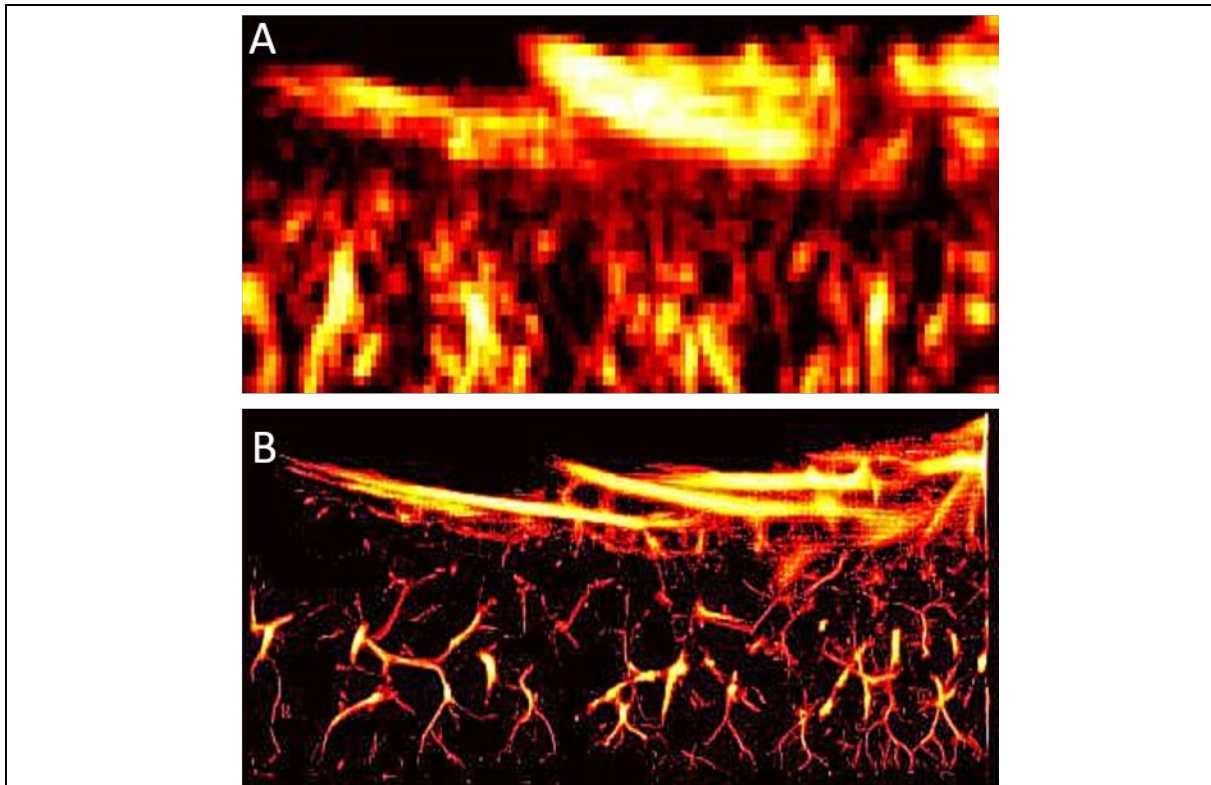


Figure 47. Ultrafast Doppler and ULM performed in a Rat's Pancreas

- a) Ultrafast Doppler reveals the large arteries and veins feeding the pancreas
- b) ULM shows the large vessels but also the small microvasculature. However, it seems to fail to image as small vessels as in the brain.

The main health-related questions of the century are cancers, cardiovascular diseases, and diabetes. In all those pathologies, the microvasculature is deeply affected and people started investigating how ULM could improve characterization of the vasculature in various models. In our team, the ULM algorithm exposed here was used to image a tumor implanted in mice were used to investigate the efficiency of drug delivery by nanodroplets [Teston et al, in prep].

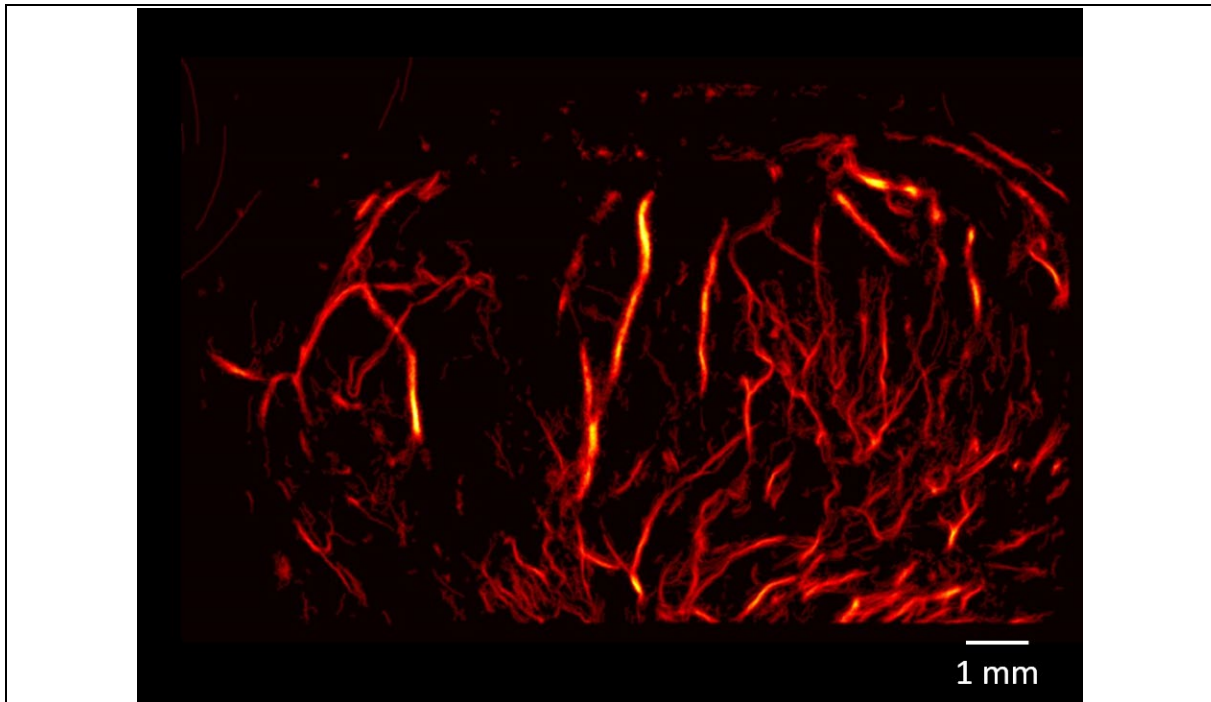


Figure 48. ULM imaging of tumor in mice

ULM in mouse tumor reveals chaotic architecture, microaneurysms, tortuosity and bypasses (Teston E et al, In prep). Tumors were implanted in the back of the mice.

Imaging the spinal cord is also a major question in medicine as it is the gateway to the nervous system. In a study on spinal cord injury, a team used a deep learning method to perform ULM in a rat model of injured spinal cord. In our team, Sophie Pezet and Julien Claron showed that the spinal cord was also submitted to vascular coupling induced by pain. To complete the study, the ULM algorithm presented here was used in the spinal cord to describe the vascular organization and to measure the velocities where functional activation was observed.

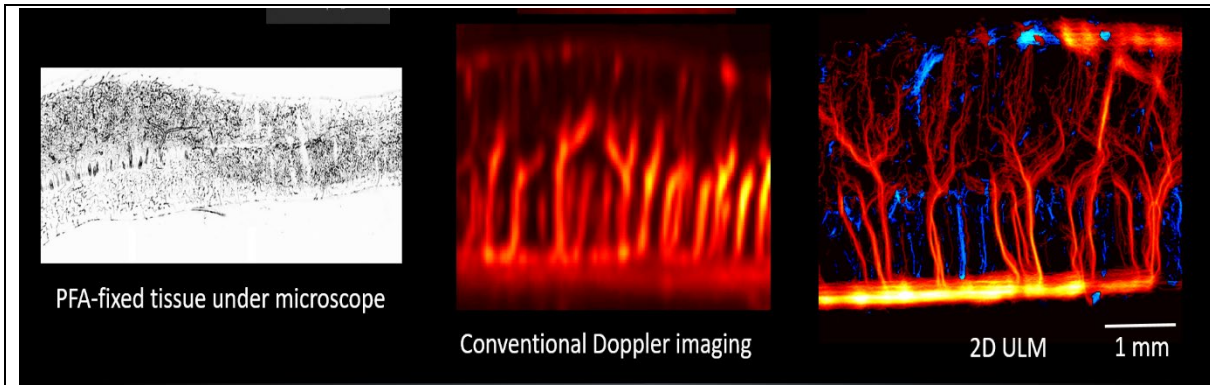


Figure 49. Spine imaging with Julien Claron, Sophie Pezet (performed by Vincent Hingot)

Spine Imaging with ULM outperforms conventional Doppler imaging in terms of resolution and for blood speed measurement. It shows a similar structure as the PFA-fixed tissue image obtained using a conventional microscope [Claron et al, in prep]

As we have seen in this chapter, access to ground truth is impossible in the rat's brain *in vivo*. However, it is possible to visualize blood cells being carried into the arteries and veins of the ChorioAllantoic Membrane (CAM) in a chicken embryo. We foresee that the chicken embryo will be an appropriate model to compare ULM to optical data obtained at the same time. In this task, I assisted an intern to develop an experimental setup to perform concurrent optic and ULM (see Figure 50). He was able to produce a first set of images. Another team is working on the same model to image tumors and has also been experimenting with ULM (Huang et al., 2019).

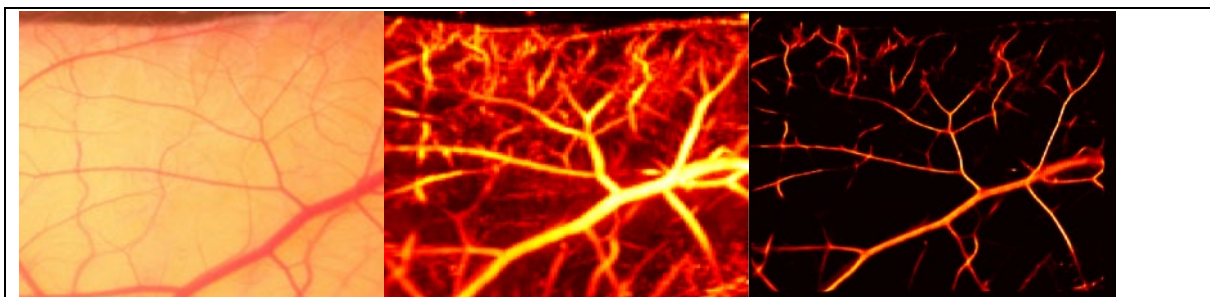


Figure 50. The Chicken Embryo Imaged with Conventional Microscope, Ultrafast Doppler and ULM

- a) Optic image of the vessels in a chicken embryo
- b) Ultrasensitive Doppler over the same vessels
- c) Incomplete ULM over the same vessels (Assaini W, Preliminary work)

- Ackermann, D., Schmitz, G., 2016. Detection and Tracking of Multiple Microbubbles in Ultrasound B-Mode Images. *IEEE Trans. Ultrason. Ferroelectr. Freq. Control* 63, 72–82. <https://doi.org/10.1109/TUFFC.2015.2500266>
- Alberti, G.S., Ammari, H., Romero, F., Wintz, T., 2018. Dynamic Spike Super-resolution and Applications to Ultrafast Ultrasound Imaging. *ArXiv180303251 Cs Math*.
- Banterle, N., Bui, K.H., Lemke, E.A., Beck, M., 2013. Fourier ring correlation as a resolution criterion for super-resolution microscopy. *J. Struct. Biol.* 5.
- Bar-Zion, A., Tremblay-Darveau, C., Solomon, O., Adam, D., Eldar, Y.C., 2017. Fast Vascular Ultrasound Imaging With Enhanced Spatial Resolution and Background Rejection. *IEEE Trans. Med. Imaging* 36, 169–180. <https://doi.org/10.1109/TMI.2016.2600372>
- Bondur, V., Grebenyuk, Y., Ezhova, E., Kandaurov, A., Sergeev, D., Troitskaya, Y., 2019. Applying of PIV/PTV Methods for Physical Modeling of the Turbulent Buoyant Jets in a Stratified Fluid 23.
- Bouakaz, A., Frigstad, S., Ten Cate, F.J., de Jong, N., 2002. Super harmonic imaging: a new imaging technique for improved contrast detection. *Ultrasound Med. Biol.* 28, 59–68. [https://doi.org/10.1016/S0301-5629\(01\)00460-4](https://doi.org/10.1016/S0301-5629(01)00460-4)
- Christensen-Jeffries, K., Browning, R.J., Tang, M.-X., Dunsby, C., Eckersley, R.J., 2015. In Vivo Acoustic Super-Resolution and Super-Resolved Velocity Mapping Using Microbubbles. *IEEE Trans. Med. Imaging* 34, 433–440. <https://doi.org/10.1109/TMI.2014.2359650>
- Christensen-Jeffries, K., Harput, S., Brown, J., Wells, P.N.T., Aljabar, P., Dunsby, C., Tang, M.-X., Eckersley, R.J., 2017. Microbubble Axial Localization Errors in Ultrasound Super-Resolution Imaging. *IEEE Trans. Ultrason. Ferroelectr. Freq. Control* 64, 1644–1654. <https://doi.org/10.1109/TUFFC.2017.2741067>
- Cikes, M., D’hooge, J., Solomon, S.D., 2019. Physical Principles of Ultrasound and Generation of Images, in: *Essential Echocardiography*. Elsevier, pp. 1-15.e1. <https://doi.org/10.1016/B978-0-323-39226-6.00001-1>
- Couture, O., Bannouf, S., Montaldo, G., Aubry, J.-F., Fink, M., Tanter, M., 2009. Ultrafast Imaging of Ultrasound Contrast Agents. *Ultrasound Med. Biol.* 35, 1908–1916. <https://doi.org/10.1016/j.ultrasmedbio.2009.05.020>
- Couture, O., Besson, B., Montaldo, G., Fink, M., Tanter, M., 2011. Microbubble ultrasound super-localization imaging (MUSLI). *IEEE*, pp. 1285–1287. <https://doi.org/10.1109/ULTSYM.2011.6293576>
- de Jong, N., Emmer, M., van Wamel, A., Versluis, M., 2009. Ultrasonic characterization of ultrasound contrast agents. *Med. Biol. Eng. Comput.* 47, 861–873. <https://doi.org/10.1007/s11517-009-0497-1>
- Demene, C., Deffieux, T., Pernot, M., Osmanski, B.-F., Biran, V., Gennisson, J.-L., Sieu, L.-A., Bergel, A., Franqui, S., Correas, J.-M., Cohen, I., Baud, O., Tanter, M., 2015. Spatiotemporal Clutter Filtering of Ultrafast Ultrasound Data Highly Increases Doppler and fUltrasound Sensitivity. *IEEE Trans. Med. Imaging* 34,

- 2271–2285. <https://doi.org/10.1109/TMI.2015.2428634>
- Desailly, Y., Couture, O., Fink, M., Tanter, M., 2013. Sono-activated ultrasound localization microscopy. *Appl. Phys. Lett.* 103, 174107. <https://doi.org/10.1063/1.4826597>
- Desailly, Y., Pierre, J., Couture, O., Tanter, M., 2015. Resolution limits of ultrafast ultrasound localization microscopy. *Phys. Med. Biol.* 60, 8723–8740. <https://doi.org/10.1088/0031-9155/60/22/8723>
- Desailly, Y., Tissier, A.-M., Correas, J.-M., Wintzenrieth, F., Tanter, M., Couture, O., 2017. Contrast enhanced ultrasound by real-time spatiotemporal filtering of ultrafast images. *Phys. Med. Biol.* 62, 31–42. <https://doi.org/10.1088/1361-6560/62/1/31>
- Eckersley, R.J., Chin, C.T., Burns, P.N., 2005. Optimising phase and amplitude modulation schemes for imaging microbubble contrast agents at low acoustic power. *Ultrasound Med. Biol.* 31, 213–219. <https://doi.org/10.1016/j.ultrasmedbio.2004.10.004>
- EDMONDS, J., 1972. Theoretical Improvements in Algorithmic Efficiency for Network Flow Problems 17.
- Errico, C., Pierre, J., Pezet, S., Desailly, Y., Lenkei, Z., Couture, O., Tanter, M., 2015a. Ultrafast ultrasound localization microscopy for deep super-resolution vascular imaging. *Nature* 527, 499–502. <https://doi.org/10.1038/nature16066>
- Errico, C., Pierre, J., Pezet, S., Desailly, Y., Lenkei, Z., Couture, O., Tanter, M., 2015b. Ultrafast ultrasound localization microscopy for deep super-resolution vascular imaging. *Nature* 527, 499–502. <https://doi.org/10.1038/nature16066>
- European Medical Agency, Committee for Medicinal Products for Human Use, 2017. Assessment report: Sonovue International non-proprietary name: sulphur hexafluoride.
- Fisher, R.B., Naidu, D.K., 1996. A Comparison of Algorithms for Subpixel Peak Detection, in: Sanz, J.L.C. (Ed.), *Image Technology*. Springer Berlin Heidelberg, Berlin, Heidelberg, pp. 385–404. https://doi.org/10.1007/978-3-642-58288-2_15
- Forsberg, F., Leeman, S., Jensen, J.A., 1991. Assessment of hybrid speckle reduction algorithms. *Phys. Med. Biol.* 36, 1539–1549. <https://doi.org/10.1088/0031-9155/36/11/013>
- Frinking, P.J.A., Cespedes, E.I., De Jong, N., 1998. Multi-pulse ultrasound contrast imaging based on a decorrelation detection strategy, in: 1998 IEEE Ultrasonics Symposium. Proceedings (Cat. No. 98CH36102). Presented at the 1998 IEEE Ultrasonics Symposium. Proceedings, IEEE, Sendai, Japan, pp. 1787–1790. <https://doi.org/10.1109/ULTSYM.1998.765296>
- Gong, P., Song, P., Chen, S., 2018. Improved Contrast-Enhanced Ultrasound Imaging with Multiplane Wave Imaging 27.
- Gramiak, Raymond, Shah, M Pravin, 1968. Echocardiography of the Aortic Root. *Invest. Radiol.* 3, 356–366. <https://doi.org/10.1097/00004424-196809000-00011>

- Grant, I., 1997. Particle image velocimetry: A review. *Proc. Inst. Mech. Eng. Part C J. Mech. Eng. Sci.* 211, 55–76. <https://doi.org/10.1243/0954406971521665>
- Heiles, B., Correia, M., Hingot, V., Pernot, M., Provost, J., Couture, O., 2019. Ultrafast 3D Ultrasound Localization Microscopy using a 32x32 Matrix Array. *Accept. IEEE Trans. Med. Imaging* 13.
- Henriques, R., Lelek, M., Fornasiero, E.F., Valtorta, F., Zimmer, C., Mhlanga, M.M., 2010. QuickPALM: 3D real-time photoactivation nanoscopy image processing in ImageJ. *Nat. Methods* 7, 339–340. <https://doi.org/10.1038/nmeth0510-339>
- Hingot, V., Errico, C., Heiles, B., Rahal, L., Tanter, M., Couture, O., 2019. Microvascular flow dictates the compromise between spatial resolution and acquisition time in Ultrasound Localization Microscopy. *Sci. Rep.* 9. <https://doi.org/10.1038/s41598-018-38349-x>
- Huang, C., Lowerison, M.R., Lucien, F., Gong, P., Wang, D., Song, P., Chen, S., 2019. Noninvasive Contrast-Free 3D Evaluation of Tumor Angiogenesis with Ultrasensitive Ultrasound Microvessel Imaging. *Sci. Rep.* 9, 4907. <https://doi.org/10.1038/s41598-019-41373-0>
- Kuhn, H.W., 1955. The Hungarian method for the assignment problem. *Nav. Res. Logist. Q.* 2, 83–97. <https://doi.org/10.1002/nav.3800020109>
- Leavens, C., Williams, R., Foster, F., Burns, P., Sherar, M., 2007. Golay Pulse Encoding for Microbubble Contrast Imaging in Ultrasound. *IEEE Trans. Ultrason. Ferroelectr. Freq. Control* 54, 2082–2090. <https://doi.org/10.1109/TUFFC.2007.503>
- Ledoux, L.A.F., Brands, P.J., Hoeks, A.P.G., 1997. Reduction of the Clutter Component in Doppler Ultrasound Signals Based on Singular Value Decomposition: A Simulation Study. *Ultrason. Imaging* 19, 1–18. <https://doi.org/10.1177/016173469701900101>
- Lin, F., Shelton, S.E., Espíndola, D., Rojas, J.D., Pinton, G., Dayton, P.A., 2017. 3-D Ultrasound Localization Microscopy for Identifying Microvascular Morphology Features of Tumor Angiogenesis at a Resolution Beyond the Diffraction Limit of Conventional Ultrasound. *Theranostics* 7, 196–204. <https://doi.org/10.7150/thno.16899>
- Lu, C.-H., Tang, W.-C., Liu, Y.-T., Chang, S.-W., Wu, F.C.M., Chen, C.-Y., Tsai, Y.-C., Yang, S.-M., Kuo, C.-W., Okada, Y., Hwu, Y.-K., Chen, P., Chen, B.-C., 2019. Lightsheet localization microscopy enables fast, large-scale, and three-dimensional super-resolution imaging. *Commun. Biol.* 2. <https://doi.org/10.1038/s42003-019-0403-9>
- Mackay, R.S., Rubissow, G., 1978. Decompression Studies Using Ultrasonic Imaging of Bubbles. *IEEE Trans. Biomed. Eng.* BME-25, 537–544. <https://doi.org/10.1109/TBME.1978.326288>
- Newhouse, V.L., Hoover, M.L., Ash, S.R., 1980. The Detection of Blood Impurities Using Ultrasound Doppler 11.

- O'Reilly, M.A., Hynynen, K., 2013. A super-resolution ultrasound method for brain vascular mapping: Super-resolution ultrasound method for brain vascular mapping. *Med. Phys.* 40, 110701. <https://doi.org/10.1118/1.4823762>
- Opacic, T., Dencks, S., Theek, B., Piepenbrock, M., Ackermann, D., Rix, A., Lammers, T., Stickeler, E., Delorme, S., Schmitz, G., Kiessling, F., 2018. Motion model ultrasound localization microscopy for preclinical and clinical multiparametric tumor characterization. *Nat. Commun.* 9. <https://doi.org/10.1038/s41467-018-03973-8>
- Ophir, J., Parker, K.J., 1988. CONTRAST AGENTS IN DIAGNOSTIC ULTRASOUND 15.
- Parthasarathy, R., 2012. Rapid, accurate particle tracking by calculation of radial symmetry centers. *Nat. Methods* 9, 724–726. <https://doi.org/10.1038/nmeth.2071>
- Sage, D., Kirshner, H., Pengo, T., Stuurman, N., Min, J., Manley, S., Unser, M., 2015. Quantitative evaluation of software packages for single-molecule localization microscopy. *Nat. Methods* 12, 717–724. <https://doi.org/10.1038/nmeth.3442>
- Sage, D., Pham, T.-A., Babcock, H., Lukes, T., Pengo, T., Chao, J., Herbert, A., Agrawal, A., Colabrese, S., Wheeler, A., Archetti, A., Rieger, B., Ober, R., Hagen, G.M., Sibarita, J.-B., Ries, J., Henriques, R., Unser, M., Holden, S., 2018. 1 Super-resolution fight club: A broad assessment of 2D & 3D 2 single-molecule localization microscopy software 25.
- Saxton, W.O., Baumeister, W., 1982. The correlation averaging of a regularly arranged bacterial cell envelope protein. *J. Microsc.* 127, 127–138. <https://doi.org/10.1111/j.1365-2818.1982.tb00405.x>
- Schneider, C.A., Rasband, W.S., Eliceiri, K.W., 2012. NIH Image to ImageJ: 25 years of image analysis. *Nat. Methods* 9, 671–675. <https://doi.org/10.1038/nmeth.2089>
- Shankar, P.M., Krishna, P.D., Newhouse, V.L., 1998. Advantages of Subharmonic Over Second Harmonic Backscatter for Contrast-To-Tissue Echo Enhancement. *Ultrasound Med. Biol.* 24, 395–399. [https://doi.org/10.1016/S0301-5629\(97\)00262-7](https://doi.org/10.1016/S0301-5629(97)00262-7)
- Siepmann, M., Schmitz, G., Bzyl, J., Palmowski, M., Kiessling, F., 2011. Imaging tumor vascularity by tracing single microbubbles, in: 2011 IEEE International Ultrasonics Symposium. Presented at the 2011 IEEE International Ultrasonics Symposium (IUS), IEEE, Orlando, FL, USA, pp. 1906–1909. <https://doi.org/10.1109/ULTSYM.2011.0476>
- Simpson, D.H., Burns, P.N., 1998. Perfusion imaging with pulse inversion Doppler and microbubble contrast agents: in vivo studies of the myocardium, in: 1998 IEEE Ultrasonics Symposium. Proceedings (Cat. No. 98CH36102). Presented at the 1998 IEEE Ultrasonics Symposium. Proceedings, IEEE, Sendai, Japan, pp. 1783–1786. <https://doi.org/10.1109/ULTSYM.1998.765295>
- Simpson, D.H., Chin, C.T., Burns, P.N., 1999. Pulse Inversion Doppler: A New Method for Detecting Nonlinear Echoes from Microbubble Contrast Agents 46, 11.

- Solomon, O., van Sloun, R.J.G., Wijkstra, H., Misch, M., Eldar, Y.C., 2018. Exploiting flow dynamics for super-resolution in contrast-enhanced ultrasound. ArXiv180403134 Phys.
- Song, P., Manduca, A., Trzasko, J.D., Daigle, R.E., Chen, S., 2018a. On the Effects of Spatial Sampling Quantization in Super-Resolution Ultrasound Microvessel Imaging. *IEEE Trans. Ultrason. Ferroelectr. Freq. Control* 65, 2264–2276. <https://doi.org/10.1109/TUFFFC.2018.2832600>
- Song, P., Trzasko, J.D., Manduca, A., Huang, R., Kadirvel, R., Kallmes, D.F., Chen, S., 2018b. Improved Super-Resolution Ultrasound Microvessel Imaging With Spatiotemporal Nonlocal Means Filtering and Bipartite Graph-Based Microbubble Tracking. *IEEE Trans. Ultrason. Ferroelectr. Freq. Control* 65, 149–167. <https://doi.org/10.1109/TUFFFC.2017.2778941>
- Song, P., Trzasko, J.D., Manduca, A., Huang, R., Kadirvel, R., Kallmes, D.F., Chen, S., 2018c. Improved Super-Resolution Ultrasound Microvessel Imaging With Spatiotemporal Nonlocal Means Filtering and Bipartite Graph-Based Microbubble Tracking. *IEEE Trans. Ultrason. Ferroelectr. Freq. Control* 65, 149–167. <https://doi.org/10.1109/TUFFFC.2017.2778941>
- Tiran, E., Deffieux, T., Correia, M., Maresca, D., Osmanski, B.-F., Sieu, L.-A., Bergel, A., Cohen, I., Pernot, M., Tanter, M., 2015. Multiplane wave imaging increases signal-to-noise ratio in ultrafast ultrasound imaging. *Phys. Med. Biol.* 60, 8549–8566. <https://doi.org/10.1088/0031-9155/60/21/8549>
- United States Air Force, 1951. Photographic Lenses.
- Van Heel, M., 1987. Similarity measures between images. *Ultramicroscopy* 21, 95–100. [https://doi.org/10.1016/0304-3991\(87\)90010-6](https://doi.org/10.1016/0304-3991(87)90010-6)
- Viessmann, O.M., Eckersley, R.J., Christensen-Jeffries, K., Tang, M.X., Dunsby, C., 2013. Acoustic super-resolution with ultrasound and microbubbles. *Phys. Med. Biol.* 58, 6447–6458. <https://doi.org/10.1088/0031-9155/58/18/6447>
- Welch, S.S., 1993. Effects of Window Size and Shape on Accuracy of Subpixel Centroid Estimation of Target Images. NASA Tech. Pap. 39.
- Wilson, S.R., Burns, P.N., 2010. Microbubble-enhanced US in Body Imaging: What Role? *Radiology* 257, 24–39. <https://doi.org/10.1148/radiol.10091210>

III

Achieving *in vitro* volumetric ultrafast ULM

III. Chapter 3: Achieving *in vitro* volumetric ultrafast ULM

III.1 Introduction to *in vitro* ULM

The main objective of my thesis was to develop a 3D ultrasound scanner for Ultrasound Localization Microscopy. I have mentioned in Chapter 1 several approaches to 3D imaging with different probes, different scanners, and different processes to reconstruct a volume. The approach we chose was to use a dedicated 3D ultrasound scanner with ultrafast capability. This should allow us to reach high frame rate, therefore, reducing acquisition time, increasing sensitivity to microbubbles, reducing destruction with respect to focused imaging, and perform velocimetry on the microbubbles in the third dimension. Moreover, a high frame rate has been demonstrated to be crucial to fast and precise ULM (Couture et al., 2018).

In this chapter, I will discuss a method to generate 2D ultrasound plane waves and detect the echoes of microbubbles moving in three dimensions. This first demonstration will be performed *in vitro*, on a wall-less flow channel in an agarose gel. To achieve this goal, we chose a fully addressed 2D matrix array probe with 32x32 elements. The combination of a 2D matrix array and a 4D capable ultrasound machine shows tremendous versatility as it is based on programmable 2D scanners and each transducer can be independently addressed. The development of ULM with this equipment would allow us to change our implementation depending on the organ we want to image, the type of imaging whether conventional or harmonic, the framerate we want to obtain, the probe we want to use, etc...

The versatility of the machine comes at higher complexity in data acquisition and processing, especially for ULM. For instance, a 32x32 matrix array means that the scanner should have 1024 independent channels for emission. In the case of the machine presented in this chapter, we have 1024 emission channels but only 512 in reception. Each emission is thus repeated twice. That means a halved pulse repetition frequency and more data to acquire and save. As we acquire radiofrequency on 1024 channels rather than on 256 in conventional plane wave imaging scanners, we generate more data per emission. That means that the approach mentioned in chapter 2 where the beamforming takes place before saving the data would help greatly in reducing transfer time and memory occupied IQ on the host computer. However, beamforming a 3D volume with 4

Chapter 3: Achieving *in vitro* volumetric ultrafast ULM

angles takes around 200 ms on the echographs computer. At 500 Hz , a volume is generated every 2 ms . That means we need to have a pause in between each block of acquisition to allow beamforming. Such a pause is too long to make that approach compatible in our setup. It was thus decided to acquire and store RF data and perform *a posteriori* beamforming. That means that a 1 s of acquisition will occupy around 20 Gb . As the ULM process requires imaging for a very long time, the data size rapidly becomes a crucial issue. The storage of data generated after an experiment would soon become a problem for us. The complexity and cost of the machine also mean that spreading its use is slow in the scientific community (only a few teams in the world have access to such a machine: Creatis/LabTau, PhysMed Paris, DTU, ...).

At first, I had to demonstrate that our approach worked and that it was possible to image, follow and track microbubbles. The easiest way to confirm that superresolution has been achieved is to image a known structure that has micrometric structure, or feature. Unfortunately, animal-based anatomical models have a high variance at that scale and thus are not the ideal way to test out algorithms. Consequently, preliminary research on superresolution is usually conducted on *in vitro* phantoms. Different models have been used:

1. A single microbubble generated at a nucleation site in water rising through the region of imaging (Couture et al., 2011)
2. Contrast agents injected in microfluidics tubes with a diameter of $100\text{ }\mu\text{m}$ (Couture et al., 2011)
3. Contrast agents injected in $60\text{ }\mu\text{m}$ diameter microchannels printed by lithography in polydimethylsiloxane (PDMS) (Desailly et al., 2015, 2013)
4. Contrast agents injected in thin-walled latex tube of internal diameter 3 mm submerged in a water bath or in two “considered to be touching” cellulose tubes (Viessmann et al., 2013)
5. A single microbubble embedded in a paraffin gel wax using a micropipette (Christensen-Jeffries and Tang, 2016)
6. Contrast agents injected inside a coiled cellulose tube with an inner diameter of $200\text{ }\mu\text{m}$ embedded in a paraffin gel wax (Christensen-Jeffries and Tang, 2016)
7. Contrast agents injected into two thin-walled cellulose capillary tubes (Hemophan®, Membrana) of internal diameter $200\text{ }\mu\text{m}$, a wall thickness of $8\text{ }\mu\text{m}$ submerged in water (Christensen-Jeffries et al., 2017)
8. Contrast agents injected into thin-walled polycarbonate microtubes (Paradigm Optics Inc., WA, USA) with inner diameters of $150\text{ }\mu\text{m}$, $75\text{ }\mu\text{m}$ and $50\text{ }\mu\text{m}$ (Lin et al., 2017)

Chapter 3: Achieving *in vitro* volumetric ultrafast ULM

9. Contrast agents injected in a tailor-made flow phantom (Gammex Inc., Middleton, WI) with a 4 mm inner diameter flow channel (Song et al., 2018a)

We have rated these different approaches with 5 criteria to make a more informed choice and grouped the results in a table for improved readability (see Table 2).

Type of phantom	Ability to demonstrate sub-wavelength separability in 3D	Contrast agents compatible	Cost	Ease of manufacture	Wall-less/impedance matching
1	No	No	Yes	Yes	Yes
2	No	Yes	No	No	No
3	Yes	Yes	No	No	No
4	No	Yes	Yes	No	No
5	No	No	Yes	Yes	Yes
6	No	Yes	Yes	Yes/No	No
7	Yes	Yes	Yes	Yes	No
8	No	Yes	Yes	Yes	No
9	No	Yes	No	No	Yes

Table 2. Summary of *in vitro* models used in the literature

The highest-rated solutions always involve using tailor-made phantoms/microcanals. The problem with these solutions is that the walls of the tubes and canals do not have an impedance coefficient matching with water and are thus visible in the image. It is possible to have this impedance match but at a higher cost and a more complex process. Another solution is to lessen the wall's reflexions by thinning the tubes.

We have decided to design our own microvessel model to demonstrate subwavelength separability in 3 dimensions with contrast agents that could be reproduced and easily manufactured.

The text below is inspired by my published article (Heiles et al., 2019).

III.2 Manufacturing *in vitro* micrometric flow phantoms

Our two limiting criteria for the phantom were that the process had to be easily repeatable and we wanted to have sub-wavelength micrometric wall-less canals. Our attention got drawn by agar as it is a hydrogel with minimal acoustic impedance mismatch with water, minimal absorption and sufficient rigidity to withheld a subwavelength wall-less canal, a rare combination. Its Young modulus can be modified by adjusting its concentration in water (see Figure 51).

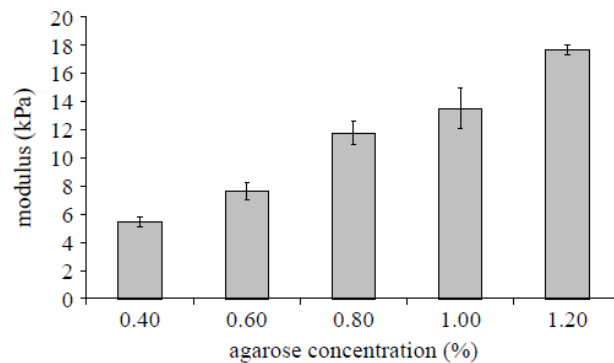


Figure 51. Young modulus as a function of agarose concentration(Ahearne et al., 2005)

Increasing the concentration of agarose in water increases the Young modulus of the final gel. This property has been demonstrated in (Ahearne et al., 2005)

This property would be useful for wall-less canals as it would allow the gel to be stiff enough to support itself if the agarose concentration is sufficiently high. We manufactured a bifurcation made of two nylon strings of $200\ \mu\text{m}$ glued together with cyanoacrylate and then separating them into a 3D structure going into two different directions. The idea behind this was to have a separating structure that is truly 3D, with the main canal branching into two sub-canals making their separation as complex as possible.

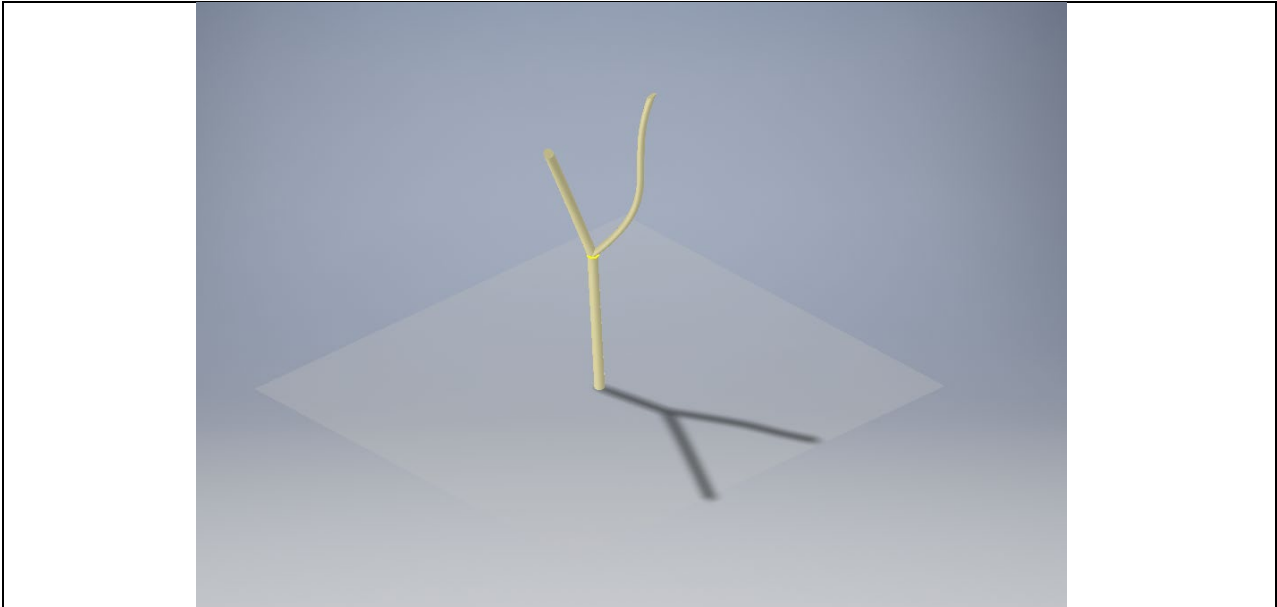


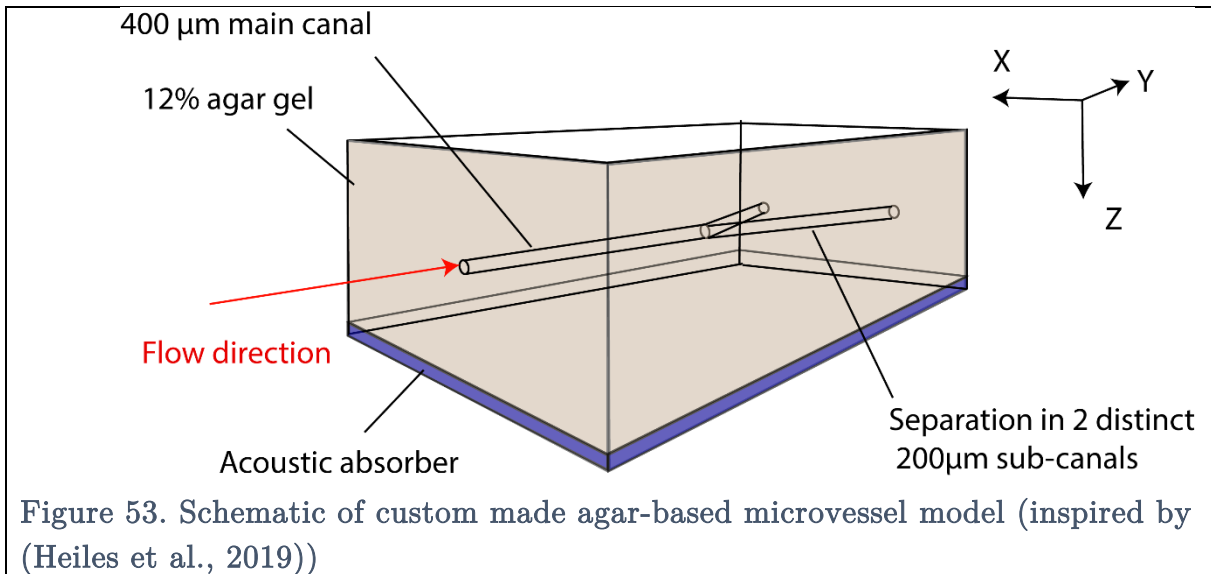
Figure 52. Modeling of the bifurcation

The two vessels are branching out of the main vessel in two different directions without staying in the same plane as the main canal. This structure is truly 3 dimensional.

The diameter of the strings was chosen to have canals of width and height similar to the imaging wavelength ($171\ \mu\text{m}$) but that could also support the weight of the agar and could be injected in. We tried using smaller strings with diameters of $150\ \mu\text{m}$, $100\ \mu\text{m}$, and $80\ \mu\text{m}$. In the first two cases, the pressure we had to apply to inject water in the canals was quite high and we feared that these would make the contrast agents explode (Talu et al., 2008) or would lead to too slow of a flow. In the last case, it was impossible to inject in the canal because of either the gel collapsing on itself or because the injecting pressure needed was too high and led to canal destruction. We thus chose the $200\ \mu\text{m}$ diameter nylon string.

12% in weight of agar powder was mixed with degassed water at a temperature of $25\ ^\circ\text{C}$. We then proceeded to heat this solution by $20\ ^\circ\text{C}$ steps with a microwave, stirring it in between cycles. The maximum temperature reached was above $80\ ^\circ\text{C}$ to melt the agar powder with water. Afterward, we proceeded to pour the gel in a box around the imprints of the bifurcation. The cyanoacrylate glue made the main canal slightly larger than $400\ \mu\text{m}$. This mold was removed after the gel solidified to allow the microbubble/water solution to flow through.

The microcanal's inlet was hooked up to a syringe whose flow rate was controlled by a syringe pump (Harvard Apparatus ® Ph.D. 2000 Infusion). The flow rate used was $1\text{mL}/\text{min}$. SonoVue ® microbubbles (Bracco S.p.A, Milan, Italy) ultrasound contrast agent was reconstituted following the manufacturer guidelines.



III.3 4D ultrafast ultrasound sequence

Our approach to ULM was previously described in chapter 2. The universal framework designed is kept and adapted to 3D ULM. A considerable portion of time and energy was spent on this crucial aspect to achieve 3D ULM during my thesis. The main issues are: data overdose, achieving high frame rate continuously or semi-continuously for a prolonged time, having sufficient signal to noise ratio than in 2D.

A customized, programmable, 1024-channel ultrasound system (Provost et al., 2014) was used to drive the 32-by-35 matrix-array probe centered at 8 MHz with a 90% bandwidth at -6 dB, a 0.3-mm pitch, and a 0.3-mm element size (Vermon, Tours, France). The 9th, 17th and 25th lines of that probe are not connected resulting in a 32x32 matrix array. We used that probe to transmit 2-D tilted plane waves at 9 MHz frequency. The ultrasound system consists of four different Aixplorer systems (Supersonic Imagine, Aix-en-Provence, France). Each system has 256 transmit channels and 128 multiplexed receive channels. All these systems are synchronized to transmit through 1024 channels and receive with 512 multiplexed channels. Each emission was thus repeated twice to sample the entire probe in receive with a pause between the transmissions of $250 \mu\text{s}$ to maximize pulse repetition frequency.

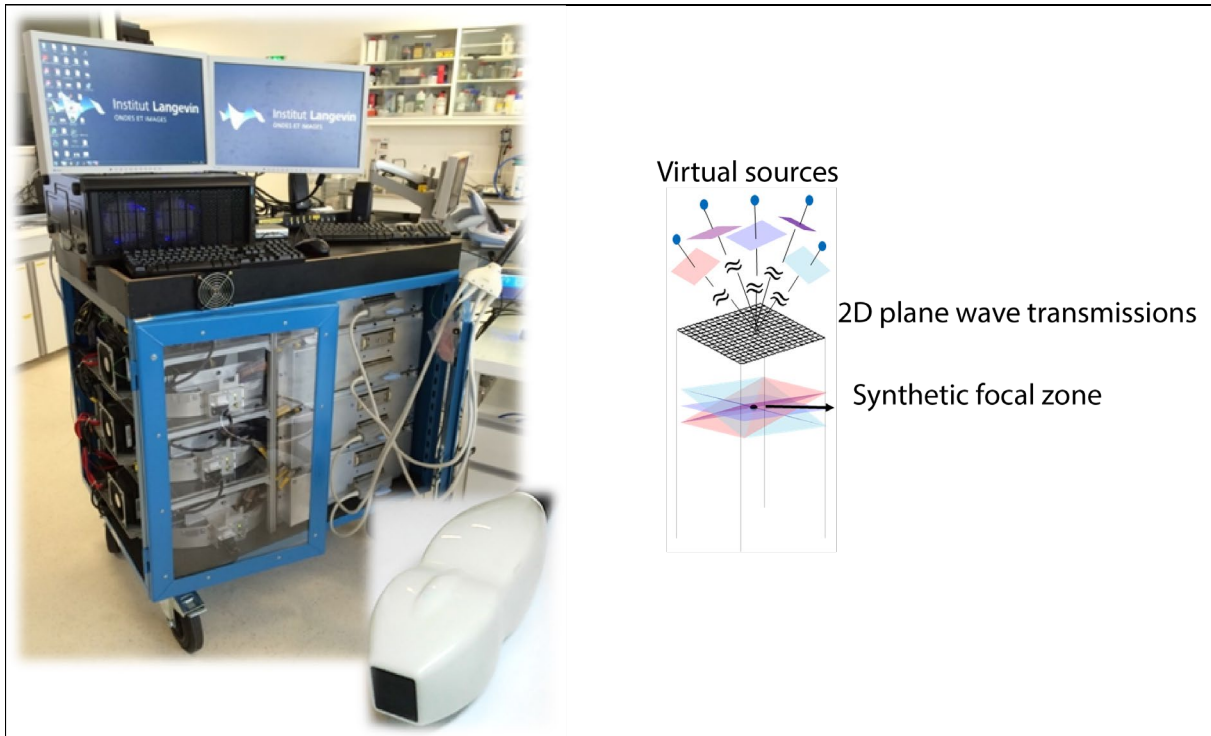


Figure 54. Picture of the 4D echograph machine with the 2D matrix array and schematics of 2D plane wave transmissions (Image inspired from (Provost et al., 2014))

The 3D ultrasound image formation is similar to what has been exposed in (Montaldo et al., 2009) but in its 3D implementation. Tilted plane waves are emitted with all transducers with delays to produce virtual sources behind the probe. 3D volumes are formed by coherently compounding multiple these emissions with varying propagation angles after beamforming (Provost et al., 2014).

In this first implementation of 3D ULM, it was decided that the simplest scheme was sufficient for a first demonstration. Instead of having a very long sequence running continuously for minutes to acquire 100,000 of images, we reduced the number of images for each acquisition to 2000. That was justified as the channel we have to image has a small diameter and should be uniformly sampled by microbubble positions fast. As there is no motion and the flowrate is constant throughout the experiment, we assumed that we could pause in between continuous block acquisition to cope with slow data transfers. The incompressible parameter of our setup is the time between emissions which is dependent on the depth of imaging and the doubled emission to have 1024 channels in reception. Other than that, we were free to customize every aspect of our sequence. We wanted to have a high frame rate to be able to follow the microbubbles and perform tracking so we set the compounded volume rate to 500Hz. This was our first limit. We experimented with various angles (from 4 to 16) and voltages (from 10 to 20 V) to

Chapter 3: Achieving *in vitro* volumetric ultrafast ULM

prevent the destruction of the bubbles while achieving highest possible SNR. Destruction was inferred from looking at the total intensity variation in a cine-loop of bubbles in a large canal. SNR was measured in the same canal with respect to noise originating from the surrounding tissue-mimicking agar gel. We found that at 4 angles and with a 12V voltage, the SNR was sufficient enough to see, filter and localize microbubbles. This gave us a second limit. To achieve a compounded volume rate of 500 Hz, we need to have a pulse repetition frequency (PRF) of 2000 Hz (and twice that because of the limited number of receive). At those transmit rates, the data transfer can be continuous for a small period of time after which it will take more time and the system will crash. To prevent this, we decided that 1 second of acquisition was enough to try to implement ULM and velocimetry. To achieve complete sampling of the microcanals set in agar however, we need to have a sufficient number of frames and localization events. That number was estimated to be around 2000. That gave us another limit regarding the number of repetitions of the acquisition. In the end, the process chosen was schematized in Figure 55. This simplified version of the universal framework proposed in the previous chapter allowed us to have more flexibility and deal with the data problem efficiently. It also allows us to reach a high frame rate of imaging during 1 second and accumulate a large number of localization events which is needed to prove that ULM with tracking and velocimetry is possible in 3D.

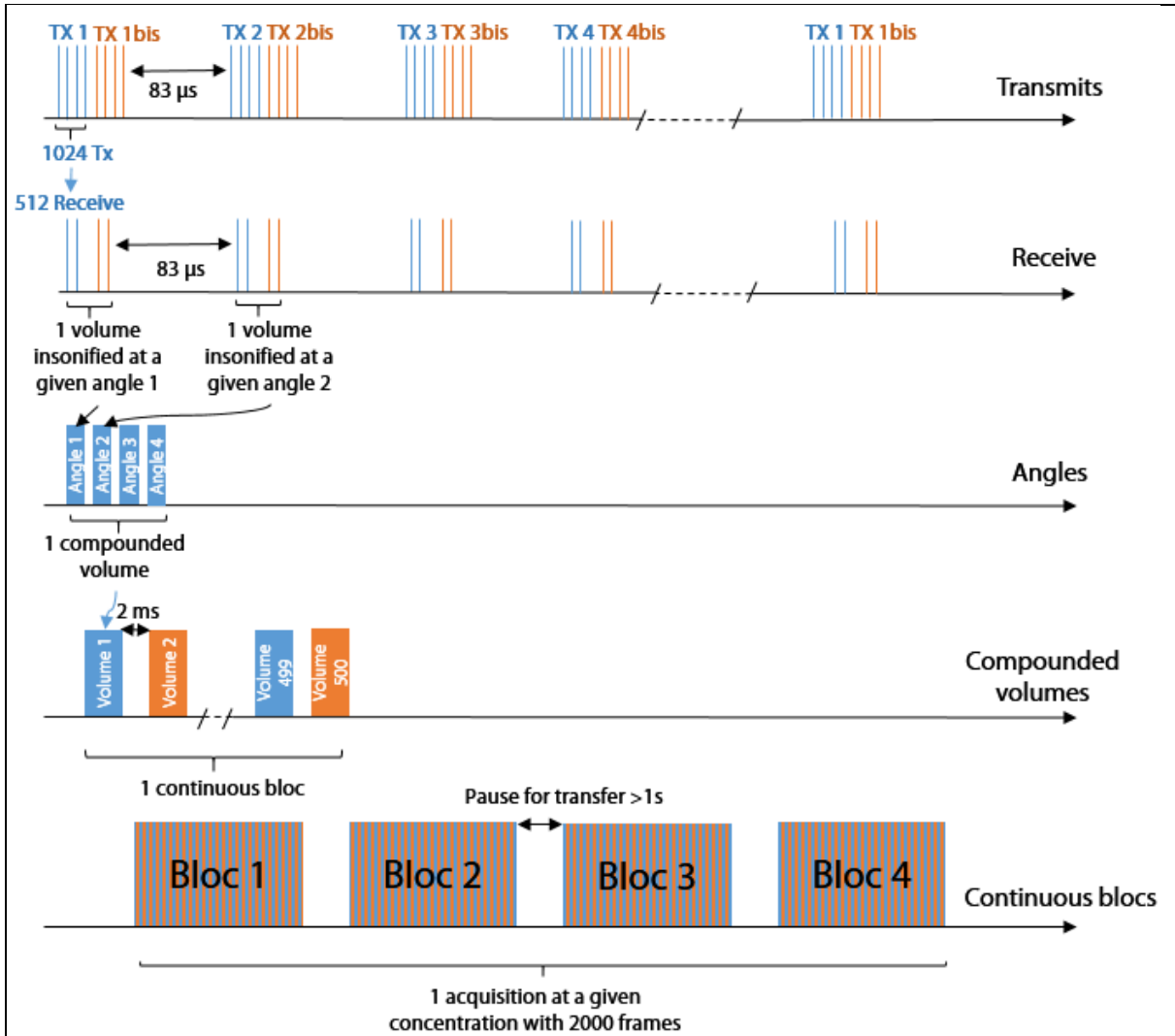


Figure 55. Schematized view of the 4D acquisition for 3D ULM *in vitro*

The 4 echographs transmit on each transducer of the matrix array simultaneously after having been synchronized through an internal clock. The transmit is repeated once to achieve full sampling in reception. Each volume in reception is composed of 1024 radiofrequency signals acquired in a two-step manner. This volume corresponds to an angled plane wave. Each beamformed volume in the end (*a posteriori* beamforming), will be a compounded version of all angles. Each of these volumes acquired continuously constitutes what we call a block, and in our case, an acquisition lasts one block.

The probe and sequences were tested out on a calibration bench with a heterodyne interferometer (Casula and Royer, 1994) to calculate both the spatial-peak temporal-average (ISPTA) and the peak negative pressure (PNP). We measured the PNP/ISPTA for 2 different depths (13 mm/25 mm), for a voltage range of [10-16] V, for a frequency range of [4-11] MHz and for [1-10] cycles to optimize the SNR/microbubble destruction ratio. A combination of 4 subsequent 2-D tilted plane waves at 9 MHz, was used. We

Chapter 3: Achieving *in vitro* volumetric ultrafast ULM

implemented a pause of 2 ms in between two imaging volumes to achieve a compounded volume rate of 500 Hz. The transmission angles were in this order $[(f(X,Z), f(Y,Z))]=[(7^\circ, 0^\circ); (0^\circ, 7^\circ); (0^\circ, -7^\circ); (7^\circ, 0^\circ)]$ with x- and y- directions parallel to the matrix-array probe. The peak-negative pressure (PNP) in this condition is -294 kPa, and the ISPTA is 385 mW/cm².

Based on the resolution model developed in (Desailly et al., 2015), it was possible to calculate the maximum resolution expected after the localization process:

$$\sigma_{\hat{y}_0} \approx 2\sqrt{3} \cdot \frac{c \cdot \sigma_\tau \cdot z_0}{\sqrt{n} \cdot L_y} \quad \sigma_{\hat{z}_0} \approx \frac{c \cdot \sigma_\tau}{2 \cdot \sqrt{n}}$$

Equation 1 Maximum theoretical resolution for 4D custom made programmable scanner with 8 Mhz probe

where σ_τ is the standard deviation of arrival time. This standard deviation can be either calculated with the Cramer-Rao lower bound or can be measured on experimental data as the error extracted from the distribution of residuals around the hyperboloid observed on reference echoes. We chose the latter method as it takes into account all types of sampling error. We simply imaged a needle with a tip finer than the wavelength. We recorded the echo from this point-like scatterer multiple times and calculated the residuals from these echoes around the reference hyperboloid. By averaging these residuals measurements we obtained σ_t . We then calculated σ_z, σ_y, z_0 being the distance between the array and the target, L_y the array apertures along the y-axis, c the sound speed and n the number of transducer elements used in the aperture. Similarly to σ_y we can deduce σ_x as the probe is isotropic.

On our experimental system, we measured a timing variance of $\sigma_t = 17 \text{ ns}$, thus leading to σ_z less than 1 μm and $\sigma_y = \sigma_x = 5 \mu\text{m}$. The estimation of the precision on velocities is thus at 500 Hz, $\sigma_{vz} = 0,5 \text{ mm/s}, \sigma_{vy} = \sigma_{vx} = 2,5 \text{ mm/s}$, then giving $\sigma_{vnorm} = 3,6 \text{ mm/s}$.

Delay-and-sum beamforming (Provost et al., 2014) was done a posteriori on a computer equipped with an Intel® Xeon Haswell 10-core @ 2.60 GHz, 128 GB of RAM and a NVIDIA® Tesla® K40 GPU with 12 Go of RAM. To reconstruct each voxel, the conventional delay and sum beamforming was applied to every element of the 2D array, thus making it a 3D DAS beamforming. The process was performed using Matlab 2017b with CUDA implementation (Mathworks Inc. Cambridge MA, USA) to beamform on the Tesla K40. The advantage of using a GPU is that each pixel is assigned to a CUDA

core and all operations are done in parallel. Each block (500 volumes), was beamformed at half wavelength in all directions. It took 45 seconds for each block including saving time. The same computer was used to implement the localization algorithm.

III.4 ULM process applied to the detection of small microvessels

After beamforming, the bubbles are still not visible because of the tissue-mimicking agar. The agar gel fabricated still contains air trapped in microholes and thus scatters signal with similar intensity as the microbubbles. This makes it impossible to distinguish the bifurcation from the agar gel on non-filtered beamformed images. To locate the bifurcation we implemented a simple pre-processing technique where we sum all filtered images of one continuous sequence and divide it by the temporal maximum intensity of each pixel as follows

$$I'(z, x, y) = \frac{\sum_{i=1}^N \text{images} I_{filt}(z, x, y, i)}{\max_i(I_{filt}(z, x, y, i))}$$

Equation 2. Filtering low concentration cases to distinguish microbubbles

This fast and simple technique allows visualizing areas where high temporal intensity gradients are located and thus the bifurcation. If the signal of a voxel is relatively constant through time, the filtered voxel will output a value close to 1. If the signal of the voxel contains one maximum, the filtered voxel will also output a value close to 1 however if the voxel contains many maxima as would be the case for a voxel through which many microbubbles are passing, the filtered voxel will output a value greater than 1 and close to the number of times a microbubble is passing through. This filter is computationally inexpensive and will reduce the memory required to visualize data as it frees itself from the 4th dimension (i.e. time). We then focused on these areas to do the 3D ULM.

After locating the bifurcation, we implemented two filters depending on the concentration on original beamformed images to filter out the phantom signal for each volume and retain microbubble signal only. The time-averaged intensity of each block was subtracted from volume data to remove non or slow-moving structures from the image. In high concentration cases, a clutter filter based on Singular Value Decomposition was implemented to better decorrelate moving and non-moving structures [(Demene et al., 2015), (Errico et al., 2015), (Desailly et al., 2015)]. 3D ULM was then applied to these images.

Chapter 3: Achieving *in vitro* volumetric ultrafast ULM

The localization process used here is based on QuickPALM (Henriques et al., 2010) and has been entirely re-implemented to fit 3D data processing in Matlab. As was previously explained in chapter 2 of this manuscript, this method determines the center of mass of the low-resolved bubble through its intensity profile. Analyzing the intensity shift and fitting a model for the point spread function on a grid with higher resolution yields the microbubble's center position in the super-resolved basis. We chose the weighted average method because it yields good results and is much faster than the interpolation schemes. We did not choose the radial symmetry based algorithm because we hadn't implemented it yet.

The local maxima were computed for each volume of each sequence in a parallelized manner. This yielded (z, x, y) triplets, along with time, corresponding to the position of particles. A first filter based on the intensity of the local maximum detected was implemented, assuming that only the maxima with high intensity correspond to microbubbles. An additional filter based on the convolution between the localized microbubble signal and a simulated microbubble was also implemented. We simulated the PSF of the microbubble with an ellipsoid model of a minor axis size of $2 \times FWHM_Z$ (Full Width at Half Maximum in the Z dimension of a microbubble), and two equal large axes of $2 \times FWHM_{X/Y}$ (Full Width at Half Maximum in the X/Y dimension of a microbubble). The FWHMs were estimated by measuring the beamformed signals of 20 microbubbles and were $FWHM_Z = 3$ pixels, $FWHM_X = FWHM_Y = 5$ pixels. The intensity of the microbubble is considered to be Gaussian distributed and the minimum acceptable value of the normalized 3-dimensional convolution is taken to be 0.6. This threshold was established, based on the inspection of detectable microbubbles on the images, as a tradeoff between the exclusion of noise points and the inclusion of microbubbles. The center of each of these microbubbles was calculated with the method explained above and this was registered as a new triplet $(z_{com}, x_{com}, y_{com})$. For a sequence, this yields a matrix containing quadruplets of coordinates (x, y, z, t) corresponding to the positions of microbubbles in the 3-dimensional basis and time without modifying the original volume or reconstructing the full super-resolved volumes.

After tracking the microbubbles with the algorithm based on the Kuhn-Munkres algorithm, we calculated the velocities of the microbubbles. It was also possible to calculate the average velocity in the canals based on the flow rate of the syringe pump and the diameters obtained in this section. With conservation of flow rate (1 mL/min) and without taking into account pressure loss, the average velocity in the main canal is 79 mm/s which assuming the flow is laminar ($V_{moy} = 0.5 \times V_{max}$) and gives a maximum velocity of 158 mm/s .

$$V_{main} = \frac{Q}{S} = \frac{Q_{main}}{\pi \times \left(\frac{D_{Lmain}}{2} * \frac{D_{lmain}}{2} \right)} = 79 \text{ mm/s}$$

Equation 3. Calculation of Main Canal Velocity from the flow rate

If we assume conservation of flow rate in the bifurcation we can write:

$$Q_{main} = Q_{left} + Q_{right}$$

$$\Leftrightarrow V_{main}(D_{Lmain} \times D_{lmain}) = V_{left}(D_{Lleft} \times D_{lleft}) + V_{right}(D_{Lright} \times D_{lright})$$

Equation 4. Conservation of flowrate in between main canal and left and right canal at the bifurcation

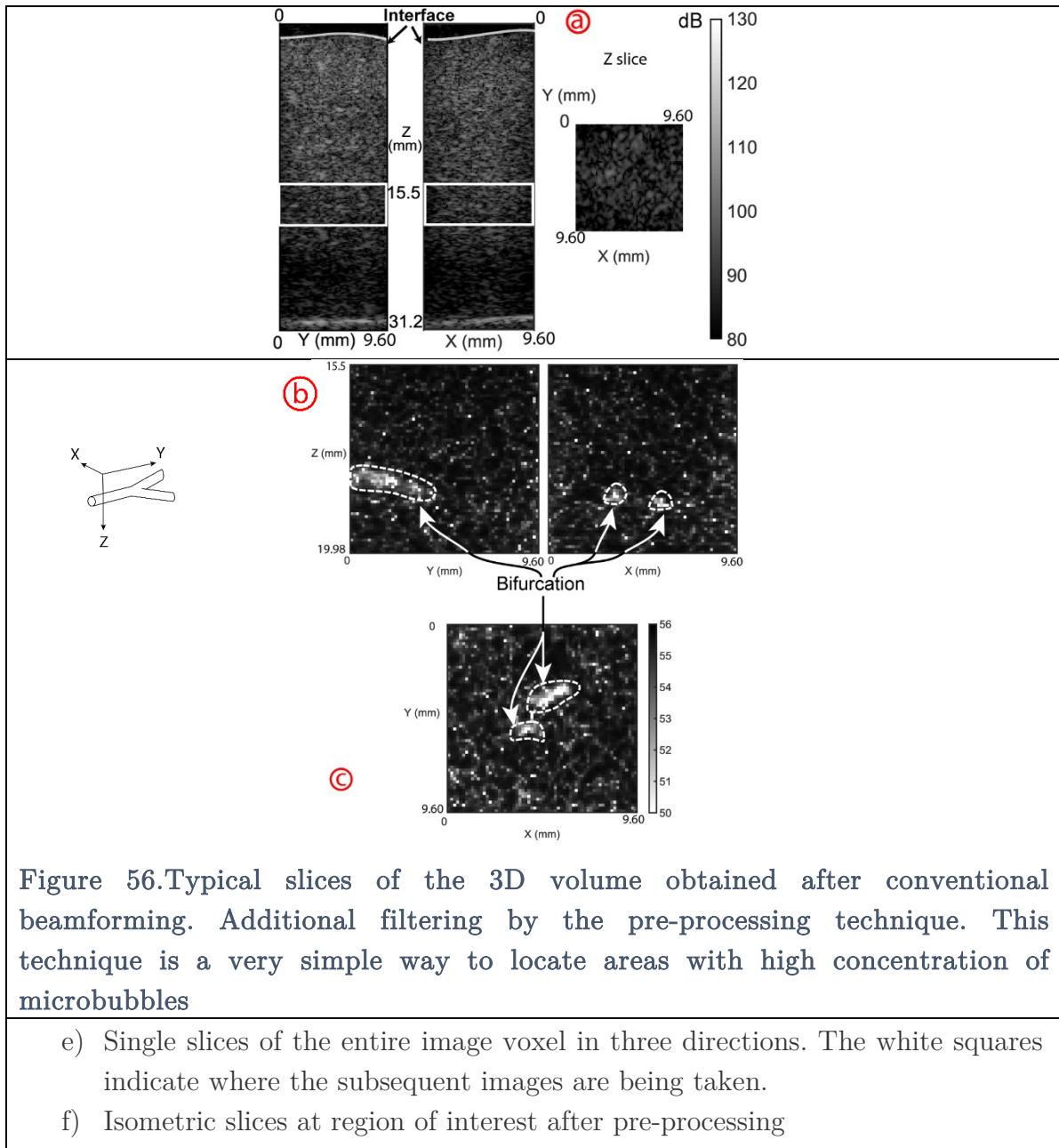
where D_L and D_l are respectively the large diameter and the small diameter for the canals.

In addition to velocimetry, the trajectories were interpolated with a spline model to achieve better spatial sampling of the bifurcation. The original points given by the trajectories served as knots to construct the break sequence according to the centripetal scheme (E. T. Y. Lee, “, 1989), by using the `cscvn` function packaged by Matlab. For each trajectory, 1 million points were calculated on its respective spline and were then resampled to obtain a uniform spatial sampling of $1 \mu m$ in all three directions. We then projected all points belonging to a section of thickness $10 \mu m$ in the Y direction. By calculating the distance between the two closest points belonging to each side canals, we can estimate a separability criterion. This measure was repeated for sections going from main to side canals.

III.5 Results

Figure 56 presents conventional beamformed images and images after filtering. A voxel in our images measures $84.5 \mu m \times 150 \mu m \times 150 \mu m$ and so the ratio of all the subsequent figures is kept according to this dimension. Figure 56 shows three slices: parallel to the main axis of the bifurcation and orthogonal to the probe plane (z, x); perpendicular to the main axis of the bifurcation and orthogonal to the probe plane (z, y); and parallel to the plane of the probe (x, y). A basis (z, x, y), was placed over the images in figure 1 and will be used in the following sections. To improve readability, the new images deduced by the way of the pre-processing were focused on the region of

interest. These images are presented in figure 2b.

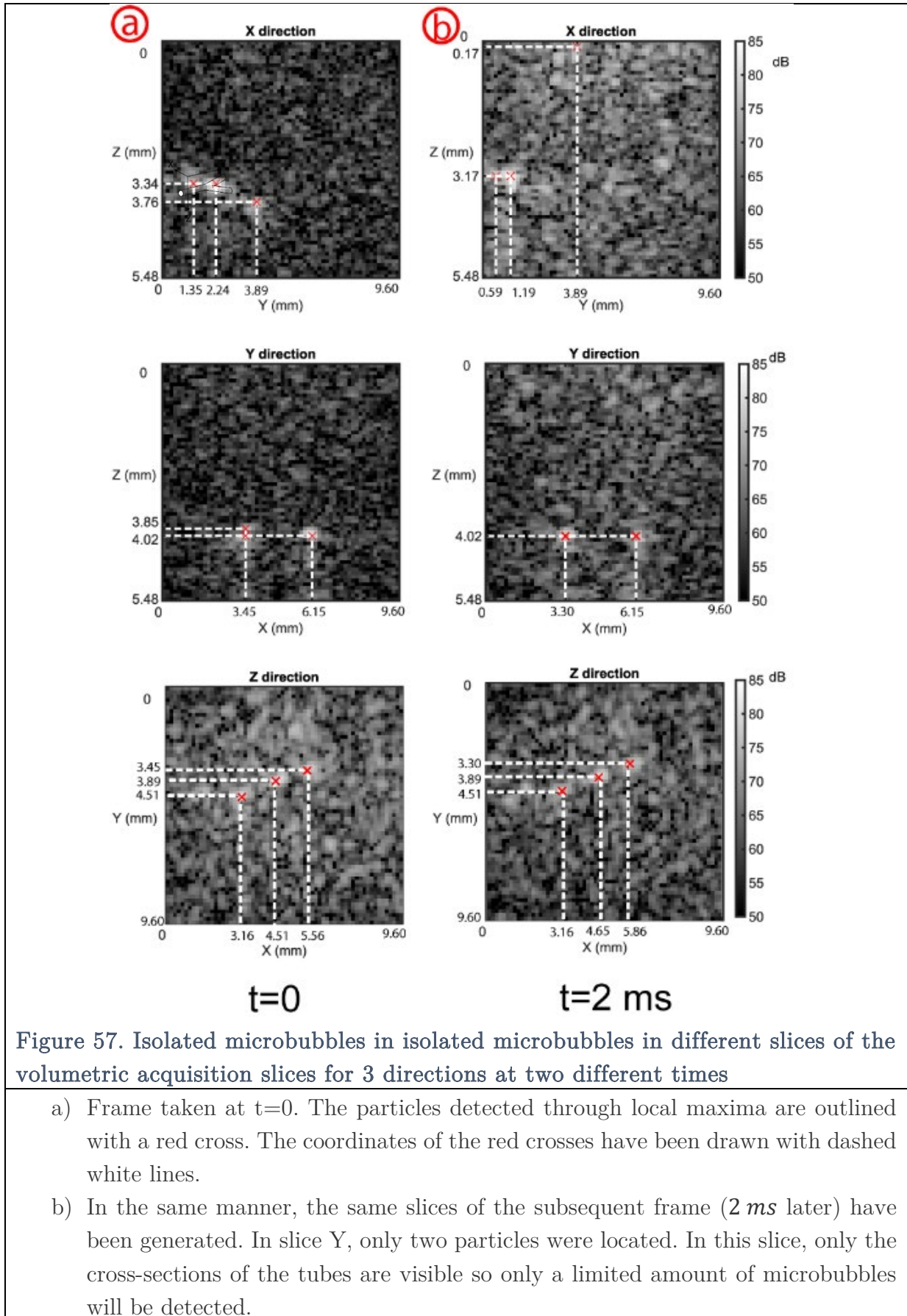


Because microbubbles appear sporadically throughout the experiment, we can locate the bifurcation by the pre-processing technique. However this does not allow to extract the microbubbles independently and track their journey due to temporal averaging. The representation of the bifurcation with this process is blurred and does not allow accurate measurement of its dimensions.

After locating the bifurcation, two different processing techniques were implemented to enhance the microbubble to agar signal ratio depending on the microbubble concentration. To visualize microbubbles in concentrations lower than

Chapter 3: Achieving *in vitro* volumetric ultrafast ULM

$1/5000^{\text{th}}$ of the Sonovue $\text{\textcircled{R}}$ vial solution, the time-averaged over a continuous sequence of 1 second was calculated and subtracted from each image. This approach benefits from a straightforward decoupling between agar background signals and microbubbles signature regardless of their velocities. However, for higher concentration, we found that this temporal averaging process, while sufficient to remove agar gel signal, also modified adjacent microbubble signals thus impeding localization. The reason why this happens is that when microbubbles are near one another (as is the case in high concentration), their signals interfere together during the temporal averaging. Rather than maximizing only the agar's intensity, the filter thus also produces high intensities where microbubbles are cluttered together. In that case, subtracting the time average to each image removes cluttered microbubbles' signal. Rather than using this filter that is based on intensity over time, we decided to use the singular value decomposition (SVD). Because SVD has been proven to be able to decorrelate tissue, blood and microbubbles based on their spatiotemporal signature (Demene et al., 2015), (Errico et al., 2015), it is less sensitive to high concentration or microbubble cluttering. This SVD filter worked by removing the first few most energetic eigenvalues in the singular value decomposition. Depending on the concentration, either the [30,20,15] most energetic eigenvalues were removed because they represent highly spatio-temporal coherent signal. The higher the concentration, the less eigenvalues were discarded. The images for low concentration obtained are shown in Figure 57. The red crosses pinpoint where microbubbles are.



Chapter 3: Achieving *in vitro* volumetric ultrafast ULM

The triplets $(z_{com}, x_{com}, y_{com})$ obtained in the methods section are plotted in a 3-dimensional space to reveal the bifurcation in the super-resolved basis (Figure 58 left column). These triplets are defined for each volume through the entire duration of acquisition. On Figure 58, we plotted the particles localized on a super-resolved basis for two different concentrations using 2000 successive volumes (4 seconds). Pre-tracking, the number of microbubbles detected for low concentration is 5 314, and 29 351 for high concentration. Post-tracking, the number of microbubbles detected for low concentration is 525, and 393 for high concentration.

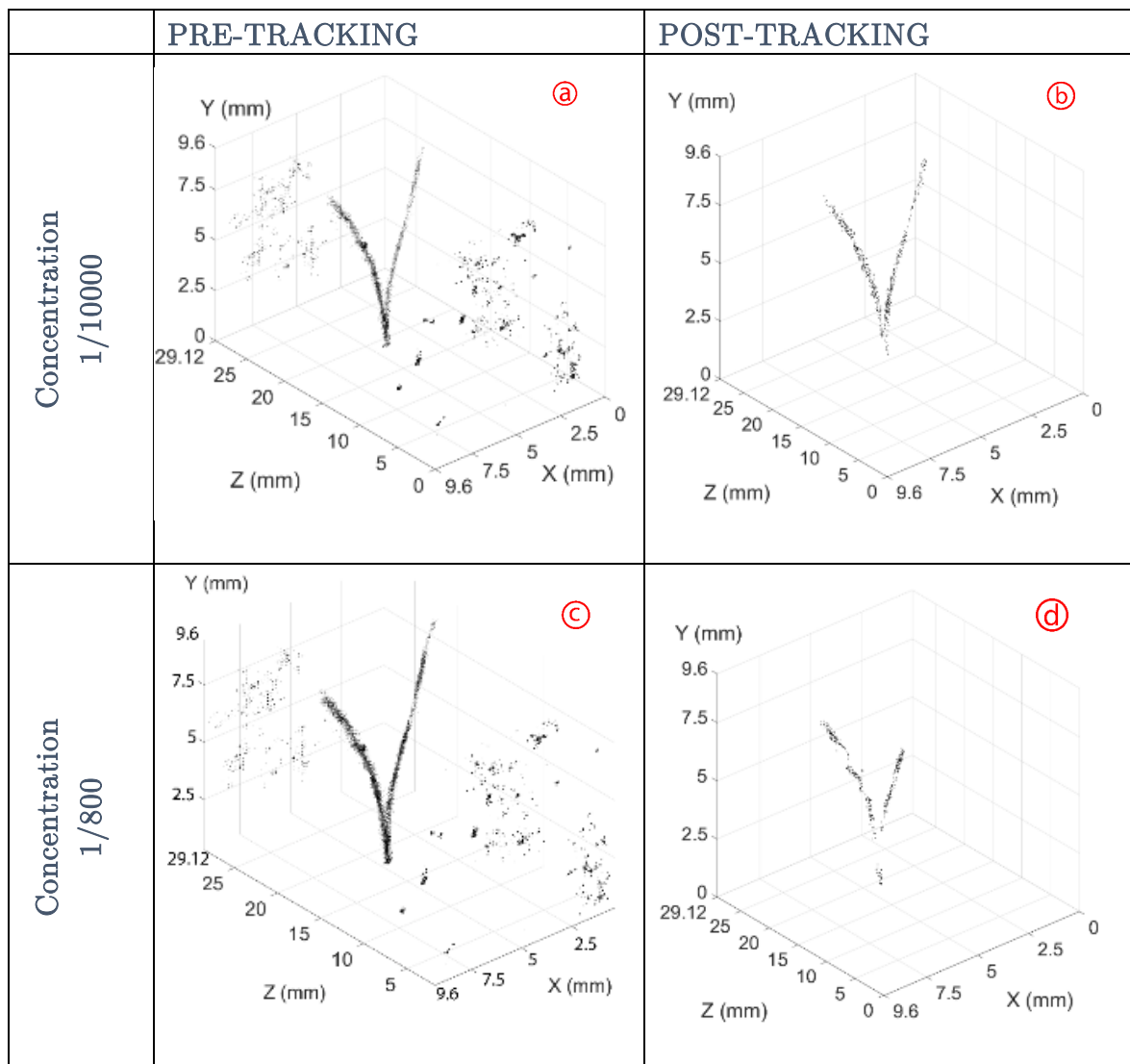


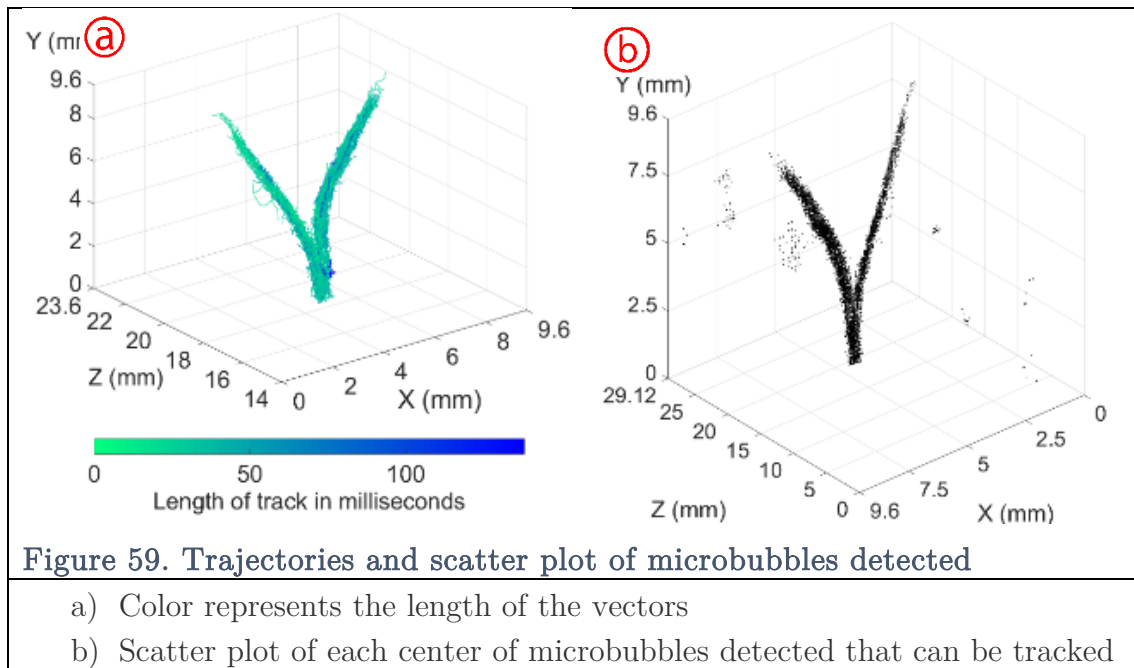
Figure 58. Cumulated scatter plot of each center of microbubbles detected for different concentrations pre and post-beamforming

- a) c) are without tracking
- b) d) are exploiting tracking algorithm.

The concentration used are 1/10000 for (a,b) and 1/800 for (c,d).

Chapter 3: Achieving *in vitro* volumetric ultrafast ULM

Microbubbles flow continuously in the canal and can be followed on ultrasound images as illustrated in Figure 57. By implementing the 3D tracking process previously discussed on the center of the microbubbles, we recovered the independent trajectories of the localized microbubbles (Figure 59). Each line is the trajectory of one microbubble. The color of each line is encoded depending on the duration of the track. Most of the tracks follow the path of the canals and are relatively short in duration: the average track duration is 32 ms, with a standard deviation of 14 ms and the longest trajectory is 138 ms.



Thanks to the additional information given by the directivity of the trajectory, we implemented a filter to keep the microbubbles following the main direction of the flow. Positions obtained after this additional filter are plotted in Figure 59. By doing these operations on all of the volumes acquired, it was possible to obtain a large number of microbubbles positions for 6 000 volumes ($n=288\ 389$ positions) which correspond to our final image.

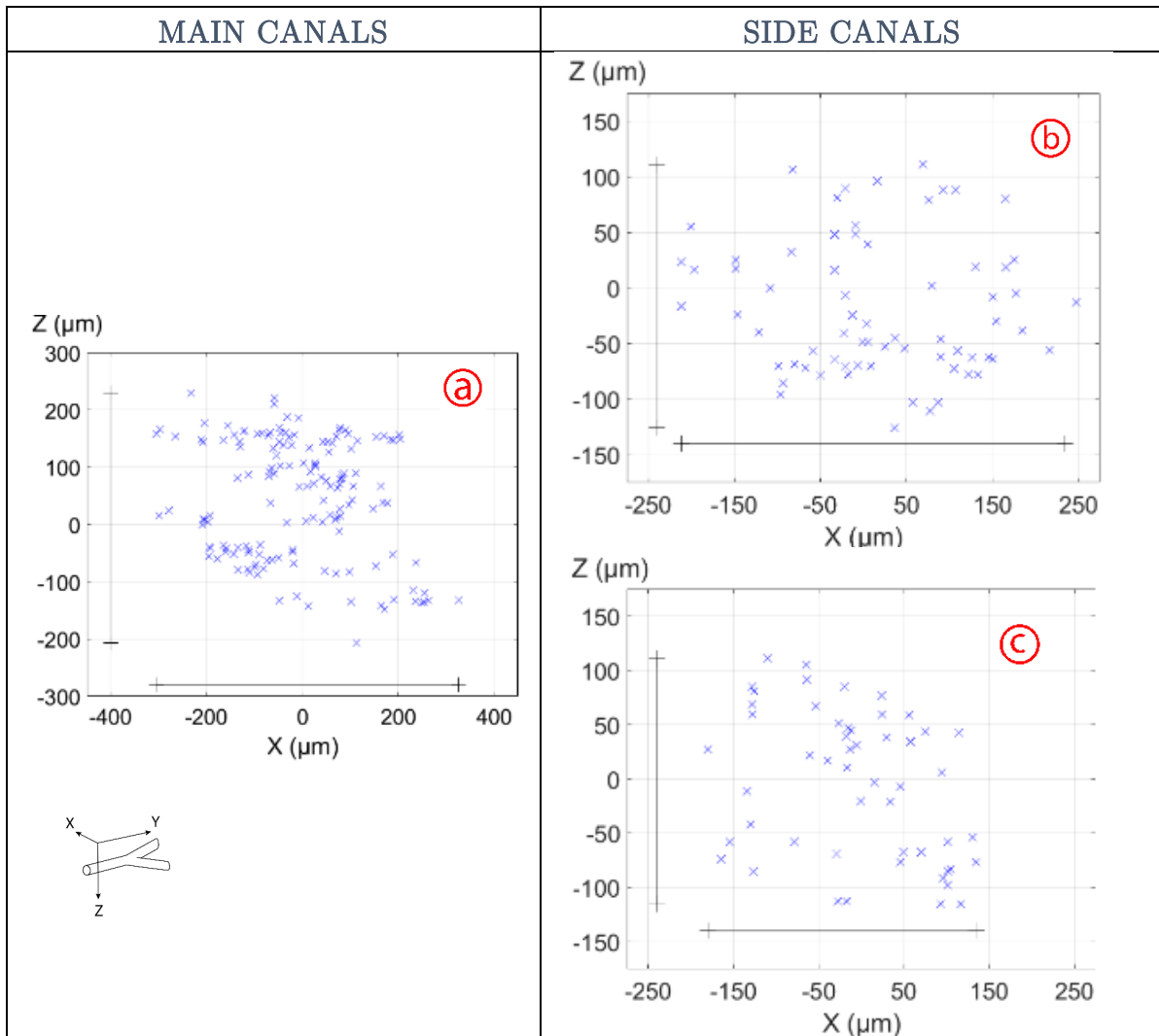


Figure 60. Slices of main and side canals

Transverse cut of the main canal (X,Z)

- a) Transverse cut of main canal (X,Z). The mean width of main canal was found to be $680 \pm 5 \mu\text{m}$ after making 21 transverse cuts of thickness $75 \mu\text{m}$ with a standard deviation of $85 \mu\text{m}$. The mean height of the main canal was found to be $396 \pm 1 \mu\text{m}$ after making 21 transverse cuts of thickness $75 \mu\text{m}$ with a standard deviation of $29 \mu\text{m}$.

Transverse cut of the left and the right canal (X,Z)

- b) The mean width of the left canal was found to be $460 \pm 5 \mu\text{m}$ after making 11 transverse cuts of thickness $300 \mu\text{m}$ with a standard deviation of $10 \mu\text{m}$. The mean height of the left canal was found to be $237 \pm 1 \mu\text{m}$ after making 11 transverse cuts of thickness $300 \mu\text{m}$ with a standard deviation of $24 \mu\text{m}$.
- c) The mean width of the right canal was found to be $310 \pm 5 \mu\text{m}$ after making 11 transverse cuts of thickness $300 \mu\text{m}$ with a standard deviation of $10 \mu\text{m}$. The mean height of the right canal was found to be $226 \pm 1 \mu\text{m}$ after making 11 transverse cuts of thickness $300 \mu\text{m}$ with a standard deviation of $24 \mu\text{m}$.

Chapter 3: Achieving *in vitro* volumetric ultrafast ULM

Subsequent to the filter based on tracking, the velocimetry algorithm was applied to each triplet to yield 3D velocity maps in the bifurcation. The velocity components in the 3 directions give us access to the angles of the trajectories and thus the direction of the bifurcation. This, in turn, allows locating the mean path by locating the center of each section and the angle of the trajectories. By having the direction of the bifurcation and the mean path, we can deduce the velocity profiles in the flow by defining a new basis centered on the mean path and with one of its vector colinear to the direction of the flow. This basis changes along the canals with their direction. After calculating each basis, we can cut profiles perfectly orthogonal to the main direction of the flow and thus have access to the section which will give the width and height of the canal. Such profiles are presented in Figure 60. For each slice, the positions of the microbubbles are plotted with crosses and calculating the width and height of the canal is done by taking the farthest positions in each direction.

Each time we applied the localization algorithm, we noted the number of microbubbles detected. Values are reported in table 1. Sometimes, the tracking algorithm implemented failed to pair the microbubbles, in particular at higher concentrations. The main resulting consequence was that the trajectories were too short or went in a direction incoherent with the direction of the flow. We assessed this by looking at the direction uniformity of each track compared to the supposed direction of the flow and to the average length of a track. We looked at the direction directly on the reconstructed images and we measured the standard deviation of the tracks over a sequence to assess the ability to track. This was labeled in Table 3 as an inability to track.

Concentration	Number of microbubbles per frame	Ability to track
1/10000	67 +/- 8	Yes
1/5000	68 +/- 7	Yes
1/3000	10 +/- 1	Yes
1/2000	10 +/- 1	No
1/1000	10 +/- 1	No
1/800	4.9 +/- 0.1	No
1/600	0	No
1/400	0	No
1/200	0	No
1/100	0	No

Table 3. Table giving the number of particles and the ability to track them

As we obtained profiles perfectly orthogonal to the main direction of the flow, it is possible to look at the velocity components of the microbubbles present in these profiles and obtain an instantaneous velocity profile at each cut. The velocity profiles averaged for several transverse slices (X,Z) are realigned and plotted over the bifurcation in Figure 61. The positions of the microbubbles localized in the canals are also plotted as black dots. The walls of the canals were drawn by hand trying to pass through the maximum number of particles with minimal deviation. It was possible to do this in the other direction (Y,Z) and yielded additional velocity profiles presented in Figure 61.

In our case, we measured a maximum velocity of 144 mm/s +/- 3.6mm/s (standard deviation as described in the Methods section). The difference between the experimental value and the one calculated with the conservation of flow rate can be explained by the fact that we do not take into account pressure loss.

Experimentally, the diameters were found to be smaller in the right side canal and the velocities higher which is confirmed by the equation (4). If we assume all of the flow goes into one of either canal, we obtain using the same equation (3) as for calculating the main velocity, $V_{left} = 195 \text{ mm/s}$, $V_{right} = 298 \text{ mm/s}$.

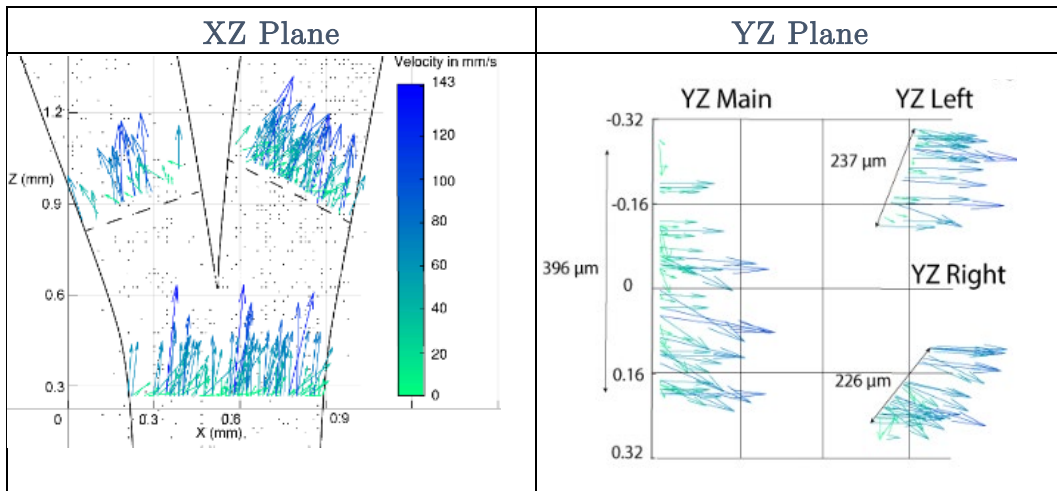
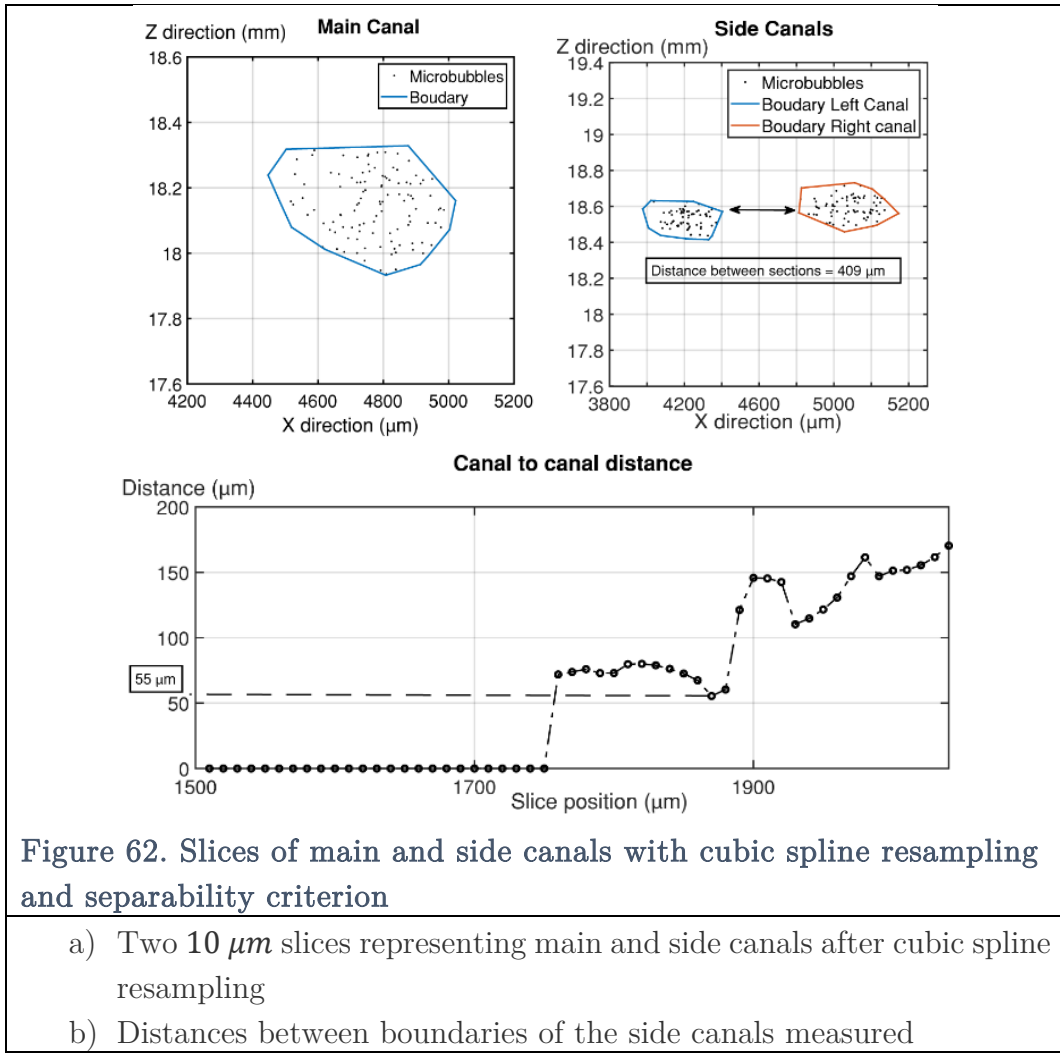


Figure 61. Velocity profiles in two orthogonal slices

- a) Velocity profiles in bifurcation (X,Z) axis. Maximum velocity is $144 \text{ mm/s} \pm 3.6 \text{ mm/s}$. Dashed lines represent the profile orthogonal to the microcanals based on the direction of the streamlines.
- b) Velocity profiles in bifurcation (Y,Z) axis. As the two canals are overlapped, the velocity profiles are shifted in this representation.

After applying the cubic spline-based spatial resampling describe in the Methods section, we were able to produce figures similar to figure 6. but with resampled data – allowing us to reach higher definition of the canals sides. The microbubbles positions plotted in Figure 62 belong to two slices of $10 \mu\text{m}$ in the Y direction. They were taken respectively at $y = 1310 \mu\text{m}$ and $y = 3600 \mu\text{m}$ ($y = 0 \mu\text{m}$ being the edge of the probe). The boundaries were automatically defined using the boundary function in Matlab. Such graphs were plotted for 54 consecutive slices ranging from $y = 1500 \mu\text{m}$ to $y = 2040 \mu\text{m}$ and the distance between two points belonging to each side canal was recorded. When such points could not be found, the distance was noted to be 0. The distances measured are plotted in Figure 62. The minimal distance measured between two distinct microbubbles was $55 \mu\text{m}$.



III.6 Discussion

In this study, we introduced and demonstrated the possibility to use 4D ultrafast ultrasound scanners to implement volumetric ultrafast Ultrasound Localization Microscopy. We developed an *in vitro* setup that allowed us to image flow in three dimensions and implemented a 3D algorithm for localization, tracking, and velocimetry of microbubbles at subwavelength resolution.

To demonstrate super-resolution, we observed the passage of microbubbles in channels at the scale of the wavelength. As the resolution is defined by the smallest structures that can be separated in an image, the easiest way to confirm ULM is to look at small structures close to each other. For this, we modified previously described microvessel phantoms [(Desailly et al., 2013), (Christensen-Jeffries and Tang, 2016)] to obtain easy to manufacture Y-shaped channels that can be oriented in three directions. A syringe pump allowed a controlled flow rate to compare the ULM velocimetry with

Chapter 3: Achieving *in vitro* volumetric ultrafast ULM

expected maximum microbubble velocities.

The intensity of beamformed volumes highlighted the vessels into which microbubbles were flowing. Thanks to the absence of movement of the phantom, clutter filtering could be performed with a simple subtraction of the mean signal for low concentrations. However for higher concentrations, we used the singular value decomposition filter [(Demene et al., 2015), (Errico et al., 2015), (Desailly et al., 2015)]. This filter has the ability to distinguish microbubbles and agar-based on their spatiotemporal signature. It is less sensitive to concentration than conventional temporal averaging filter but puts additional complexity to the post-processing and lacks the ability to distinguish slow-moving microbubbles. Usually, tissue signal is concentrated in high singular values because its dynamics are slower than average microbubble movement and noise. However, for slow-moving microbubbles in small microvasculature, this is no longer true and removing large singular values actually removes some of the slow-moving microbubbles. The implemented filter and the SVD threshold are thus a compromise between microbubble specificity and sensitivity. In our case, the thresholds were chosen empirically to improve the quality of the image enough to be able to see microbubbles moving in the tube while keeping these thresholds to a minimum to avoid losing microbubbles. Adaptive filtering, as described by (Baranger et al., 2018), could also be explored. For *in vivo* experiment, the dose of Sonovue commonly used [(Errico et al., 2015), (Foiret et al., 2017), (Couture et al., 2018)] leads to a high concentration of microbubbles in the blood. We predict that similarly to 2D ULM, SVD based filtering will be preferred to the temporal averaging filter for 3D ULM.

An additional challenge was to have sufficient signal-to-noise ratio to be able to implement ULM while limiting the amount of energy transmitted to each microbubble to prevent destruction. This leads to our selection of peak-negative-pressure around **300 kPa**. Along with acoustic pressure, hydrostatic pressure in small channels could also have led to microbubble disruption. However, according to (Talu et al., 2008) there is less than 3% destruction of microbubble with a 27 gauge syringe (**400 μm** diameter), **0.1 mL/s**. Since we have a maximum flow rate inside canals of **0.016 mL/s**, we conclude that we have no microbubble destruction due to hydrostatic pressure.

The new localization process was implemented on each volume. As pictured in Figure 58, the higher the concentration, the more particles are detected pre-tracking for the same acquisition duration. This means that higher concentration of microbubbles leads to a faster reconstruction of the canals. The high concentration of microbubbles makes it very easy to distinguish the bifurcation compared to the tissue surroundings but requires a less discriminative tissue/bubble filtering to cope with microbubble

cluttering. However after tracking, a lot of microbubbles detected are filtered out because the tracking is unable to perform well. The high concentration of microbubbles and possible cluttering makes tracking the same microbubble through the bifurcation more difficult. This is because, in the case of high concentration, microbubble signals are so close to each other, that the Munkres assignment can not assign microbubbles to one another. In terms of algorithm, it is the minimization step of the cost matrix that poses problem. Having so many particles means that the minima found after the Kuhn-Munkres algorithm are not unique. Fewer particles are detected and whole areas of the canals are missing. In both concentrations, the tracking algorithm correctly removes false detections in tissue which greatly improves the quality of the image. The trade-off is similar to that between Particle Image Velocimetry (PIV) where concentrations of tracers are high and thus do not allow individual tracking and Particle Tracking Velocimetry (PTV), where concentrations of tracers are low and allow tracking but take longer to do velocimetry. PTV allows individual tracking but is more difficult and takes longer to implement. In our case, if the concentration is further increased, the Rayleigh criterion of separation in between microbubbles will not apply anymore and will lower the number of microbubbles taken in each frame. A new algorithm should be implemented to separate close microbubbles in this case. These phenomena illustrate the importance of concentration on localization.

The number of microbubbles counted gives us information about the efficiency of the algorithm but cannot be correlated with the real number of microbubbles in our setup. This shortcoming is due to the fact that we cannot know the exact number of microbubbles we inject because the concentration of the microbubbles in a Sonovue vial varies by a factor as much as 5 (Schneider, 1999). It would be useful to know how many microbubbles we actually inject to assess the quality of our algorithm and we could do that by using another means of visualizing them such as a microscope and coating the microbubbles in fluorescent material. This measurement could be performed with a Coulter counter before injection or fluorescent microscopy in the measurement chamber itself. It would also allow us to determine what sub-population of the injected microbubbles actually contributes to the echo signals processed. This has impact on the uniformity of detection sensitivity in vascular imaging especially when microbubbles are polydisperse which is our case.

The tracking algorithm allowed us to implement velocimetry and yielded geometric information about the channels like their mean paths, angles and their profiles along each axis. The information is accessible even with a low number of detected microbubbles as only a dozen of velocity vectors were sufficient to measure the angle of

Chapter 3: Achieving *in vitro* volumetric ultrafast ULM

the flow. It is important to note that these velocity profiles were obtained in vessels the size of the wavelength, demonstrating that ULM can provide super-resolution both for microbubble densities and velocities. This opens up the way towards fast basis projection to determine mean path and streamlines in 3 dimensions, as well as, easy tortuosity measurement in the microvasculature.

The trajectories after localization were relatively short (a few dozens of a millisecond) compared to the time of one acquisition. Theoretically the longest trajectory could be 1 s as each acquisition lasts 1 s, however, this would be the case only if the velocity of the microbubble was below 10 mm/s. The average velocity in the main canal being around 79 mm/s, most of the microbubbles leave the observed volume in much less than 1 second. *In vivo*, for these vessel diameters, we expect slower flow, which would facilitate tracking at these compounded volume rates.

The widths of the canals measured on the super-resolved image are larger than their height. It is hypothesized that this is due to agar collapsing on itself when it is molded over the nylon strings. These features were verified by cutting slices of the agar gel and observing them with a microscope (Leica DMIL LED FLUO). Overall, the minimum height was close to the imaging wavelength (226 μm for the right side canal to be compared with a wavelength of 171 μm) and the B mode resolution ($\frac{\lambda f}{D} = 1,6 \times \lambda = 276 \mu\text{m}$). We are able to measure such distances because the precision of our localization algorithm yields images with a resolution enhanced with respect to the B-mode resolution. However the resolution for ULM is not only the localization precision but also depends on the number of particles accumulated.

Spatial resampling has been documented in the field of Particle Tracking Velocimetry [(Lüthi et al., 2005), (Hoyer et al., 2005)] where the need for high spatial sampling in 3D is a problem for Lagrangian flow measurement. Drawing from this, we turned to cubic spline interpolation to reconstruct trajectories. This scheme achieves smoother tracks than the linear interpolation scheme and supports continuity at the breakpoints which ensures continuity on speed and acceleration. This process performed in the final stage of the ULM framework allowed us to reach higher spatial sampling of the bifurcation and so resulted in a denser representation of the canals. Thanks to this denser representation, we were able to have sufficient particle positions in 10 μm thick slices to be able to distinguish the canals branching out with a resolution of 55 μm . With that measurement and velocimetry we have retrieved 3-dimensional information with precision much smaller than the diffraction limit in all dimensions. Our resampling could be further improved by using other schemes or we could dispense of it if we acquire with

Chapter 3: Achieving *in vitro* volumetric ultrafast ULM

higher volume-rate but this poses problems of data overload. Moreover the measurement of $55\ \mu\text{m}$ represents a higher limit on the resolution we can reach because it largely depends on the probability of a microbubble running along the edge of the canal. This probability is linked to velocity profile - as low-velocity areas have less renewal rate and so fewer microbubbles present throughout the acquisition - and also to the concentration of microbubble. As there is a constraint on the maximum concentration allowing ULM, it is likely that the solution would be to acquire longer to get a more complete seeding of the canals. The scheme developed here is likely to be useful to further improve the velocimetry in areas where microbubble counts are low *in vivo*.

An advantage of the volumetric ULM process is the sparsity degree of super-resolved images. As this degree is high, it is useful to compute and save the positions of the microbubbles through the algorithm. This technique allows to manipulate smaller dataset: a 1 second acquisition is about **23 GBytes** for volumetric images (Radiofrequency and beamformed images) alone whereas a matrix containing intensities, positions of the microbubbles weighs only **800 kBytes**. After filtering the positions by tracking, this scales down to **75 kBytes**. This represents a compression factor of about 300 000. In a case where the ULM algorithm would take around the same amount of time than the acquisition and beamforming of the data (as is already the case in 2D), it would save a considerable amount of space and could allow for faster visualization.

Currently, volumetric ultrafast ULM retains some drawbacks. An important aspect is that the size of the data produced with 1024 channels limits the speed at which we can transfer the data from the ultrasound machine to the computer memory. This doesn't restrict the framerate per se but limits the time between blocks of acquisitions thus increasing the overall experimental time and reducing the number of detected microbubbles. Another drawback is that this technique requires computational power which presents a challenge to implement in a clinical setting. However this requirement will decrease in the coming years according to Moore's law. The increase of computational power, as well as, performance in ultrasound systems will minimize such drawbacks and increase the interest in this technique.

Beyond computer processing limitations, a more important issue is the signal-to-noise ratio of the microbubble. Due to the size of the elements in 2D matrix-arrays, the SNR is often lower than with conventional 1D probes. Due to the element size, the sensitivity problem of 2D matrix arrays is common and is usually solved by driving the probe with a higher voltage. However, this leads to an increase in the energy transmitted to the medium and the ISPTA and PNP values, bringing them close to the destruction threshold of microbubbles. Because we would like to limit destruction of microbubbles,

Chapter 3: Achieving *in vitro* volumetric ultrafast ULM

we deliberately chose a low voltage to drive the probe but increased the number of transmissions employed to produce an image. In the end, we found that a total of 4 titled angles with a $\frac{f}{D}$ ratio of 1,6 enabled us to obtain sufficient image quality to localize microbubbles (SNR of bubbles is around 20 dB increase on filtered images). Thanks to the ultrafast capability of the electronic, transmitting such a number of angles still allowed us to achieve compounded volume rates up to 1000 Hz. We chose a volume rate of 500 Hz to limit data size. Fortunately, the experiment presented here faces no issue due to motion and the response of the tissue is easily filtered out.

The sensitivity problem is likely to be more important in-vivo. More transmissions would be required to obtain images of appropriate quality for localization. The problem with this is firstly that the compounded volume rate is lowered and secondly that the amount of data to transfer to make an image gets larger. The first problem can be solved for ULM of microvasculature as it was shown that high frame rates are not needed as microbubbles move slowly in small structures (Hingot et al, 2019). The second issue, however, is more important as the limitations come from the hardware capability of the system: 512 channels only in reception, SATA buses are limited to 6 Gb/s, RAM available for each machine is 16 Gb. We hope that with the growing interest in 4D imaging, the quality of the probes and electronics will improve.

In general, we have achieved super-resolution imaging of a micro-vessel phantom in a full 3D volume using volumetric ultrafast ultrasound localization microscopy in a limited time. Not only does the measured size of the wavelength-scale vessels compares well with expectations and their separation can be defined with a resolution of tens of microns, but the microbubble velocimetry also corresponds to predicted sub-wavelength flow patterns. The processes developed here to filter out microbubbles, track them and use the direction, length and velocity magnitude information drawn from the trajectories are already commonly used in 2D *in vivo* applications [(Foiret et al., 2017), (Song et al., 2018b), (Hingot, et al., 2018)]. The related thresholds and parameters will have to be modified and adapted for each *in vivo* applications.

Our attention is now turned towards the application of this technique *in vivo* in small animal models, as it would allow us to answer many difficulties we face in 2D. In particular, plane-by-plane ULM acquisitions require several boli or long infusion times to reconstruct an entire organ such as the rat brain. The volumetric ULM technique described in this paper would allow the observation of the majority of this organ volume in a single sequence. Also, the 3D vascular network in organs is currently badly represented by its 2D projection in planar ULM and requires, in the future, a full

Chapter 3: Achieving *in vitro* volumetric ultrafast ULM

volumetric method. Moreover, appropriate motion correction *in vivo* requires information in the three dimensions. Future work includes the investigation of alternative options to reduce the number of electronic channels needed to acquire volumetric images.

III.7 Conclusion

Volumetric ultrafast Ultrasound Localization Microscopy delivers volumes with enhanced resolution in the three dimensions compared to conventional 3D B-mode imaging within acceptable acquisition times. Moreover, by tracking the microbubbles through time, it allows velocimetry to retrieve dynamics of the observed flows and to access geometric properties at the scale of the wavelength. *In vitro* feasibility was demonstrated but additional *in vivo* applications remain to be explored. Volumetric ULM could be a solution to the main limitations, encountered in planar ULM, such as microbubble tracking and motion correction related to the absence of elevation information.

Chapter 3: Achieving *in vitro* volumetric ultrafast ULM

- Ahearne, M., Yang, Y., El Haj, A.J., Then, K.Y., Liu, K.-K., 2005. Characterizing the viscoelastic properties of thin hydrogel-based constructs for tissue engineering applications. *J. R. Soc. Interface* 2, 455–463. <https://doi.org/10.1098/rsif.2005.0065>
- Baranger, J., Arnal, B., Perren, F., Baud, O., Tanter, M., Demene, C., 2018. Adaptive Spatiotemporal SVD Clutter Filtering for Ultrafast Doppler Imaging Using Similarity of Spatial Singular Vectors. *IEEE Trans. Med. Imaging* 37, 1574–1586. <https://doi.org/10.1109/TMI.2018.2789499>
- Casula, O., Royer, D., 1994. Visualisation des champs ultrasonores par interférométrie hétérodyne. *J. Phys. IV* 04, C5-1217-C5-1220. <https://doi.org/10.1051/jp4:19945269>
- Christensen-Jeffries, K., Harput, S., Brown, J., Wells, P.N.T., Aljabar, P., Dunsby, C., Tang, M.-X., Eckersley, R.J., 2017. Microbubble Axial Localization Errors in Ultrasound Super-Resolution Imaging. *IEEE Trans. Ultrason. Ferroelectr. Freq. Control* 64, 1644–1654. <https://doi.org/10.1109/TUFFC.2017.2741067>
- Christensen-Jeffries, K., Tang, M., 2016. 3-D In Vitro Acoustic Super-Resolution and Super-Resolved Velocity Mapping Using Microbubbles 9.
- Couture, O., Besson, B., Montaldo, G., Fink, M., Tanter, M., 2011. Microbubble ultrasound super-localization imaging (MUSLI). *IEEE*, pp. 1285–1287. <https://doi.org/10.1109/ULTSYM.2011.6293576>
- Couture, O., Hingot, V., Heiles, B., Muleki-Seya, P., Tanter, M., 2018. Ultrasound localization microscopy and super-resolution: a state-of-the-art. *IEEE Trans. Ultrason. Ferroelectr. Freq. Control* 1–1. <https://doi.org/10.1109/TUFFC.2018.2850811>
- Demene, C., Deffieux, T., Pernot, M., Osmanski, B.-F., Biran, V., Gennisson, J.-L., Sieu, L.-A., Bergel, A., Franqui, S., Correas, J.-M., Cohen, I., Baud, O., Tanter, M., 2015. Spatiotemporal Clutter Filtering of Ultrafast Ultrasound Data Highly Increases Doppler and fUltrasound Sensitivity. *IEEE Trans. Med. Imaging* 34, 2271–2285. <https://doi.org/10.1109/TMI.2015.2428634>
- Desailly, Y., Couture, O., Fink, M., Tanter, M., 2013. Sono-activated ultrasound localization microscopy. *Appl. Phys. Lett.* 103, 174107. <https://doi.org/10.1063/1.4826597>
- Desailly, Y., Pierre, J., Couture, O., Tanter, M., 2015. Resolution limits of ultrafast ultrasound localization microscopy. *Phys. Med. Biol.* 60, 8723–8740. <https://doi.org/10.1088/0031-9155/60/22/8723>
- E. T. Y. Lee, “, 1989. Choosing nodes in parametric curve interpolation. *Comput.-Aided Des.* 21, 363–370.
- Errico, C., Pierre, J., Pezet, S., Desailly, Y., Lenkei, Z., Couture, O., Tanter, M., 2015. Ultrafast ultrasound localization microscopy for deep super-resolution vascular imaging. *Nature* 527, 499–502. <https://doi.org/10.1038/nature16066>
- Foiret, J., Zhang, H., Ilovitsh, T., Mahakian, L., Tam, S., Ferrara, K.W., 2017.

Chapter 3: Achieving *in vitro* volumetric ultrafast ULM

- Ultrasound localization microscopy to image and assess microvasculature in a rat kidney. *Sci. Rep.* 7. <https://doi.org/10.1038/s41598-017-13676-7>
- Heiles, B., Correia, M., Hingot, V., Pernot, M., Provost, J., Couture, O., 2019. Ultrafast 3D Ultrasound Localization Microscopy using a 32x32 Matrix Array. *Accept. IEEE Trans. Med. Imaging* 13.
- Henriques, R., Lelek, M., Fornasiero, E.F., Valtorta, F., Zimmer, C., Mhlanga, M.M., 2010. QuickPALM: 3D real-time photoactivation nanoscopy image processing in ImageJ. *Nat. Methods* 7, 339–340. <https://doi.org/10.1038/nmeth0510-339>
- Hingot, Vincent, Errico, Claudia, Heiles, Baptiste, Rahal, Line, Tanter, Mickael, Couture, Olivier, 2018. Microvascular flow dictates the compromise between spatial resolution and acquisition time in ultrasound localization microscopy.
- Hoyer, K., Holzner, M., Lüthi, B., Guala, M., Liberzon, A., Kinzelbach, W., 2005. 3D scanning particle tracking velocimetry. *Exp. Fluids* 39, 923–934. <https://doi.org/10.1007/s00348-005-0031-7>
- Lin, F., Shelton, S.E., Espíndola, D., Rojas, J.D., Pinton, G., Dayton, P.A., 2017. 3-D Ultrasound Localization Microscopy for Identifying Microvascular Morphology Features of Tumor Angiogenesis at a Resolution Beyond the Diffraction Limit of Conventional Ultrasound. *Theranostics* 7, 196–204. <https://doi.org/10.7150/thno.16899>
- Lüthi, B., Tsinober, A., Kinzelbach, W., 2005. Lagrangian measurement of vorticity dynamics in turbulent flow. *J. Fluid Mech.* 528, 87–118. <https://doi.org/10.1017/S0022112004003283>
- Montaldo, G., Tanter, M., Bercoff, J., Benezek, N., Fink, M., 2009. Coherent plane-wave compounding for very high frame rate ultrasonography and transient elastography. *IEEE Trans. Ultrason. Ferroelectr. Freq. Control* 56, 489–506. <https://doi.org/10.1109/TUFFC.2009.1067>
- Provost, J., Papadacci, C., Arango, J.E., Imbault, M., Fink, M., Gennisson, J.-L., Tanter, M., Pernot, M., 2014. 3D ultrafast ultrasound imaging *in vivo*. *Phys. Med. Biol.* 59, L1–L13. <https://doi.org/10.1088/0031-9155/59/19/L1>
- Schneider, M., 1999. Characteristics of SonoVue™. *Echocardiography* 16, 743–746. <https://doi.org/10.1111/j.1540-8175.1999.tb00144.x>
- Song, P., Manduca, A., Trzasko, J.D., Daigle, R.E., Chen, S., 2018a. On the Effects of Spatial Sampling Quantization in Super-Resolution Ultrasound Microvessel Imaging. *IEEE Trans. Ultrason. Ferroelectr. Freq. Control* 65, 2264–2276. <https://doi.org/10.1109/TUFFC.2018.2832600>
- Song, P., Trzasko, J.D., Manduca, A., Huang, R., Kadirvel, R., Kallmes, D.F., Chen, S., 2018b. Improved Super-Resolution Ultrasound Microvessel Imaging With Spatiotemporal Nonlocal Means Filtering and Bipartite Graph-Based Microbubble Tracking. *IEEE Trans. Ultrason. Ferroelectr. Freq. Control* 65, 149–167. <https://doi.org/10.1109/TUFFC.2017.2778941>
- Talu, E., Powell, R.L., Longo, M.L., Dayton, P.A., 2008. Needle Size and Injection Rate

Chapter 3: Achieving *in vitro* volumetric ultrafast ULM

Impact Microbubble Contrast Agent Population. *Ultrasound Med. Biol.* 34, 1182–1185. <https://doi.org/10.1016/j.ultrasmedbio.2007.12.018>

Viessmann, O.M., Eckersley, R.J., Christensen-Jeffries, K., Tang, M.X., Dunsby, C., 2013. Acoustic super-resolution with ultrasound and microbubbles. *Phys. Med. Biol.* 58, 6447–6458. <https://doi.org/10.1088/0031-9155/58/18/6447>

IV

Using *in vivo* volumetric ultrafast ULM as a blood flow
sensor

IV. Chapter 4: Using *in vivo* volumetric ultrafast ULM as a blood flow sensor

IV.1 Introduction

Few imaging systems are portable, possess real-time capability, can image large portions of tissue, while remaining inexpensive. Even fewer possess all of these abilities at the same time. However, echography is portable, real-time and relatively inexpensive (Cobbold, 2005). It can also image large field of views compared to the relatively small size of the sensor. It is limited to a few tens of centimeters at most but this is more than sufficient for most organs in the clinical setting and for small animal imaging (Abee, 2012). A more profound challenge is that most contemporary ultrasound imaging is limited to a single plane. Such impediment is one of its key drawback, making it blind to many 3D phenomena, but also user dependent.

The problem with imaging larger portions of tissue or entire organs at once originates in the way an image an ultrasound image is formed. A probe is comprised of many transducers that use the piezoelectric effect to emit ultrasound waves. Each transducer will give information about what is in front of it, or in the neighborhood of what is in front of it depending on its directivity. That means that if a larger field of view is wanted, more transducers are needed. More transducers means more channels to transmit and receive ultrasound waves and thus more acquisition cards, more RAM, more computational power (Jensen et al., 2013). Although widespread 3D ultrasound has been an objective for many years, it suffers from a tight bottleneck in the electrical capabilities of the ultrasound probe or ultrasound scanner.

Reducing the cable size and the amount of data to be transferred to the ultrasound scanner resides in changing the way transducers receive data. A first beamforming step can take place directly in the probe cable (near the transducers) which delays the signals related to a packet of elements and sums them. This is called microbeamforming and was implemented for CMUT arrays (Matrone et al., 2014; Wygant et al., 2009) and even for portable ultrasound (Fisher et al., 2005). The Acuson SC2000 scanner (Siemens ®) equipped with the 4Z1C matrix array transducer is one of the commercially available implementation of the microbeamformer technique. The probe integrates six electronic boards each with 120 custom Application Specific Integrated Circuits (ASIC) which are performing the microbeamforming. The Acuson scanner performs a second beamforming

step. The X61-X matrix used with the iE33 Echocardiography system from Philips®, or the 3V probe with the Vivid 7 from General Electrics® works similarly. These implementations are useful for 3D clinical applications.

Reducing the number of channels needed to form a volume can also imply modifying the transducers. The transducers organization can be organized in rows and columns rather than in 2D matrix arrays with independent elements (Chen et al., 2016; Christiansen et al., 2015; Logan et al., 2011; Rasmussen et al., 2015; Rasmussen and Jensen, 2013). Instead of having small almost square transducers filling in the grid of the 2D matrix array, this grid is sampled by large rectangle transducers in rows and columns. The absence of elevational focusing in two directions can be recovered by using specific beamformers such as Orthogonal Plane Wave or line element beamforming (Flesch et al., 2017; Rasmussen et al., 2015). Another approach to reduce the number of channels is to reduce the number of active elements. Instead of insonifying the volume with a complete matrix array, the matrix is sparse following a pattern that can be either deterministic or stochastic. The most basic example is provided by (Smith and Pavy, 1991) where they use a cross shape to insonify X and Y planes. Later, regular and radially periodic arrays were introduced following an on-grid setup where elements are located on a regular lattice (Austeng and Holm, 2002; Brunke and Lockwood, 1997). (Martínez-Graullera et al., 2010; Ramadas et al., 2014; Ramalli et al., 2015) have introduced deterministic 2D arrays with out-of-grid arrays where the lattice is unregular, and allows even further sparsity. Finally, stochastic patterns are also possible. Instead of having a fixed pattern in mind, various patterns are tested out with either on-grid (Turnbull and Foster, 1991; Weber et al., 1994) or out-of-grid patterns (Boni et al., 1994), fixed number of elements (Holm et al., 1997), presence of symmetry or not (Davidsen et al., 1994), identical transmit and receive elements (Austeng and Holm, 2002; Sciallero and Trucco, 2015). Recently, (Roux et al., 2016) introduced novel energy functions in the optimization algorithm to limit main lobe width while decreasing side and grating lobes.

Finally, with the increase of the number of channels available in research ultrasound scanners, the brute-force approach of using a fully addressed 2D matrix array has become popular. As detailed in chapter 1, a few systems exist with at least 1024 transmit channels: SARUS (Jensen et al., 2013), the 4D ultrasound scanner (Petrusca et al., 2018; Provost et al., 2014). 2D matrix arrays enable ultrafast imaging and with such a high number of channels, provide higher SNR and CTR than sparse or RCA probes (Rasmussen and Jensen, 2013; Roux et al., 2016).

The interest of 3D imaging in clinical or preclinical research is three-fold : wider imaging, higher quality imaging, easier imaging. Wider imaging is needed because organs

are 3D and it is difficult to reconstruct mentally the observed volume by acquiring slices. Another issue with imaging organs in slices is that in humans or animals the organs move with breathing, vascular flow or digestion. In 2D, the organs move in and out of the imaging plane, making it difficult to observe the same region for a prolonged time. The other motion that can be responsible for this is simply the probe motion. It was also shown that using high frame rate imaging, one could compensate for plane motion of the organs (Pernot et al., 2004; Tanter et al., 2007). We believe (and will demonstrate here), that it is possible to compensate for 3D motion using high frame rate volumetric imaging. 3D will lead to higher quality imaging. Finally, if the probe is handheld by a clinician, it requires skills and hours of practice to stay in the same plane of imaging with minimal movement. Volumetric imaging would allow the radiologist to relax. This also means that it would make ultrasound accessible to untrained manipulators like general practitioners, astronauts, (Law and Macbeth, 2011), remote doctors (O'Mahony et al., 2016). 3D volume could be analyzed a posteriori, finding the right plane in the stack of acquired data.

In the clinical and preclinical field, echography has demonstrated 3D capabilities since the advent of parallel receive processing in the 1980s and its implementation in Explososcan (Olaf T. von Ramm et al., 1991). Thanks to sparse synthetic aperture beamforming, the quest towards real-time 3D progressed over time up until its high frame rate implementation using plane wave imaging (Jensen et al., 2013; Prager et al., 2010). However, although the field of volumetric ultrasound imaging has expanded dramatically in the last few years for research purposes, its use in a clinical setting is quite low. Compared to MRI and CT scans which are standardly used in 3D mode, the use of 3D echography is limited to obstetrics and cardiology departments in hospitals.

The interest of 3D ultrasound imaging of *foeti* was limited to aesthetics until recently when a team proposed to 3D print the 3D ultrasound scan to help one of his blind patient see his baby (Werner et al., 2019a). The same team demonstrated that 3D printing could be useful in more precise diagnostics for surgery preparation of conjoined twins (Werner et al., 2019b). The intensive use in obstetrics can be explained by the fact that the contrast between the *foetus* and the amniotic liquid is naturally high thus producing high SNR images. SNR is critical for 3D applications as the 2D matrix array probes are usually of a lower quality than conventional single line transducers (mainly because their manufacture is limited to small scale/tailor-made applications).

3D ultrasound is used increasingly in clinical research for cardiac imaging (Dave, 2018). Its first use with 2D matrix array in a clinical setting dates back to 1999 when (Arbeille et al., 2000) used a Model 1 (3D Volumetrics ®) to drive a 256x256 elements

2MHz probe and image the whole heart in one cardiac cycle. 3D ultrasound is recommended to perform quantitative volumetric assessment of the Left Ventricular (LV) and measuring Left Ventricular Ejection Fraction (LVEF) (Lang et al., 2015). It can be used to analyze mitral valve function such as prolapse (Zekry, 2011), mitral and aortic regurgitation (Buck and Plicht, 2015) or stenosis (Schlosshan et al., 2011). Finally, in the clinical research with ultrafast imaging, it has shown tremendous capability in measuring cardiac fiber orientation (Papadacci et al., 2017b), measure stiffness of the myocardium (Papadacci et al., 2017a), or performing Doppler on tissue and blood (Papadacci et al., 2019).

For rodent imaging, the conventional approach to 3D imaging is to reconstruct volumes using multiple 2D images in the elevational direction (Coatney, 2001), and has been shown in the heart of the mice (Scherrer-Crosbie et al., 1999). A different approach to perform volumetric imaging with conventional single line probes has been demonstrated by (Demené et al., 2016) by using a tomographic approach. 18 successive rotations are applied to the probe through the use of step motors to produce 18 different sets of 2D Doppler images. A Wiener filter based deconvolution is then applied and a volume is reconstructed. While this technique yields good results with Doppler imaging, its slow temporal resolution (incompressible to a few tens of minutes) makes it costly to use that technique to reconstruct 3D images of microbubbles in the vasculature.

The absence of localization in the elevational direction with 1D probes also has important implications for 3D ULM. Indeed, single microbubbles would not be localized in the third dimension to the same resolution as in the plane. To solve this, one would have to increase the number of rotations to the resolution wanted in the ULM rendering, and as this resolution is around a few micrometers, the number of angles would need to be $N = \frac{N_{angles} \times \delta_{elevation}}{\delta_{ULM}} = \frac{18 \times 300}{10} = 540$, where N_{angles} , $\delta_{elevation}$, δ_{ULM} are respectively the number of angles for the traditional approach, the width of the elevation plane for a probe at 15 MHz, the resolution wanted for ULM. Moreover, one would have to change the method to reconstruct 3D images from the rotations, as there is a projection in the elevation direction in 2D ULM. An attempt at producing tomographic ULM by performing ULM on each of the 18 rotations could have been made assuming loss of elevational resolution, but the number of *boli* needed would still probably cause hypervolemia even if pauses are implemented. This solution far from ideal for our application was abandoned and our mind turned to the translation of 3D ULM *in vivo* using a dedicated ultrasound machine.

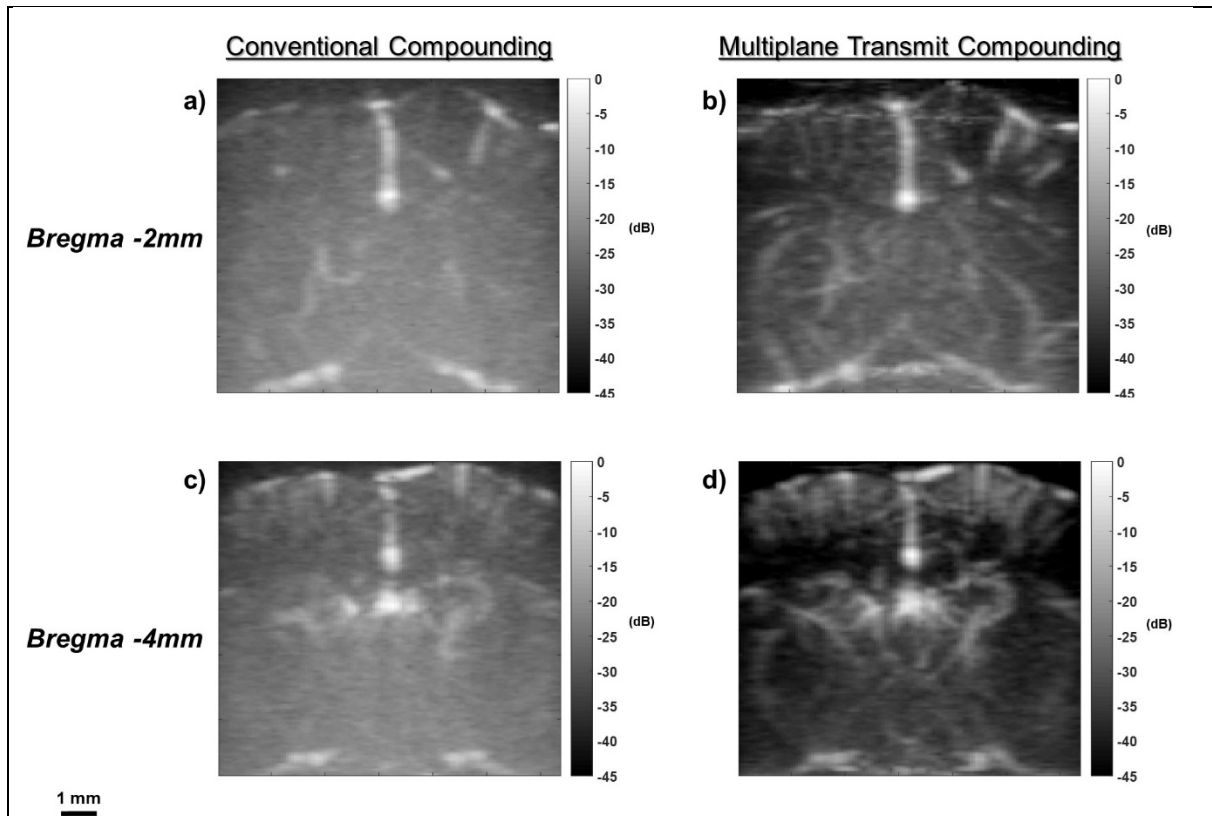
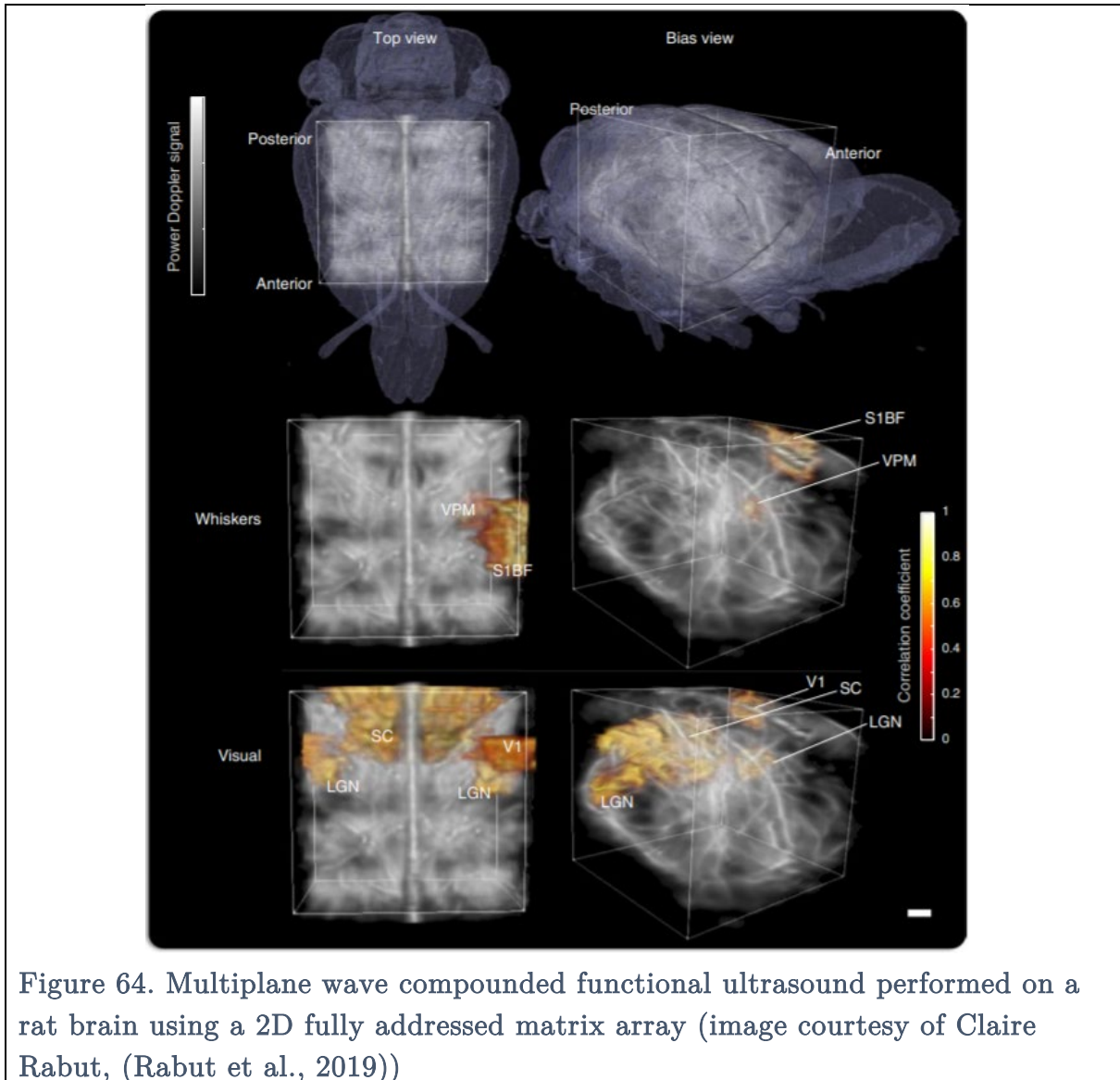


Figure 63. Compounded Plane Wave imaging and Multiplane wave compounded power Doppler imaging performed on a rat brain using a 2D fully addressed matrix array (image courtesy of Claire Rabut, (Rabut et al., 2019))

The conventional compounded images are obtained at 10V using 8 angled 2D plane wave with the 2D matrix array centered at 8MHz. The Multiplane Transmit Compounding is obtained at 10V using 8x8 angled 2D plane wave. With Hadamard encoded pulses, the resolution is estimated to be $180 \mu\text{m}$ in the axial direction, and $240 \mu\text{m}$ in the lateral direction.

The problem recurrent with 3D rodent ultrasound imaging is that 2D matrix arrays usually have a low transmit frequency with narrow bandpass (Czernuszewicz et al., 2018). This has to do with grounding/electrifying such small elements in a complex matrix shape. Hadamard encoded pulses have recently been proposed by (Rabut et al., 2019) and have shown to increase the SNR of volumetric imaging compared to compounded plane wave. They have also shown that sensitivity was sufficient enough to perform volumetric functional ultrasound in the rat brain (Rabut et al., 2019). The resolution of the images is however still limited: elevational resolution is $192 \mu\text{m}$, axial resolution is $180 \mu\text{m}$ and the lateral resolution is $240 \mu\text{m}$.



ULM had already been implemented in 3D using a 1.5D probe in (Desailly et al., 2015), but the geometry of the array is 2x64 and thus offers a very limited field of view. Volumetric ultrafast Ultrasound Localization Microscopy using a 32x32 matrix array can deliver volumes with enhanced resolution in the three dimensions of a large field of view compared to conventional 3D B-mode imaging within acceptable acquisition times and delivers velocimetry at the scale of a few tens of microns (Heiles et al, 2019). The goal of developing ULM *in vivo* is thus to provide images of the rodent organs at a resolution beyond the wavelength with added velocimetry.

We had already demonstrated that 3D ULM using a 2D matrix array was possible *in vitro*. The challenge was to port this in *vivo*. It was already outlined in the previous chapter that data overload is one of the main concern with 3D ULM. Various schemes

were put in place *in vitro* such as lowering the number of angled transmits to a minimum, implementing pauses in between block of acquisitions, performing *a posteriori* beamforming to reduce pauses for calculation, or reducing the number of images to a minimum value adapted to the volume of imaging. For *in vivo*, the data challenge remains the same, but is augmented by three other issues: signal to noise ratio is lower *in vivo* than in an agar phantom, the total number of images needed to reconstruct ULM of the complex brain vasculature is much higher than that of *in vitro* (around 50 times more), and the model is now a living animal and ethical considerations come into view (imaging time needs to be limited, *boli* can not be repeated too many times or they will cause hypervolemia, the animal needs to be monitored etc...). The scheme developed in chapter 3 was thus not usable for the *in vivo* case as such and new sequences were needed.

We were at first interested by mapping the anatomy of the rat brain at the micrometric level: while our technique lacks the resolution brought by tissue clearing techniques such as CLARITY (Chung et al., 2013), iDISCO (Renier et al., 2014), 3DISCO (Ertürk et al., 2012; Ertürk and Bradke, 2013), it is an *in vivo* measurement. We can take advantage of this to try and measure the variations in anatomy over time. Thanks to velocimetry, we can also accurately measure the variations in average blood speed in vessels. We decided to use a notorious side effect of anesthesia to our advantage. Ketamine is a well-known vasoconstrictor of microcirculation in the brain and pulmonary arteries. On the contrary, Isoflurane is a vasodilator. Both of these anesthesia is routinely used in our lab, either alone or in combination with others, either as inducers or in long surgeries.

The aim of that chapter is to demonstrate that the technique developed in 3D is able to provide information about anatomy and vascular flow at the scale of a few microns with a precision allowing to monitor drug-induced physiological changes. Demonstrating this 3D technique would open a new door for ultrasound imaging as an operator-independent micrometric blood flow sensor.

IV.2 Materials and Methods

IV.2.1 Animals

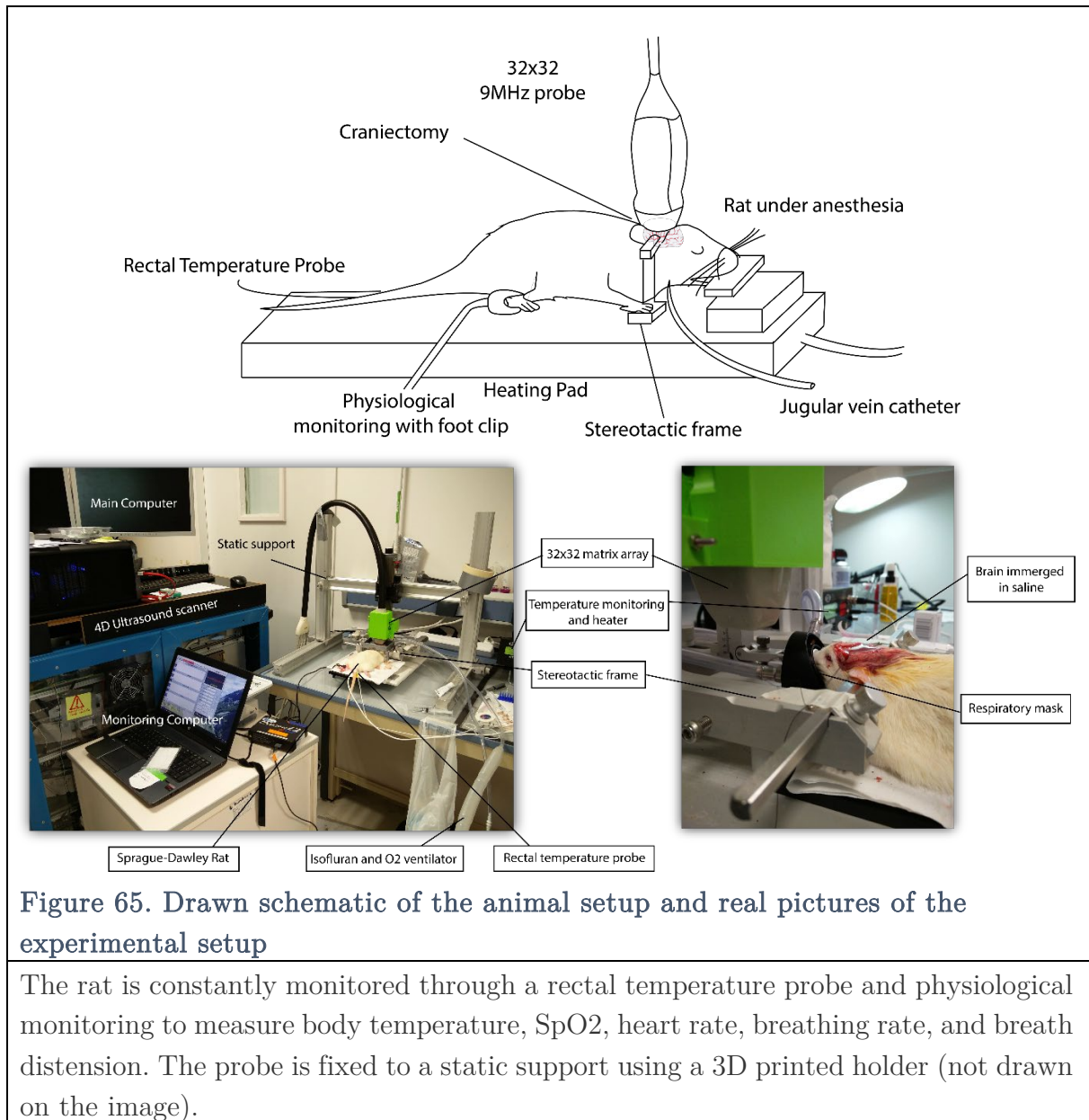
All animals received humane care in compliance with the European Communities Council Directive of 2010 (2010/63/EU), and the study was approved by the institutional and regional committees for animal care (Comité d’Ethique pour l’Expérimentation Animale no. 59—‘Paris Centre et Sud’ Protocole no. 2017-23).

8-10 weeks Sprague-Dawley rats were obtained from Janvier Labs (Le Genest-Saint-Isle, France). Animals were free from pathogens and were placed in our in-house facilities. Housed in Techniplast® cages by groups of 2 minimum and 3 when the total animal per volume ratio did not exceed values fixed by regulations, the animals were kept for at least a week before surgery. The temperature in the cages was controlled to be between 21-23°C, the humidity rate in between 40-60%. The day-night cycle was divided as follows: 7h-19h/19h-7h. Water and a commercial pelleted diet SAFE A04-10 were available *ad libitum*. SAFE Flake sawdust was used as bedding, enrichment such as pieces of cardboard, paper tunnels were provided and the facility vet went to visit them daily. This allowed to reduce stress during manipulation before anesthesia induction and increase the anesthesia's performance in terms of speed and robustness in time.

After 5 minutes in the induction cage filled with a mix of air and 5% of Isoflurane, the animal was placed on the back on a heated plate with a respiratory mask. The mix was replaced with O₂ mixed with 4% of Isoflurane. The depth of the anesthesia was tested by the absence of withdrawal reflex when pinching the toes of the hind limb. An incision was made just above the first rib in the thoracic area. The absence of movement from the animal during that incision was considered as a confirmation of the depth of the anesthesia. After tissue was dilacerated to give easy access to the jugular vein, two suturing strings were threaded under it. The string closer to the brain was knotted to close blood flow returning from the brain. An incision perpendicular to the direction of the vein was made and a 180 μm inner diameter polyethylene tubing (Instech/A-M Systems®) was placed inside the vein to serve as a catheter. The surgery was deemed successful when blood was observed in the catheter under negative pressure applied by the syringe on the other end. The other string was knotted over the catheter to prevent it from sliding out of the vein. Moreover, the incision made was closed with Vetbond to prevent the jugular vein from drying and for added security.

The animal was then placed in a stereotactic frame equipped with a respiratory mask. The percentage of Isoflurane was decreased to 3% while maintaining the absence of reflexes. 5mL of saline at 37°C was injected subcutaneously in two different doses in the left and right sides of the back of the rat to prevent dehydration. Such a procedure was repeated every 2 hours. An incision was made in the scalp following a line between Bregma and Lambda points but extending from over the olfactory bulb to just behind the cerebellum. The scalp was retracted and the side and the cerebellum muscles were disjoined from the skull to allow easy access to the skull. The muscles were kept away from the skull by using suturing thread. After this, the percentage of Isoflurane was decreased as low as possible but above 1% to prevent lethal side-effects such as

hyperventilation, cardiac deficiencies while maintaining absence of reflexes.



A drill was used to remove a large portion of the skull to provide an ultrasound transparent window. This window began over the lambda sutures, went along the sides of the skull just below the ridge and then joined 3 *mm* after the Bregma point just before the beginning of the olfactory bulb. Such a window measured approximately 12 *mm* in width and 15 *mm* in height. This allowed unprecedented access to large areas of the brain.

IV.2.2 Physiological constants

The heartbeat, breath rate, breath distension, temperature, and SpO₂ were all

monitored using MouseOx Plus pulse oximeter (Starr ® Life Sciences Corporation). A decrease in SpO₂ was remedied by an increase in the O₂ fraction of the gas mix breathed by the animal. A decrease in temperature implied covering the back of the animal with a heated glove until the appropriate temperature was recovered. An increase in temperature implied lowering the temperature of the heating plate. A sudden decrease in breath rate was usually solved by lowering the percentage of Isoflurane in the mix. Breath distension measurements were discarded because of a large standard deviation due to inaccuracies in the measurement device.

IV.2.3 Isoflurane and Ketamin-Medetomidin acquisitions.

The surgery took in between 2 to 6 hours. The imaging process began 30 minutes after the skull was removed. In the meantime, the brain was immersed with saline which will also serve as an ultrasound coupling medium. This allowed the physiological constants to stabilize and be less affected by surgery. We recorded these and considered them as a baseline for the rest of the experiment. Just before the injection of Ketamine-Medetomidin, Isoflurane was decreased to around 0.8% and then decreased by 0.2% steps in less than one minute after the injection of Ketamine Medetomidin (KD). This allowed preventing overdosing the animal. After Isoflurane was stopped completely, we waited for 60 minutes to make sure that the Isoflurane completely disappeared in the blood and that its effects were null after that time. Additional time was sometimes required to make sure the physiological constants returned to the baseline. KD was injected every hour and a half after the first injection or if reflexes were observed. A half dosage was injected to prevent overdosing.

IV.2.4 Ultrasound sequence

We designed our ultrasound sequence to fit the universal framework laid out in chapter 2. In our case, working with RF data is mandatory for the 3D approach as the 1024 channel capability ultrasound scanner is unable to beamform as it is acquiring data.

A customized, programmable, 1024-channel ultrasound system (Provost et al., 2014) was used to drive a 32-by-35 matrix-array probe centered at 8 MHz with a 90% bandwidth at -6 dB, a 0.3-mm pitch and a 0.3-mm element size (Vermon, Tours, France). The 9th, 17th and 25th lines of that probe are not connected resulting in a 32x32 matrix array. We used that probe to transmit 2-D tilted plane waves at 9MHz frequency at 12V. The probe was coupled to the brain using either water, ultrasound gel, or low concentration agar (less than 2% in water). It was placed directly over the brain

with a spacing higher than 3 mm. The ultrasound system consists of four different Aixplorer systems (Supersonic Imagine, Aix-en-Provence, France) as described in chapter 3. A combination of 12 tilted plane waves was transmitted with this order:

$$[(f(X,Z), f(Y,Z))]=[(-3^\circ,0^\circ);(-2^\circ,0^\circ);(-1^\circ,0^\circ);(1^\circ,0^\circ);(2^\circ,0^\circ);(3^\circ,0^\circ);(0^\circ;-3^\circ);(0^\circ;-2^\circ);(0^\circ;-1^\circ);(0^\circ;1^\circ)(0^\circ;2^\circ)(0^\circ;3^\circ)]$$

with x- and y- directions parallel to the matrix-array probe. We increased the number of angles compared to the *in vitro* sequence to increase Signal to Noise Ratio without increasing the voltage which could induce microbubble destruction. As mentioned in chapter 2, a crucial factor in *in vivo* implementation of 3D ULM is the management of data. To prevent data overload and to succeed in prolonged high frame rate imaging, we decided to develop a specific sequence with only a few milliseconds of imaging and a long pausing time: during 0.370 s, 185 compounded volumes were acquired with parameters above, then the data was transferred from the DAQ cards to the RAM memory on each of the four ultrasound scanners' computers. In total, 540 blocks of 185 volumes were acquired during 18 minutes (see Figure 66). To provide continuous perfusion with microbubbles, 0.1 mL boli were renewed every 90 seconds, yielding a total volume injected of 1.2 mL in 18 minutes which is well below the recommended value of 5mL/kg for a single bolus recommended by the Institutional Animal Care and Use Committee (IACUC).

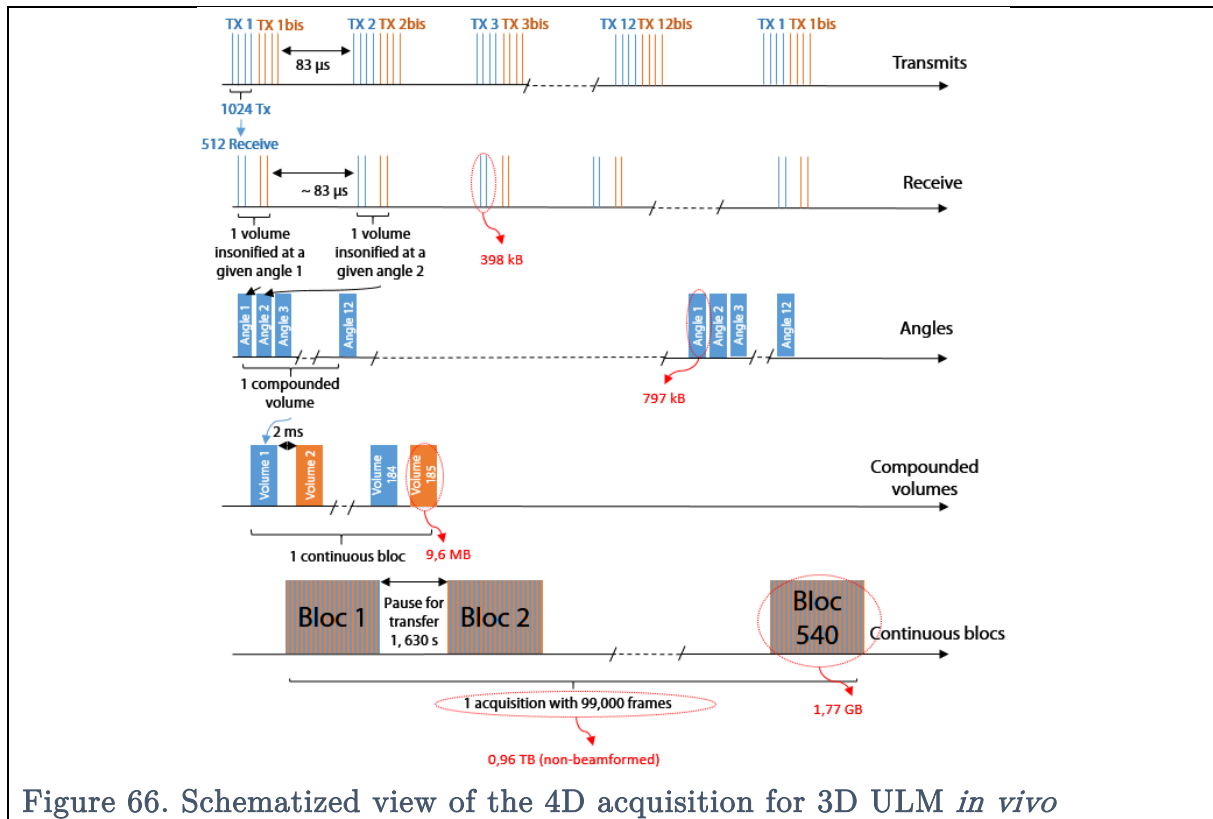


Figure 66. Schematized view of the 4D acquisition for 3D ULM *in vivo*

In terms of ultrasound transmits, this sequence is very similar to what was done *in vitro*. The only difference is the number of angles increased from 4 *in vitro* to 12 *in vivo*. However, the number of continuous frames has been decreased to 185 from 500 and the number of blocks increased from 4 to 540. That allows us to produce 99,900 images without restarting the ultrasound scanner, changing the hard drives, or any elaborate hardware action.

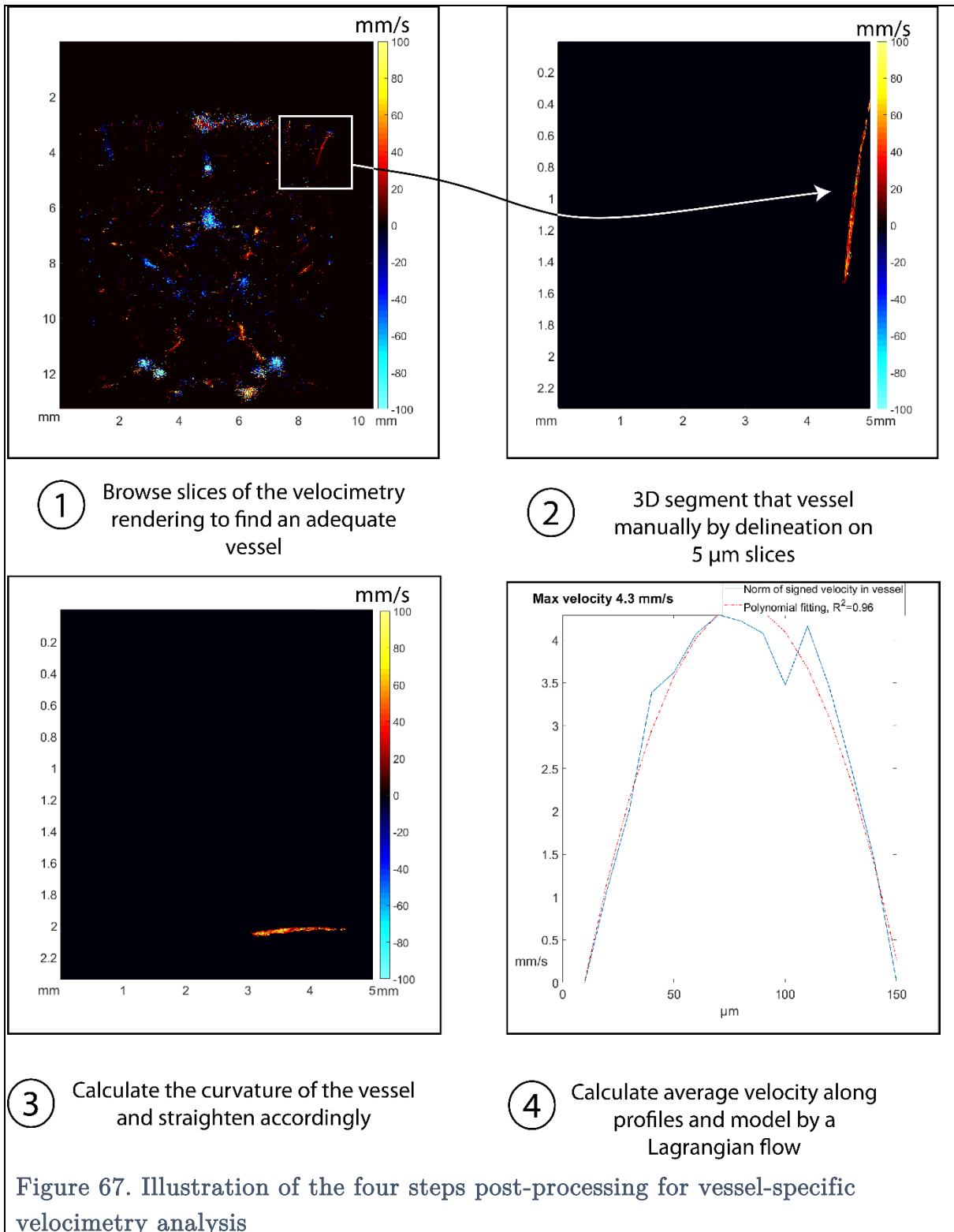
After acquiring of all of the data, each of the four SSDs belonging to each ultrasound machine was removed and its contents were entirely transferred to another computer where storage has a large capacity. This data was then processed according to the radial symmetry based localization scheme and Hungarian based tracking algorithm (see chapter 2 for more details).

IV.2.5 ULM processing

The ULM processing is based on the algorithm explained in chapter 2. The radiofrequency data is beamformed in all directions on a $\frac{\lambda}{2} \times \frac{pitch}{2} \times \frac{pitch}{2} = 80 \times 150 \times 150 \mu\text{m}^3$ grid. The singular value decomposition is done on each of the 185 volumes. Of the 185 singular vectors, the first 4 are discarded and the volume is reconstructed using 181 of the lowest energy vectors. The radial symmetry based localization algorithm is used for localization with an assumed full width at half maximum of 5 pixels in the three directions. The positions of the microbubbles are then converted from pixels to μm . The tracking algorithm is implemented on each block of acquisition separately. Tracks are interpolated following the interpolation scheme exposed in chapter 3 with a slightly faster implementation. Velocities are calculated using differentiation on a custom-built time vector corresponding to the interpolation of the trajectories. The results of this process are the list of non-interpolated microbubble centers, the list of trajectories with the velocities measured at each point of the trajectories. The beamformed data is not saved in the computer's hard drives. The parallel implementation of this process takes one and a half minute for one block if velocimetry is performed, only one minute if no velocimetry is performed, making the whole implementation for 540 blocks of 1TB run in 14 hours.

IV.2.6 Additional processing for velocimetry analysis

Additional processing steps were required to measure the effect of anesthesia on the vasculature of the rat brain. The two sets of volumetric ULM were applied velocimetry with the same parameters. Because the probe scarcely moved in between acquisitions, it is possible to target specific vessels in the two sets and compare them. The processing steps are illustrated in Figure 67.



1. The first step is to browse the ULM rendering obtained and choose the vessel that we want to analyze. This is done using a custom made Graphical User Interface (GUI) made in Matlab[®] to render slices with different thicknesses, colormaps, and orientation.

2. Next, we focus on the slice where the vessel is starting to appear. We use the interactive polygon tool `roipoly` that comes with Matlab[®] to define a manually segmented volume. In order to do this accurately, we work on slices of thickness $10\ \mu\text{m}$.
3. We measure the curvature of the vessel segmented and we apply a rigid transformation to the vessel to straighten it. The goal behind this is to be able to have a simple x-axis oriented mean path for the vessel to make the measurement of the flow profile easier.
4. Finally, the velocity profiles are averaged along the mean path of the vessels and the normed velocity is computed for each $10\ \mu\text{m}$ pixel. The sign based on the up or down direction in the brain is added to distinguish arteries from veins in the neocortex. A quadratic flow profile is fitted on the measured velocities and the R^2 value of that fit is computed. The maximum velocity measured is also computed.

This specific processing will yield velocity, diameter and flow-rate information in the measured vessels.

IV.3 Results

IV.3.1 Density-based renderings for anatomical viewings

Thanks to the algorithm developed and explained in IV.2.5, we can obtain microbubble density and velocimetry at any point in our region of imaging. The volumetric representation of the density of microbubbles along trajectories is shown in Figure 68. This figure shows three perspective viewings in perspective from the coronal, sagittal and transverse point of view. Some structures can be clearly identified such as the superior transverse sinus, the azygos pericallosal artery. The top of the Willis circle is also visible. The small descending/ascending vessels in the neocortex are also visible albeit they all overlap because of the perspective viewing in coronal and sagittal POV. In the transverse view, their structure can clearly be descending or ascending from the main pial vessels. The renderings were obtained using Amira[®] software from FEI[®].

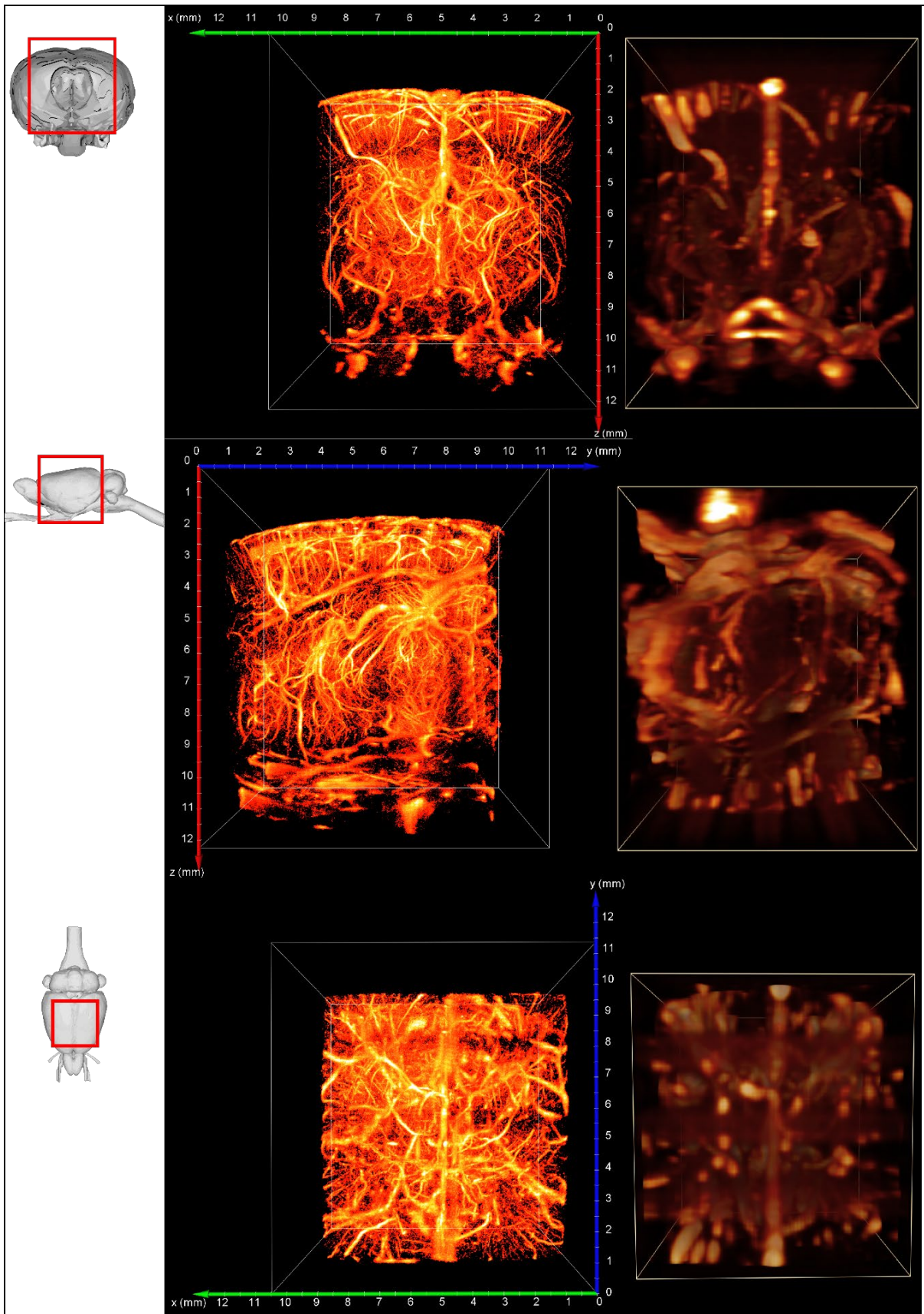


Figure 68. Anatomical 3D viewings of 3D ULM performed on a rat brain (color encoded based on microbubble density) next to contrast-enhanced power Doppler volumes obtained with the same sequence parameters

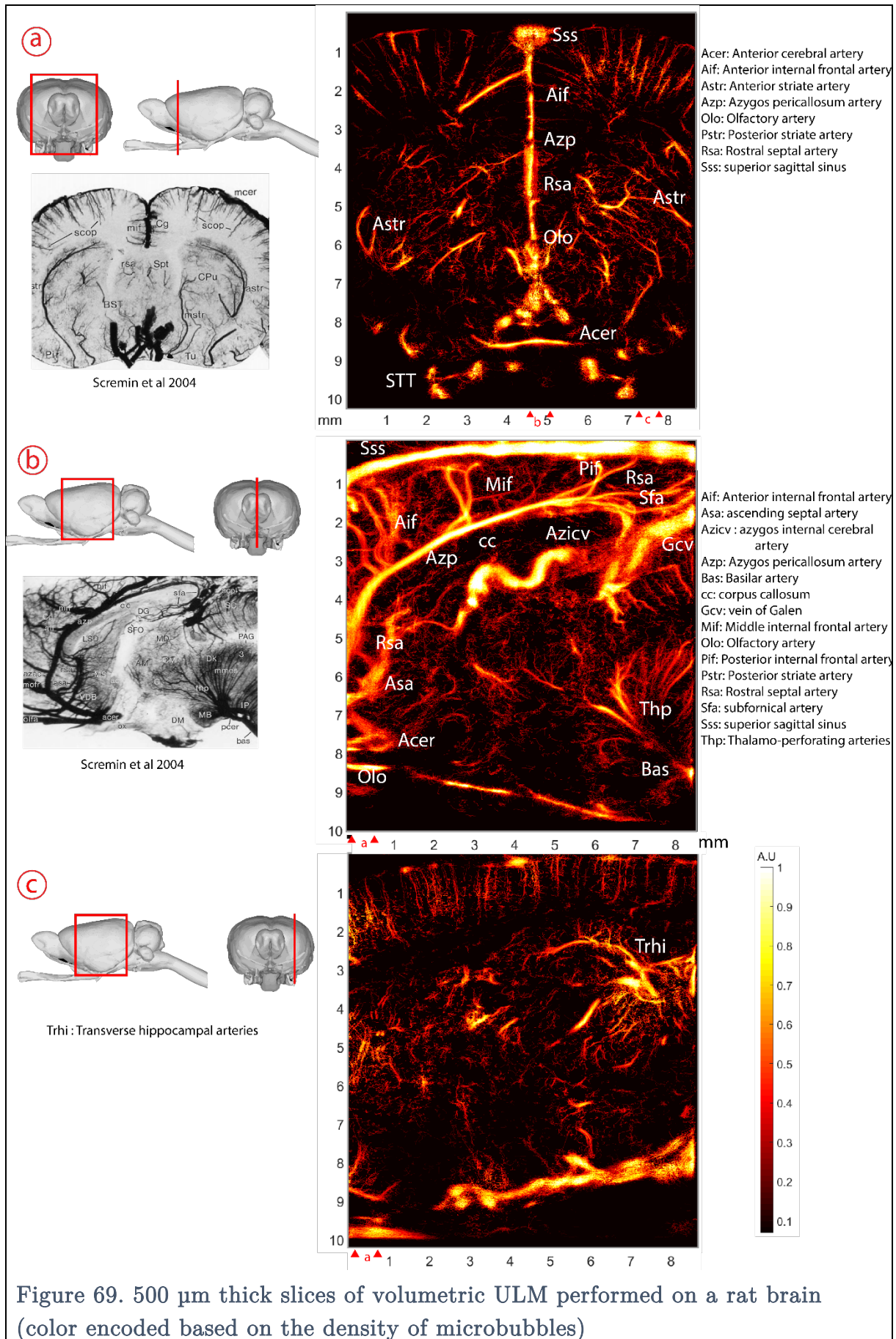
- c) Coronal view: in that view, the vessels of the cortex are clearly visible well described by their descending/ascending structure. The superior transverse sinus is also visible
- d) Sagittal view: in that view, the superior transverse sinus and azygos pericallosal artery are clearly visible. The complex structure forming the cortex is however projected in the perspective
- e) Transverse view: the pial vessels are visible above the ascending/descending vessels of the cortex. Note that the superior sinus is only visible in the top and bottom parts of the image. The inferior sinus, however, is visible from Bregma to Lambda.

The contrast enhanced power Doppler was obtained over an integration period of 0.370 s with 12 angled plane wave emitted at 9MHz with a 12V voltage.

It is also possible to look at the volumetric data in a 2D fashion by making slices in the coronal and sagittal directions. We have printed out the density of microbubbles for a slice of $500 \mu\text{m}$ in thickness in Figure 69. The intensities were treated using a Contrast Limited Adaptive Histogram Equalization (CLAHE) algorithm with 20×20 contextual regions and a contrast enhancement limit of 0,08 to avoid oversaturation due to the projection of particularly populated vessels such as the main arteries and veins.

The coronal cut is taken approximately a few hundreds of micrometers anterior Bregma. The neocortex vessels are clearly visible and so are the vessels in the striatum. Directly below the basal forebrain region also exhibits vessels albeit fewer. The sagittal cut (b) clearly shows absence of vessels in the corpus callosum while exhibiting the descending/ascending neocortex vessels. The disorganized way the vessels of the striatum and basal forebrain region are arranged can also be seen in the coronal cut. The second sagittal cut (c) shows the main transverse arteries and veins and their Lambda-Bregma direction. A few vessels are identified in the legend of Figure 69.

Thanks to increased resolution in the three directions, it is possible to look at smaller slices than the one in Figure 69. We have made $50 \mu\text{m}$ slices in all of the three directions at the proximity of the previous ones (see Figure 70).



- a) Coronal cut: this cut shows the main vessels. The anterior cerebral arteries (Acer) are also visible at the bottom of the image just above the spinal trigeminal tract (STT). The superior sagittal sinus (Sss) is well resolved and we hypothesize the almost continuous vessel plunging from the sagittal sinus to the basilar artery is the projection of various vessels: rostral septal artery (Rsa), anterior internal frontal artery (Aif), middle internal frontal artery (Mif), olfactory artery (Olo), azygos pericallosum artery (Azp). The cortical vessels are clearly identified by their plunging structures. On the left of the image, a vessel is arranged in a boomerang shape: that is the posterior striate artery (Pstr). On the right of the image, the anterior striate artery (symmetrical to the posterior striate artery) is seen as the Y-shaped vessel (Astr).
- b) Sagittal cut centered on the sinuses: this cut is of low interest if one is interested in looking at small vessels but many large structures can be identified. From top to bottom the superior sagittal sinus (Sss), the azygos pericallosal artery (Azp), the azygos internal cerebral vein (Azicv) and the vein of Galen (Gcv). Branching from the azygos pericallosal artery, the anterior internal frontal artery (Aif), the middle internal frontal artery (Mif) and the posterior internal frontal artery (Pif) can be seen. Two vessels in the rear of the brain can be seen branching away from the Azp, these are the retrosplinal artery (Rsa) and the subforaminal artery (Sfa). The large tree-like structure on the right of the image at depth **8 mm** might be ramifications of the posterior medial choroidal artery (Pmch).
- c) Sagittal cut: this cut does not show the transverse sinus as it is away from the Lambda-Bregma line. The large vessel at the bottom of the image is identified as the principal carotid artery (Pcer). The large vessel with the Y shape going from right to left is the caudal rhinal vein (Crhv). The vessels in the cortex are less visible than in the coronal cut as they tend to plunge orthogonally to the surface of the brain in a different plane than the coronal plane.

The red triangles indicate where the different cuts were taken.

All pixels are rendered as the sum of the intensity over **50 μm** in the appropriate direction. The CLAHE algorithm mentioned earlier can be dispensed with as the projections are smaller than before. Most of the large vessels that can be seen in the 500 μm slices are still visible in the **50 μm** slices. The smaller vessels of the cortex are also visible in the coronal cut and in the first sagittal cut. In the second sagittal cut, the smaller vessels are highly affected by the high intensity of the large vessels and the tree-like structure identified as ramifications of the posterior medial choroidal artery earlier on is barely visible.

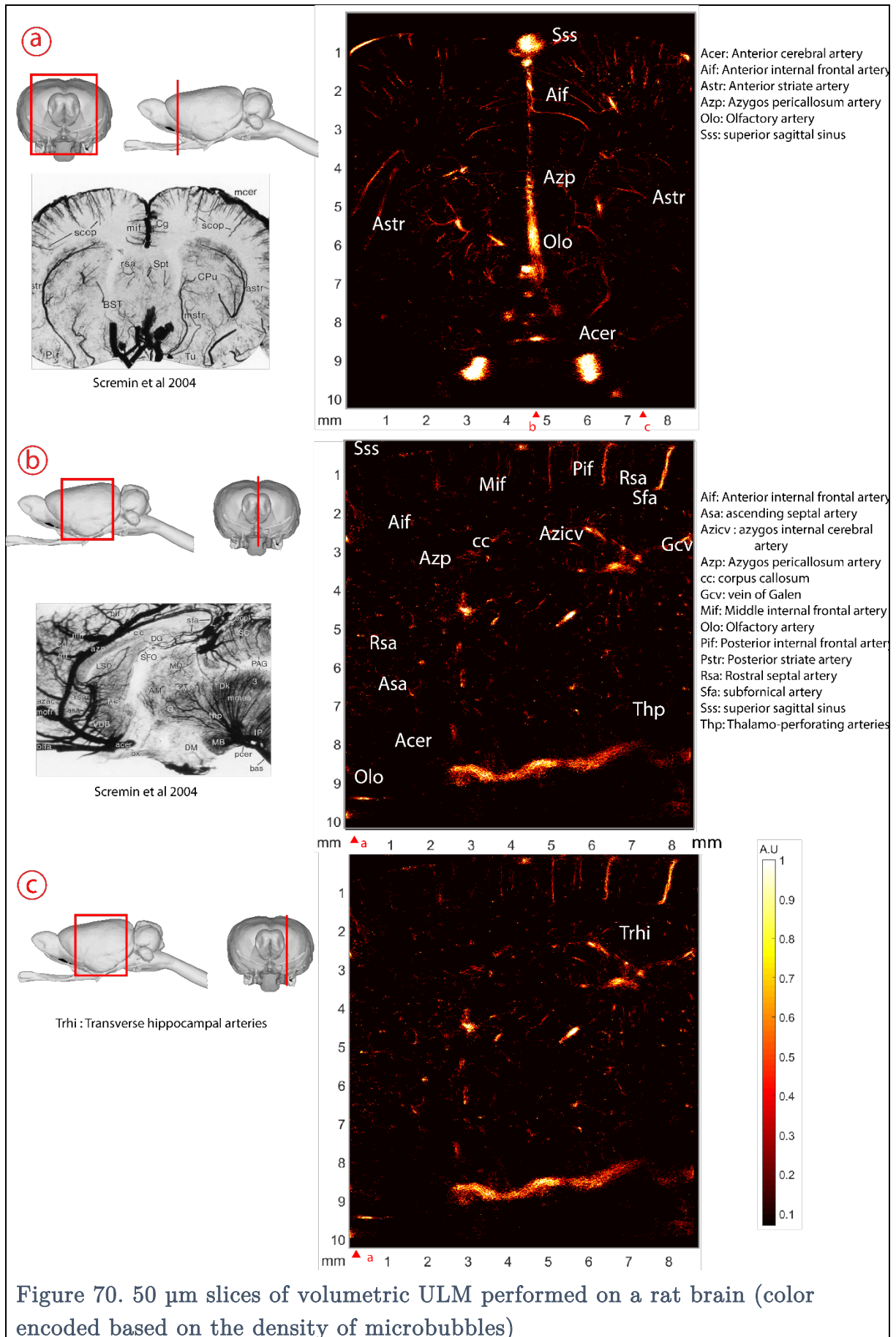


Figure 70. 50 μm slices of volumetric ULM performed on a rat brain (color encoded based on the density of microbubbles)

- a) Coronal cut: In this cut, the main veins and arteries are still visible (superior sagittal sinus, rostral septal artery, anterior cerebral artery). Small vessels in the cortex are also visible although the projection in such a small plane attenuates their signal and separates them in half sometimes.
- b) Sagittal cut: The superior sagittal vein and the azygos pericallosal artery are clearly visible with their different branches. The azygos internal cerebral vein is also clearly visible.
- c) Sagittal cut: Almost all of the vessels in the striatum are invisible because their organization is not in plane with the cut. Some vessels in the neocortex are still visible. The main vessel in the basal forebrain region is identified as the principal carotid artery.

The red triangles indicate where the different cuts were taken.

IV.3.2 Velocimetry renderings for qualitative analysis and vasculature labeling

Thanks to the high frame rate, we are able to track microbubbles throughout an entire block of images. The results of tracking and velocimetry are produced in the two next figures. $500\ \mu\text{m}$ slices are made at the same coordinates as the slices presented in Figure 71. $50\ \mu\text{m}$ slices are not reproduced as the range of velocities in the various vessels makes it impossible to distinguish small vasculatures without oversaturating the bigger vessels. The velocities are color encoded based on their magnitudes and on their direction. Microbubbles carried towards the top of the brain appear cyan to deep blue and microbubbles carried down the brain appear yellow to red. The arterioles in the neocortex always carry the red blood cells from the top of the brain down to the corpus callosum. On the contrary, the veinules always carry the oxidized red blood cells from the inside of the brain towards the top of the cortex. The colormap chosen allows to accurately distinguish veinules and arterioles in the neocortex.

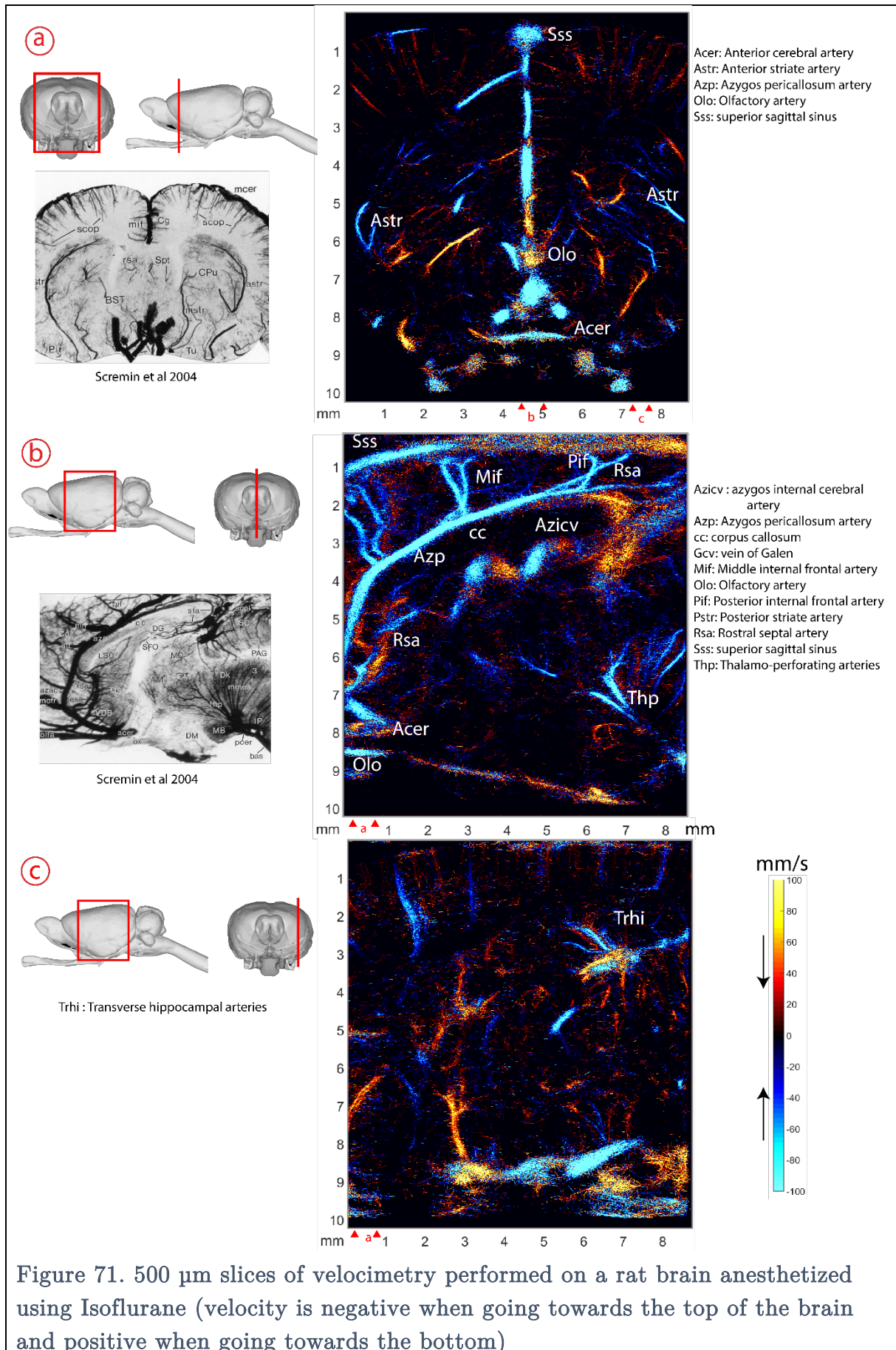
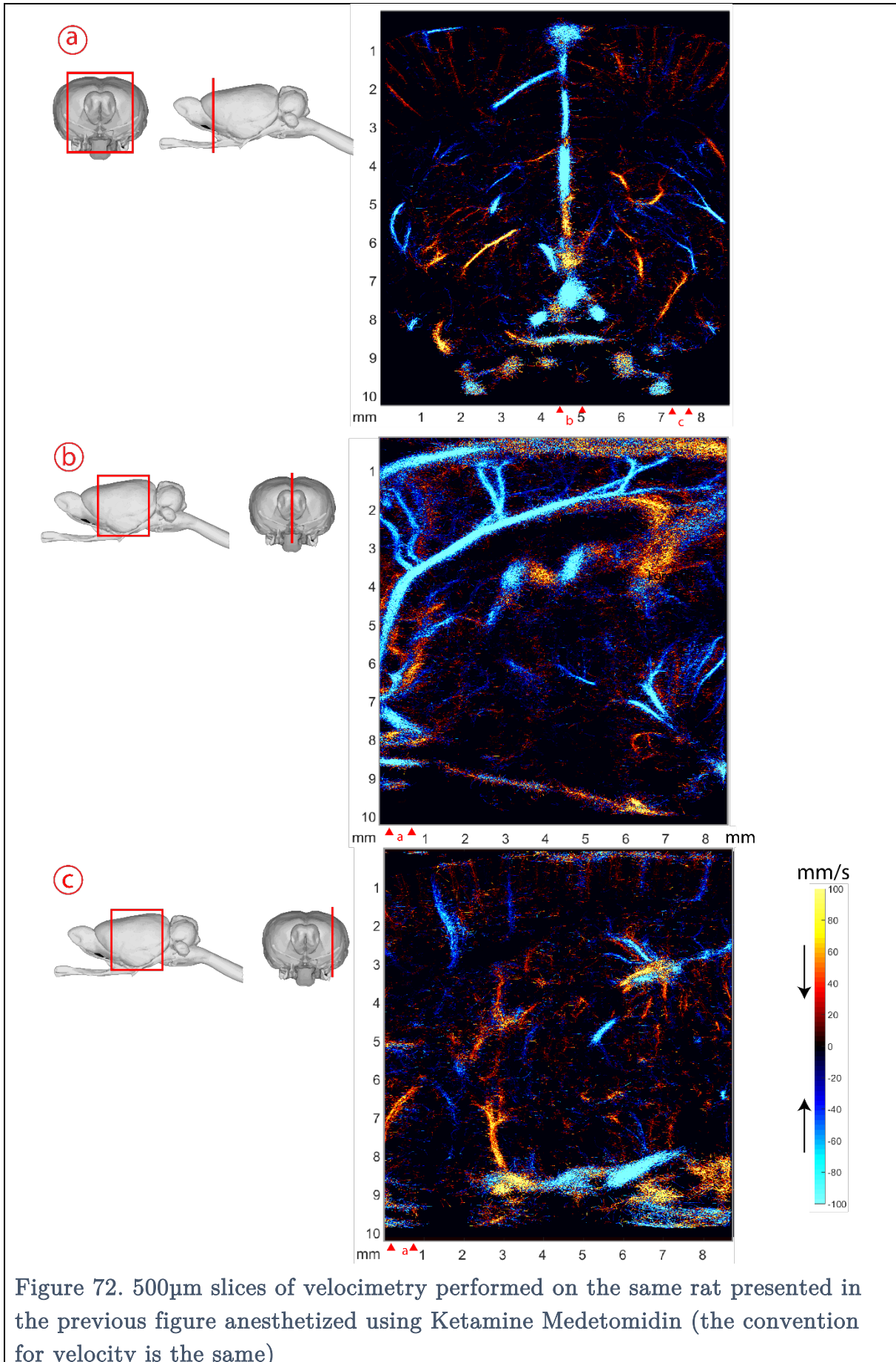


Figure 71. 500 μm slices of velocimetry performed on a rat brain anesthetized using Isoflurane (velocity is negative when going towards the top of the brain and positive when going towards the bottom)

- a) Coronal cut: The cortex vessels are visible as in the density images but the large range of velocities makes them less distinguishable. The veinules in the neocortex carry the blood from inside the brain towards the pial vessels. They are adequately labeled in blue. The posterior striate artery, however, is also labeled in blue. The blue/red distinction is only valid in the neocortex.
- b) Sagittal cut centered over the sinuses.
- c) Sagittal cut in the left hemisphere.

The same slices were taken for the Ketamine Medetomidin anesthetized rat. The results are presented in Figure 72. They are taken on the same rat, 45 minutes after the Isoflurane anesthesia has been switched off. Neither the probe nor the rat has changed positions and the same ULM post-processing is applied.

When looking at the characteristics of the brightest vessels in between Figure 71 and Figure 72, one can already notice quite a few differences. The vein ascending in the neocortex towards the superior sagittal sinus (circled in red) is visibly smaller in the Ketamine Medetomidin case than in the Isoflurane case. It is also noticeably less intense, meaning the velocity magnitude in that vein decreases when the anesthesia is changed. This effect can clearly be seen in the posterior striate artery as well as in the anterior striate artery. Larger vessels seem unaffected in size by the anesthesia but their velocities appear slower in the KD case: it is flagrant when looking at the azygos pericallosal artery. These large vessels carry a large amount of blood and as such, an equally large amount of microbubbles. They perform their vascular function with great speed and we see a higher amount of false positives in these vessels than in intermediate (λ to a few λ in diameters) or small vessels ($< \lambda$). Consequently, we have chosen smaller vessels to segment and compare between the two cases.



- f) Coronal cut
- g) Sagittal cut centered on sinuses
- h) Sagittal cut

IV.3.3 Velocimetry renderings for quantitative analysis of the vasculature

According to the additional processing described in IV.2.6, we have picked four different vessels: two in the neocortex, two in the striatum. We have picked two veins and two arteries. We picked the same vessels for the Isoflurane dataset and the Ketamine-Medetomidin dataset. The veins and arteries picked are presented in Table 4.

The maximum radius was measured by hand by computing the L2-norm of a vector orthogonal to the mean path of the vessel as it appears in the images presented above. Out of the four vessels, three undergo vasodilatation when the anesthesia is changed from Ketamine-Medetomidin to Isoflurane. The fourth one that does not show a dilatation shows vasoconstriction of 9 %. The vessel does appear larger in the Isoflurane case but as the measure is done on 3D projected slices, we hypothesize that another vessel is branching out of that vessel in the elevation direction increasing the perceived radius. The minimum radius measured in the same way shows a value for Isoflurane of $R_{Iso} = 58 \mu m$ and for Ketamin-Medetomidin $R_{KD} = 57 \mu m$. The variability of the measures is high for that vessel.

	Isoflurane	KD
Vessel 1	<p>First vessel pick : vein in the neocortex</p>	<p>First vessel pick : vein in the neocortex</p>
Radius	$R_{Iso} = 80 \mu m$	$R_{KD} = 69 \mu m$
Dilatation	$\tau_{Iso/KD} = 14 \%$	
Vessel 2	<p>Second vessel pick : artery in the neocortex</p>	<p>Second vessel pick : artery in the neocortex</p>
Radius	$R_{Iso} = 49 \mu m$	$R_{KD} = 18 \mu m$
Dilatation	$\tau_{Iso/KD} = 64 \%$	

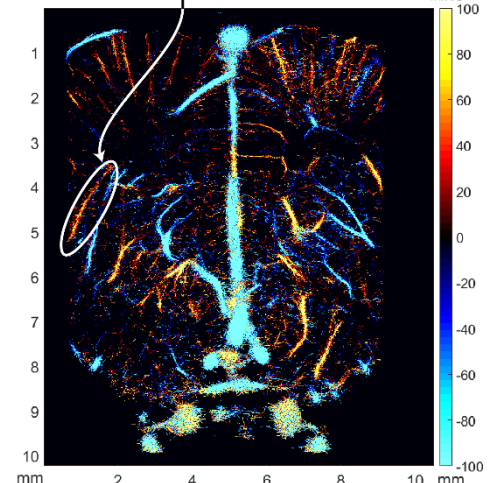
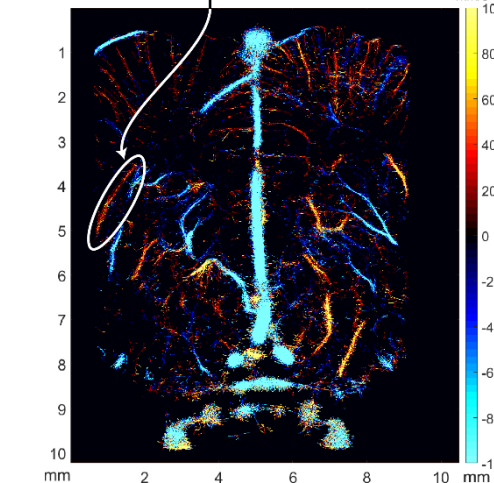
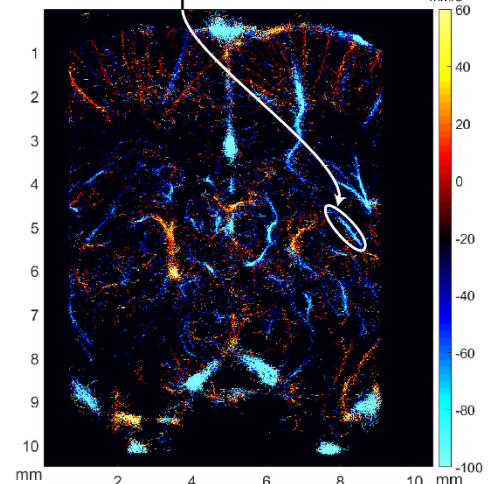
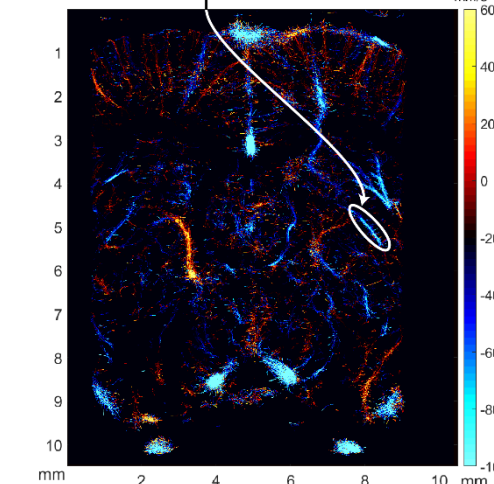
Vessel 3	<p>Third vessel pick : artery in the striatum</p> 	<p>Third vessel pick : artery in the striatum</p> 
	Radius	$R_{ISO} = 80 \mu m$
Dilatation	$\tau_{ISO/KD} = -9 \%$	
Vessel 4	<p>Fourth vessel pick : "vein" in the striatum</p> 	<p>Fourth vessel pick : "vein" in the striatum</p> 
	Radius	$R_{ISO} = 56 \mu m$
Dilatation	$\tau_{ISO/KD} = 14 \%$	

Table 4. Velocimetry renderings in 500 μm slices with overlaid picked vessels. The maximum radius measured by hand is computed in the last column

IV.3.4 Additional processing for velocimetry analysis in specific vessels

The velocity profiles were computed and are presented in Table 5.

	Vessel 1: vein in the neocortex	Vessel 2: artery in the far left hemisphere in the neocortex
Isoflurane	<p>Max velocity -5.6 mm/s</p>	<p>Max velocity 4.3 mm/s</p>
KD	<p>Max velocity -4.24 mm/s</p>	<p>Max velocity 3.7 mm/s</p>
$V_{maxIso} - V_{maxKD}$	$V_{maxIso} - V_{maxKD} = 1,4 \text{ mm/s}$ $\tau_{\%Iso/KD} = 24 \%$	$V_{maxIso} - V_{maxKD} = 0,6 \text{ mm/s}$ $\tau_{\%Iso/KD} = 14 \%$
Radius	$R_{Iso} = 75 \mu\text{m}$ $R_{KD} = 110 \mu\text{m}$ $\tau_{\%Iso/KD} = -46 \%$	$R_{Iso} = 70 \mu\text{m}$ $R_{KD} = 80 \mu\text{m}$ $\tau_{\%Iso/KD} = -14 \%$

	Vessel 3: artery in the striatum (connected to the posterior striate artery)	Vessel 4: “vein” in the striatum (non-cortical vessel going towards the top of the brain)
Isoflurane	<p>Max velocity 4.7 mm/s</p> <p>Norm of signed velocity in vessel Polynomial fitting, $R^2=0.82$</p>	<p>Max velocity -9.0 mm/s</p> <p>Norm of signed velocity in vessel Polynomial fitting, $R^2=0.73$</p>
KD	<p>Max velocity 5.2 mm/s</p> <p>Norm of signed velocity in vessel Polynomial fitting, $R^2=0.51$</p>	<p>Max velocity -6.3 mm/s</p> <p>Norm of signed velocity in vessel Polynomial fitting, $R^2=0.85$</p>
$V_{maxIso} - V_{maxKD}$	$V_{maxIso} - V_{maxKD} = -0,5 \text{ mm/s}$ $\tau_{\%Iso/KD} = -10 \%$	$V_{maxIso} - V_{maxKD} = 2,7 \text{ mm/s}$ $\tau_{\%Iso/KD} = 30 \%$
Radius	$R_{Iso} = 190 \mu\text{m}$ $R_{KD} = 175 \mu\text{m}$ $\tau_{\%Iso/KD} = 7 \%$	$R_{Iso} = 85 \mu\text{m}$ $R_{KD} = 90 \mu\text{m}$ $\tau_{\%Iso/KD} = -6 \%$

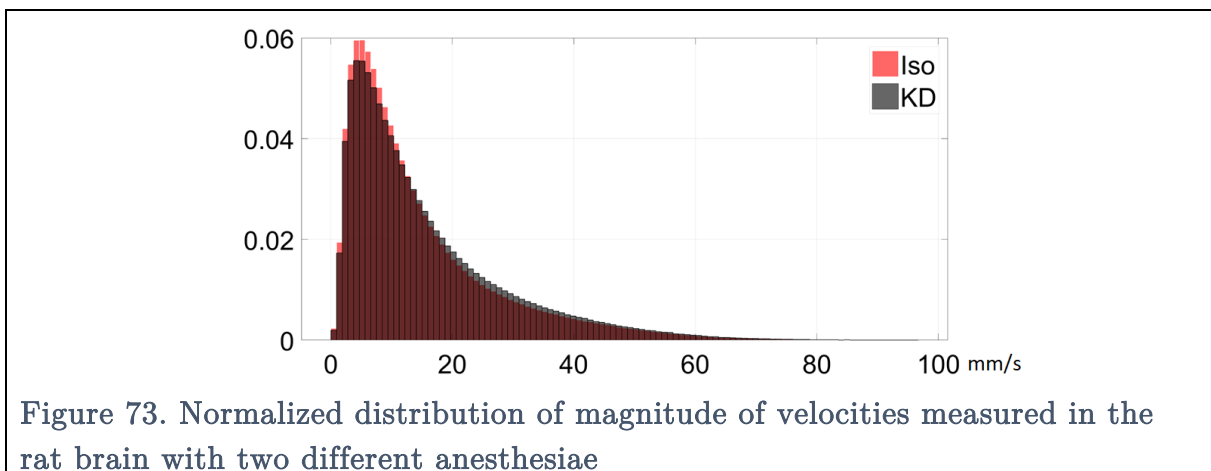
Table 5. Velocimetry analysis of the four vessels segmented: parabolic profile fitting, the maximum velocity measured, diameter inferred from the parabolic profile, dilatation coefficient

The maximum velocities measured in three out of the four vessels are higher under an Isoflurane than under a Ketamine-Medetomidin based anesthesia. In one out of the four vessels, this is not confirmed. The values measured for vessel 3 are poorly fitted with a second-order polynomial in the Ketamine Medetomidin case ($R^2 = 0,51$) and should be discarded. The profiles for vessels 1, 2 and 3 are well fitted with the second-order polynomial. One can observe that the velocity profiles seem “cleaner” for the Isoflurane cases than for the Ketamine-Medetomidin cases. This is confirmed when looking at the data as the vessels in the Ketamine-Medetomidin are usually smaller than the Isoflurane cases and thus contain fewer microbubble trajectories.

This is not confirmed when measuring the radii for the different vessels based on the velocity profiles, as the KD radii are always larger than Isoflurane radii. We have a large variation in the percentage of radius ratio in between the Iso/KD cases for various vessels.

There is no noticeable difference between the flow profile of a vein and the flow profile of an artery.

Furthermore, we can look at the distribution of velocities over all the vessels in the two different volumes. By calculating their histograms, we obtain the results presented in Figure 73. The vascular flow in a rat anesthetized with Isofluran has a higher number of small velocities below 12 mm/s and a lower overall count for velocities higher. One can notice that the peak of the distribution are aligned at the same velocities, meaning the distributions have the same mode. They have however a different mean with the KD’s distribution inflexion point being slightly higher than in the Isofluran case.



IV.4 Discussion

We have outline the steps for porting volumetric ULM *in vivo* in the rat brain model. Furthermore, we have extended the capability of velocimetry to blood flow and anatomical measurements. Several issues were overcome at the various stages.

IV.4.1 Animal

The most common issue we had with this experiment is related to the control of the physiological constants of the animals around the baseline. The surgery is quite long as we remove a large part of the skull and during this time, several cardio-respiratory deficiencies arise due to anesthesia (Constantinides et al., 2012). Contrary to hypothermia which can be monitored and solved quite easily, or dehydration which can be prevented, cardio-respiratory deficiencies are difficult to remedy. Because they are usually caused by overdosing the anesthesia, our protocol was to reduce the percentage of Isoflurane when possible but for Ketamine-Medetomidin, as it can not be reversed and as anyway it would be hard to precisely control it, the only thing we found effective was to maintain the animal under 100% O₂, keep it warm and hydrated and wait for recovery. This is quite inefficient in terms of time and other issues might arise in the meantime but we had good success in bringing back the animal to acceptable physiological constants.

We have observed that during the switch from Isoflurane to Ketamine-Medetomidin based anesthesia, the heart rate and breath rate dropped by as much as respectively 100 bpm and 40 bpm. We hypothesized that this is due to slight over dosing in anesthesia but due to the latency inherent to intra-peritoneal injection of Ketamine-Medetomidin this is hard to control. We tried to inject lower dosages of Ketamine-Medetomidin repeatedly until full dosage was attained without success. We simply injected the full dosage intra-peritoneously and decreased the percentage of Isoflurane to 0% in less than a minute while controlling the physiological constants and the withdrawal reflex. The animal was immediately covered by a lab glove filled with hot water to prevent hypothermia and return to the baseline was observed after a time in between 15 to 45 minutes at most. As we had to wait for an hour before acquiring Ketamine-Medetomidin images anyway to make sure Isoflurane was completely washed out by the organism, this process did not cost us too much time.

The bolus technique employed here requires 0.1 mL injection every 90 seconds. The total volume injected is 1.2 mL over 18 minutes. If this was to be done in perfusion

rather than with boli, the perfusion rate would be $1 \mu\text{L}/\text{s}$. We have tried doing perfusion rather than multiple boli however, we have deemed it unpractical for several reasons. The first is technical, our remote syringe pump (PHD Ultra Nanomite from Harvard Apparatus ®) does not let us set the perfusion rate and diameter of the syringe independently. One is ruled by the other. As we need a 1.2 mL volume, the syringe we had to employ had a too high diameter for the rate we wanted. The second reason is also technical albeit a bit more physical. Microbubbles are composed of gas, therefore they float if left in a syringe for too long. In a catheter, they will also float and the less the flow rate, the more they float. For a $1 \mu\text{L}/\text{s}$ perfusion rate, at our concentration, the microbubbles all float after being carried in the catheter for around 7 to 10 cm. That means reducing the length in between the point of entry in the vein of the catheter and the tip of the needle where the syringe is connected. Having such a small catheter is not easy with the stereotactic frame. Moreover, we are not sure microbubbles do not float before the visually determined length of 7 to 10 centimeters. We decided against that and chose to inject multiple boli. It has to be noted that another way to remedy microbubbles floating on the top of the catheter is to use a 3-way connector and perform flushes every couple of minutes. The problem with that solution is two-fold: it will increase the total volume injected, the concentration injected is not constant and therefore we lose the advantage of continuous perfusion.

A crucial part of the surgery is separating the dura mater from the skull window. This tissue is fixed to the skull in a few places. We use a micro-spatula made by FST (Ref 10091-12) to slowly detach the dura mater from the skull by sliding the end of the tool from the outer sutures towards the Bregma-Lambda line. Unfortunately, even with all the care in the world, sometimes, the dura mater was ripped. In this situation, two things could happen, either nothing and we would carry on surgery, or hemorrhage. In the latter case, the tool was removed, and pressure was applied to the skull to prevent further bleeding. Surgery was later carried on from another side. In a handful of cases where hemorrhage happened, we have not seen an impact of the bleeding on the brain. However, when the dura mater was ripped over a large area, we could see the brain rearranging under increased intracranial pressure. The brain seemed to be “popping out” from the dura mater and the imaging was deemed unusable for our anatomical studies. Sometimes, the dura mater ripped over the entire window and while it is certainly not good for the animal, the image could be used for anatomical studies.

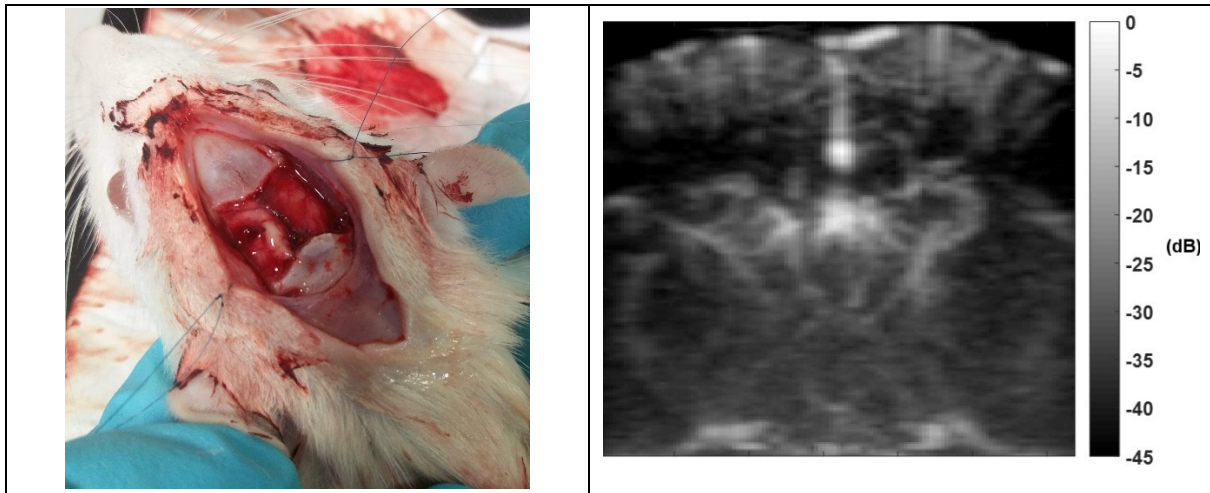


Figure 74. Picture of the effect of ripped dura mater on a craniotomized rat and ultrasound power Doppler image of corresponding coronal plane

The S-shape rearrangement of the brain seen in white in the picture is a direct consequence of ripped dura mater. The intracranial pressure is not compensated by the dura mater and subsequently, the brain expands. It can be seen using B-mode imaging on the right image, where the top of the right hemisphere cortex expands largely above the superior sagittal sinus. There are no consequences for the health of the rat and no unanticipated death has been seen in these cases. It is, however, better to keep the dura mater intact during surgery.

IV.4.2 Ultrasound sequence

For 3D imaging with the 1024 channel ultrasound scanner, the pause in between two continuous block of acquisition increases dramatically: **0.370 s** of acquisition at a compounded volume rate of 500Hz will require **1.630** seconds of pause. That allows us to image continuously for more than 18 minutes to acquire an amount of 99,900 images. The duration of this transfer step was reduced considerably by using SSDs connected by SATA 6GB/s on each of the four motherboards. Unfortunately because of aging material, using NVMEs was not possible as the motherboards were not compatible with such a technology. The pausing time was set to **1.630** seconds. The pause is also due to the data transfer rates between the DAQs and the host computers of each machine being low. The echographs used to build the 1024 channel ultrasound system are more than 7 years old and so data transfers and data handling by the operating system is very poor (7 years ago, SSD were not a common thing, NVMe did not exist, RAM was limited to 4GB/s and floppy disks were still sold).

The probe was placed directly over the brain with a spacing higher than 3 mm. This allowed us to avoid imaging the brain in the near field of the probe which has lower

SNR and where one can see the 3 disconnected lines of the probe. These caused black zones in our ULM renderings where the signal to noise ratio is low and fewer microbubbles are detected and localized accurately by the algorithm. The problem with this trick is two-fold: it does not allow us to image as deep as we want to, it yields additional data where there is nothing of interest except for signal coming from the coupling medium. Because of the way our ultrasound machines acquire the data, the radiofrequency data contains that useless information and it needs to be transferred from the DAQs to the computers in each machine. In the case where that data could be dispensed with before the DAQs record it, we would have a decrease in data from 10% to 15%.

The 1.640 s pause implemented in between each 0.370 s of acquisition implied that we could not use the conventional bolus based technique for microbubble injection. Instead, we relied on several smaller boli of 0.1 mL every 90 seconds to achieve an overall 0.80mL/min. The issue with this is that a lot of time where microbubbles are present in the organ is wasted and as such, one has to be careful not to cause hypervolemia which could lead to kidney failure. However, Arthur Chavignon has conducted new experiments with a Verasonics system driving a Multiplexed 2D matrix array similar to ours and successfully written a sequence following my framework but achieving true continuous imaging at 500 Hz with fewer angles and similar signal to noise ratio. The gain in signal to noise ratio is likely to be due to the progress made by Vermon® for blinding of the probe. The way the ultrasound machine acquires the data, the gap between the probe and the brain is also dispensed with, allowing the decrease in data mentioned above. This is a wonderful follow up to our framework and we hope that it will lead to wider usage of 3D ULM not only in our team but also in other teams around the world.

IV.4.3 ULM processing

The ULM processing was described in IV.2.5. The parallel implementation of this processing is essential to reducing computation time and to test out different parameters. The beamformed data is not saved during ULM computation to keep data storage to a minimum. Saving the beamformed volumes would yield 25% more data and as one acquisition of 540 blocks already weighs several hundreds of gigabytes, this is simply not a good option. Several tricks were implemented in the algorithms to keep data size to a minimum such as rounding the localized center of microbubbles to the theoretical precision of 1 μm demonstrated in chapter 2, rounding the velocities to 100 $\mu\text{m/s}$, interpolating the tracks on grids corresponding to the resolution, etc... Overall, considerable time was spent coming out with an algorithm that can run fast, keeps data

consumption to a minimum and renders both accurate and high-quality renderings without resorting to filters. We are convinced that computationally simple and fast algorithms are crucial to spreading the use of both 2D and 3D ULM in ultrasound labs but also wider in preclinical and clinical studies led by biologists and clinicians alike.

IV.4.4 Anatomical variations

We have tried to recognize and label as many vessels as possible in the density-based images. To do so, we have looked at the literature on the brain and vasculature of the mouse (Dong, 2008; Franklin and Paxinos, 2013; Xiong et al., 2017). The need for a precise brain vascular atlas for the rat is dire. The anatomical variations in the brain vasculature between animals are actually quite large and although we have not presented two different sets of data here, we know from experience that it is almost impossible to completely register two brains coming from different animals together. This is due to the high level of deviation in the organization of the microvasculature in the brain. In our case, it is problematic as we can not register the datasets from the same anesthesia on different rats together. To circumvent that problem, we chose to extract physical characteristics of the anatomy of the brains and compare them together. I have presented here in the results a glimpse of what is possible in terms of quantitative measurements and we believe we will be able to generate more in the future: diameter of the vessels, end-points, branches, tortuosity, curvature, skeletonized rendering of the brain, mean section, surface of the vessels... To achieve this, our minds should be turned to automatic segmentation tools while taking the precaution that our volumes are of a size considerably larger than what these tools were originally made for. Care should be taken when adapting already existing processes to ULM data at the risk of crashing the computer and losing data.

The problem with anatomical variations happens inter-animal but also during the experiment. Isofluran is known for increasing intracranial pressure. This is noticeable in all of the figures in Table 4 where vessels appear smaller in the KD case than in the Isofluran and where the brain has sunk down. The relative position of the brain to the probe can also change a bit during the experiment. Because the probe is quite large and the brain should only expand or deflate uniformly in the region of imaging, this variation can be compensated for using a simple translation or a combination of a translation and a rotation.

IV.4.5 Velocimetry results

The velocities computed reflect the assumed Poiseuille flow profiles in most vessels. These can be fitted with a quadratic curve with a good fit even in the smallest vessels. The range of the velocity measured is high from a few mm/s to 100mm/s . The limitation of maximum velocity comes from the tracking algorithm where a maximum distance allowed in between microbubbles is set to prevent pairing distinct microbubbles. This maximum distance is set to $200\ \mu\text{m}$ and at 500 Hz compounded volume rate this gives a maximum velocity of $100\ \text{mm/s}$. This limit can be surpassed if the volume rate is increased, however, a maximum velocity of $100\ \text{mm/s}$ is already quite high for the rat brain and as we are limited by the aging echographs for data acquisition, we kept 500 Hz as a compounded volume rate.

The range of velocity, however, makes it difficult to see all of the vessels with the same contrast. We recommend using density-based images for vasculature visualization and velocimetry for quantitative analysis. The complex nature of velocimetry renderings as it is composed of velocities in the three directions makes it quite hard to really render dynamic images of the flow in the brain. We have tried experimenting with arrows defined by the magnitude and directions but failed. The range of velocities and the range of diameters of the vasculature is simply too complex to render at this stage.

IV.4.6 Additional processing for velocimetry analysis

The radius measurements were done using two techniques either manually or by calculating the diameter of measured flow profiles. The radii are consistently lower when calculated manually than when calculated with the flow profiles. This is due to the way the flow profiles are computed: the velocities along the mean path of the vessels are averaged. The vessel was re-projected to be straight in the calculation basis but curvature remains. The flow profile is obtained by averaging all speeds along the straightened vessel, and as such, the final profile will appear larger than what it really is. A way to circumvent this would be to only look at a profile in one section rather than averaging all of the sections of the vessel at the risk of having less information to reconstruct the profile. This would be similar to what was done in chapter 3 for reconstruction of all the velocities along the profile of the microcanals.

Because of this overestimation, the vasodilation is not observable anymore when looking at the velocity-measured diameters although it is clearly visible when looking at the images presented in Table 4. It is important to note, however, that the vessels 1, 2 and 4 are all sub-wavelength ($\lambda = 170\ \mu\text{m}$) and that it is possible to construct a velocity

profile at a resolution down to 10 μm with R^2 coefficients over 75%.

In vessel 3, we have outlined many discrepancies in the results for radius calculation and flow profiles compared to the other vessels. We hypothesized that this vessel separates into a branch in the elevation dimension in the IV.3 Results section. When we looked at the sagittal slices we noticed that this vessel is much larger in the elevation direction than in the lateral direction. The explanation is as follows: after segmenting the vessel manually, we compute its curvature and straighten the vessel accordingly. We then proceed to average the velocity profiles in the elevation direction and then along the mean path of the vessel. Our error appears when we average in the elevation direction. The vessel is straight in the lateral dimension but is still curved in the elevation plane! 3D curvature computing should be implemented to remedy that error. This is more computationally expensive albeit it would be useful to compute the curvature automatically for every vessel in the image and then straighten them all to perform velocity profile analysis.

The velocity is higher for three cases out of four in Isoflurane induced anesthesia than in Ketamine-Medetomidin. As there is vasodilatation in Isoflurane, one could assume that velocity should be lower by applying conservation of flow rate. However, (Li et al., 2014; Madsen et al., 1987) have proven that there is a cerebral blood flow increase with Halothane and Isoflurane in both humans and macaque monkeys. This seems to be confirmed in rats by our study. Blood flow can be modeled in a cylindrical vessel as $Q_{BF} = \int V dS = V_{moy} \times \frac{\pi R^2}{4}$ and for a Poiseuille flow, $V_{moy} = \frac{V_{max}}{2}$, and so $Q_{BF} = \frac{V_{max}\pi R^2}{8}$. An increase in both the maximum velocity and the radius of the vessel should then result in an increase of cerebral blood flow.

Additionally, histograms of the velocity distribution have been plotted in the two anesthesia cases. The noticeable difference of both maximum distribution and inflexion points has been highlighted. The exact mechanism is not yet explained but it seems that the location of the mode being the same and the mean being different point to a difference in overall blood flow. Further study should be carried on with various isoflurane concentration and with semi-automatic or automatic velocimetry processing.

IV.5 Conclusion

We have successfully scaled up the second and third chapter to *in vivo* cases. The work described in the second chapter allowed us to perform fast and accurate localization of microbubbles flowing inside the vasculature of a rat brain. The processing and ultrasound

sequences described in the third chapter guided us to go further in volumetric ULM and acquire large volumes at a compounded volume rate of 500 Hz for thousands of seconds with sufficient SNR to perform millions of localizations, assigned these localizations to form thousands of trajectories and finally perform velocimetry. The animal model used allowed us to experiment with our technique and go beyond improving resolution of the volume to provide micrometric scale vascular analysis. The volumetric ULM tool was demonstrated as a blood flow sensor, capable of detecting vascular changes both on an anatomic and dynamic scale induced by anesthesia. Work remains to be done to prove the robustness of the results presented here such as statistical analysis on different animals. The main disadvantage of the technique proposed here is the fact that it is based on manual segmentation and manual adjustment of the curvature to straighten the vessel. Developing an automatic tool that could also perform quantitative analysis in 3D would alleviate that problem and port volumetric ULM into a fully automated microvascular sensor.

- Abee, C.R. (Ed.), 2012. Nonhuman primates in biomedical research, Second edition. ed, American College of Laboratory Animal Medicine series. Academic Press, an imprint of Elsevier, Amsterdam.
- Arbeille, P., Eder, V., Casset, D., Quillet, L., Hudelo, C., Herault, S., 2000. Real-time 3-D ultrasound acquisition and display for cardiac volume and ejection fraction evaluation. *Ultrasound Med. Biol.* 26, 201–208. [https://doi.org/10.1016/S0301-5629\(99\)00125-8](https://doi.org/10.1016/S0301-5629(99)00125-8)
- Austeng, A., Holm, S., 2002. Sparse 2-D arrays for 3-D phased array imaging - design methods. *IEEE Trans. Ultrason. Ferroelectr. Freq. Control* 49, 1073–1086. <https://doi.org/10.1109/TUFFFC.2002.1026019>
- Boni, C., Richard, M., Barbarossa, S., 1994. Optimal configuration and weighting of nonuniform arrays according to a maximum ISLR criterion, in: Proceedings of ICASSP '94. IEEE International Conference on Acoustics, Speech and Signal Processing. Presented at the ICASSP '94. IEEE International Conference on Acoustics, Speech and Signal Processing, IEEE, Adelaide, SA, Australia, p. V/157-V/160. <https://doi.org/10.1109/ICASSP.1994.389424>
- Brunke, S.S., Lockwood, G.R., 1997. Broad-bandwidth radiation patterns of sparse two-dimensional vernier arrays. *IEEE Trans. Ultrason. Ferroelectr. Freq. Control* 44, 1101–1109. <https://doi.org/10.1109/58.655635>
- Buck, T., Plicht, B., 2015. Real-Time Three-Dimensional Echocardiographic Assessment of Severity of Mitral Regurgitation Using Proximal Isovelocity Surface Area and Vena Contracta Area Method. Lessons We Learned and Clinical Implications 11.
- Chen, K., Hae-Seung, L., Charles, G., Sodini, 2016. A Column-Row-Parallel ASIC Architecture for 3-D Portable Medical Ultrasonic Imaging. *IEEE J. Solid-State Circuits* 51, 738–751. <https://doi.org/10.1109/JSSC.2015.2505714>
- Christiansen, T.L., Rasmussen, M.F., Bagge, J.P., Moesner, L.N., Jensen, J.A., Thomsen, E.V., 2015. 3-D imaging using row-column-addressed arrays with integrated apodization— part ii: transducer fabrication and experimental results. *IEEE Trans. Ultrason. Ferroelectr. Freq. Control* 62, 959–971. <https://doi.org/10.1109/TUFFFC.2014.006819>
- Chung, K., Wallace, J., Kim, S.-Y., Kalyanasundaram, S., Andalman, A.S., Davidson, T.J., Mirzabekov, J.J., Zalocusky, K.A., Mattis, J., Denisin, A.K., Pak, S., Bernstein, H., Ramakrishnan, C., Grosenick, L., Gradinaru, V., Deisseroth, K., 2013. Structural and molecular interrogation of intact biological systems. *Nature* 497, 332–337. <https://doi.org/10.1038/nature12107>
- Coatney, R.W., 2001. *Ultrasound Imaging: Principles and Applications in Rodent Research* 42, 15.
- Cobbold, R.S.C., 2005. *Foundations of Biomedical Ultrasound* 14.
- Constantinides, C., Mean, R., Janssen, B.J., 2012. Effects of Isoflurane Anesthesia on

- the Cardiovascular Function of the C57BL/6 Mouse 20.
- Czernuszewicz, T.J., Papadopoulou, V., Rojas, J.D., Rajamahendiran, R.M., Perdomo, J., Butler, J., Harlacher, M., O'Connell, G., Zukić, D., Aylward, S.R., Dayton, P.A., Gessner, R.C., 2018. A new preclinical ultrasound platform for widefield 3D imaging of rodents. *Rev Sci Instrum* 10.
- Dave, J.K., 2018. Recent technological advancements in cardiac ultrasound imaging 12.
- Daidsen, R.E., Jensen, J.A., Smith, S.W., 1994. Two-dimensional random arrays for real time volumetric imaging. *Ultrason. Imaging*.
- Demené, C., Tiran, E., Sieu, L.-A., Bergel, A., Gennisson, J.L., Pernot, M., Deffieux, T., Cohen, I., Tanter, M., 2016. 4D microvascular imaging based on ultrafast Doppler tomography. *NeuroImage* 127, 472–483. <https://doi.org/10.1016/j.neuroimage.2015.11.014>
- Desailly, Y., Pierre, J., Couture, O., Tanter, M., 2015. Resolution limits of ultrafast ultrasound localization microscopy. *Phys. Med. Biol.* 60, 8723–8740. <https://doi.org/10.1088/0031-9155/60/22/8723>
- Dong, H., 2008. The Allen reference atlas: A digital color brain atlas of the C57Bl/6J male mouse.
- Ertürk, A., Becker, K., Jährling, N., Mauch, C.P., Hojer, C.D., Egen, J.G., Hellal, F., Bradke, F., Sheng, M., Dodt, H.-U., 2012. Three-dimensional imaging of solvent-cleared organs using 3DISCO. *Nat. Protoc.* 7, 1983–1995. <https://doi.org/10.1038/nprot.2012.119>
- Ertürk, A., Bradke, F., 2013. High-resolution imaging of entire organs by 3-dimensional imaging of solvent cleared organs (3DISCO). *Exp. Neurol.* 242, 57–64. <https://doi.org/10.1016/j.expneurol.2012.10.018>
- Fisher, R., Thomenius, K., Wodnicki, R., Thomas, R., Cogan, S., Hazard, C., Lee, W., Mills, D., Khuri-Yakub, B., Ergun, A., Yaralioglu, G., 2005. Reconfigurable arrays for portable ultrasound, in: *IEEE Ultrasonics Symposium, 2005. Presented at the IEEE Ultrasonics Symposium, 2005., IEEE, Rotterdam, The Netherlands*, pp. 495–499. <https://doi.org/10.1109/ULTSYM.2005.1602899>
- Flesch, M., Pernot, M., Provost, J., Ferin, G., Nguyen-Dinh, A., Tanter, M., Deffieux, T., 2017. 4D *in vivo* ultrafast ultrasound imaging using a row-column addressed matrix and coherently-compounded orthogonal plane waves. *Phys. Med. Biol.* 62, 4571–4588. <https://doi.org/10.1088/1361-6560/aa63d9>
- Franklin, K.B.J., Paxinos, G., 2013. *Paxinos and Franklin's: The mouse brain in stereotaxic coordinates*, 4th ed. Amsterdam: Academic Press.
- Holm, S., Elgetun, B., Dahl, G., 1997. Properties of the beampattern of weight- and layout-optimized sparse arrays. *IEEE Trans. Ultrason. Ferroelectr. Freq. Control* 44, 983–991. <https://doi.org/10.1109/58.655623>
- Jensen, J.A., Holten-Lund, H., Nilsson, R.T., Hansen, M., Larsen, U.D., Domsten, R.P., Tomov, B.G., Stuart, M.B., Nikolov, S.I., Pihl, M.J., Yigang Du, Rasmussen, J.H., Rasmussen, M.F., 2013. SARUS: A synthetic aperture real-time ultrasound

- system. IEEE Trans. Ultrason. Ferroelectr. Freq. Control 60, 1838–1852. <https://doi.org/10.1109/TUFFFC.2013.2770>
- Lang, R.M., Badano, L.P., Mor-Avi, V., Afilalo, J., Armstrong, A., Ernande, L., Flachskampf, F.A., Foster, E., Goldstein, S.A., Kuznetsova, T., Lancellotti, P., Muraru, D., Picard, M.H., Rietzschel, E.R., Rudski, L., Spencer, K.T., Tsang, W., Voigt, J.-U., 2015. Recommendations for Cardiac Chamber Quantification by Echocardiography in Adults: An Update from the American Society of Echocardiography and the European Association of Cardiovascular Imaging. J. Am. Soc. Echocardiogr. 28, 1-39.e14. <https://doi.org/10.1016/j.echo.2014.10.003>
- Law, J., Macbeth, P.B., 2011. Ultrasound: From Earth to Space 13, 4.
- Li, C.-X., Patel, S., Wang, D.J.J., Zhang, X., 2014. Effect of high dose isoflurane on cerebral blood flow in macaque monkeys. Magn. Reson. Imaging 32, 956–960. <https://doi.org/10.1016/j.mri.2014.04.019>
- Logan, A.S., Wong, L.L.P., Chen, A.I.H., Yeow, J.T.W., 2011. A 32 x 32 element row-column addressed capacitive micromachined ultrasonic transducer. IEEE Trans. Ultrason. Ferroelectr. Freq. Control 58, 1266–1271. <https://doi.org/10.1109/TUFFFC.2011.1937>
- Madsen, J.B., Cold, G.E., Hansen, E.S., Bardrum, B., 1987. The Effect of Isoflurane on Cerebral Blood Flow and Metabolism in Humans during Craniotomy for Small Supratentorial Cerebral Tumors. Anesthesiology.
- Martínez-Graullera, O., Martín, C.J., Godoy, G., Ullate, L.G., 2010. 2D array design based on Fermat spiral for ultrasound imaging. Ultrasonics 50, 280–289. <https://doi.org/10.1016/j.ultras.2009.09.010>
- Matrone, G., Savoia, A.S., Terenzi, M., Caliano, G., Quaglia, F., Magenes, G., 2014. A volumetric CMUT-based ultrasound imaging system simulator with integrated reception and μ -beamforming electronics models. IEEE Trans. Ultrason. Ferroelectr. Freq. Control 61, 792–804. <https://doi.org/10.1109/TUFFFC.2014.2971>
- Olaf T. von Ramm, Stephen W. Smith, Henry G. Pavy Jr., 1991. High-speed Ultrasound Volumetric Imaging System- Part II: Parallel Processing and Image Display.
- O’Mahony, E., Araujo Junior, E., Ferreira, A.C., Da Silva Costa, F., 2016. Telemedicine 3D- and 4D-ultrasound in Obstetrics and Gynecology., in: Advanced Topics on Three-Dimensional Ultrasound in Obstetrics and Gynecology. Bentham Science Publishers, pp. 47–61.
- Papadacci, C., Bunting, E.A., Wan, E.Y., Nauleau, P., Konofagou, E.E., 2017a. 3D Myocardial Elastography In Vivo. IEEE Trans. Med. IMAGING 36, 10.
- Papadacci, C., Finel, V., Provost, J., Villemain, O., Bruneval, P., Gennisson, J.-L., Tanter, M., Fink, M., Pernot, M., 2017b. Imaging the dynamics of cardiac fiber orientation in vivo using 3D Ultrasound Backscatter Tensor Imaging. Sci. Rep. 7, 830. <https://doi.org/10.1038/s41598-017-00946-7>
- Papadacci, C., Finel, V., Villemain, O., Goudot, G., Provost, J., Messas, E., Tanter, M.,

- Pernot, M., 2019. 4D simultaneous tissue and blood flow Doppler imaging: revisiting cardiac Doppler index with single heart beat 4D ultrafast echocardiography. *Phys. Med. Biol.* 64, 085013. <https://doi.org/10.1088/1361-6560/ab1107>
- Pernot, M., Tanter, M., Fink, M., 2004. 3-D real-time motion correction in high-intensity focused ultrasound therapy. *Ultrasound Med. Biol.* 30, 1239–1249. <https://doi.org/10.1016/j.ultrasmedbio.2004.07.021>
- Petrusca, L., Varray, F., Souchon, R., Bernard, A., Chapelon, J.-Y., Liebgott, H., N'Djin, W., Viallon, M., 2018. Fast Volumetric Ultrasound B-Mode and Doppler Imaging with a New High-Channels Density Platform for Advanced 4D Cardiac Imaging/Therapy. *Appl. Sci.* 8, 200. <https://doi.org/10.3390/app8020200>
- Prager, R.W., Ijaz, U.Z., Gee, A.H., Treece, G.M., 2010. Three-dimensional ultrasound imaging. *Proc. Inst. Mech. Eng. [H]* 224, 193–223. <https://doi.org/10.1243/09544119JEIM586>
- Provost, J., Papadacci, C., Arango, J.E., Imbault, M., Fink, M., Gennisson, J.-L., Tanter, M., Pernot, M., 2014. 3D ultrafast ultrasound imaging *in vivo*. *Phys. Med. Biol.* 59, L1–L13. <https://doi.org/10.1088/0031-9155/59/19/L1>
- Rabut, C., Correia, M., Finel, V., Pezet, S., Pernot, M., Deffieux, T., Tanter, M., 2019. 4D functional ultrasound imaging of whole-brain activity in rodents. *Nat. Methods* 16, 994–997. <https://doi.org/10.1038/s41592-019-0572-y>
- Ramadas, S.N., Jackson, J.C., Dziewierz, J., O'Leary, R., Gachagan, A., 2014. Application of conformal map theory for design of 2-D ultrasonic array structure for ndt imaging application: a feasibility study. *IEEE Trans. Ultrason. Ferroelectr. Freq. Control* 61, 496–504. <https://doi.org/10.1109/TUFFC.2014.2933>
- Ramalli, A., Boni, E., Savoia, A.S., Tortoli, P., 2015. Density-tapered spiral arrays for ultrasound 3-D imaging. *IEEE Trans. Ultrason. Ferroelectr. Freq. Control* 62, 1580–1588. <https://doi.org/10.1109/TUFFC.2015.007035>
- Rasmussen, M.F., Christiansen, T.L., Thomsen, E.V., Jensen, J.A., 2015. 3-D imaging using row-column-addressed arrays with integrated apodization - part i: apodization design and line element beamforming. *IEEE Trans. Ultrason. Ferroelectr. Freq. Control* 62, 947–958. <https://doi.org/10.1109/TUFFC.2014.006531>
- Rasmussen, M.F., Jensen, J.A., 2013. 3D ultrasound imaging performance of a row-column addressed 2D array transducer: a simulation study, in: Bosch, J.G., Doyley, M.M. (Eds.), . p. 86750C. <https://doi.org/10.1117/12.2007083>
- Renier, N., Wu, Z., Simon, D.J., Yang, J., Ariel, P., Tessier-Lavigne, M., 2014. iDISCO: A Simple, Rapid Method to Immunolabel Large Tissue Samples for Volume Imaging. *Cell* 159, 896–910. <https://doi.org/10.1016/j.cell.2014.10.010>
- Roux, E., Tortoli, P., Liebgott, H., 2016. 2-D Ultrasound Sparse Arrays Multidepth Radiation Optimization Using Simulated Annealing and Spiral-Array Inspired Energy Functions 63, 12.

- Scherrer-Crosbie, M., Steudel, W., Hunziker, P.R., Liel-Cohen, N., Ullrich, R., Zapol, W.M., Picard, M.H., 1999. Three-Dimensional Echocardiographic Assessment of Left Ventricular Wall Motion Abnormalities in Mouse Myocardial Infarction. *J. Am. Soc. Echocardiogr.* 12, 834–840. [https://doi.org/10.1016/S0894-7317\(99\)70188-4](https://doi.org/10.1016/S0894-7317(99)70188-4)
- Schlosshan, D., Aggarwal, G., Mathur, G., Allan, R., Cranney, G., 2011. Real-Time 3D Transesophageal Echocardiography for the Evaluation of Rheumatic Mitral Stenosis. *Cardiovasc. IMAGING* 4, 9.
- Sciallero, C., Trucco, A., 2015. Design of a sparse planar array for optimized 3D medical ultrasound imaging, in: 2015 23rd European Signal Processing Conference (EUSIPCO). Presented at the 2015 23rd European Signal Processing Conference (EUSIPCO), IEEE, Nice, pp. 1341–1345. <https://doi.org/10.1109/EUSIPCO.2015.7362602>
- Smith, S.W., Pavy, H.G., 1991. High-speed Ultrasound Volumetric Imaging System- Part I: Transducer Design and Beam Steering 9.
- Tanter, M., Pernot, M., Aubry, J.-F., Montaldo, G., Marquet, F., Fink, M., 2007. Compensating for bone interfaces and respiratory motion in high-intensity focused ultrasound. *Int. J. Hyperthermia* 23, 141–151. <https://doi.org/10.1080/02656730701209996>
- Turnbull, D.H., Foster, F.S., 1991. Beam steering with pulsed two-dimensional transducer arrays. *IEEE Trans. Ultrason. Ferroelectr. Freq. Control* 38, 320–333. <https://doi.org/10.1109/58.84270>
- Weber, Schmitt, Tylkowski, Steck, 1994. Optimization of random sparse 2-D transducer arrays for 3-D electronic beam steering and focusing, in: Proceedings of IEEE Ultrasonics Symposium ULTSYM-94. Presented at the Proceedings of IEEE Ultrasonics Symposium ULTSYM-94, IEEE, Cannes, France, pp. 1503–1506 vol.3. <https://doi.org/10.1109/ULTSYM.1994.401875>
- Werner, H., Castro, P., T., Matos, A., P., Lopes, J., Ribeiro, G., Daltro, P., Campbell, S., 2019a. 3D printing in fetal medicine. *Abstr. 29th World Congr. Ultrasound Obstet. Gynecol.* 12–16 Oct. 2019 Berl. Ger. 54, 1.
- Werner, H., Matos, A., P., Castro, P., T., Daltro, P., Fazecas, T., Nogueira, R., Lopes, J., Ribeiro, G., 2019b. Conjoined twins: how 3D printing can help. *Abstr. 29th World Congr. Ultrasound Obstet. Gynecol.* 12–16 Oct. 2019 Berl. Ger. 54, 1.
- Wygant, I.O., Jamal, N.S., Lee, H.J., Nikoozadeh, A., Oralkan, O., Karaman, M., Khuriyakov, B.T., 2009. An integrated circuit with transmit beamforming flip-chip bonded to a 2-D CMUT array for 3-D ultrasound imaging. *IEEE Trans. Ultrason. Ferroelectr. Freq. Control* 56, 2145–2156. <https://doi.org/10.1109/TUFFFC.2009.1297>
- Xiong, B., Li, A., Lou, Y., Chen, S., Long, B., Peng, J., Yang, Z., Xu, T., Yang, X., Li, X., Jiang, T., Luo, Q., Gong, H., 2017. Precise Cerebral Vascular Atlas in Stereotaxic Coordinates of Whole Mouse Brain. *Front. Neuroanat.* 11, 128.

<https://doi.org/10.3389/fnana.2017.00128>

Zekry, S.B., 2011. Comparative Accuracy of Two- and Three-Dimensional Transthoracic and Transesophageal Echocardiography in Identifying Mitral Valve Pathology in Patients Undergoing Mitral Valve Repair: Initial Observations. *J. Am. Soc. Echocardiogr.* 24, 7.

V

Towards whole-brain imaging

V. Chapter 5: Towards whole-brain imaging

We have been imaging the brain in our lab for more than 10 years, from the earliest demonstration of elasticity mapping in 2009 (Macé et al., 2009) to the demonstration of angiography (Macé et al., 2010) and functional ultrasound (Macé et al., 2011). It was also the organ chosen for the demonstration of 2D Ultrasound Localization Microscopy *in vivo* (Errico et al., 2015). We have accumulated considerable experience in surgery and imaging of this specific anatomical region in rodents.

In chapter 4, we have demonstrated that 3D ULM can be implemented on this organ as well. In this chapter, we ask the question of whether we can use that technique to perform whole-brain imaging and velocimetry. The motivation behind this is to produce an atlas of the brain *in vivo* at a micrometric level with information on velocities. This is as far as we know the first time this has ever be attempted.

V.1 Anatomical whole-brain imaging: a state of the art

The brain is the most sophisticated, complex and significant of all organs regardless of the species. It is the subject of many seminal papers in both anatomical studies, functional decoding, cellular studies but also computer vision. It is made of several highly different components such as neurons (diameter of 10-30 μm , up to 50 pyramidal cells), glial cells (2-5 μm), blood vessels (5-several hundreds of μm), neuritis (less than a μm). Imaging such a diverse organ is rendered even more complicated by its size and by its location in the body under the protective skull.

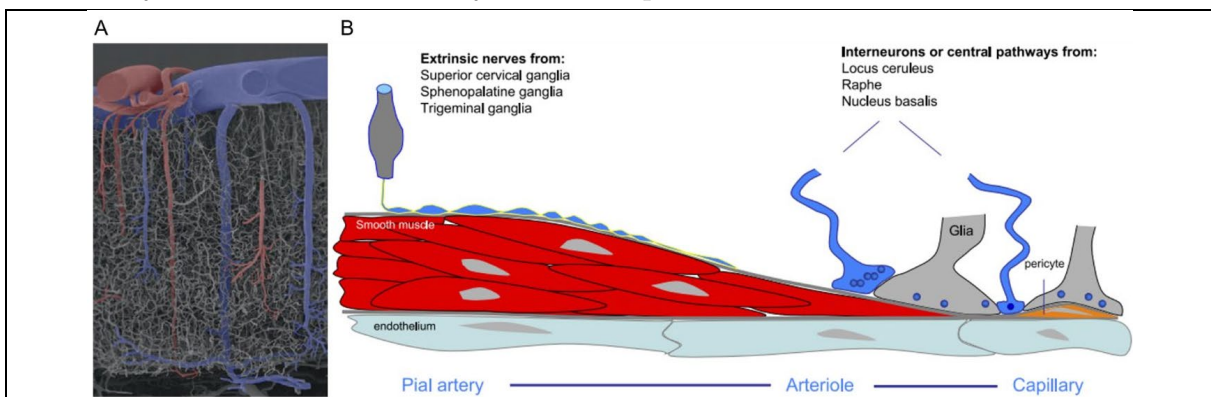


Figure 75. Anatomical structures in the brain (Girouard and Iadecola, 2006)

- a) Scanning Electron Microscope imaging of a monkey's cortex 1.7 *mm* from the surface
- b) Representation of the links between the vascular and the neuronal network in the brain

To ensure proper functionality, the brain has to be continuously provided with oxygen and nutrients which are transported through the circulatory system. This system is a closed and complex network of vessels going from the heart in arteries and then going back through the veins. The blood supply to the brain is ensured by four arteries, two common carotids, and two vertebrals. Three main veins, dorsal, ventral and caudal carry the blood out of the brain. Branching out from these main vessels, specific arteries and veins go deep in the brain to carry out their function. The microvasculature is largely responsible for neurovascular coupling (Hamilton, 2010). Linked to the pial vessels in the surface, the arterioles carry blood several millimeters down the neocortex. Their diameter diminishes progressively until arterioles become capillaries linked with pericytes. Oxygen and nutrients are exchanged between blood and tissues (Girouard and Iadecola, 2006) in the capillary bed. The venules follow a similar architecture with an increasing diameter towards veins and pial veins.

Initially, it was thought that an increase in blood flow was linked to a metabolic signal such as oxygen or glucose decrease or an increase in carbon dioxide. It was recently shown that this increase is piloted by neurotransmitters liberated by astrocytes (Orozco-Cabal et al., 2006). *In vitro* and *in vivo* studies confirm that an increase in neuronal activity induces liberation of vasoactive agents. Astrocytes act as regulators of the vasoconstriction/vasodilatation process.

Microvasculature plays a key role in the brain's function and is thought to be linked to many neuro-generative diseases (Kanbay et al., 2011). The development of arteriolosclerosis impairs autoregulation of blood flow pressure in the brain and increases the risk of stroke and vascular dementia (Manolio et al., 2003). For example, increasing or lowering blood pressure in patients with microvascular disease may increase the risk for hemorrhagic or ischemic stroke. A decrease or modification in the microvascular network induces modification of the oxygen supply and plays a role in aging cerebral disease. The study of flow inside the microvasculature and its interest has been shown in (Peyrounette et al., 2018). The microvascular network, however, has received less emphasis than other components of the brain for a practical reason: it is hard to image small structures deep in the brain. *In vivo*, no imaging modality is able to provide insights about vascular function at the microscopy scale deep in the brain. Two-photon imaging can provide such information but is limited to a few hundreds of micrometres on the surface of the brain. *Post-mortem*, however, it is possible to render the whole microvasculature using optical sectioning.

For rodents, the brain is protected by a skull that can be as thick as 2 mm and that has a complex arrangement to fit the anatomical arrangement of the brain (see

Figure 75). This complexity can reach a very high level for example around the olfactory bulb where the brain is kept in place by a structure resembling an upside-down gothic dome: the frontal bone. The extraction of the brain to perform post-mortem studies is thus complicated and people usually resort to breaking the bones in small pieces. For *in vivo* studies without the skull, this is even more complicated because the brain should be kept intact and so should its protective cover, the *dura mater*.



Figure 76. 3D renderings of Sprague Dawley rat's skull

The olfactory bulb is enclosed in the forward section of the skull, in between the maxillary bone and the Bregma +4 mm line. The frontal bone covering the bulb (white triangles) is thin on the top but has an increased thickness near the ridges.

The need for an atlas to be able to label structures whether it be arteries, vessels or neuronal areas is crucial and has been answered many times. Optical microscopy techniques provide the best access for exploring both the vascular and neuronal network at single-neuron resolution. Combined with labeling, a number of atlases have been established and used in anatomical studies (Dong, 2008; Franklin and Paxinos, 2013).

Fluorescence-based labeling has demonstrated that it can trace neurite projections and transsynaptic circuits (Josh Huang and Zeng, 2013; Madisen et al., 2010; Markram et al., 2004). Multiple fluorescent probes can label diverse neurons in different regions at the same time (Dumas et al., 2015; Livet et al., 2007; Shaner et al., 2005). For long-distance and local connections, genetic dissection can provide systematic mapping and classification (Luo et al., 2008). The main problem arising in all of these techniques however is the probability of fluorescence quenching during the highly complex procedures which impact weak connections detection (Chung et al., 2013; Gong et al., 2013; Renier et al., 2014; Susaki et al., 2014; Yang et al., 2014).

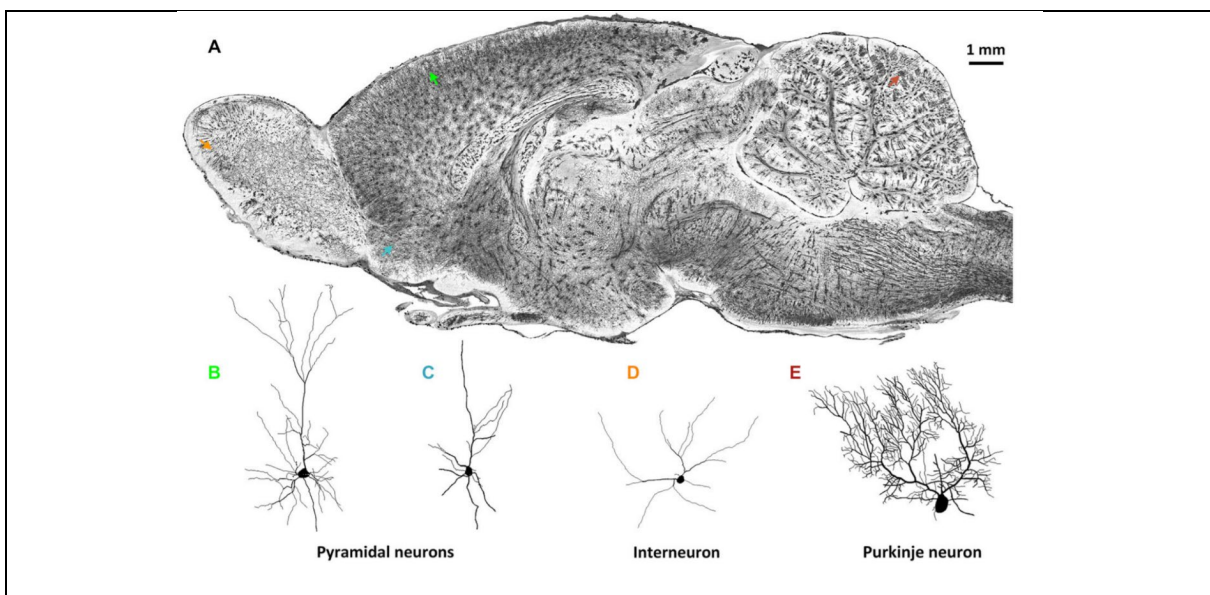


Figure 78. Whole-brain imaging of rat neuronal morphology with Golgi staining(Li et al., 2010) (VBN, 2015)

- a) A sagittal image of a 200 μm thickness projection from a whole-brain imaging dataset acquired by the Micro-Optical Sectioning Tomography (MOST) method (Li et al., 2010) (Li et al., 2010). Arrowheads in different colors in (A) indicate individual neurons.
- b) Pyramidal neuron in the somatomotor cortex (green in a))
- c) Pyramidal neuron in the anterior olfactory nucleus of olfactory bulb (blue)
- d) Interneuron in the glomerular layer of olfactory bulb (orange)
- e) The Purkinje cell in cerebellum (brown)

Even though labeling is crucial to improve the optical contrast of nervous tissue, optical imaging is restricted to a few hundreds of microns by the absorption and scattering of light in tissue. Histology has been combined with optical microscopy to achieve a large range of resolution up to less than a micrometer in three dimensions. (Dodt et al., 2007) combined Light-Sheet Illumination Microscopy and chemical clearing

to achieve fast imaging of transparent intact mouse brain with a technique dubbed Ultramicroscopy. Side illumination is employed in parallel on a thin layer of brain tissue perpendicular to the optical imaging light path. Three-dimensional imaging can be achieved with the displacement of the brain sample or of the illumination beam. Several methods have been derived from this to generate transparent brain tissue so that the illumination light can pass through the entire sample:

Immersion in a clearing agent (reducing the amount of light scattering by clearing scatterers)

- Scale (Hama et al., 2011)
- CUBIC (Susaki et al., 2014)
- SeeDB (Ke et al., 2013)
- 3DISCO (Ertürk et al., 2014, 2012; Ertürk and Bradke, 2013)
- iDISCO (Renier et al., 2014)
- ClearT (Kuwanjima et al., 2013)

Electrophoresis to remove lipids (transparent tissue)

- CLARITY (Chung et al., 2013; Chung and Deisseroth, 2013; Tomer et al., 2014)
- (Yang et al., 2014)

Compared to point-scanning brain-wide optical imaging techniques, wide-field LSM is faster, making it easy to image one slice multiple times and to process whole-brain imaging in “acceptable” times. However, two problems remain: the inhomogeneity of tissue clearing means inhomogeneity of imaging contrast and of the resolution, and the axial resolution of LSM is limited to $10\ \mu\text{m}$. To improve axial resolution issues, two solutions have been developed:

Optical sectioning

- STP combines a microtome (to slice imaged layer) and a two-photon excitation microscope in mosaic splicing mode (high axial resolution) based on mechanical scanning (Ragan et al., 2012, 2007). So far this method has been applied with improved axial resolution ($2.5\ \mu\text{m}$) in the olfactory bulb but not for entire mouse brains

A major disadvantage of this technique is that it takes several days for whole-brain processing which asks for prolonged system stability

Ultrathin physical sectioning

- Knife-Edge Scanning Microscopy (KESM) which combines a knife and a collimator to respectively cut sections and illuminate the tissue (Mayerich et al., 2008; McCormick et al., 2004) but this fails to produce whole-brain imaging because of damage caused by the knife
- Micro-Optical Sectioning Tomography which decouples illumination and cutting and improves physical sectioning to make it free of chatter (Li et al., 2010). Its implementation with Nissl staining (Wu et al., 2014) compared to the original Golgi staining has shown similar results for 3D mapping of a whole mouse brain at a $1 \mu m$ resolution. Finally, fMOST which is the implementation of MOST with fluorescence has successfully imaged a fluorescent protein transgenic whole mouse brain with long-distance pathways traced for the first time with a $1 \mu m$ resolution.

These techniques show very promising results in terms of vascular and neuronal imaging and open the way towards, high-resolution vascular atlases, systematic classification of neurons, which is a great leap forward for neuroscience. However, they have an inherent problem: they are all post-mortem techniques. Another issue as far as vascular imaging is concerned is that they do not image vascular function: they do not provide information about vascular flow, artery and vein deformation, brain pulsatility or intra-vascular pressure. Such lack of information fails to make these images useful for comparison with functional imaging of the brain.

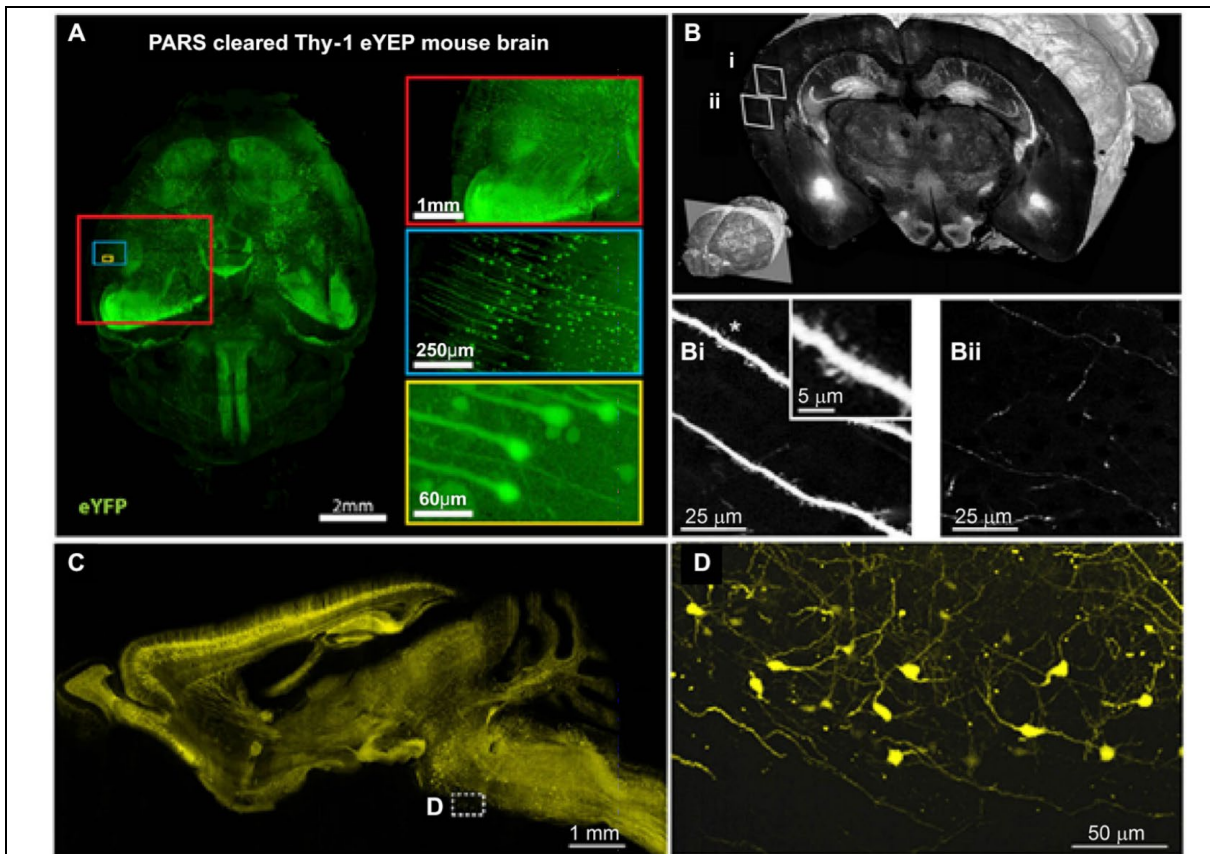


Figure 79. Brain-wide distribution of Thy-1 neurons imaged by LSM, STP, and fMost

- a) Whole-brain image ($z = 6 \text{ mm}$) of adult Thy1-eYFP mouse after PARS clearing for 10 days. The boxes on the right show high-magnification images of indicated areas. PARS, perfusion-assisted agent release *in situ*. Taken from (Yang et al., 2014).
- b) 3D view of a coronal section of the GFP brain. Lower left: position of the coronal plane in the imaged mouse brain (approximately 2.5 mm from Bregma). Enlarged views demonstrating the visualization of dendritic spines (Bi) and fine axon fibers (Bii). Adapted from (Ragan et al., 2012).
- c) Sagittal image reconstructed from a stack of virtual sagittal sections (thickness: $50 \mu\text{m}$) of an adult Thy1-eYFP mouse
- d) Higher magnification views of some soma and fine neurites in the white box of c).

Extracted from (Yuan et al., 2015)

Our tool has successfully measured vessels up to a few micrometers which is coarser than optical imaging methods but can perform these measurements *in vivo* to measure vascular deformations and velocimetry to obtain velocity information even in small arteries or veins. It can also image the brain up to 20 mm in depth making it an

ideal tool for both mouse and rat imaging. The only downside to this is that to achieve such a resolution, this tool has so far needed a craniectomy surgery to prevent aberration of the ultrasound waves.

In this chapter, I will describe my approach to image the microvasculature of the entire brain of a rat. It is based on the advanced 3D ULM techniques presented in the previous chapters and on careful surgical resection of a large window in the skull.

V.1.1 Material and methods

V.1.1.1 Surgery for whole-brain craniectomy

All animals received humane care in compliance with the European Communities Council Directive of 2010 (2010/63/EU), and the study was approved by the institutional and regional committees for animal care (Comité d’Ethique pour l’Expérimentation Animale no. 59—‘Paris Centre et Sud’ Protocole no. 2017-23).

8-10 weeks Sprague-Dawley rats were obtained from Janvier Labs (Le Genest-Saint-Isle, France). Animals were free from pathogens and were placed in our in-house facilities. Housed in Techniplast® cages by groups of 2 minimum and 3 when the total animal per volume ratio did not exceed values fixed by regulations, the animals were kept for at least a week before surgery. The temperature in the cages was controlled to be between 21-23°C, the humidity rate in between 40-60%. The day-night cycle was divided as follows: 7h-19h/19h-7h. Water and a commercial pelleted diet SAFE A04-10 were available *ad libitum*. SAFE FLAKE sawdust was used as bedding, enrichment such as pieces of cardboard, paper tunnels were provided and the facility vet went to visit them three to five times a week. This allowed to reduce stress during manipulation before anesthesia induction and increase the anesthesia’s performance in terms of speed and robustness in time.

The animal was taken out of his cage and manipulated for 15 minutes before receiving an intraperitoneal injection of Ketamine-Xylazine. After confirmation of the depth of anesthesia based on absence of withdrawal reflex when pinching the toes of the hindlimb, the animal was placed on the back on a heated plate. An incision was made just above the first rib in the thoracic area. The absence of movement from the animal during that incision was considered as a confirmation of the depth of the anesthesia. After tissue was dilacerated to give easy access to the jugular vein, two suturing strings were threaded under it. The string closer to the brain was knotted to close blood flow returning from the brain. An incision perpendicular to the direction of the vein was made and a 180 μm inner diameter tubing was placed inside the vein to serve as a catheter. The surgery was deemed successful when blood was observed in the catheter under

negative pressure applied by the syringe on the other end. The other string was knotted over the catheter to prevent it from sliding out of the vein. Moreover, the incision made was closed with Vetbond to prevent the jugular vein from drying and for added security.

The animal was then placed in a stereotactic frame equipped with a respiratory mask. The mix was composed of 100% O₂. 5 mL of saline at 37°C was injected subcutaneously in two different doses in the left and right sides of the back of the rat to prevent dehydration. Such a procedure was repeated every 2 hours. An incision was made in the scalp following a line between Bregma and Lambda points but extending from over the olfactory bulb to just behind the cerebellum. The scalp was retracted and the side and the cerebellum muscles were disjoined from the skull to allow easy access to the skull. The muscles were kept away from the skull by using suturing threads. The percentage of isoflurane was increased as soon as hindlimb withdrawal reflex was observed to 2%. As soon as possible, we tried decreasing the isoflurane percentage as low as possible (0.8-1%) to prevent lethal side-effects such as hyperventilation, cardiac deficiencies while maintaining absence of reflexes.

The craniectomy was done in three separate steps, to prevent damaging the *dura mater*. First, a large portion of the skull in between Bregma +4 mm and the interaural line and in between the two side ridges was drilled. The drilling on the sides took place as deep as possible to provide a window as large as possible. Once this portion of the skull was removed, a second portion, directly over the cerebellum was removed. Finally, a third section directly over the olfactory bulb was drilled and removed.

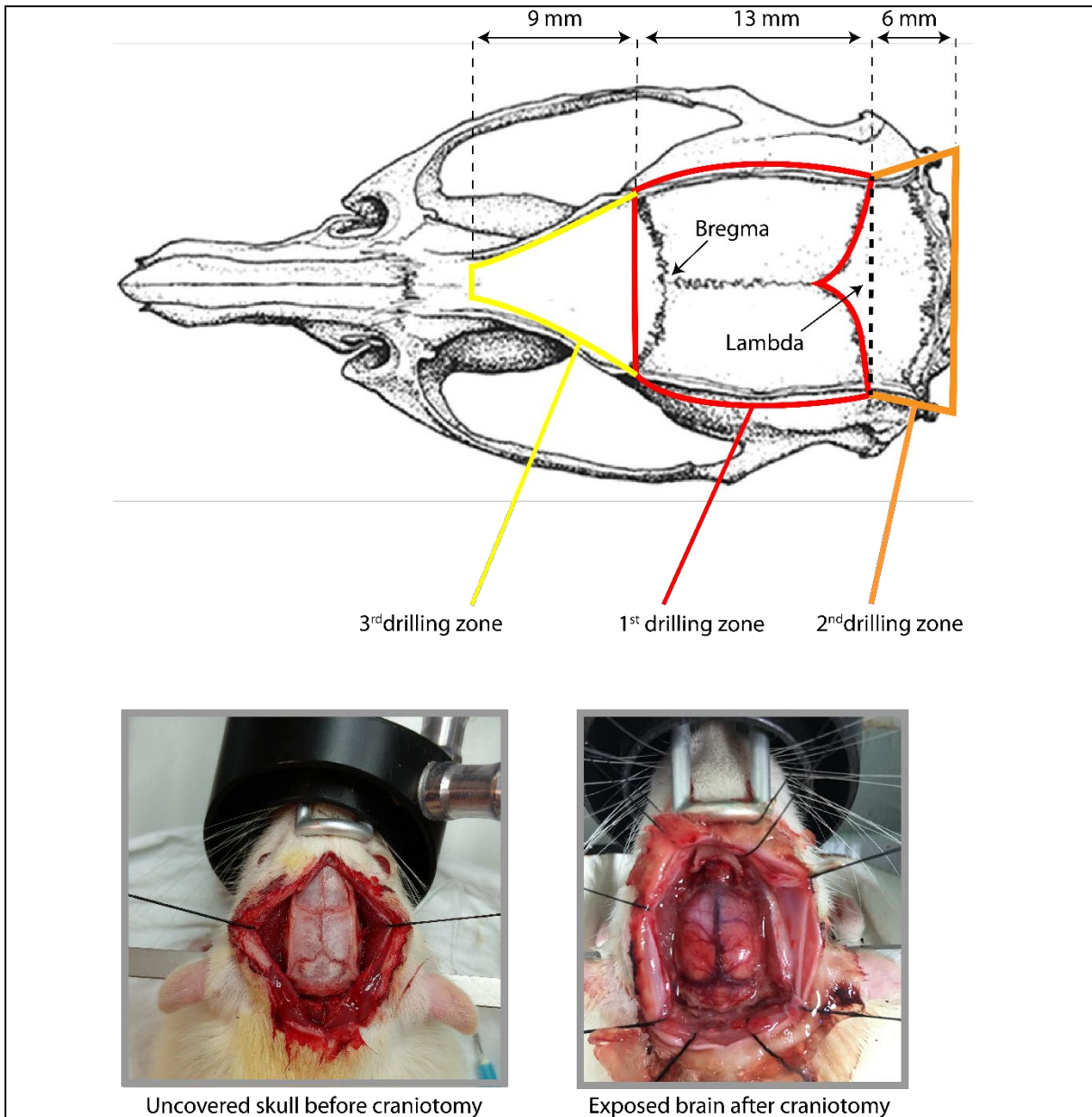


Figure 80. Drilling procedure for whole-brain craniotomy of the rat

The first drilling zone contains the ridges. Drilling is performed below the ridges to take advantage of the thinner skull there and also to try and uncover as much brain as possible. The skull bone on the side would surely create aberrations and make the lateral pial vessels invisible to ultrasound.

The second drilling zone follows the same pattern for cerebellum uncover.

The third drilling does not go below the ridges as it would take too long. The olfactory bulb is well imaged without removing the ridges.

Each time a portion was removed, saline was dripped over the brain and small pieces of bones resulting from drilling were carefully removed by using surgery tweezers. After the brain was deemed clean, ultrasound gel was applied to prevent the *dura mater* from drying.

In the final stage, where all portions have been removed and the brain was deemed clean enough to image, a layer of agarose was sometimes applied. The mix of 2% of agar and degassed water was heated in the microwave to 80°C in steps of 20°C to perform mixing. The mix's temperature was then decreased by leaving it at room temperature to 37°C. It was then applied in a thick layer over the brain. A thin film of rigid plastic was then pressed over it to smooth its surface and to render a flat layer on which the probe could be translated and rotated around freely.

V.1.1.2 Ultrasound sequence

The ultrasound sequence is the same as the one described in chapter 4. A small variation is that this sequence is repeated 7 to 9 times to cover the entire brain. The first portion imaged is the upper right corner of the brain over the transverse sinus just below the olfactory bulb. The probe is then translated towards the rear of the brain, leaving a mutual ROI with the previous image, over the right part of the cerebellum. It is then translated towards the left portion of the cerebellum while keeping the true Lambda point in the ROI. The upper left part of the brain is then imaged leaving a mutual ROI again, and then finally, the olfactory bulb is imaged.

Leaving mutual ROIs should allow us to register the rendered ULM volumes in between each other and perform the reconstruction. This will be done in the same manner as what is done for motion correction. In total, the whole process takes 1 hour and 6 minutes. With a speedier ultrasound acquisition process like what is possible on new Verasonics based 4D echographs, or with multiplexed probes, this should take no more than respectively 13 or 25 minutes.

V.1.1.3 Motion correction

For 2D ULM, it has been demonstrated that motion estimation and registration can be combined to perform sub-wavelength motion correction (Hingot et al., 2017). We will demonstrate below its implementation in three dimensions.

Let's assume motion in between two images Im_k and Im_{k+1} is a 3-dimensional translation: $(\Delta z_k, \Delta x_k, \Delta y_k)$, the shift can be written in the Fourier domain as a multiplication:

$$F_{k+1}(u, v, w) = F_k(u, v, w)e^{-2i\pi\varphi_k}$$

where F_k and F_{k+1} are the 2D Fourier transform of the images Im_k and Im_{k+1} and φ_k a constant phase shift that can be expressed in the unitary Fourier base (u, v, w) where L_z, L_x, L_y are the size of the image.

$$\varphi_k = \frac{u\Delta z_k}{L_z} + \frac{v\Delta x_k}{L_x} + \frac{w\Delta y_k}{L_y}$$

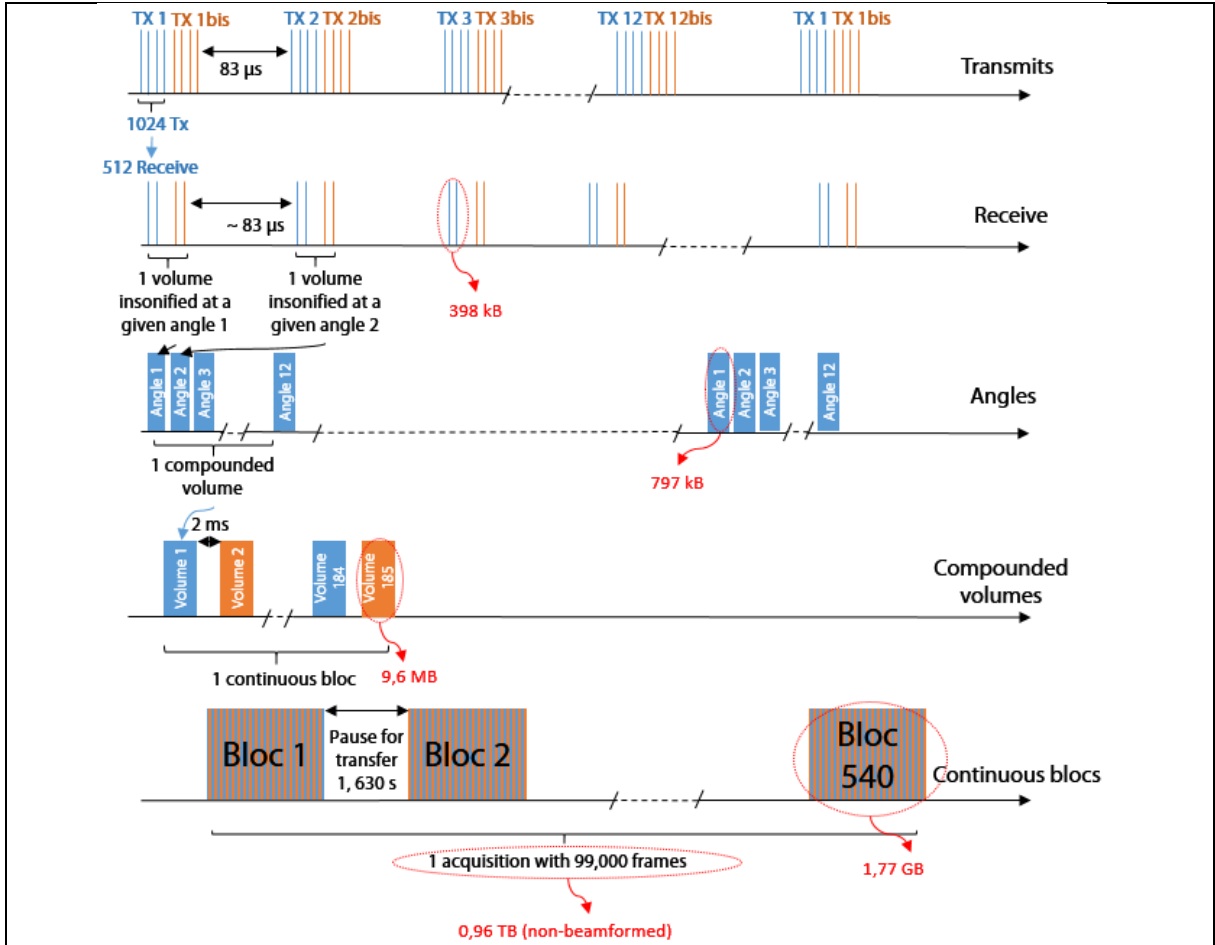


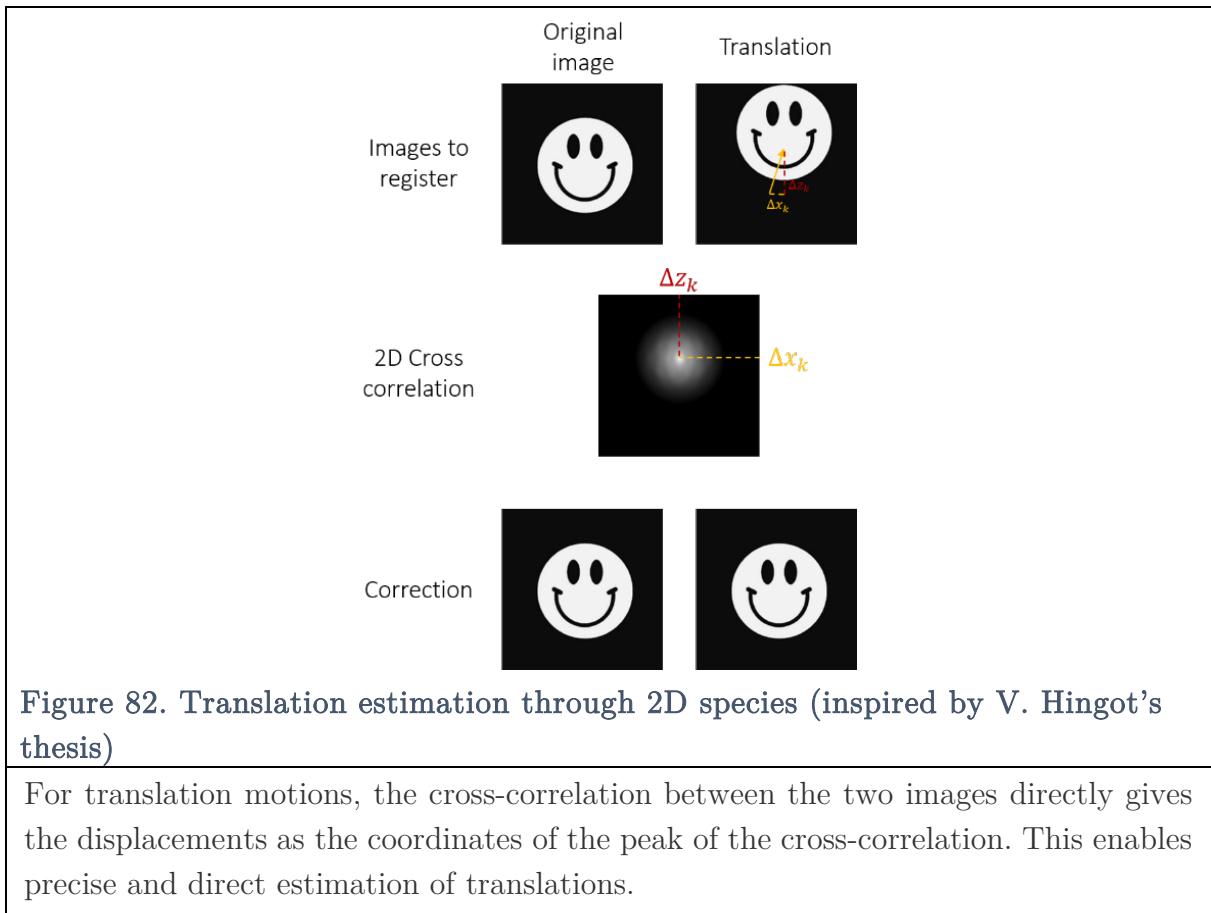
Figure 81. Schematized view of the 4D acquisition for 3D ULM in vivo

In terms of ultrasound transmits, this sequence is very similar to what was done *in vitro*. The only difference is the number of angles increased from 4 *in vitro* to 12 *in vivo*. However, the number of continuous frames has been decreased to 185 from 500 and the number of blocks increased from 4 to 540. That allows us to produce 99,900 images without restarting the ultrasound scanner, changing the hard drives, or any elaborate hardware action. The whole sequence is repeated for each section of the brain (x5).

The cross-correlation can easily be calculated and is a simple Dirac function whose coordinates are $(\Delta z_k, \Delta x_k, \Delta y_k)$.

$$C_k = F^{-1} \left(\frac{F_k F_{k+1}^*}{|F_k F_{k+1}^*|} \right) = \delta(\Delta z_k, \Delta x_k, \Delta y_k)$$

The position of the maximum of this cross-correlation in the base mentioned above is the direct measure of the translation. The estimation of this displacement is linked to the SNR of the image and as such, can be much finer than the characteristic dimension of the image (i.e. the wavelength).



Now, if the motion is made up of translation, rotation or scaling, the Fourier transform has a very interesting property: it separates translation and rotations/scaling in the magnitude and phase of the spectrum. In a log-polar plot in the Fourier domain, the scaling and rotation appear as constant phase shifts on the magnitudes. It was demonstrated that the Fourier Mellin transform can successfully estimate translation, rotation and scaling in between two images.

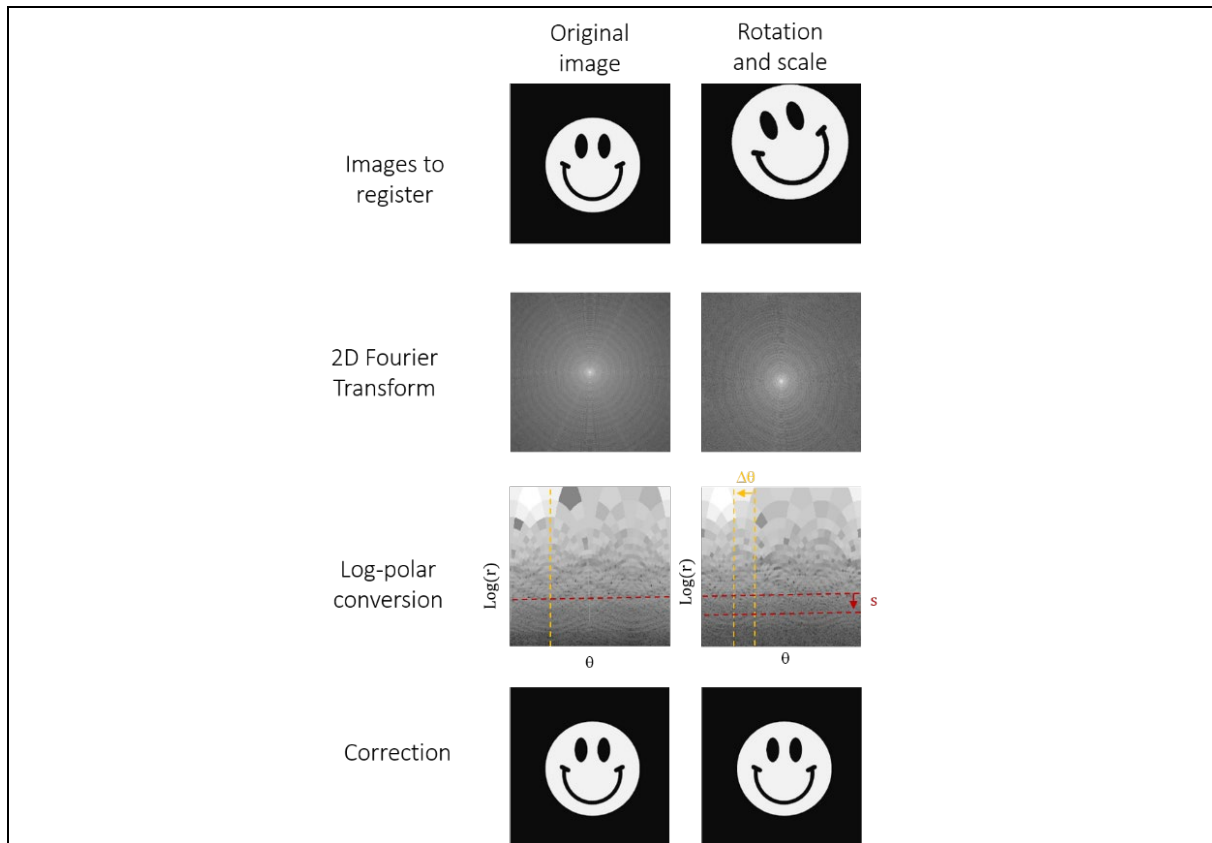


Figure 83. Rotation and scaling estimation using 2D cross-correlation on the log-polar transform of the magnitude of the 2D Fourier transforms (inspired by V. Hingot's thesis)

Rotation and scaling can be estimated using 2D cross-correlation not on the images but on the Fourier spectrums. After computation of the 2D Fourier transforms for each image, conversion to log-polar coordinates simplify the estimation of the rotation and scale to a translation and can be measured using cross-correlation as previously. The original images can then be corrected using the angle and the scale factor determined.

For more complex motion, these simple algorithms fail and we have to proceed iteratively. Fortunately for us, some iterative registration algorithms exist in Matlab[®] to compute the general transformation matrix: `imregister` and `imregtform`. They are both based on the estimation of a multi-variable gradient of the mutual information present in two frames and will try to converge on a set of coordinates for that gradient that maximizes mutual information. They were successfully applied in 2D ULM on a rat whose head was not fixed in the stereotactic frame. The motion is essentially due to breathing so it can be estimated with a rigid transform which is a combination of translation and rotation.

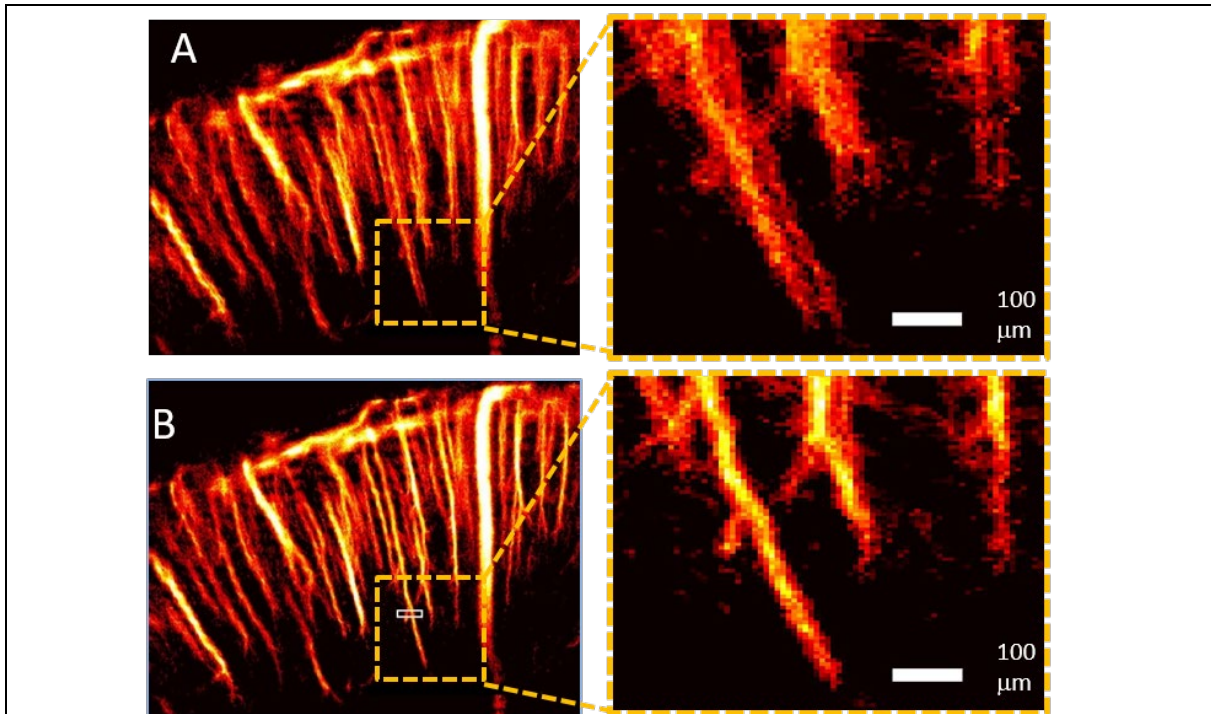


Figure 84. Motion Estimation and correction performed on 2D ULM of the rat brain (Hingot et al., 2017)

- a) 2D ULM of a rat's brain whose head was not fixed in the stereotactic frame
- b) 2D ULM after rigid motion correction

The goal was to translate such 2D algorithms in 3D. The functions used in Matlab® are 3D compatible and as so, our task was simplified. The data issue, however, becomes quite large as each volume must be corrected throughout the acquisitions. To assess the performance of our algorithm for motion correction, we performed a similar experiment to what was implemented by (Hingot et al., 2017). The rat was released from the stereotactic frame and 50 blocks were acquired in the same manner as in the general ultrasound sequence. Two algorithms were developed: one that only corrects for motion between blocks, another one that corrects frame to frame motion, then applies a rigid transform based on motion between blocks on the post-ULM rendered trajectories. The outline of these two algorithms is presented in Figure 84.

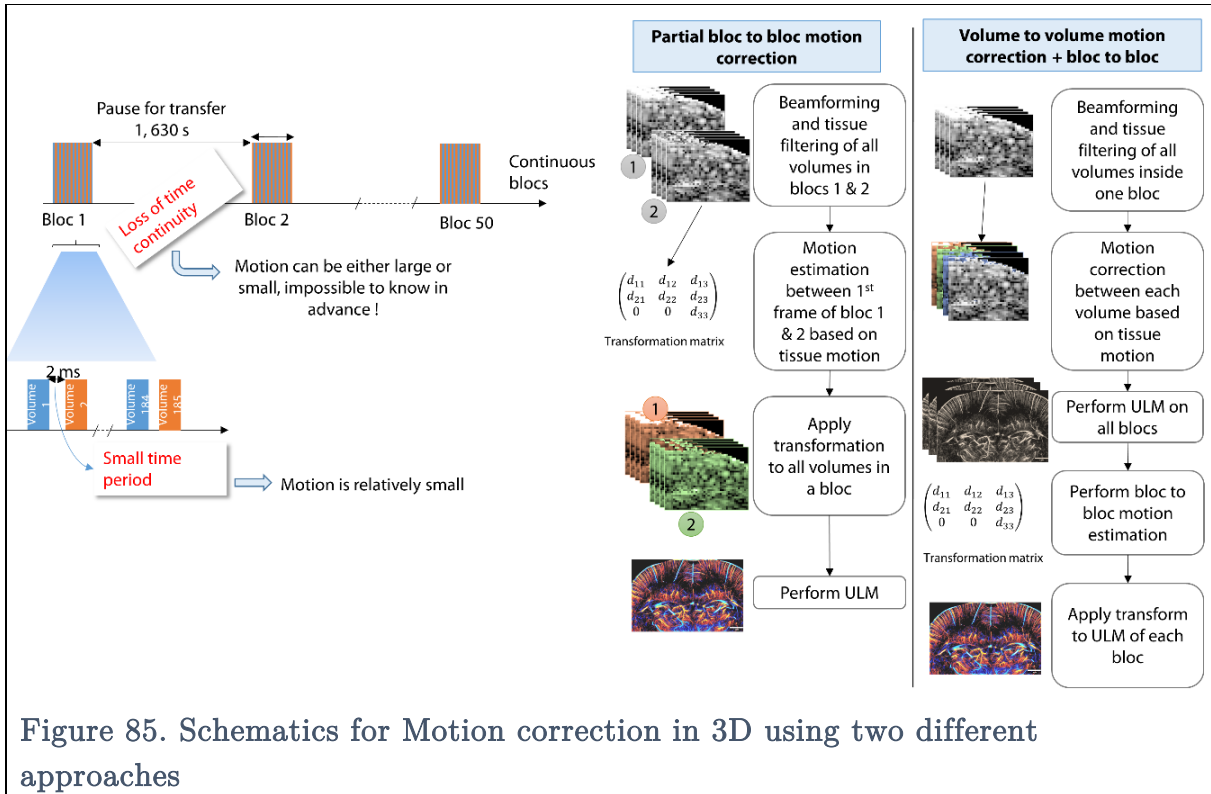


Figure 85. Schematics for Motion correction in 3D using two different approaches

The partial block-to-block (BTB) motion correction performs motion correction in between blocks. The beamformed volumes are filtered to keep only tissue signal with Singular Value Decomposition (SVD). This is done by keeping only the highest energy singular values, which excludes the signal from the microbubbles. The first frames of each block are then compared to each other to estimate motion in between blocks. This motion is computed as a rigid transformation matrix. The transformation is then applied to all volumes in the corresponding block: block 1 does not undergo any transformation, block 2 undergoes transformation computed on the motion in between block 2 and 1, block 3 undergoes transformation computed on the motion in between block 3 and 1, etc... ULM is then performed on the motion-corrected volumes as outlined in the previous chapter. In this algorithm, only the unknown motion due to loss of time continuity is computed.

The volume-to-volume (VTV) motion correction algorithm takes place in two steps. First, each volume in each block is filtered using SVD to keep only the tissue signal. The motion is computed between every 185 volumes as 184 independent rigid transformation matrices. Each volume is modified with the corresponding transformation: volume 1 does not undergo any transformation, volume 2 undergoes transformation computed on the motion in between volume 2 and 1, volume 3 undergoes transformation computed on the motion in between volume 3 and 1, etc... After correcting each block

in a similar manner, the ULM process is applied to each block and ULM renderings are built. Finally, the BTB motion correction is implemented again on non-corrected blocks. For each block, the transformation matrices are then applied directly to the corresponding ULM renderings. The final ULM rendering is built by adding coherently all the motion-corrected ULM renderings.

V.1.1.4 Registration of the different volumes for whole-brain imaging

Similarly to what was explained in the previous paragraph, it is possible to use the `imregister` function to register the ULM volumes acquired at different zones in the brain. However, reconstructing all volumes and manually placing them with respect to each other helps the registration algorithm a lot as an initial guess. Our attention turned to the software we use for 3D renderings: Amira from Visualization Sciences Group. In medical imaging, it is often mandatory to register images from a subject taken with different imaging modalities. Amira is designed to perform that task on modalities as various as Computed Tomography (CT), Magnetic Resonance Tomography (MRT) or Positron Emission Tomography (PET). Our idea was to use that functionality to our advantage to register two different volumes with overlapping areas.

Firstly, manual registration is performed by aligning the different volumes on a surface rendering of the rat brain (Scalable Brain Atlas (Papp et al., 2014)). By following easily identifiable vascular landmarks such as the Superior Sagittal Sinus (Sss), the Olfactory artery (Olo), the Posterior cerebral artery (Pcer) and the cerebellum, the task is performed using a combination of translation, rotation of the volumetric ULM renderings and scaling independently the surface mesh of the rat brain.

Secondly, large vascular structures are identified in overlapping volumetric ULM renderings, usually the Sss, the Spinal Trigeminal Tract, the Azygos Pericallosal artery and the Olo. The optic nerves are particularly useful for the manual registration of the olfactory bulb. The different volumes are moved by hand using rigid transformations.

Thirdly, Amira (FEI ®) is asked to perform automatic registration via optimization of a quality function. The similarity metric chosen is the correlation. The algorithm will compute a correlation value between the two volumes and will try to minimize this correlation by applying transformations. This is recommended for images acquired using the same modality but not having a similar intensity range which is the case for us. The optimizer was set to extensive direction with an initial step of 20 voxels (200 μm) and a final step of 0.05 voxel (0.5 μm). The same values were used for all the different volumes.

V.1.2 Results

V.1.2.1 *Motion correction*

We performed motion correction using the two different algorithms described in V.1.1.3. The SVD filtered imaging of tissue signal in a block of acquisition is represented at different times in Figure 85. There is a noticeable sinking down of the brain advancing through time. The motion inside one block is non-negligible and even less in between blocks.

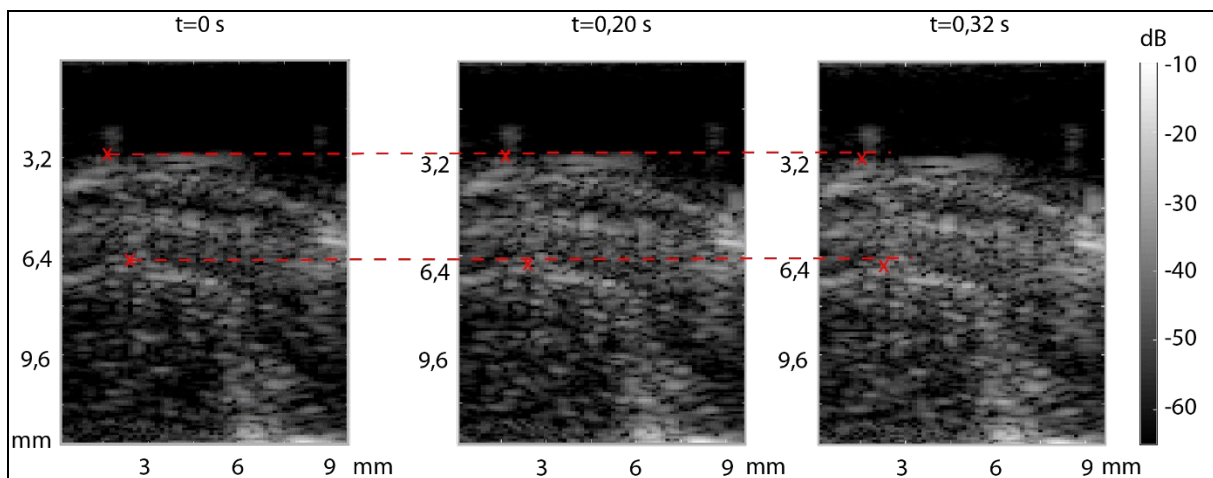


Figure 86. SVD filtered imaging of tissue signal in the brain of a rat released from the stereotactic frame

The red crosses indicate landmarks chosen by the user at each time. The dashed lines go through the first landmark at $t = 0$ s and are parallel to the x-axis. Theoretically, if the brain did not move, the dashed lines are supposed to pass by every cross. The sinking down of the brain is noticeable in this block.

After implementing the motion correction algorithms, we reconstructed density-based volumetric ULM renderings for three cases: one where the motion is not corrected, one where the BTB motion is corrected and one where VTV and BTB motion are corrected. The renderings are pictured in Figure 86.

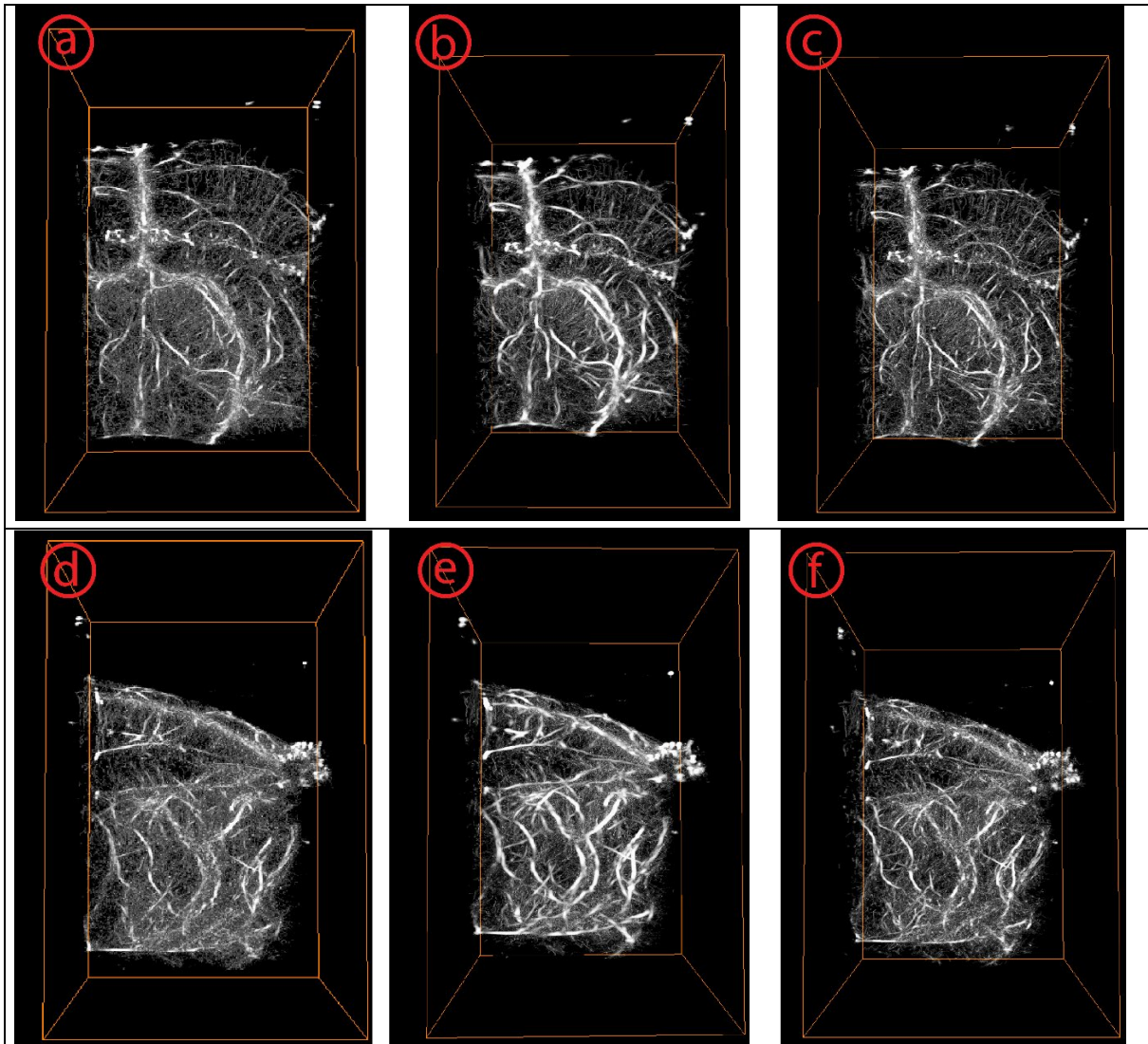


Figure 87. Coronal and Sagittal planes projected volumetric ULM renderings obtained without, with BTB and with VTV and BTB motion correction

The difference between the volumetric ULM renderings in their coronal plane projection is important. When BTB motion correction is applied, the large vessels appear brighter, but they also appear to be blurred. When VTV and BTB motion correction are applied, all of the vessels appear brighter but the volume rendering retains its sharpness. The salt and pepper noise seen on the no-motion corrected volumetric ULM rendering a) completely disappears in the VTV and BTB corrected c). Some vessels can be seen in c) although they were not visible when the motion was not corrected, most notably in the hippocampal formation region where large vessels form a ring and smaller vessels can be seen converging from that ring to its center. The large vessels are sharper and have a narrower diameter in the c) case.

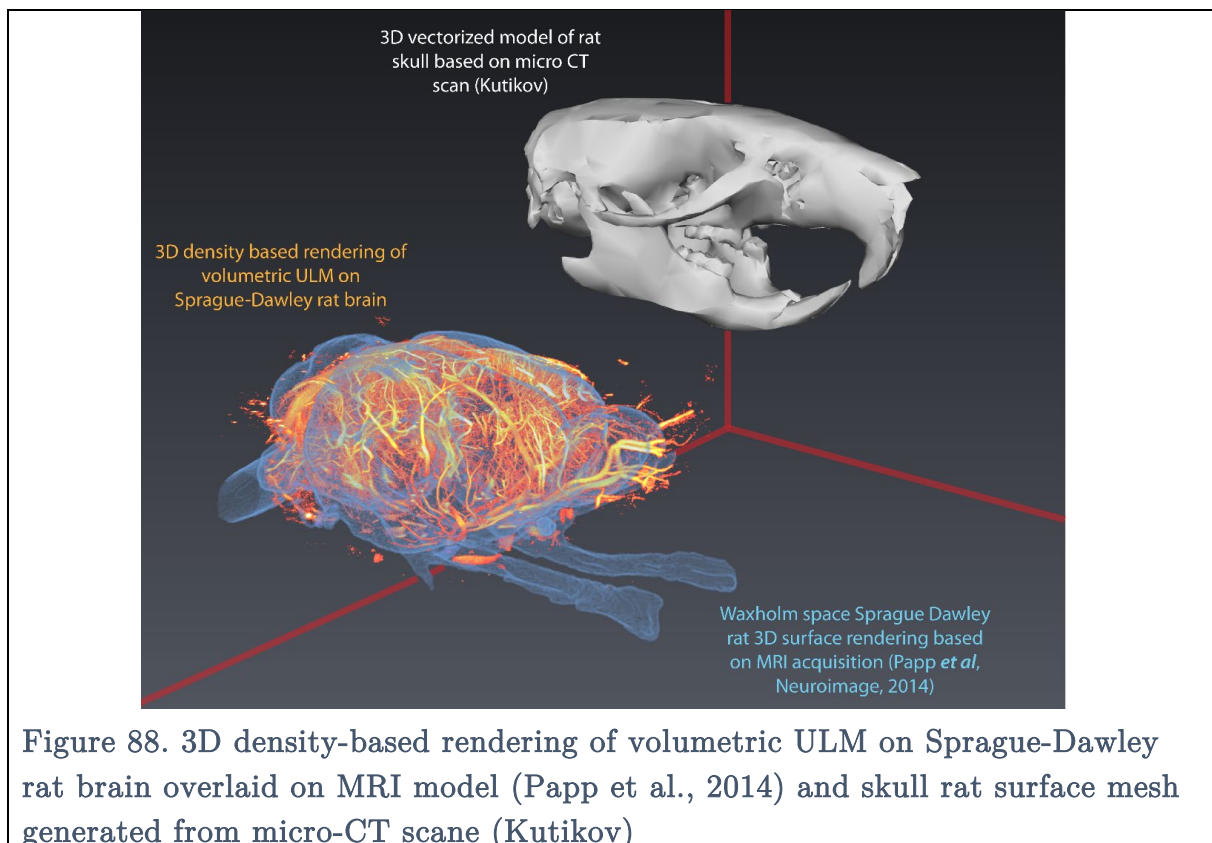
Similar differences are observable in the sagittal plane projections. The azygos pericallosal artery is considerably brighter in the motion-corrected cases but appears

enlarged in the BTB motion correction scheme. The larger vessels in the BTB motion-corrected dataset seem greatly affected by the blurring effect, so much that it is hard to distinguish smaller vasculature. This is not the case in the VTV and BTB motion-corrected case where vessels appear brighter while retaining their sharp appearance.

V.1.2.2 *Whole-brain imaging*

Note : The results presented here are partial. In between the submission and the defense, three rats were imaged again and whole brain imaging was obtained.

The five volumes acquired were loaded into Amira® software and after performing the registration for overlapping volumes, a surface rendering based on MRI acquisition was loaded (Papp et al., 2014). This surface rendering helped us to arrange the volumes that did not overlap together by aligning the main pial arteries and veins on the surface of the brain. The superior sagittal sinus, the transverse sinuses, the spinal trigeminal tract, and the inferior and olfactory sinus were especially used for that purpose as they are contained in easily identifiable landmarks in the anatomy. Furthermore, a vectorized model of a rat skull based on micro-CT scan was loaded for added anatomical information. The resulting volumes are presented in Figure 87. The density-based rendering fits almost all of the brain except for the spinal trigeminal tracts and optical nerves who are visible by ultrasound only when then are not covered by bone.



Additional 3D volume renderings are produced in Figure 88. Three-point of view are represented, two from the anterior side in the left and right hemisphere and a perspective rendering in the sagittal plane. Similarly to what was done in the previous chapter, main vasculature structures are labeled. The labeling is quite easily done when comparing with (Scremin, 2004). The smaller structures are not visible as they would be quite hard to pinpoint in the 2D projected rendering here.

In the end, two out of five volumes had an overlap. This overlap was used to register the two volumes according to the process explained in V.1.1.4. The area where the stitching was done is enlarged in Figure 89. The stitching line is drawn as a white dashed line. The lateral orbitofrontal arteries appear continuous after stitching in between the two volumes. The olfactory vessels also appear continuous although it is harder to tell as they are very close together at the stitching plane. The smaller vessels just above the sinuses also seem to be continuous and thus the stitching is deemed satisfactory.

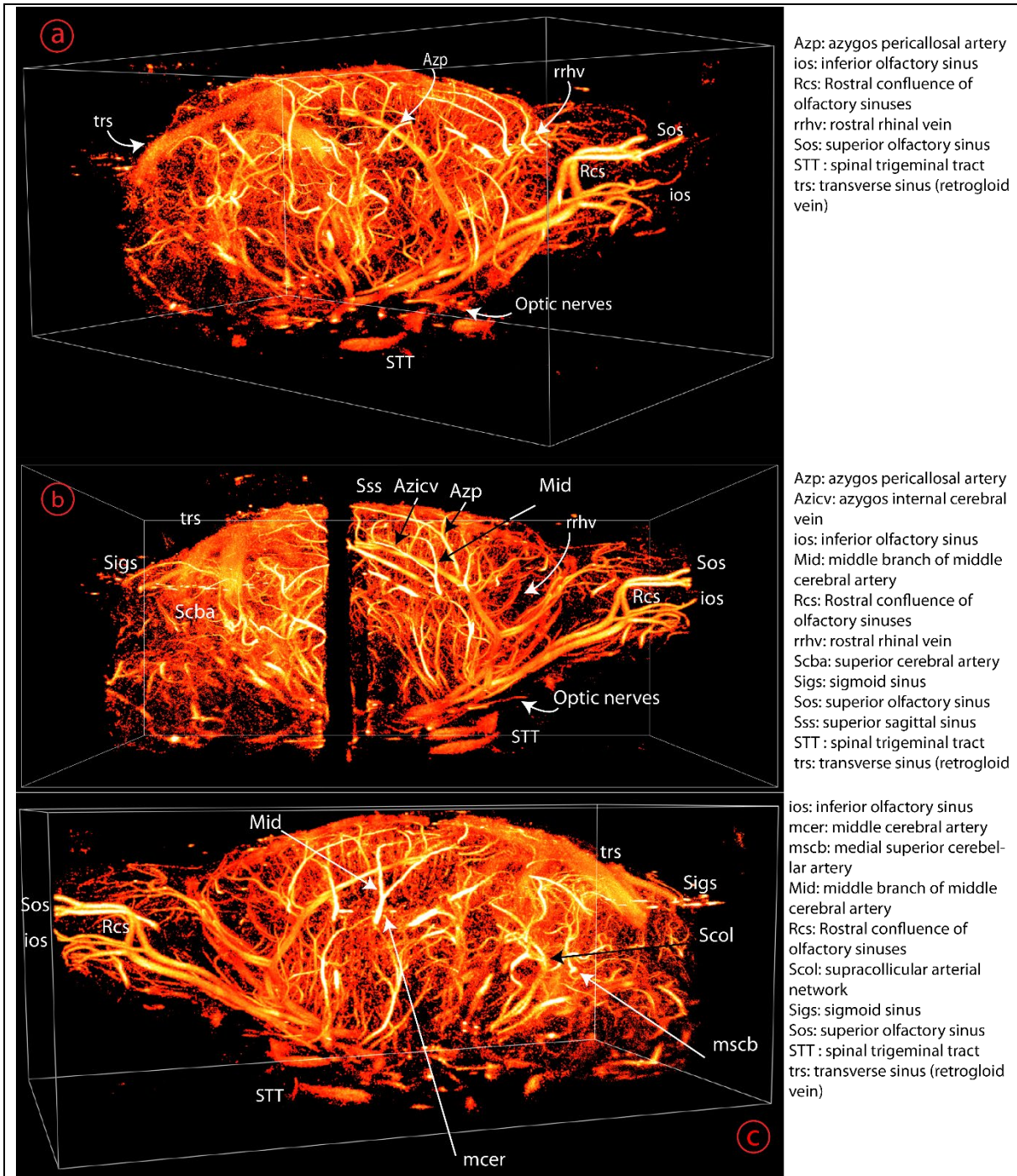
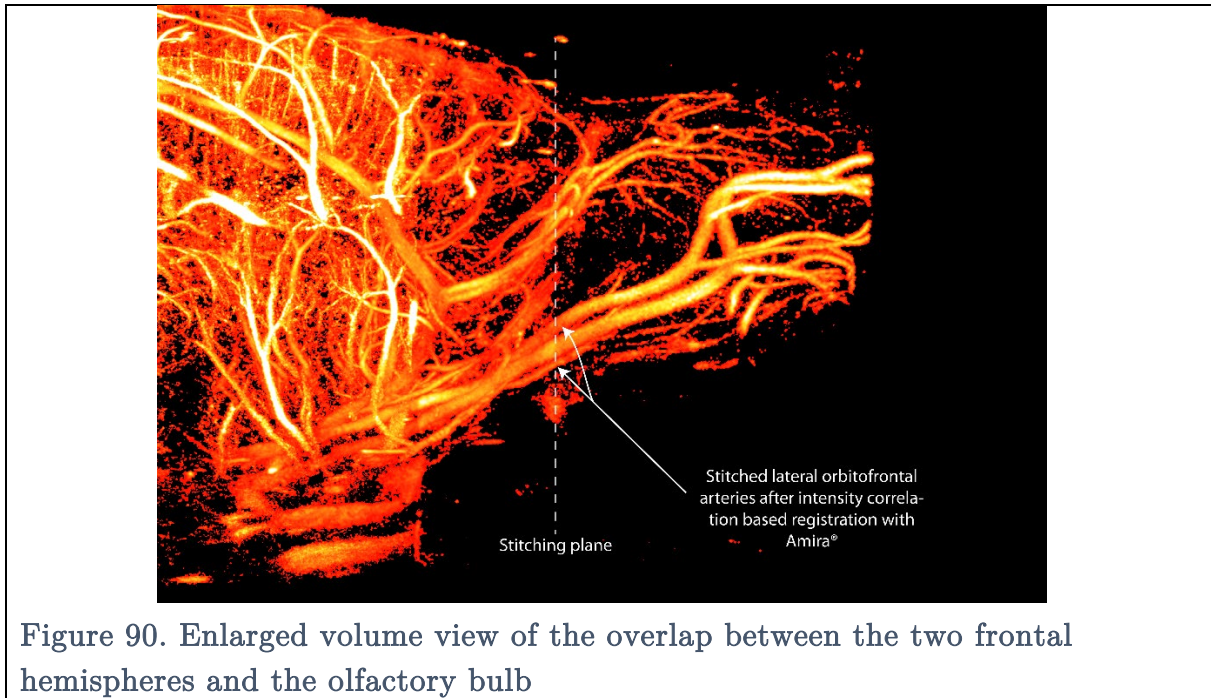


Figure 89. Whole-brain imaging *in vivo* using 3D ULM with vasculature labeling

- a) This picture is rendered from an anterior point of view facing the right hemisphere.
- b) This picture is taken in a sagittal viewing from the right hemisphere. The missing overlap can be clearly seen.
- c) This picture is rendered from an anterior point of view facing the left hemisphere.



Thanks to 3D data, it is also possible to make cuts in the coronal, sagittal and transversal planes. Various planes have been chosen to illustrate the wide diversity of vessels present in the brain. The results are presented in Figure 90, 91, 92.

Coronal cuts are presented in Figure 90. The cuts are $500 \mu\text{m}$ wide and are spaced every 3.5 mm . Labelling of the vessels was done with the help of both the rat brain atlas developed by (Scremin, 2004) and on the mouse vascular atlas from (Xiong et al., 2017). The microvasculature in all the volumes are imaged with sufficient resolution to enable small arteries and vein labelling such as the pstr (posterior striate artery), the lhi (lower hippocampal artery/vein) or the trhi (transverse hippocampal artery).

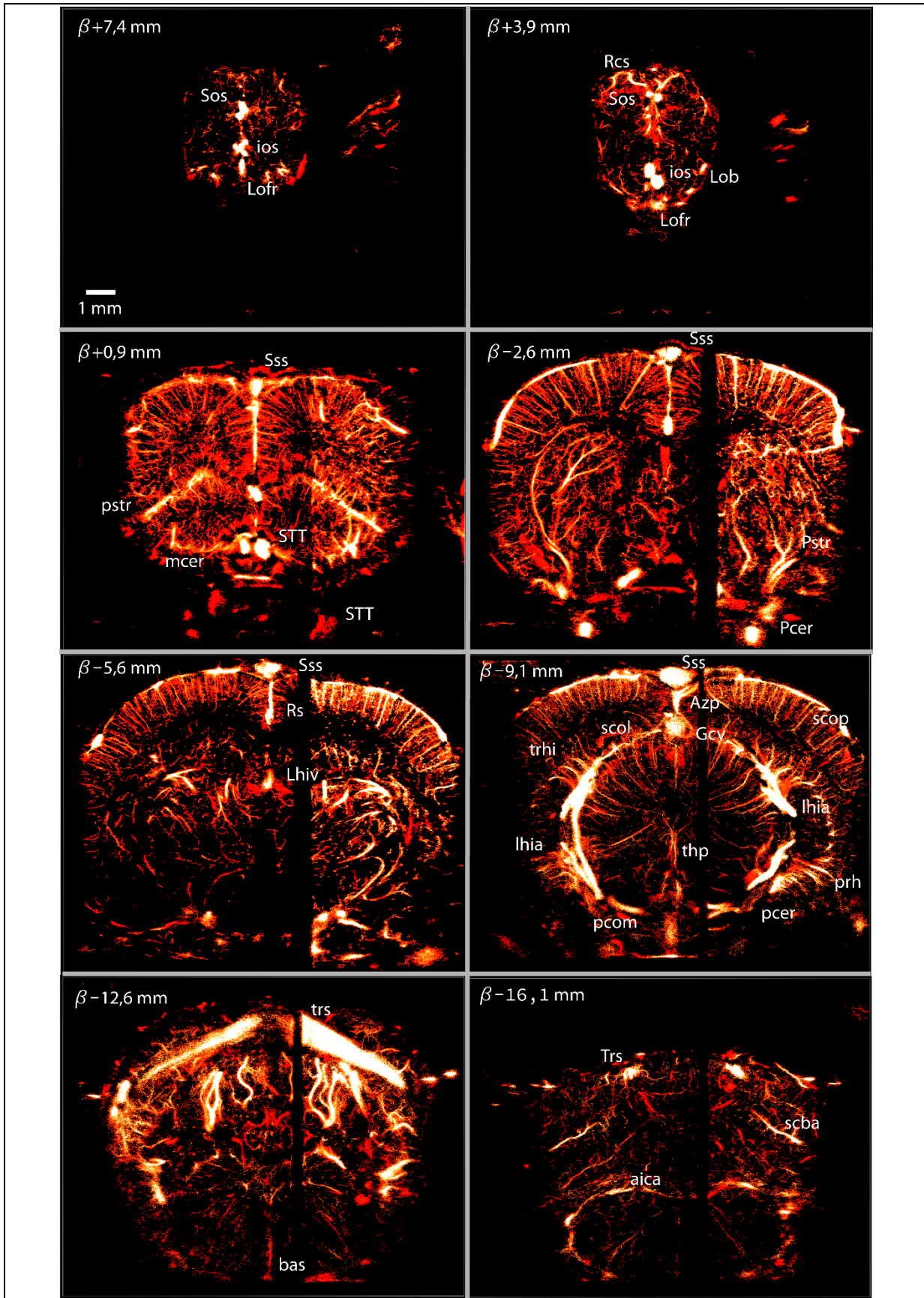


Figure 91. 500 μ m coronal cuts taken at various planes rendered based on density

Aica: Inferior anterior cerebellar artery

Pcom: Posterior communicating artery

Azp: Azygos pericallosal artery	prh: Prepositus hipoglossal nucleus*
bas: basilar artery	Pstr: posterior striate artery
Gcv: vein of Galen	Rs: retrosplinal cortex*
ios: inferior olfactory sinus	Scba: superior cerebellar artery
lhia: longitudinal hippocampal artery	Scop: subcortical penetrating artery
Lhiv: longitudinal hippocampal vein	Sss: Superior sagittal sinus
Lob: Lateral orbital branch	STT: Spinal Trigeminal tract*
Lofr: Lateral orbitofrontal artery	Thp: thalamo-perforating artery
Mcer: middle cerebral artery	Trs: transverse sinus
Pcer: posterior cerebral artery	trhi: transverse hippocampal artery

Sagittal cuts of width $500 \mu m$ are presented in Figure 91. The missing overlap is well seen and measures approximately one millimeter. A lot of vessels are labeled easily using the Scremin atlas especially in the areas near the center of the brain. As the cuts go further away from the center of the brain, less vessels are distinguishable because of the vasculature structures which don't project well in the sagittal planes. A few pial vessels can be identified successfully such as the middle branch of the middle cerebral artery, the posterior cerebral artery, and the transverse sinuses. Contrary to coronal cuts, the median medullary arteries, the thalamo perforating arteries the supracollicular network are clearly visible in their characteristic fanlike structure.

$500 \mu m$ thick transverse cuts are presented in Figure 92. These cuts are particularly useful to visualize how the blood flows in from the main vasculature bed. The Willis circle is not present in the acquisition but several vessels can be seen : sigmoid sinus, middle cerebral artery the medial collicular vein the longitudinal hippocampal artery and the intracavernous vein. The structure of descending and ascending vessels in the neocortex can be clearly seen in transverse views as the vessels appear as single bright spots.

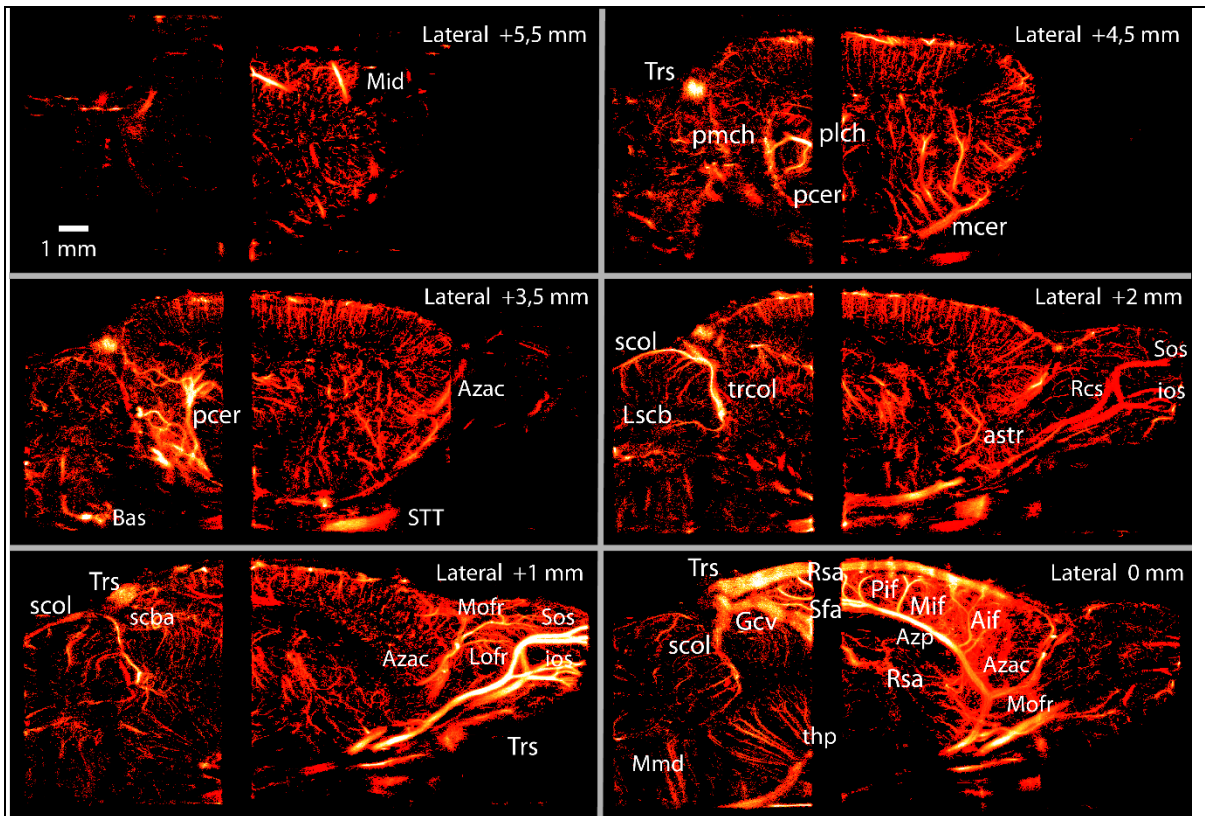


Figure 92. 500 μm sagittal cuts taken at various planes rendered based on density

Aif: Anterior internal frontal artery
 Azp: Azygos pericallosal artery
 Azac: Azygos anterior cerebral arter
 astr: anterior striate artery
 bas: basilar artery
 Gcv: vein of Galen
 ios: inferior olfactory sinus
 Lscb: lateral superior cerebral artery
 lhia: longitudinal hippocampal artery
 Lhiv: longitudinal hippocampal vein
 Lofr: Lateral orbitofrontal artery
 Mcer: middle cerebral artery
 Mid: middle branch of mcer
 Mif: Medial internal frontal artery
 Mmd: Median medullary arteries
 Mofr: Medial orbitofrontal artery
 Pcer: posterior cerebral artery

Pcom: Posterior communicating artery
 Pif: Posterior internal frontal artery
 prh: Prepositus hipoglossal nucleus*
 Pstr: posterior striate artery
 Rs: retrosplinal cortex*
 Rsa: retrosplinal artery
 Scba: superior cerebellar artery
 Scop: subcortical penetrating artery
 Scol: supracollicular arterial network
 Sfa: Subfornical artery
 Sss: Superior sagittal sinus
 STT: Spinal Trigeminal tract*
 Thp: thalamo-perforating artery
 Trs: transverse sinus
 trhi: transverse hippocampal artery

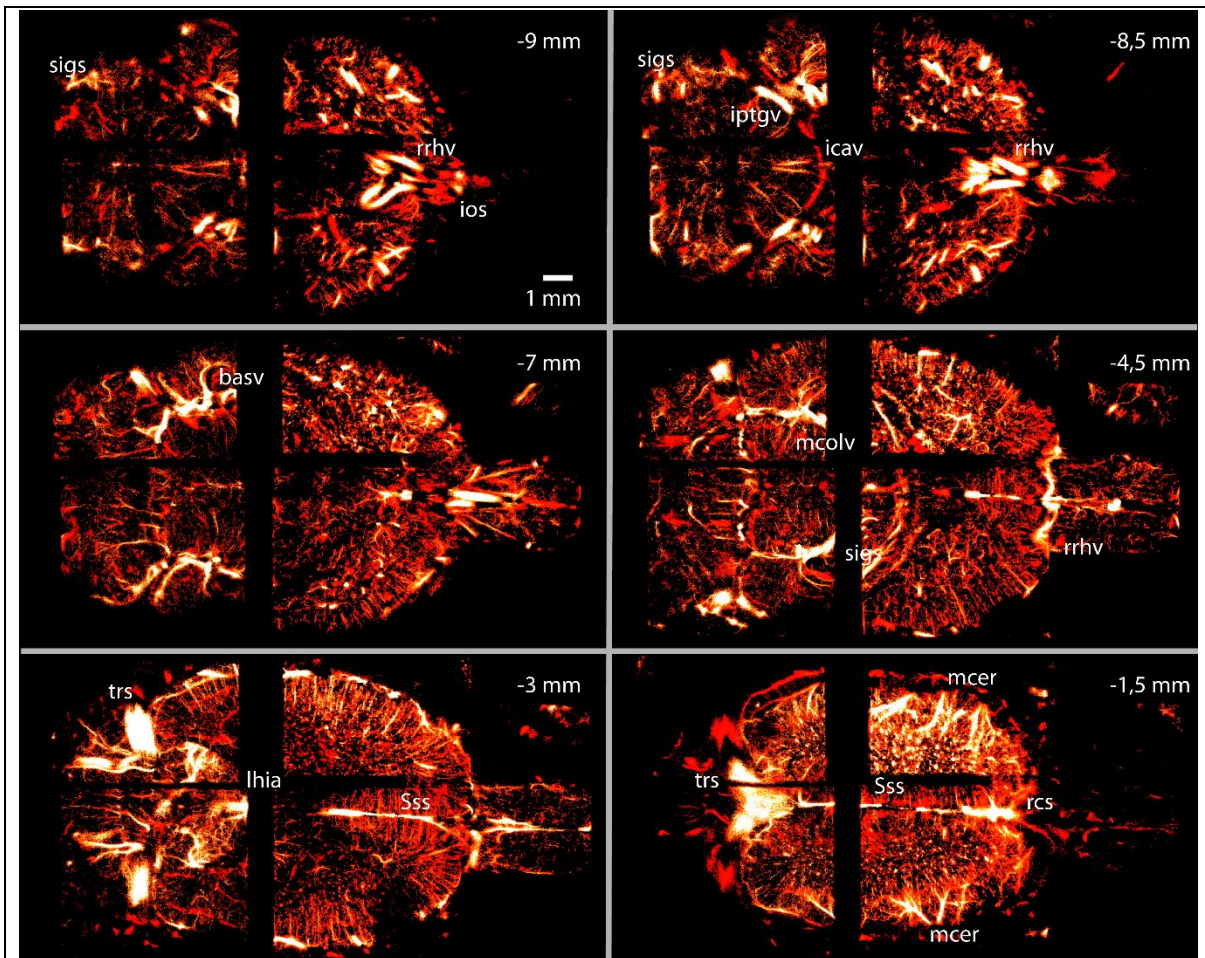


Figure 93. 500 μm transverse cuts taken at various planes rendered based on density

Basv: basal vein	mcolv: medial collicular vein
icav: intercavernous vein	rsc: rostral confluence of sinuses
iptgv: Interpterygoid emissary	rrhv: rostral rhinal vein
ios: inferior olfactory sinus	sigs: sigmoid sinus
lhia: longitudinal hippocampal artery	Sss: Superior sagittal sinus
mcer: middle cerebral artery	trs: transverse sinus

Discussion

V.1.2.3 *Surgery for whole-brain craniectomy*

The craniotomy was done in three separate steps on three separate sections. This is done to prevent ripping the *dura mater* open by pulling large pieces of the skull at once. Each section presents difficulties:

- Portion 1: the dimension of this portion is the largest ranging from almost 3 cm in height to close to 2 cm in width. Such a large window is difficult to separate from the *dura mater* as the attachment points are numerous and can be concealed by the round shape of the skull. Another problem is the risk of drilling too deep

due to large inhomogeneities in skull thickness throughout the window.

- Portion 2: the cerebellum is a densely vascularized area of the brain. Its spheroid shape means that it is also difficult to drill a regular window and hemorrhages are current. A lot of practice will help.
- Portion 3: the main issue with this portion is the shape that completely covers the olfactory bulb. The trick in drilling this portion of the brain is to avoid areas with high thickness and drill on the sides of the bulb. This method is counter-intuitive as we usually try to preserve as much skull as possible to limit damages but here, it proves fruitful as the surgery time and complexity is considerably reduced by drilling less deep but larger area.

The advantage of using agarose over using conventional ultrasound gel is that it is less affected by heat from the tissue. For long acquisitions, we have seen that the ultrasound gel tends to liquefy and slide on the sides of the brain, leaving areas with no contact gel. The only remedy to this would be to re-apply gel but this would mean moving the probe away from the brain and thus losing the reference position. Another method involving the application of TPX film over the rat's brain drowned in saline was proposed in [Déméné et al, 2015]. Such a method can not be applied to our protocol as the size of the craniectomy performed means that we don't have bone left to support that TPX film. One could attempt to shape a support for the TPX film made of dental cement, but this would lengthen the procedure considerably. Another method that can be used is to drown the brain in saline and use the threads maintaining the muscles as walls for this tiny swimming pool. This was applied preferentially when possible but sometimes, the initial transverse cut of the skin was too big to provide a waterproof swimming pool.

V.1.2.4 Motion correction

Two different algorithms were tested out on the rat brain. The VTV algorithm produces better results than the BTB motion correction algorithm as expected. The BTB algorithm only corrects motion in between blocks but leaves out small motion in-between volumes. This small rigid motion induces enlarging of the vessels as the rat's head moves rigidly. Applying the BTB motion correction is equivalent to registering the mean path of the vessels in between each blocks. The motion correction in between volumes will deform the trajectories of microbubbles inside a vessel. That means that the trajectory of a microbubble inside a straight vessel will not appear straight but will reflect volume to volume motion (i.e. a straight line will have a stair pattern) and the vessel will appear larger. The mean paths of the vessels in the ULM rendering are superimposed on top of

one another after BTB motion correction. As the enlargement of the vessels due to motion in between volumes is still present, it will be added coherently when reconstructing ULM rendering and thus, the registered vessels will appear both larger than they actually are and brighter than in non-corrected ULM where the mean paths are added incoherently. An illustration of these effects is pictured in Figure 94.

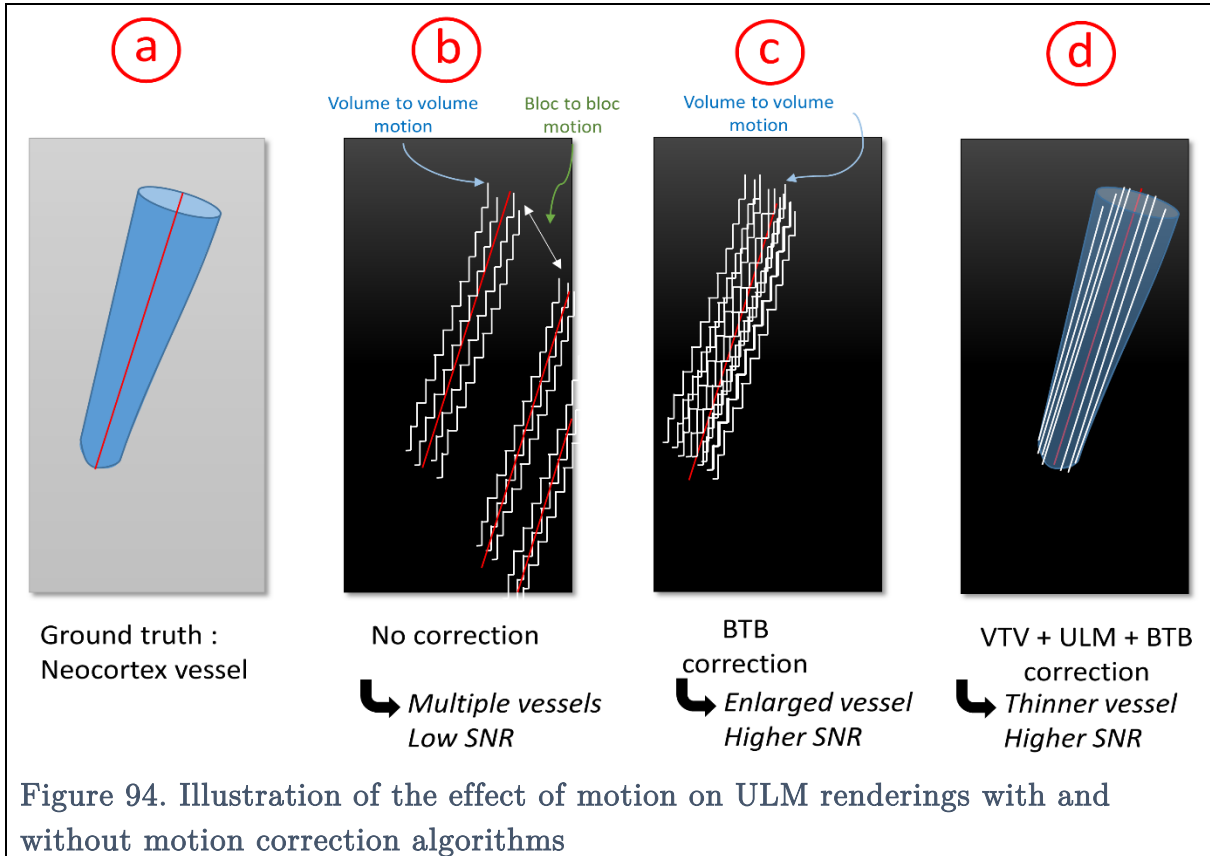
The VTV+ULM+BTB motion correction is thus recommended when processing motion affected data. The main problem with this technique, however, is the computational power needed: motion correction takes around 5 hours for 9,250 volumes while BTB alone takes around 10 minutes for 50 blocks. In the case where a global aspect of the anatomy is sufficient, we recommend using only BTB motion correction. When quantitative analysis is required, the heavier VTV+ULM+BTB motion correction is recommended. For continuous acquisitions, the BTB motion correction algorithm can be implemented by making artificial stacks in the dataset. These algorithms are efficient when motion is rigid and small, but fail when scale or shear is involved such as what is seen when imaging digestive organs, heart. For imaging tumors, however, these algorithms are predicted to perform quite well.

V.1.2.5 Whole-brain imaging

The volumes presented here are well registered within the MRI acquisition exposed in (Papp et al., 2014). The large pial vasculature can be correctly identified in the surface rendering of the brain. The advantage of having an MRI based atlas is that we have access to *in vivo* anatomical renderings. This is particularly useful for shape and geometry analysis of the brain based on the MRI image contrast and our density-based rendering. Using the (Scremin, 2004) vascular atlas for the rat brain based on vascular casts, we were able to combine the MRI data and the vascular data exposed to our 3D ULM renderings to register volumes even more accurately. Still, issues subsist. The shape of the brain is different in our case than in the MRI rendering: the two main hemispheres of the brain seems to be bigger in the vertical axis in ULM. We hypothesize that this is due to the increase in intracranial pressure after craniectomy. The cerebellum appears to be significantly lower in our case than in the MRI obtained surface rendering.

Thanks to the cast based atlas, several vascular structures could be labeled. The labeling was easily done thanks to the high resolution provided by our technique. For the smaller vessels, we recommend using cuts rather than volumes as this has proven even easier in the previous chapter. The advantage of having a 3D volume, however, is that sometimes complex structures are not well rendered in 2D slices. In those cases, we are faced with two choices: either we make larger cuts, but risk projection of several

vessels on top of one another and so this is not adapted to small microvasculature, or we do manual segmentation of the vessel in 3D and then label them in corresponding 2D slices. The last solution is however quite difficult and as the microvasculature is dense and the vessels are numerous, it is not adapted to whole-brain processing.



- a) Ground truth: the typical vessel in the neocortex. The mean path is indicated by a red line
- b) ULM rendering with no correction. The volume to volume motion is clearly seen in the stair pattern of the trajectories. The vessel in one block is constructed using only a few trajectories. The block to block motion is seen as replicas of the vessel down below due to large motion.
- c) The large motion in between block is accurately corrected but the stair pattern persists. The vessel appears brighter as all the trajectories are added coherently with respect to the mean path. The stair pattern enlarges the size of the ULM rendered vessel.
- d) The stair pattern is corrected in the VTV motion correction step. ULM is then performed and renders straight vessel but with mean paths affected by the block to block motion. BTB motion correction registers the mean paths and adds the trajectories coherently on the same mean path. The vessel appears brighter and is not enlarged.

The registration of the different volumes based on overlapping yields very good

results as pictured in Figure 90. The manual registration step might take a bit of time but we found that after identification of the main arteries and veins, the Amira[®] intensity correlation-based algorithm converged on a solution after a couple of minutes. As the number of volumes to be registered together is quite small, and as the volumetric ULM algorithm applied on all acquisition takes more than a day, the computation time of this registration is not an issue. It would be interesting to see how the registration performs when trying to match two volumetric ULM renderings coming from different rats.

The coronal cuts presented here show the complex vascular structure deep in the brain. Even though the lack of overlapping areas sometimes leads to the absence of information in the cuts, several vessels and veins can be labeled. The resolution of 3D ULM, while lower than what is observable in 2D ULM renderings, is sufficient enough to compare vasculature obtained with 2D ULM or with the conventional methods for imaging vasculature listed in the introduction. We encountered a problem when producing transverse cuts: the whole-brain imaging volume is quite big (around 40 to 50 Gb) if rendered with voxels of $10 \times 10 \times 10 \mu\text{m}$. When resampling the data in Amira to produce, $500 \mu\text{m}$ cuts, the software simply crashed. This technological issue can be easily overcome by producing these slices using Matlab rather than Amira.

The velocimetry was not represented here. The highly complex nature of the vasculature in the brain makes it hard to render velocity in 3D. We have yet to find a solution to render signed velocities in the rat brain without resorting to slices.

The main challenges in whole-brain imaging using volumetric ULM remain the same as those for single acquisition volumetric ULM but grow even bigger in importance: one whole-brain acquisition takes up to 6.2 TB of Radiofrequency data, localization, tracking, and velocimetry take more than a day, the size of the volume-rendered are so big that the RAM in the renderer's computer must be above 64Gb for visualization and at least 128Gb if the registration between the different volumes has to be performed.

The biological challenges posed by volumetric ULM on whole-brain are also numerous: for now, the 5 acquisitions take about an hour and a half. Under anesthesia, however, the rat undergoes a lot of hemodynamic changes. The data acquired is thus time-dependent and can be affected by pulsatility of the brain, a change in the heart function, pulmonary alterations, etc... This has to be kept in mind when the velocimetry data provided with volumetric ULM is used. The advantage of using newer system would be considerable as it would reduce the time of imaging to under 13 minutes if four echographs are used or 25 minutes using a multiplexer.

V.1.3 Conclusion

The first *in vivo* proof of concept of whole-brain imaging using Ultrasound Localization Microscopy was presented. The volume presented here is not complete as there was not sufficient overlap in all acquired data to stitch everything together. The issue here is not technological as overlap can be insured by moving the probe more accurately using micrometric screws rather than moving it by hand as what was done here. The two overlapping acquisitions, however, were successfully registered and stitched together. The motion correction algorithm presented in section V.1.1.3 is also robust and could be used to compensate inter-acquisition motion. Since the redaction of this manuscript, 3 rats have been imaged in the same way and have been successfully reconstructed to provide complete whole brain imaging.

In this chapter, we have successfully proved that the volumetric ULM technique can be implemented on large organs even though some adjustments have to be made. The whole-brain imaging presented here is very promising as far as vascular labeling is concerned but opens up the way towards many other applications: comparison of hemodynamic changes observed at different stages in the rat's life, imaging the morphological modifications of the brain, imaging angiogenesis or stroke in 3D. It was also proven in this chapter that we can deal with large amounts of data in a limited amount of time (in fact 3D is now faster than the 2D implementation presented in (Errico et al., 2015)), that we are able to correct for breathing motion, register different acquisitions together and rendering a larger organ. We believe that these aspects are crucial to widespread the use of 3D ULM at our lab and in teams around the world.

- Chung, K., Deisseroth, K., 2013. CLARITY for mapping the nervous system. *Nat. Methods* 10, 508–513. <https://doi.org/10.1038/nmeth.2481>
- Chung, K., Wallace, J., Kim, S.-Y., Kalyanasundaram, S., Andalman, A.S., Davidson, T.J., Mirzabekov, J.J., Zalocusky, K.A., Mattis, J., Denisin, A.K., Pak, S., Bernstein, H., Ramakrishnan, C., Grosenick, L., Gradinaru, V., Deisseroth, K., 2013. Structural and molecular interrogation of intact biological systems. *Nature* 497, 332–337. <https://doi.org/10.1038/nature12107>
- Dodt, H.-U., Leischner, U., Schierloh, A., Jährling, N., Mauch, C.P., Deininger, K., Deussing, J.M., Eder, M., Zieglgänsberger, W., Becker, K., 2007. Ultramicroscopy: three-dimensional visualization of neuronal networks in the whole mouse brain. *Nat. Methods* 4, 331–336. <https://doi.org/10.1038/nmeth1036>
- Dong, H., 2008. The Allen reference atlas: A digital color brain atlas of the C57Bl/6J male mouse.
- Dumas, L., Heitz-Marchaland, C., Fouquet, S., Suter, U., Livet, J., Moreau-Fauvarque, C., Chédotal, A., 2015. Multicolor analysis of oligodendrocyte morphology, interactions, and development with Brainbow: Multicolor Imaging of Myelination. *Glia* 63, 699–717. <https://doi.org/10.1002/glia.22779>
- Errico, C., Pierre, J., Pezet, S., Desailly, Y., Lenkei, Z., Couture, O., Tanter, M., 2015. Ultrafast ultrasound localization microscopy for deep super-resolution vascular imaging. *Nature* 527, 499–502. <https://doi.org/10.1038/nature16066>
- Ertürk, A., Becker, K., Jährling, N., Mauch, C.P., Hojer, C.D., Egen, J.G., Hellal, F., Bradke, F., Sheng, M., Dodt, H.-U., 2012. Three-dimensional imaging of solvent-cleared organs using 3DISCO. *Nat. Protoc.* 7, 1983–1995. <https://doi.org/10.1038/nprot.2012.119>
- Ertürk, A., Bradke, F., 2013. High-resolution imaging of entire organs by 3-dimensional imaging of solvent cleared organs (3DISCO). *Exp. Neurol.* 242, 57–64. <https://doi.org/10.1016/j.expneurol.2012.10.018>
- Ertürk, A., Lafkas, D., Chalouni, C., 2014. Imaging Cleared Intact Biological Systems at a Cellular Level by 3DISCO. *J. Vis. Exp.* 51382. <https://doi.org/10.3791/51382>
- Franklin, K.B.J., Paxinos, G., 2013. Paxinos and Franklin's: The mouse brain in stereotaxic coordinates, 4th ed. Amsterdam: Academic Press.
- Garey, L., 1999. Cortex: Statistics and Geometry of Neuronal Connectivity, 2nd edn. By V. BRAITENBERG and A. SCHUZ. (Pp. xiii+249; 90 figures; ISBN 3 540 63816 4). Berlin: Springer. 1998. *J. Anat.* 194, 153–157. <https://doi.org/10.1046/j.1469-7580.1999.194101535.x>
- Girouard, H., Iadecola, C., 2006. Neurovascular coupling in the normal brain and in hypertension, stroke, and Alzheimer disease. *J. Appl. Physiol.* 100, 328–335. <https://doi.org/10.1152/jappphysiol.00966.2005>
- Gong, H., Zeng, S., Yan, C., Lv, X., Yang, Z., Xu, T., Feng, Z., Ding, W., Qi, X., Li, A., Wu, J., Luo, Q., 2013. Continuously tracing brain-wide long-distance axonal projections in mice at a one-micron voxel resolution. *NeuroImage* 74, 87–98.

- <https://doi.org/10.1016/j.neuroimage.2013.02.005>
- Hama, H., Kurokawa, H., Kawano, H., Ando, R., Shimogori, T., Noda, H., Fukami, K., Sakaue-Sawano, A., Miyawaki, A., 2011. Scale: a chemical approach for fluorescence imaging and reconstruction of transparent mouse brain. *Nat. Neurosci.* 14, 1481–1488. <https://doi.org/10.1038/nn.2928>
- Hamilton, N.B., 2010. Pericyte-mediated regulation of capillary diameter: a component of neurovascular coupling in health and disease. *Front. Neuroenergetics* 2. <https://doi.org/10.3389/fnene.2010.00005>
- Hingot, V., Errico, C., Tanter, M., Couture, O., 2017. Subwavelength motion-correction for ultrafast Ultrasound Localization Microscopy. *IEEE Trans. Ultrason. Ferroelectr. Freq. Control* 1–1.
- Josh Huang, Z., Zeng, H., 2013. Genetic Approaches to Neural Circuits in the Mouse. *Annu. Rev. Neurosci.* 36, 183–215. <https://doi.org/10.1146/annurev-neuro-062012-170307>
- Kanbay, M., Sanchez-Lozada, L.-G., Franco, M., Madero, M., Solak, Y., Rodriguez-Iturbe, B., Covic, A., Johnson, R.J., 2011. Microvascular disease and its role in the brain and cardiovascular system: a potential role for uric acid as a cardiorenal toxin. *Nephrol. Dial. Transplant.* 26, 430–437. <https://doi.org/10.1093/ndt/gfq635>
- Ke, M.-T., Fujimoto, S., Imai, T., 2013. SeeDB: a simple and morphology-preserving optical clearing agent for neuronal circuit reconstruction. *Nat. Neurosci.* 16, 1154–1161. <https://doi.org/10.1038/nn.3447>
- Kuwajima, T., Sitko, A.A., Bhansali, P., Jurgens, C., Guido, W., Mason, C., 2013. ClearT: a detergent- and solvent-free clearing method for neuronal and non-neuronal tissue. *Development* 140, 1364–1368. <https://doi.org/10.1242/dev.091844>
- Li, A., Gong, H., Zhang, B., Wang, Q., Yan, C., Wu, J., Liu, Q., Zeng, S., Luo, Q., 2010. Micro-Optical Sectioning Tomography to Obtain a High-Resolution Atlas of the Mouse Brain. *Science* 330, 1404–1408. <https://doi.org/10.1126/science.1191776>
- Livet, J., Weissman, T.A., Kang, H., Draft, R.W., Lu, J., Bennis, R.A., Sanes, J.R., Lichtman, J.W., 2007. Transgenic strategies for combinatorial expression of fluorescent proteins in the nervous system. *Nature* 450, 56–62. <https://doi.org/10.1038/nature06293>
- Luo, L., Callaway, E.M., Svoboda, K., 2008. Genetic Dissection of Neural Circuits. *Neuron* 57, 634–660. <https://doi.org/10.1016/j.neuron.2008.01.002>
- Macé, E., Cohen, I., Gennisson, J., Miles, R., Tanter, M., Fink, M., 2009. Ultrasound transient elastography of the brain : an in vivo feasibility study in small animals. Presented at the International Conference on the ultrasonic measurement and imaging of Tissue Elasticity.
- Macé, E., Montaldo, G., Cohen, I., Baulac, M., Fink, M., Tanter, M., 2011. Functional ultrasound imaging of the brain. *Nat. Methods* 8, 662–664.

- <https://doi.org/10.1038/nmeth.1641>
- Macé, E., Montaldo, G., Fink, M., Tanter, M., Cohen, I., Miles, R., 2010. High sensitivity brain angiography using ultrafast Doppler. Presented at the International Ultrasonics Symposium. <https://doi.org/10.1109/ultsym.2010.5935810>
- Madisen, L., Zwingman, T.A., Sunkin, S.M., Oh, S.W., Zariwala, H.A., Gu, H., Ng, L.L., Palmiter, R.D., Hawrylycz, M.J., Jones, A.R., Lein, E.S., Zeng, H., 2010. A robust and high-throughput Cre reporting and characterization system for the whole mouse brain. *Nat. Neurosci.* 13, 133–140. <https://doi.org/10.1038/nn.2467>
- Manolio, T.A., Olson, J., Longstreth, W.T., 2003. Hypertension and cognitive function: Pathophysiologic effects of hypertension on the brain. *Curr. Hypertens. Rep.* 5, 255–261. <https://doi.org/10.1007/s11906-003-0029-6>
- Markram, H., Toledo-Rodriguez, M., Wang, Y., Gupta, A., Silberberg, G., Wu, C., 2004. Interneurons of the neocortical inhibitory system. *Nat. Rev. Neurosci.* 5, 793–807. <https://doi.org/10.1038/nrn1519>
- Mayerich, D., Abbott, L., McCORMICK, B., 2008. Knife-edge scanning microscopy for imaging and reconstruction of three-dimensional anatomical structures of the mouse brain. *J. Microsc.* 231, 134–143. <https://doi.org/10.1111/j.1365-2818.2008.02024.x>
- McCormick, B.H., Koh, W., Choe, Y., Abbott, L.C., Keyser, J., Mayerich, D., Melek, Z., Doddapaneni, P., 2004. Construction of anatomically correct models of mouse brain networks. *Neurocomputing* 58–60, 379–386. <https://doi.org/10.1016/j.neucom.2004.01.070>
- Miyamichi, K., Amat, F., Moussavi, F., Wang, C., Wickersham, I., Wall, N.R., Taniguchi, H., Tasic, B., Huang, Z.J., He, Z., Callaway, E.M., Horowitz, M.A., Luo, L., 2011. Cortical representations of olfactory input by trans-synaptic tracing. *Nature* 472, 191–196. <https://doi.org/10.1038/nature09714>
- Orozco-Cabal, L., Pollandt, S., Liu, J., Shinnick-Gallagher, P., Gallagher, J.P., 2006. Regulation of Synaptic Transmission by CRF Receptors. *Rev. Neurosci.* 17. <https://doi.org/10.1515/REVNEURO.2006.17.3.279>
- Papp, E.A., Leergaard, T.B., Calabrese, E., Johnson, G.A., Bjaalie, J.G., 2014. Waxholm Space atlas of the Sprague Dawley rat brain. *NeuroImage* 97, 374–386. <https://doi.org/10.1016/j.neuroimage.2014.04.001>
- Peyrounette, M., Davit, Y., Quintard, M., Lorthois, S., 2018. Multiscale modelling of blood flow in cerebral microcirculation: Details at capillary scale control accuracy at the level of the cortex. *PLOS ONE* 13, e0189474. <https://doi.org/10.1371/journal.pone.0189474>
- Ragan, T., Kadiri, L.R., Venkataraju, K.U., Bahlmann, K., Sutin, J., Taranda, J., Arganda-Carreras, I., Kim, Y., Seung, H.S., Osten, P., 2012. Serial two-photon tomography for automated ex vivo mouse brain imaging. *Nat. Methods* 9, 255–258. <https://doi.org/10.1038/nmeth.1854>
- Ragan, T., Sylvan, J.D., Kim, K.H., Huang, H., Bahlmann, K., Lee, R.T., So, P.T.C.,

2007. High-resolution whole organ imaging using two-photon tissue cytometry. *J. Biomed. Opt.* 12, 014015. <https://doi.org/10.1117/1.2435626>
- Renier, N., Wu, Z., Simon, D.J., Yang, J., Ariel, P., Tessier-Lavigne, M., 2014. iDISCO: A Simple, Rapid Method to Immunolabel Large Tissue Samples for Volume Imaging. *Cell* 159, 896–910. <https://doi.org/10.1016/j.cell.2014.10.010>
- Scremin, O.U., n.d. Cerebral Vascular System 36.
- Shaner, N.C., Steinbach, P.A., Tsien, R.Y., 2005. A guide to choosing fluorescent proteins. *Nat. Methods* 2, 905–909. <https://doi.org/10.1038/nmeth819>
- Shi, S.-R., Shi, Y., Taylor, C.R., 2011. Antigen Retrieval Immunohistochemistry: Review and Future Prospects in Research and Diagnosis over Two Decades 20.
- Sotelo, C., 2003. Viewing the brain through the master hand of Ramon y Cajal. *Nat. Rev. Neurosci.* 4, 71–77. <https://doi.org/10.1038/nrn1010>
- Susaki, E.A., Tainaka, K., Perrin, D., Kishino, F., Tawara, T., Watanabe, T.M., Yokoyama, C., Onoe, H., Eguchi, M., Yamaguchi, S., Abe, T., Kiyonari, H., Shimizu, Y., Miyawaki, A., Yokota, H., Ueda, H.R., 2014. Whole-Brain Imaging with Single-Cell Resolution Using Chemical Cocktails and Computational Analysis. *Cell* 157, 726–739. <https://doi.org/10.1016/j.cell.2014.03.042>
- Tomer, R., Ye, L., Hsueh, B., Deisseroth, K., 2014. Advanced CLARITY for rapid and high-resolution imaging of intact tissues. *Nat. Protoc.* 9, 1682–1697. <https://doi.org/10.1038/nprot.2014.123>
- Windhorst, U., Johansson, H., 1999. *Modern Techniques in Neuroscience Research*.
- Wu, J., He, Y., Yang, Z., Guo, C., Luo, Q., Zhou, W., Chen, S., Li, A., Xiong, B., Jiang, T., Gong, H., 2014. 3D BrainCV: Simultaneous visualization and analysis of cells and capillaries in a whole mouse brain with one-micron voxel resolution. *NeuroImage* 87, 199–208. <https://doi.org/10.1016/j.neuroimage.2013.10.036>
- Xiong, B., Li, A., Lou, Y., Chen, S., Long, B., Peng, J., Yang, Z., Xu, T., Yang, X., Li, X., Jiang, T., Luo, Q., Gong, H., 2017. Precise Cerebral Vascular Atlas in Stereotaxic Coordinates of Whole Mouse Brain. *Front. Neuroanat.* 11, 128. <https://doi.org/10.3389/fnana.2017.00128>
- Yang, B., Treweek, J.B., Kulkarni, R.P., Deverman, B.E., Chen, C.-K., Lubeck, E., Shah, S., Cai, L., Gradinaru, V., 2014. Single-Cell Phenotyping within Transparent Intact Tissue through Whole-Body Clearing. *Cell* 158, 945–958. <https://doi.org/10.1016/j.cell.2014.07.017>
- Yuan, J., Gong, H., Li, A., Li, X., Chen, S., Zeng, S., Luo, Q., 2015. Visible rodent brain-wide networks at single-neuron resolution. *Front. Neuroanat.* 9. <https://doi.org/10.3389/fnana.2015.00070>
- Zhang, B., Li, A., Yang, Z., Wu, J., Luo, Q., Gong, H., 2011. Modified Golgi-Cox method for micrometer scale sectioning of the whole mouse brain. *J. Neurosci. Methods* 197, 1–5. <https://doi.org/10.1016/j.jneumeth.2010.10.001>

V

Conclusions and perspectives

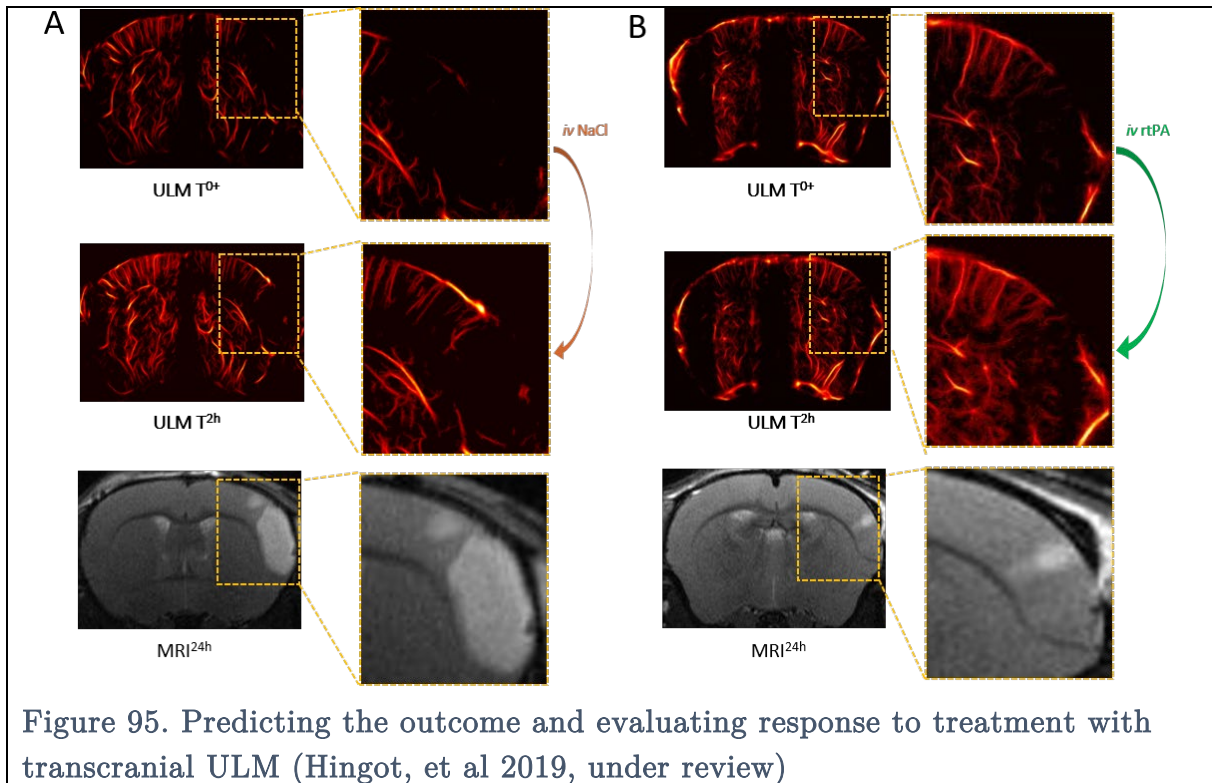
VI. Chapter 6: Conclusion and perspectives

The brain is a fascinating organ, the control room of thoughts, actions, the road junction where main arteries and veins develop to form a dense and complex vascular bed, the concert hall for complex chemical reactions, electrical stimulations. But, due to its importance, the brain is also the seat of major diseases, such as Alzheimer's, Parkinson's, depression, cancer, and many others. My work is set in a larger scheme focused on finding out how the brain is affected by stroke and how to approach its diagnostic in a novel way through ultrasound localization microscopy.

Brain imaging has benefited enormously from ultrafast ultrasound imaging in the last 10 years. From the earliest demonstration of elasticity mapping in 2009 (Macé et al., 2009) to the demonstration of angiography (Macé et al., 2010) and functional ultrasound (Macé et al., 2011), mouse, rat, primate, newborn and adult brains have been observed and characterized with ultrasound. The technological breakthrough brought by the development of 2D Ultrasound Localization Microscopy *in vivo* also focused on that model (Errico et al., 2015).

VI.1 Objectives

The main project of our team, dubbed ResolveStroke aims at providing fast and qualitative analysis of ischemic and hemorrhagic stroke in the care path. Thanks to the improvements highlighted in Chapter 2, 2D ULM in the preclinical study of the stroke was achieved by my colleague Vincent Hingot. The enhanced resolution brought by ULM allowed him to provide a qualitative analysis of the gravity of the stroke Figure 95. Accurate reperfusion assessment was also possible thanks to microvessel imaging, and in some cases outperform T2* weighted MRI which is the gold standard. His studies were done transcranially and in mice. The difficulties associated with reproducing these results in humans are threefold: motion, limited field of view, skull bone induced wavefront aberrations, and user-dependency.



The incompressible acquisition time to perform ULM implies that the imaging plane will be affected by patient or doctor motion. Radiologists train for thousands of hours to be as still as possible when performing echography. The longer the acquisition takes, the harder the task. Only a handful of radiologists in France would be able to stay in the same plane for several minutes to perform 2D ULM, and because “time is brain”, the faster the patient is imaged, the smaller the consequences of stroke. Waiting in line for the best radiologist to be available is not an option; stroke patient care already involves waiting in line for the MRI machine. Having a 2D matrix array probe producing volumetric data means that out of plane motion is dispensed with and motion correction can be applied. The imaging part of the clinical diagnosis would no longer be operator dependent.

Conventional 1D probes have a field of view limited in elevation to a couple of wavelengths. For Ultrasound Localization Microscopy this means that there is a problem with vessels going in and out of the focal plane as they are barely seen and thus vessels can not be reconstructed well. Scanning is usually implemented by a radiologist by freehanding the probe in different planes of imaging, however for ULM, multiple acquisitions mean more time spent to image and thus more motion. 2D probes have an enlarged field of view and suffer less from elevation projection as they can focus in 3 directions. They are able to insonify large volumes and image them at very high frame rates (Jensen et al., 2013; Provost et al., 2014). The increased field of view not only

provides better quality imaging but is also useful for scanning the brain rapidly to find out where the hemorrhage or ischemia appeared post-stroke.

Finally, the mice skull is relatively thin and ultrasound is barely affected by wavefront aberration. For humans, ultrasound angiography is usually done through the temporal bone Figure 96. The resolution and image quality is quite poor because of the aberration of the skull that deforms the ultrasound wavefront, the low frequency of the probe to limit aberration and attenuation, and because of motion. Having a 2D probe would solve motion and limited field of view but would not improve the resolution a lot and would not prevent aberration.

This is where the need for 3D ULM is: provide fast volumetric imaging of complex 3D vasculature of organs *in vivo* with an improved resolution. My thesis thus aimed to enhance 2D ULM, make the first proof of concept of 3D ULM with a 2D matrix array and implement it *in vivo*.

The aberration correction problem was studied during my thesis but not explained here as part of a work done in collaboration with my colleagues Justine Robin and Charlie Deméné. Transcranial ultrasound data were acquired on adults in the Clinical Neuroscience Department, LUNIC at Hôpitaux Universitaires de Genève in Switzerland. Aberration correction schemes were developed and implemented a posteriori (Robin et al, 2020, under review, Déméné et al, 2020, under review). Much work remains to be done to port these techniques in 3D and should be taken on by Arthur Chavignon, a new Ph.D. student in the ResolveStroke project.

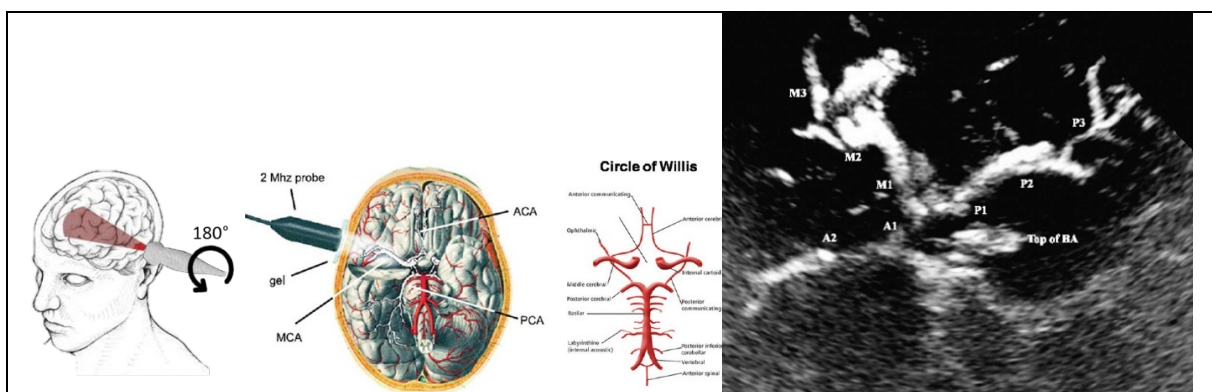


Figure 96. Transcranial Doppler imaging of the human brain: only large structures are visible (Holscher et al., 2007)

VI.2 Developing 3D ULM

The work exposed in this manuscript follows the original goal of developing 3D ULM *in vivo*.

As the main problem with 3D ULM is data overdose, my first task was to develop faster algorithms for localization and tracking. As a lucky bonus, it turned out that the new algorithms developed improved image quality. To really assess this gain, specific metrics were designed and most of the algorithms used by the community were benchmarked (see Chapter 2).

After developing new algorithms for both 2D and 3D ULM, we aimed to prove the feasibility of 3D ULM using a fully addressed 2D matrix array. To achieve our goal, we designed an *in vitro* phantom that could provide us a complex shape to render, arranged in 3 dimensions and with a bifurcation to measure the resolution of our system. Chapter 3 details the path followed to achieve 3D ULM *in vitro*.

After taking small steps, the giant leap towards *in vivo* ULM in 3D was attempted. With some unforeseen difficulties related to aging echographs and data overdose, a complete framework for data acquisition and processing was designed. The framework is exposed in chapter 4. Additionally to improved resolution in 3 dimensions, I also proved that 3D ULM could be used as a flow sensor to map vascular changes induced by anesthesia.

Finally, as the problem of motion and of limited volumes remain for human applications of the 3D ULM, I decided to take on motion correction in 3D and try to register large volumes together to render the first whole rat brain imaging at a microscopic scale *in vivo* with vascular flow mapping. The work done to meet these objectives is summed up in chapter 5. The proof of concept of registration for whole-brain imaging is complete and we aim to go further in that direction.

Some additional work such as Row Column Addressed based 3D ULM was not detailed here. Preliminary work was done in collaboration with a fellow Ph.D. student Jack Sauvage. The algorithm detailed here should work on other types of imaging such as Sparse arrays.

VI.3 Perspectives

The field of Ultrasound Localization Microscopy has been booming in recent years: more presentations at IEEE IUS but also more parallel sessions and more papers each

year. A few paths presented by these papers are interesting to explore:

VI.3.1 Non-microbubble based ULM

There are two issues with the microbubbles used conventionally for ULM *in vivo*. The first one is their circulation time, after a couple of minutes, all the microbubbles have been eliminated in the vascular system and another bolus is required to continue imaging. The second problem is their size: on the order of several micrometer, it is still larger compared to red blood cells and capillaries. A typical human red blood cell has a disk diameter of approximately $6 - 8 \mu\text{m}$ and a thickness as low as 800 nm . It is known that red blood cells deform when they pass through capillaries, a behavior that is difficult for microbubbles. The community is unsure whether microbubbles actually go through capillaries. Having smaller contrast agents would also allow to increase the ratio of contrast agents over red blood cells and thus map the vascular bed faster.

(Kawabata et al., 2005; S. Sheeran and A. Dayton, 2012) proposed replacing gas-based microbubbles by small droplets containing perfluorocarbon gas. These droplets can be vaporized using ultrasound and become stable microbubbles. Thanks to their lower size than conventional contrast agents, they can be injected in greater numbers and reach structures where microbubbles can not go such as the lymphatic system of the extravascular space. (Zhang et al., 2018) showed that such nanodroplets could be activated with vaporization and as such could provide an equivalent to blinking photo sources developed in PALM.

More recently, a team led by Mikhail Shapiro demonstrated that gas vesicles produced by bacteria could not only be used as ultrasound contrast agents but could be implanted in cells (their size is a few hundreds of nanometers), and genetically engineered to serve as acoustic reporters gene (Szablowski et al., 2018; Wu et al., 2019). These contrast agents are the equivalent of Green Fluorescent Protein in optics but for ultrasound. This line of work is very interesting and combining ULM with nanometer-size acoustic reporters gene would be a giant leap forward for ULM.

VI.3.2 Non-localization based ULM

Similarly to optical fluctuation imaging, a method was proposed by (Bar-Zion et al., 2017; Solomon et al., 2018) to provide increased resolution using statistical decorrelation of microbubbles rather than localization. It was shown to be able to reduce acquisition times in big vessels but the incompressible time linked to the passage of microbubbles in the small vasculature is unaffected by this method. It is, however, a

good method when big vessel imaging is wanted.

Another interesting approach that does not involve localization is based on Structured Illumination Microscopy. (Ilovitsh et al., 2018) showed that acoustic structured illumination could improve the axial resolution two-fold with no loss in temporal resolution.

Much work remains to be done to improve the temporal resolution of ULM and to increase its potential as a blood flow sensor.

VI.3.3 Towards multi-modality imaging

Lastly, I strongly believe that multimodality imaging of organs involving ULM and for example, optical sectioning methods would provide an interesting line of research. ULM implemented *in vivo* would allow verifying what optical sectioning measures such as vessel diameters, tortuosity, intraspecies variability but would provide additional information that is lacking in *post mortem* imaging such as blood flow analysis, variation of microvasculature induced by drugs, remodeling of the vasculature under external stimuli, etc... The strong correlation between the images presented in chapter 5 and the CLARITY, 3DISCO, iDISCO images is a strong incentive for extensive collaboration between these different fields.

Another modality that could be combined with ULM is photo-acoustics (Vilov et al., 2017). By sending high energy light into tissue, heating provokes thermal expansion which emits a pressure wave. Measuring that pressure wave with transducer allows reconstructing vascular structures of complete organs of a few centimeters with a resolution of a few hundreds of nanometers. While the resolution is much higher than what can be done with ULM, using these two techniques to provide anatomical, chemical and dynamic imaging on larger organs could be quite interesting.

VI.3.4 Clinical applications

Lastly, the clinical applications of ULM are numerous. A lot of preclinical studies have been presented in chapter 1 and I believe that the potential of these will be demonstrated in humans in the coming years. The wider usage of high frame rate ultrasound imaging in hospitals, the heightened interest in plane wave imaging in clinical research and the advent of new contrast agents are strong indicators of the direction ultrasound imaging is going towards. Motion related problems in the clinical practice will be solved for with widespreading of 3D ultrasound at high frame rate. This will lead to operator-independent diagnosis and combined with ULM, the mapping of

microvasculature for angiogenesis monitoring in stroke, inflammation, cancer, and cardiovascular-related diseases will become a reality. Targeted gas-vesicles combined with ULM can maximize the potential of ultrasound as a bioimaging tool opening up a vascular or elastography limited imaging tool to the field of physiology and biochemistry.

- Bar-Zion, A., Tremblay-Darveau, C., Solomon, O., Adam, D., Eldar, Y.C., 2017. Fast Vascular Ultrasound Imaging With Enhanced Spatial Resolution and Background Rejection. *IEEE Transactions on Medical Imaging* 36, 169–180. <https://doi.org/10.1109/TMI.2016.2600372>
- Errico, C., Pierre, J., Pezet, S., Desailly, Y., Lenkei, Z., Couture, O., Tanter, M., 2015. Ultrafast ultrasound localization microscopy for deep super-resolution vascular imaging. *Nature* 527, 499–502. <https://doi.org/10.1038/nature16066>
- Holscher, T., Sattin, J., Raman, R., Wilkening, W., Fanale, C.V., Olson, S.E., Mattrey, R.F., Lyden, P.D., 2007. Real-time Cerebral Angiography : Sensitivity of a New Contrast-Specific Ultrasound Technique. *American Journal of Neuroradiology*.
- Ilovitsh, T., Ilovitsh, A., Foiret, J., Fite, B.Z., Ferrara, K.W., 2018. Acoustical structured illumination for super-resolution ultrasound imaging. *Communications Biology* 1. <https://doi.org/10.1038/s42003-017-0003-5>
- Jensen, J.A., Holten-Lund, H., Nilsson, R.T., Hansen, M., Larsen, U.D., Domsten, R.P., Tomov, B.G., Stuart, M.B., Nikolov, S.I., Pihl, M.J., Yigang Du, Rasmussen, J.H., Rasmussen, M.F., 2013. SARUS: A synthetic aperture real-time ultrasound system. *IEEE Transactions on Ultrasonics, Ferroelectrics, and Frequency Control* 60, 1838–1852. <https://doi.org/10.1109/TUFFFC.2013.2770>
- Kawabata, K., Sugita, N., Yoshikawa, H., Azuma, T., Umemura, S., 2005. Nanoparticles with Multiple Perfluorocarbons for Controllable Ultrasonically Induced Phase Shifting. *Japanese Journal of Applied Physics* 44, 4548–4552. <https://doi.org/10.1143/JJAP.44.4548>
- Macé, E., Cohen, I., Gennisson, J., Miles, R., Tanter, M., Fink, M., 2009. Ultrasound transient elastography of the brain : an in vivo feasibility study in small animals. Presented at the International Conference on the ultrasonic measurement and imaging of Tissue Elasticity.
- Macé, E., Montaldo, G., Cohen, I., Baulac, M., Fink, M., Tanter, M., 2011. Functional ultrasound imaging of the brain. *Nat Methods* 8, 662–664. <https://doi.org/10.1038/nmeth.1641>
- Macé, E., Montaldo, G., Fink, M., Tanter, M., Cohen, I., Miles, R., 2010. High sensitivity brain angiography using ultrafast Doppler. Presented at the International Ultrasonics Symposium. <https://doi.org/10.1109/ultsym.2010.5935810>
- Provost, J., Papadacci, C., Arango, J.E., Imbault, M., Fink, M., Gennisson, J.-L., Tanter, M., Pernot, M., 2014. 3D ultrafast ultrasound imaging *in vivo*. *Physics in Medicine and Biology* 59, L1–L13. <https://doi.org/10.1088/0031-9155/59/19/L1>
- S. Sheeran, P., A.Dayton, P., 2012. Phase-Change Contrast Agents for Imaging and Therapy. *Current Pharmaceutical Design* 18, 2152–2165. <https://doi.org/10.2174/138161212800099883>
- Solomon, O., van Sloun, R.J.G., Wijkstra, H., Mischi, M., Eldar, Y.C., 2018. Exploiting flow dynamics for super-resolution in contrast-enhanced ultrasound. [arXiv:1804.03134](https://arxiv.org/abs/1804.03134) [physics].

- Szablowski, J.O., Lee-Gosselin, A., Lue, B., Malounda, D., Shapiro, M.G., 2018. Acoustically targeted chemogenetics for the non-invasive control of neural circuits. *Nature Biomedical Engineering* 2, 475–484. <https://doi.org/10.1038/s41551-018-0258-2>
- Vilov, S., Arnal, B., Bossy, E., 2017. Overcoming the acoustic diffraction limit in photoacoustic imaging by the localization of flowing absorbers. *Optics Letters* 42, 4379. <https://doi.org/10.1364/OL.42.004379>
- Wu, D., Baresch, D., Cook, C., Malounda, D., Maresca, D., Abundo, M.P., Mittelstein, D.R., Shapiro, M.G., 2019. Genetically encoded nanostructures enable acoustic manipulation of engineered cells. *bioRxiv*. <https://doi.org/10.1101/691105>
- Zhang, G., Harput, S., Lin, S., Christensen-Jeffries, K., Leow, C.H., Brown, J., Dunsby, C., Eckersley, R.J., Tang, M.-X., 2018. Acoustic wave sparsely activated localization microscopy (AWSALM): Super-resolution ultrasound imaging using acoustic activation and deactivation of nanodroplets. *Applied Physics Letters* 113, 014101. <https://doi.org/10.1063/1.5029874>

List of publications

Publications in peer-reviewed journal:

- O. Couture, V. Hingot, **B. Heiles**, P. Muleki-Seya, M. Tanter, Ultrasound Localization Microscopy and Super-Resolution: A State of the Art, *IEEE Transactions on Ultrasonics, Ferroelectrics, and Frequency Control* 65, 1304–1320 (**2018**).
- V. Hingot, C. Errico, **B. Heiles**, L. Rahal, M. Tanter, O. Couture, Microvascular flow dictates the compromise between spatial resolution and acquisition time in Ultrasound Localization Microscopy, *Scientific Reports* 9 (**2019**).
- **B. Heiles**, M. Correia, V. Hingot, M. Pernot, J. Provost, M. Tanter, O. Couture, Ultrafast 3D Ultrasound Localization Microscopy using a 32×32 Matrix Array, *IEEE Transactions on Medical Imaging*, 1–1 (**2019**).

Under-review, in preparation publications:

- V. Hingot, C. Brodin, **B. Heiles**, A. Chagnot, M. Yetim, C. Orset, M. Tanter, O. Couture, T. Deffieux, D. Vivien, Preclinical evidences that early ultrafast ultrasound imaging can be used to predict ischemic stroke outcome and response to treatment. (*Submitted*)
- **B. Heiles**, V. Hingot, L. Rahal, P. Lopez, C. Rabut, A. Bergel, M. Pernot, M. Tanter, O. Couture, Volumetric ultrafast Ultrasound Localisation Microscopy in vivo reveals microvascular (*In prep*)
- **B. Heiles**, A. Chavignon, V. Hingot, O. Couture, Single particle localization algorithms for ultrasound localization microscopy *in silico* and *in vivo*. (*In prep*)
- **B. Heiles**, A. Chavignon, A. Bergel, V. Hingot, M. Tanter, O. Couture, Whole rat brain microvascular imaging *in vivo* with volumetric Ultrasound localization Microscopy (*In prep*)
- J. Robin, C. Demené, **B. Heiles**, L. Puke, F. Perren-Landis, M. Tanter, *In vivo* Adaptive focusing for clinical Transcranial Ultrasound Imaging with Contrast

Agents (*In prep*)

- C. Demené, J. Robin, L. Pukke, B. Heiles, A. Dizeux, M. Pernot, M. Tanter* F. Perren* Deep Transcranial Adaptive Ultrasound Localization Microscopy of the human brain vascularization, (*In Prep*)

Oral presentations (1st author only)

- **B. Heiles**, M. Correia, M. Pernot, J Provost, M. Tanter, O. Couture, Volumetric ultrafast Ultrasound Localization Microscopy using a 32x32 Matrix Array, IEEE International Ultrasound Symposium, Washington D.C., USA, 2017
- **B. Heiles**, M. Correia, M. Pernot, J Provost, M. Tanter, O. Couture, Volumetric ultrafast Ultrasound Localization Microscopy using a 32x32 Matrix Array, Echocontrast, Rotterdam, Netherlands, 2018
- **B. Heiles**, C. Rabut, V. Hingot, L. Rahal, P. Lopez, M. Pernot M. Tanter, O. Couture, Volumetric ultrafast Ultrasound Localization Microscopy *in vivo*, IEEE International Ultrasound Symposium, Kobe, Japan, 2018
- **B. Heiles**, C. Rabut, V. Hingot, L. Rahal, P. Lopez, M. Pernot M. Tanter, O. Couture, Volumetric ultrafast Ultrasound Localization Microscopy *in vivo*, Invited seminar on Ultrasound Localization Microscopy at Fudan University, Shanghai, China, 2018
- **B. Heiles**, C. Rabut, V. Hingot, L. Rahal, P. Lopez, M. Pernot M. Tanter, O. Couture, Volumetric ultrafast Ultrasound Localization Microscopy *in vivo*, Echocontrast Rotterdam, Netherlands, 2019
- **B. Heiles**, C. Rabut, V. Hingot, L. Rahal, P. Lopez, M. Pernot M. Tanter, O. Couture, Volumetric ultrafast Ultrasound Localization Microscopy, Invited seminar on Ultrasound Localization Microscopy at Fudan University, Shanghai, China, 2019
- **B. Heiles**, V. Hingot, L. Rahal, P. Lopez, C. Rabut, A. Bergel, M. Pernot, M. Tanter, O. Couture, Volumetric ultrafast ultrasound Localization Microscopy *in vivo*, IEEE International Symposium on Biomedical Imaging, Venezia, Italy, 2019 [POSTER]
- **B. Heiles**, V. Hingot, L. Rahal, P. Lopez, C. Rabut, A. Bergel, M. Pernot, M. Tanter, O. Couture, Volumetric ultrafast ultrasound Localization Microscopy *in vivo*, 4th ESMI Imaging Technology Summer Conference, TOPIM TECH, 2019 [POSTER]
- **B. Heiles***, A. Chavignon*, V. Hingot, O. Couture, Single particle localization algorithms for ultrasound localization microscopy *in silico* and *in vivo*, IEEE International Ultrasound Symposium, Glasgow, Scotland, 2019
- **B. Heiles**, V. Hingot, L. Rahal, P. Lopez, C. Rabut, A. Bergel, M. Pernot, M. Tanter, O. Couture, Volumetric ultrafast ultrasound Localization Microscopy *in vivo*,

IEEE International Symposium on Biomedical Imaging, Venezia, Italy, 2019 [POSTER]

Awards

- Visualizing Physical Acoustics Research Picture Prizes: 3rd place, Volumetric ultrafast Ultrasound Localization Microscopy *in vivo*, **B. Heiles**, V. Hingot, L. Rahal, P. Lopez, A. Bergel, M. Pernot, M. Tanter, O. Couture

- ESMI Poster Award : Volumetric ultrafast Ultrasound Localization Microscopy *in vivo*, **B. Heiles**, V. Hingot, L. Rahal, P. Lopez, A. Bergel, M. Pernot, M. Tanter, O. Couture

Appendix I

3D radial symmetry based localization

Appendix I

We consider the 3D extension of the radial symmetry based localization exposed in chapter 2. The microbubble signal is set in a basis (z, x, y) similarly to the 2D case. We define the new basis (u, v, w) as :

$$(u, v, w) = \left(\begin{pmatrix} 1 \\ 1 \\ 1 \end{pmatrix}, \begin{pmatrix} -1 \\ 1 \\ -1 \end{pmatrix}, \begin{pmatrix} -1 \\ -1 \\ 1 \end{pmatrix} \right)_{(z,x,y)}$$

The rotation matrix from (z, x, y) to (u, v, w) is defined as :

$$R = \begin{bmatrix} 1 & 0 & 1 + \sqrt{2} \\ 1 + \sqrt{2} & 1 & 0 \\ 0 & 1 + \sqrt{2} & 1 \end{bmatrix}$$

The cofactor matrix of R is calculated as:

$$Cof(R) = \begin{bmatrix} 1 & -(1 + \sqrt{2}) & (1 + \sqrt{2})^2 \\ (1 + \sqrt{2})^2 & 1 & -(1 + \sqrt{2}) \\ -(1 + \sqrt{2}) & (1 + \sqrt{2})^2 & 1 \end{bmatrix}$$

And as such the transpose is:

$$\text{Cof}(R)^T = \begin{bmatrix} 1 & (1 + \sqrt{2})^2 & -(1 + \sqrt{2}) \\ -(1 + \sqrt{2}) & 1 & (1 + \sqrt{2})^2 \\ (1 + \sqrt{2})^2 & -(1 + \sqrt{2}) & 1 \end{bmatrix}$$

The determinant is : $\det(R) = 8 + 5\sqrt{2}$.

The inverse of R is thus :

$$R^{-1} = \frac{1}{8 + 5\sqrt{2}} \begin{bmatrix} 1 & (1 + \sqrt{2})^2 & -(1 + \sqrt{2}) \\ -(1 + \sqrt{2}) & 1 & (1 + \sqrt{2})^2 \\ (1 + \sqrt{2})^2 & -(1 + \sqrt{2}) & 1 \end{bmatrix}$$

And it is the change of basis matrix from (u, v, w) to (z, x, y) .

We define:

$$\begin{cases} dI du = \frac{dI}{du} \\ dI dv = \frac{dI}{dv} \\ dI dw = \frac{dI}{dw} \end{cases}$$

As the differentiate of I with respect to (u, v, w) in the (u, v, w) basis. Their counterpart in the (z, x, y) basis are:

$$\begin{cases} dI dz = \frac{1}{8 + 5\sqrt{2}} (dI du + (1 + \sqrt{2})^2 dI dv - (1 + \sqrt{2}) dI dw) \\ dI dx = \frac{1}{8 + 5\sqrt{2}} (dI dv + (1 + \sqrt{2})^2 dI dw - (1 + \sqrt{2}) dI du) \\ dI dy = \frac{1}{8 + 5\sqrt{2}} (dI dw + (1 + \sqrt{2})^2 dI du - (1 + \sqrt{2}) dI dv) \end{cases}$$

By applying the same reasoning as in the 2D case, we can calculate the distance from the initial guess of the center (z_c, x_c, y_c) to the vector \mathbf{u}_d directed by the gradients in each pixel K :

$$d_K = \frac{\|KC \wedge \mathbf{u}_d\|_{(z,x,y)}}{\|\mathbf{u}_d\|_{(z,x,y)}}$$

And we define the weights as

$$w_K = \frac{\|\mathbf{u}_d\|_{(u,v,w)}}{\|KC\|_{(z,x,y)}}$$

The notation $\| \cdot \|_{(z,x,y)}$, $\| \cdot \|_{(u,v,w)}$ defines in which basis the norm is calculated.

The goal of the radial symmetry based localization is to minimize the value of $\chi^2 = \sum_k d_k^2 w_k$, meaning we have to solve for

$$\begin{cases} \frac{d\chi^2}{dz_c} = 0 & (1) \\ \frac{d\chi^2}{dx_c} = 0 & (2) \\ \frac{d\chi^2}{dy_c} = 0 & (3) \end{cases}$$

$\frac{\partial d_k}{\partial z_c}, \frac{\partial d_k}{\partial x_c}, \frac{\partial d_k}{\partial y_c}$ were calculated and can be written as:

$$\begin{bmatrix} \frac{\partial d_k}{\partial z_c} \\ \frac{\partial d_k}{\partial x_c} \\ \frac{\partial d_k}{\partial y_c} \end{bmatrix} = \Omega_k \begin{bmatrix} z_k - z_c \\ x_k - x_c \\ y_k - y_c \end{bmatrix}$$

$$\text{With } \Omega_k = \begin{bmatrix} -2(dI dx^2 + dI dy^2) & 2dI dx dI dz & 2dI dy dI dz \\ 2dI dx dI dz & -2(dI dx^2 + dI dy^2) & 2dI dy dI dx \\ 2dI dy dI dz & 2dI dy dI dx & -2(dI dx^2 + dI dy^2) \end{bmatrix}$$

We can then write (1), (2), and (3)

As:

$$(1) \Leftrightarrow \sum_k w_k (\Omega_{11} z_k + \Omega_{12} x_k + \Omega_{13} y_k) = (\sum_k w_k \Omega_{11}) z_c + (\sum_k w_k \Omega_{12}) x_c + (\sum_k w_k \Omega_{13}) y_c$$

$$(2) \Leftrightarrow \sum_k w_k (\Omega_{21} z_k + \Omega_{22} x_k + \Omega_{23} y_k) = (\sum_k w_k \Omega_{21}) z_c + (\sum_k w_k \Omega_{22}) x_c + (\sum_k w_k \Omega_{23}) y_c$$

$$(3) \Leftrightarrow \sum_k w_k (\Omega_{31} z_k + \Omega_{32} x_k + \Omega_{33} y_k) = (\sum_k w_k \Omega_{31}) z_c + (\sum_k w_k \Omega_{32}) x_c + (\sum_k w_k \Omega_{33}) y_c$$

If we write these equations in the matrix form, we have:

$$\begin{bmatrix} \sum_k w_k (\Omega_{11} z_k + \Omega_{12} x_k + \Omega_{13} y_k) \\ \sum_k w_k (\Omega_{21} z_k + \Omega_{22} x_k + \Omega_{23} y_k) \\ \sum_k w_k (\Omega_{31} z_k + \Omega_{32} x_k + \Omega_{33} y_k) \end{bmatrix} = \begin{bmatrix} (\sum_k w_k \Omega_{11}) & (\sum_k w_k \Omega_{12}) & (\sum_k w_k \Omega_{13}) \\ (\sum_k w_k \Omega_{21}) & (\sum_k w_k \Omega_{22}) & (\sum_k w_k \Omega_{23}) \\ (\sum_k w_k \Omega_{31}) & (\sum_k w_k \Omega_{32}) & (\sum_k w_k \Omega_{33}) \end{bmatrix} \begin{bmatrix} z_c \\ x_c \\ y_c \end{bmatrix}$$

$$= \mathcal{M} \begin{bmatrix} z_c \\ x_c \\ y_c \end{bmatrix}$$

We now have to invert \mathcal{M}

The determinant of \mathcal{M} is expressed as

$$\begin{aligned} \det(\mathcal{M}) = & (\Sigma_k w_k \Omega_{11}) [(\Sigma_k w_k \Omega_{22})(\Sigma_k w_k \Omega_{33}) - (\Sigma_k w_k \Omega_{23})^2] \\ & - (\Sigma_k w_k \Omega_{12}) [(\Sigma_k w_k \Omega_{12})(\Sigma_k w_k \Omega_{33}) - (\Sigma_k w_k \Omega_{13})(\Sigma_k w_k \Omega_{23})] \\ & + (\Sigma_k w_k \Omega_{13}) [(\Sigma_k w_k \Omega_{12})(\Sigma_k w_k \Omega_{23}) - (\Sigma_k w_k \Omega_{13})(\Sigma_k w_k \Omega_{22})] \end{aligned}$$

Which can also be rewritten as

$$\det(\mathcal{M}) = (\Sigma_k w_k \Omega_{11})\alpha - (\Sigma_k w_k \Omega_{12})\beta + (\Sigma_k w_k \Omega_{13})\gamma$$

If we write

$$\delta = (\Sigma_k w_k \Omega_{11})(\Sigma_k w_k \Omega_{33}) - (\Sigma_k w_k \Omega_{13})^2$$

$$\phi = (\Sigma_k w_k \Omega_{11})(\Sigma_k w_k \Omega_{22}) - (\Sigma_k w_k \Omega_{12})^2$$

$$\epsilon = (\Sigma_k w_k \Omega_{11})(\Sigma_k w_k \Omega_{23}) - (\Sigma_k w_k \Omega_{13})(\Sigma_k w_k \Omega_{12})$$

Then we can calculate \mathcal{M}^{-1} :

$$\mathcal{M}^{-1} = \frac{1}{\det(\mathcal{M})} \begin{bmatrix} \alpha & -\beta & \gamma \\ -\beta & \delta & -\epsilon \\ \gamma & -\epsilon & \phi \end{bmatrix}$$

And thus finally we obtain (z_c, x_c, y_c) :

$$\begin{pmatrix} z_c \\ x_c \\ y_c \end{pmatrix} = \mathcal{M}^{-1} \begin{bmatrix} \Sigma_k w_k (\Omega_{11} z_k + \Omega_{12} x_k + \Omega_{13} y_k) \\ \Sigma_k w_k (\Omega_{21} z_k + \Omega_{22} x_k + \Omega_{23} y_k) \\ \Sigma_k w_k (\Omega_{31} z_k + \Omega_{32} x_k + \Omega_{33} y_k) \end{bmatrix}.$$

The Matlab implementation of this is *relatively* straightforward.

RÉSUMÉ

La microscopie par localisation ultrasonore a montré qu'il était possible de s'affranchir du compromis entre la pénétration et la résolution en échographie grâce aux ultrasons ultrarapides et à l'utilisation d'agents de contraste. Cependant, cette technique sera difficilement transposable dans un environnement clinique car elle implique : 1. de longs temps d'acquisitions, 2. un champ de vue limité à un plan, 3. l'impossibilité de corriger les mouvements hors plan, 4. des quantités de données importantes et 5. des temps de calculs extrêmement longs.

L'objectif de cette thèse a été de démontrer qu'il était possible de faire de la microscopie par localisation ultrasonore en 3D, et de montrer son potentiel *in vitro* et *in vivo*. Le point de départ a été de développer des nouvelles techniques de localisation de particules, ce qui a permis leur implémentation en 3 dimensions, et l'amélioration des l'imagerie ULM 2D. Ensuite, nous avons créé des séquences d'imagerie 4D spécifiques pour la microscopie en 3D et montré qu'il était possible d'imager avec une résolution sub-longueur d'onde un fantôme de canaux microfluidiques 3D. Après avoir éprouvé notre technique *in vitro*, nous l'avons appliquée *in vivo* sur le cerveau de rat et démontré qu'il était possible d'avoir accès à la vasculature ainsi qu'aux flux sanguins à une échelle de quelques microns. Une étape supplémentaire a été ajoutée dans le *framework* de l'algorithme afin de corriger le mouvement en 3 dimensions et de recalibrer des volumes super-résolus entre eux afin de produire le premier volume d'un cerveau de rat entier.

MOTS CLÉS

microscopie par localisation ultrasonore, super-résolution, super-localisation, ultrafast, imagerie du cerveau, 3D, 4D, imagerie volumétrique

ABSTRACT

Ultrasound Localization Microscopy has demonstrated the ability to overcome the penetration/resolution conundrum in ultrasound imaging thanks to high frame rate imaging and contrast agents. However, this approach will fall short in its clinical translation if its main disadvantages aren't addressed: 1- long time of acquisition 2- limited two dimensional field of view 3- motion artifacts 4-data overdose and 5- data processing times.

The objective of this thesis was to perform, for the first time, volumetric ultrasound localization microscopy and unveil its potential *in vitro* and *in vivo*. For this purpose, I first developed new post-processing techniques, allowing implementation of ULM on 3D data and increasing image quality. Then, I implemented new ultrasound sequences and demonstrated that sub-wavelength features could be resolved in a tailor made wall-less phantom. I then demonstrated that 3D imaging of the rat brain microvasculature with blood flow velocimetry was achievable with micrometric resolution, and implemented 3D motion correction and image registration to provide whole brain imaging.

KEYWORDS

ultrasound localization microscopy, super-resolution, super-localization, ultrafast, brain imaging, 3D, 4D, volumetric imaging